

Nonlocal collective electronic fluctuations: From model systems to realistic materials

Dissertation
zur Erlangung des Doktorgrades
an der Fakultät für Mathematik, Informatik und Naturwissenschaften
des Fachbereichs Physik
der Universität Hamburg

vorgelegt von
Viktor Harkov

Hamburg
2022

Gutachter der Dissertation:	Prof. Dr. Alexander Lichtenstein Dr. Evgeny Stepanov
Zusammensetzung der Prüfungskommission:	Prof. Dr. Alexander Lichtenstein Dr. Evgeny Stepanov Prof. Dr. Serguei Molodtsov Prof. Dr. Michael Potthoff Prof. Dr. Tim Wehling
Vorsitzende der Prüfungskommission:	Prof. Dr. Michael Potthoff
Datum der Disputation:	25.11.2022
Vorsitzender Fach- Promotionsausschusses Physik:	Prof. Dr. Wolfgang J. Parak
Leiter des Fachbereichs Physik:	Prof. Dr. Günter H. W. Sigl
Dekan der Fakultät MIN:	Prof. Dr.-Ing. Norbert Ritter

Zusammenfassung

Gegenstand der vorliegenden Arbeit ist die Entwicklung und Anwendung numerischer Methoden basierend auf quantenmechanischen Gittermodellen zur Beschreibung kollektiver Anregungen in Systemen stark korrelierter Fermionen. Zu diesem Zweck wird die effiziente D-TRILEX Methode vorgestellt, deren Herleitung auf der partiellen bosonisierung kollektiver elektronischer Anregungen basiert. Mit geringen numerischen Aufwand schafft es die Methode, die wesentlichen Effekte räumlicher Korrelationen in stark korrelierten Systemen zu beschreiben. Dabei erlaubt die spezielle Wahl der nicht renormierter Wechselwirkungen die bekannte Fierz Mehrdeutigkeit zu umgehen, die üblicherweise in Methoden basierend auf partieller Bosonisierung auftritt. Die Anwendung aufwendiger Methoden zur Berechnung realistische Systeme mit mehreren Orbitalen ist oft sehr schwierig oder gar unmöglich aufgrund der komplexen diagrammatischen Struktur und der aufwendigen Berechnung der Zwei-Teilchen Vertexfunktion. In der D-TRILEX Theorie wird die Zwei-Teilchen Vertexfunktion durch den führenden longitudinalen Beitrag bosonischer Moden genähert, sodass die diagrammatische Struktur der Selbstenergie sich drastisch vereinfacht und aufwendige Berechnung der Zwei-Teilchen Vertexfunktion entfällt. Dies ermöglicht die Berechnung komplexer Mehrorbitalsysteme.

Der Hauptteil der Arbeit behandelt die D-TRILEX Methode. Dabei wird die Methode vorgestellt und ihre Anwendung am Beispiel des zweidimensionalen Ein-Band Hubbard Models untersucht. Des Weiteren wird eine ausführliche Diagrammanalyse durchgeführt. Dabei werden Methoden mit unterschiedlichen Diagrammklassen und Näherungen für die Zwei-Teilchen Vertexfunktion miteinander verglichen. Es wird gezeigt, dass die in D-TRILEX berücksichtigten longitudinal bosonischen Moden den führenden Beitrag zu der Selbstenergie bilden. Ferner wird die D-TRILEX Methode verwendet, um Effekte kollektiver Anregungen im dotierten monolagen InSe zu studieren. Im betrachteten Parameterbereich befindet sich das System größtenteils in einem Zustand der Ladungsdichtewelle. Innerhalb dieses Zustandes wurde in Koexistenz eine ferromagnetische Phase gefunden.

D-TRILEX kann als eine Näherung der Theorie dualer Bosonen betrachtet werden. Die Theorie dualer Bosonen ist eine diagrammatische Erweiterung der dynamischen Molekularfeldtheorie, welche nicht-lokale Korrelationen störungstheoretisch behandelt. Als weiteres Resultat der Arbeit wird das Regime schwacher Wechselwirkung im Rahmen der Leiternäherung für duale Bosonen untersucht. Die Ergebnisse werden außerdem mit der numerisch exakten diagrammatischen Quanten Monte Carlo Methode verglichen. Dabei stimmen die Ergebnisse für die Ein- und Zwei-Teilchen-Größen für hohe und mittlere Temperaturen quantitativ gut überein. Jedoch werden bei niedrigen Temperaturen die antiferromagnetischen Fluktuationen in der Leiternäherung unterschätzt. Dies führt zu leichten Abweichungen zwischen den Ergebnissen der beiden Methoden.

In der letzten Untersuchung der Arbeit wird eine Parametrisierung der lokalen Zwei-Teilchen Vertexfunktion durchgeführt. Dabei wird der Vertex mittels des Hedin Vertex und renommierter Wechselwirkungen ausgedrückt im Rahmen der Ein-Boson-Austausch Zerlegung. Ähnlich zu der D-TRILEX Methode wird hier der wechselwirkungsirreduzible Teil des Vertex vernachlässigt und dadurch der Rechenaufwand erheblich reduziert. Diese Näherung für die Vertexfunktion wird verwendet, um die Suszeptibilität im Rahmen der dynamischen Molekularfeldtheorie bei unterschiedlichen Wechselwirkungsstärken und Temperaturen zu berechnen. Es wird gezeigt, dass die Näherung gute Übereinstimmung im Bereich schwacher und starker Wechselwirkungen aufweist. Im Rahmen der Untersuchung wird die wichtige Bedeutung des Hedin Vertex deutlich.

Abstract

The main focus of the present thesis lies on the development and application of numerical approaches based on quantum lattice models to describe collective excitations in strongly correlated materials. To this end, an efficient and balanced dual triply irreducible local expansion (D-TRILEX) approach that captures the major effects of spatial correlations in strongly correlated fermionic systems is presented, which is based on partial bosonization of the collective electronic fluctuations. Thereby, a specific choice of the bare interaction in the corresponding channel of instability allows a simultaneous description of collective excitations in different channels without facing the Fierz ambiguity problem which usually arises in methods based on partial bosonization. Compared to more elaborate methods, D-TRILEX does not require the computation of the numerically expensive four-point vertex. Furthermore, taking into account only the leading longitudinal contribution of the bosonic modes to the self-energy reduces the complexity of the diagrammatic structure drastically making the method applicable to more complex realistic multi-orbital systems.

As the main result of this thesis, the D-TRILEX approach is introduced and its limit of applicability is studied by applying it to the two-dimensional single-band Hubbard model. Performing a comprehensive diagrammatic analysis by comparing D-TRILEX with methods, which consider different sets of diagrams and different approximations for the four-point vertex, we find that contributions that are not considered by the partially bosonized approximation of the four-point vertex have only a minor effect on electronic degrees of freedom and the longitudinal bosonic modes taking into account in D-TRILEX self-energy are the leading ones in a broad range of control parameters. After investigating the applicability of the D-TRILEX approach we apply the method to study collective electronic effects in the hole-doped InSe monolayers using a realistic electronic-structure model. Thereby, we find that due to the weakly screened long-range Coulomb interaction the system shows a charge density waves phase for the broad range of considered parameters, however, inside this regime we have found a coexisting ferromagnetic phase.

D-TRILEX can be considered as an approximation of the more elaborate dual

boson (DB) theory, which accounts for local correlations within the dynamical mean-field theory (DMFT) and nonlocal correlations perturbatively. As a further result of this thesis, we investigate the weak coupling regime of the two-dimensional single-band Hubbard model within the ladder DB approximation and compare our results to the numerically exact diagrammatic quantum Monte Carlo (DiagMC) method. We find that the DB method qualitatively captures all the different regimes. Even quantitatively DB shows a good agreement with the exact results for single- and two-particle quantities at high and moderate temperatures. However, the ladder approximation slightly underestimates the strong antiferromagnetic fluctuations that appear in the system at low temperatures.

As the final result of this thesis, we perform a parametrization of the local four-point vertex in terms of the (three-point) Hedin vertex and screened interactions in the framework of single-boson exchange (SBE) decomposition. Similar to the D-TRILEX approach the computational costs are reduced by neglecting the interaction-irreducible part of the four-point vertex. The approximated vertex is used to calculate the DMFT susceptibility for different interaction strengths at different temperatures. We find that the approximation shows a good agreement in the limits of weak and strong couplings. Thereby, our study highlights the importance of the Hedin vertex for local vertex corrections.

Contents

Introduction	1
I Theory	7
1 Models	9
1.1 Hubbard model	9
1.2 Anderson impurity model	14
2 Concepts	15
2.1 Matsubara Green's functions	15
2.2 Dyson equation	18
2.3 Bethe-Salpeter equation and the four-point vertex	20
2.4 Coherent state path integral	24
3 Methods	27
3.1 Dynamical mean-field theory	27
3.2 Dual Boson approach	31
3.3 Partially bosonized approximation for the four-point vertex	39
3.4 D-TRILEX approach	43
3.5 Single-boson exchange decomposition for the four-point vertex	48
II Results	51
4 DB	53
4.1 Tracking the Footprints of Spin Fluctuations: A MultiMethod, MultiMessenger Study of the Two-Dimensional Hubbard Model	53
4.2 Dual boson diagrammatic Monte Carlo approach applied to the extended Hubbard model	65
5 D-TRILEX	79
5.1 Consistent partial bosonization of the extended Hubbard model	79

5.2	Impact of partially bosonized collective fluctuations on electronic degrees of freedom	94
5.3	Coexisting charge density wave and ferromagnetic instabilities in monolayer InSe	114
6	SBE	125
6.1	Parametrizations of local vertex corrections from weak to strong coupling: Importance of the Hedin three-leg vertex	125
	Summary and Outlook	143
	Bibliography	147
	List of Publications	171
	Acknowledgments	177

Introduction

Each of us meets *many-body problems* in our daily life. For example, I interact with members of my family who live in the same household. When I leave my home in the morning I may encounter the neighbour living next door picking up his newspaper. While walking down the street, I might see a neighbour from the next street, as we usually leave for work at the same time.

So far, these have been, so called, few body encounters – I’ve met a well defined and easily countable number of people, and I can simultaneously think about them: How do I handle the family argument we had this morning, can I ask my neighbour for a favor, and is the next-street-neighbour, whom I did not see today, left for vacations or just got sick today?

Then, I enter the subway and, together with hundreds of other people, go to the main station. Thousands of people are on their way to work at exactly the same moment. Nearly two million people are living in Hamburg right now. How am I related to each of them? How knows, but may be the tax accountant of mine is sitting in another wagon. The student next to me might work as a waiter in a cafe where I will go this afternoon. The guy who’s bag I stepped on accidentally might be my future dentist. And, maybe, the cookie I will have with coffee later today will be responsible for me visiting the dentist next week. And all of this happens, without any of us being aware of improbable correlations between these actions.

I keep thinking about these countless encounters, the uncountable number of people surrounding me, and the ‘if’s and ‘when’s of each of them. How do I determine which of them are relevant for me and which of them I don’t need to think about? There are just so many entities and interactions, so it’s impossible to account for all of them at every moment. But do I really have to?

Similar questions one asks in many-body physics. In particular, in condensed matter theory we want to understand how the behaviour of some electrons affects macroscopic properties of the entire system. And we ask the same question: What interaction of the many particles lead to significant outcomes and which of them can be neglected in order to make the calculations feasible?

For all practical purposes (e.g., when neglecting relativistic effects) the fundamental laws, that determine many-body phenomena we are interested in, are clear and given by the static Schrödinger equation:

$$H\psi = E\psi.$$

In solids, the position of atoms in a crystal lattice can be considered as fixed due to the significant mass difference between the nuclei and the electrons. Therefore, the first and rather accurate approximation is to consider only the motion of the electrons in a static potential V and the interaction between them. Upon neglecting the relativistic effects, the Hamiltonian of this so-called Born-Oppenheimer approximation is the following:

$$H = \sum_{i=1}^N \left(\frac{p_i^2}{2m} + V(r_i) \right) + e^2 \sum_{i<j} \frac{1}{|r_i - r_j|}. \quad (1)$$

The first term in this expression is the non-interacting part of the Hamiltonian that describes the motion of N electrons in the presence of the ionic potential $V(r_i)$. Thereby, the i -th electron with the mass m has the momentum p_i . The mutual Coulomb interaction between the electrons is described by the second term. This interaction is inversely proportional to the distance between two electrons of an elementary charge e . Due to a large number of electrons N in a macroscopic system, which is of the order of the Avogadro constant ($\mathcal{O}(10^{23})$), the exact solution for the Hamiltonian (1) is practically impossible to obtain. To approach the solution numerous approximations have been developed over time.

In many materials the interaction between the electrons can be considered as rather weak due to screening effects related, e.g., to the spatially extended nature of the s - and p -orbitals. In this case, mean-field theories, where the many-electron problem is mapped onto an effective problem of a single electron interacting with an effective field caused by the other electrons, yield results in good agreement with experiments. The most famous mean-field like approaches are the Landau-Fermi liquid theory (FL) [1] and the local density functional approximation (LDA). The latter is the most common approximation used in the framework of the density functional theory (DFT) theory [2, 3]. DFT is based on the Kohn-Sham theorem [2] that says that the ground state of a material is a functional of only the density of the electrons and can be obtained by minimizing the universal functional. Even though this would yield the exact ground state of the system, the universal functional is *a priori* unknown and thus has to be approximated. The most common approach is the LDA [4], where the exchange-correlation energy (the unknown part of the universal functional) is approximated by a homogeneous but interacting electron gas. With this approximation, DFT can be successfully applied to simple metals,

semiconductors, and band-insulators. However, it fails even at a qualitative level when applied to strongly correlated materials, like the Mott insulator NiO, where it predicts a metallic phase.

All the theories mentioned so far are not suitable for addressing physical phenomena when electronic correlations in the system become strong, i.e. the interaction of electrons among each other cannot be correctly described within a mean-field approach only. For instance, it happens when the Coulomb interaction between the electrons is of the same order of magnitude as their kinetic energy. Such behavior can be found in materials with partially filled d - and f -orbitals, like lanthanides, actinides, and transition metal oxides. A standard way to tackle the problem is to introduce an interacting electronic model for the system of interest. The simplest model that describes the behavior of interacting electrons in a crystal is the Hubbard model. In this model, the interaction between the electrons is assumed to be local, which means that only electrons that are sitting at the same lattice site interact between themselves. (This will be discussed in more detail in section 1.1). However, this approximation still allows one to capture the essential properties of the system. Despite seeming simplicity, the exact analytical solution for the Hubbard model can be obtained only in one dimension [5]. In higher dimensions, solving the Hubbard model requires the use of some approximations or numerical techniques. One of the most famous numerical approaches that can be used for this purpose is the dynamical mean-field theory (DMFT) [6]. This theory performs a self-consistent mapping of the Hubbard model onto an Anderson impurity model (AIM) that is solved numerically exactly. Even though this mapping is exact only in infinite dimensions, DMFT turns out to be a very good approximation also in finite dimensions in the case when local correlations in the system are dominant.

A significant advance in our understanding of correlated materials has come through the development of DMFT. For the first time, it allowed to capture the coherent quasi particles at Fermi energy and incoherent excitations at high energies (Hubbard bands) simultaneously and provided a proper understanding of the Mott transition [7]. Nowadays, LDA combined with DMFT is an established approach to capture the effect of local correlations in real materials¹. A famous example is the successful description of the many-body features of the single electron spectrum and magnetic properties in iron and nickel [9]. However, DMFT accounts only for the local part of electronic correlations while the nonlocal ones are completely neglected. But the latter can have a crucial impact on several physical phenomena, e.g., in low-dimensional systems, where the interaction between electrons is usually long-range and weakly-screened [10–14].

¹For an extensive review on LDA+DMFT the reader is referred to [8].

One way to consider the nonlocal correlations is a mean-field theory (MFT) based on a partial bosonization of collective electronic fluctuations in leading channels of instability. Thereby, these collective excitations are taken into account by performing a diagrammatic expansion around a proper reference system. This procedure enables a simple diagrammatic treatment of a problem in terms of electrons interacting using effective bosonic fields. Still, as has already been mentioned, MFT only yields proper results when correlations between electrons are rather weak. In the case of strongly-correlated electronic systems more advanced approaches are required. Such methods are usually based on DMFT in order to ensure a proper description of local correlation effects. One possible way to take into account nonlocal correlations based on DMFT is to perform a cluster extension of this theory, where a single site AIM is replaced by a cluster problem that contains several lattice sites. Theories like CDMFT [15, 16] and DCA [17–19] belong to this class. However, such an extension often breaks the translational symmetry of the system [17, 20] and is able to account for only short-range correlation effects limited by the size of the cluster². To capture correlations at all length scales diagrammatic extensions around the DMFT solution, which serves as the reference system, can be performed. Thereby, following the mean-field idea, a partially bosonized description of collective electronic excitations leads to methods like $GW+DMFT$ [21–27] and triply irreducible local expansion (TRILEX) [28–30]. $GW+DMFT$ is a simple method and does not involve any vertex corrections. This makes the approach numerically inexpensive and, for this reason, it is often used in realistic multi-band calculations [22, 31–37]. However, these vertex corrections are known to play a very important role for an accurate description of magnetic, optical, and transport properties of the system [37–46]. In addition, $GW+DMFT$ takes into account only collective charge fluctuations and neglects magnetic ones. The diagrammatic structure of the TRILEX method is similar to the one of $GW+DMFT$, but contains exact local three-point Hedin vertex corrections [47]. In addition, the TRILEX approach attempts to account for the fluctuations in the magnetic channel, which, however, leads to a famous Fierz ambiguity problem when both, charge and spin channels are considered simultaneously [30, 48, 49]. This means that the way these channels are introduced in the theory has a significant impact on the result of the calculation. More elaborate methods that perform a diagrammatic expansion on top of (E)DMFT are the dynamical vertex approximation (D Γ A) [50–53], the dual fermion (DF) method [54–57], and the dual boson (DB) approach [58–62]. In general, the calculations using these methods are rather accurate but suffer from high computational costs due to the complex diagrammatic structure and the use of the four-point vertex functions. Therefore, to this day, realistic multi-band calculations

²Note that increasing the size of the cluster increases the computational costs drastically since the Hilbert space grows exponentially with the number of sites in a cluster.

in the framework of these methods are limited to only a few works [63–66].

In this thesis, a new method called dual triply irreducible local expansion (D-TRILEX) which can be seen as an approximation of the DB approach is presented. The derivation of this method is based on the partially bosonized representation for the renormalized local four-point vertex function, which approximates the four-point vertex in terms of the three-point (Hedin) vertices and bosonic propagators. Similar vertex decomposition can be found in [67–71]. It is demonstrated that the specific choice of the partially bosonized approximation introduced in D-TRILEX [72], namely taking into account only longitudinal bosonic modes, reduces the complexity of the diagrammatic structure to the level of $GW+DMFT$ or TRILEX methods while keeping the efficiency of DB theory even in strongly correlated regimes. Such a representation allows one to explicitly consider the contributions of collective excitations from different channels of instability. Another advantage of D-TRILEX is that considering different channels, e.g., charge and magnetic channels, does not lead to the Fierz ambiguity problem. Furthermore, unlike in the original formulation of the TRILEX method, D-TRILEX takes into account vertex corrections in the self-energy and in the polarization operator in a symmetric way. Overall, D-TRILEX shows the most optimal balance between computational efficiency and complexity. It was already successfully applied to several multi-orbital systems [38, 73, 74].

Additionally, in the framework of this thesis, a similar parametrization of the local four-point vertex is performed. This parametrization is called single-boson exchange (SBE) decomposition [70]. The SBE approximation is applied on the four-point vertex to study two-particle quantities within DMFT and its diagrammatic extensions [75]. The study highlights the importance of the Hedin vertex in the weak and strong coupling limits. Similar to D-TRILEX, the SBE approximation reduces computational costs by excluding the U -irreducible part of the four-point vertex. However, in SBE approximation the transverse and particle-particle bosonic modes are taken into account.

As the main part of this thesis, the D-TRILEX approach is introduced and applied to the single-band Hubbard model. The thesis consists of three parts. In **Part I** the Hubbard and Anderson models as well as the basic concepts which are relevant to this thesis are introduced. Further, DMFT and the DB approach are introduced followed by the partially bosonized approximation for the four-point vertex. Then the D-TRILEX formalism is presented. Finally, an overview of the SBE decomposition is given. In the main part, **Part II**, the results are presented. This part is divided into three. First, in **Chapter 4** DB approach is compared to numerically exact DiagMC results in different regimes. **Chapter 5** is the main part of this thesis. Here, the D-TRILEX theory is introduced and the limits of applicability of the method are studied. In the last part, **Chapter 6**, a parametrization of the local four-point vertex of the Anderson impurity model in terms of SBE is used to calculate the

Néel temperature of DMFT and investigate the role of the tree-point Hedin vertex corrections.

Finally, the main conclusions and an outlook on prospective research based on the findings of this work are given.

Part I

Theory

Chapter 1

Models

In this chapter, the single-band Hubbard model and its extension as well as the Anderson model are introduced. The concepts presented here can be found in standard literature about many-body physics and condensed matter field theory like e.g. [76–79]. Knowledge of fundamental quantum mechanics and second quantization is required.

1.1 Hubbard model

In condensed matter physics, when it comes to systems with strong electronic correlations the computational costs needed to accurately solve the many-electron problem are usually very high or even not affordable at all. Hence, in practice, simpler methods that are able to capture the main properties of the system are used. Such methods are usually constructed using methods of quantum field theory. Thereby, the many-body Hamiltonian 1 can be written in a second quantization form in terms of field operators $\Psi_\sigma(\mathbf{r})$ as follows:

$$\begin{aligned}
 H &= H_0 + H_{int} \\
 &= \sum_{\sigma} \int d^d r \Psi_{\sigma}^{\dagger}(\mathbf{r}) \left(-\frac{\hbar^2 \Delta}{2m} + V(\mathbf{r}) \right) \Psi_{\sigma}(\mathbf{r}) \\
 &\quad + \frac{1}{2} \sum_{\sigma\sigma'} \int d^d r d^d r' \Psi_{\sigma}^{\dagger}(\mathbf{r}) \Psi_{\sigma'}^{\dagger}(\mathbf{r}') \frac{e^2}{|\mathbf{r} - \mathbf{r}'|} \Psi_{\sigma'}(\mathbf{r}') \Psi_{\sigma}(\mathbf{r}). \tag{1.1}
 \end{aligned}$$

In this expression the lattice potential $V(\mathbf{r}) = V(\mathbf{r} + \mathbf{R})$ is periodic with respect to the lattice vector \mathbf{R} . The up or down projection of the spin of an electron is denoted by $\sigma \in \{\uparrow, \downarrow\}$. The mass of an electron is given by m , and the elementary charge is denoted by e . The antisymmetric properties of the many-body states impose anticommutation relations between creation and annihilation operators, respectively,

which are given by¹

$$[\Psi_\sigma(\mathbf{r}), \Psi_{\sigma'}(\mathbf{r}')]_+ = 0, \quad [\Psi_\sigma(\mathbf{r}), \Psi_{\sigma'}^\dagger(\mathbf{r}')]_+ = \delta_{\sigma\sigma'} \delta(\mathbf{r} - \mathbf{r}'). \quad (1.2)$$

Since the single-particle part of the Hamiltonian H_0 is periodic, the eigenfunctions of H_0 , according to the Bloch theorem, are Bloch states with the eigenvalues $\varepsilon_{\mathbf{k}}$ that have the following form

$$\Psi_{\mathbf{k}}(\mathbf{r}) = e^{i\mathbf{k}\mathbf{r}} u_{\mathbf{k}}(\mathbf{r}), \quad (1.3)$$

with the wave vector \mathbf{k} which takes values in the first Brillouin zone. The function $u_{\mathbf{k}}(\mathbf{r})$ obeys the symmetry of the lattice. The Bloch states form a complete basis with respect to the non-interacting Hamiltonian H_0 and, hence, each field operator can be expressed in terms of this basis. Bloch states suit well as a basis for systems with the extended s - and p -valence electrons. However, for strongly correlated systems, where valence electrons are rather localized d - and f -shell electrons, we can use the freedom to choose the phases of the Bloch function and construct a new basis using more appropriate localized Wannier functions ϕ . Wannier functions are related to the Bloch function in the following way

$$\Psi_{\mathbf{k}}(\mathbf{r}) = \frac{1}{\sqrt{N}} \sum_{\mathbf{R}} e^{i\mathbf{k}\mathbf{R}} \phi(\mathbf{r} - \mathbf{R}), \quad \phi(\mathbf{r} - \mathbf{R}) = \frac{1}{\sqrt{N}} \sum_{\mathbf{k}} e^{-i\mathbf{k}\mathbf{R}} \Psi_{\mathbf{k}}(\mathbf{r}). \quad (1.4)$$

Next, one can define the annihilation (creation) operator in the Wannier space $c_{i\sigma}^{(\dagger)}$ and rewrite the Hamiltonian (1.1) using the following basis transformation from the real to the Wannier space,

$$\Psi_\sigma^{(\dagger)}(\mathbf{r}) = \sum_i \phi^{(*)}(\mathbf{r} - \mathbf{R}_i) c_{i\sigma}^{(\dagger)}. \quad (1.5)$$

As the result, one gets the lattice representation for the Hamiltonian:

$$H = \sum_{ij,\sigma} t_{ij} c_{i\sigma}^\dagger c_{j\sigma} + \sum_{ijkl} \sum_{\sigma\sigma'} U_{ijkl} c_{i\sigma}^\dagger c_{j\sigma'}^\dagger c_{l\sigma'} c_{k\sigma}, \quad (1.6)$$

with the following matrix elements for the hopping amplitude

$$\begin{aligned} t_{ij} &= - \int d^d r \phi^*(\mathbf{r} - \mathbf{R}_i) \left(- \frac{\hbar^2 \Delta}{2m} + V(\mathbf{r}) \right) \phi(\mathbf{r} - \mathbf{R}_j) \\ &= - \frac{1}{N} \sum_{\mathbf{k}} e^{i\mathbf{k}(\mathbf{R}_i - \mathbf{R}_j)} \varepsilon_{\mathbf{k}}, \end{aligned} \quad (1.7)$$

¹Note that in this thesis we only consider fermionic many-body states.

and the interaction

$$U_{ijkl} = \frac{1}{2} \int d^d r \int d^d r' \phi^*(\mathbf{r} - \mathbf{R}_i) \phi^*(\mathbf{r}' - \mathbf{R}_j) \frac{e^2}{|\mathbf{r} - \mathbf{r}'|} \phi(\mathbf{r}' - \mathbf{R}_k) \phi(\mathbf{r} - \mathbf{R}_l). \quad (1.8)$$

The Hamiltonian (1.6) is the exact *tight-binding representation* of Eq. (1.1). We limit ourselves to the nearest-neighbor approximation for the hopping amplitude: $t_{ij} = -t$ if i and j are nearest-neighbor lattice sites, and $t_{ij} = 0$ otherwise. This approximation is valid for materials, where the valence electrons are tightly bounded to the rest of the atom, which is the case of systems with partially filled d - and f -shells. In some cases mentioned explicitly, we additionally take into account more distant hopping processes. Further, we assume that the intra-atomic Coulomb interaction is much larger than the inter-atomic one and consider only the local part of the Coulomb interaction:

$$\sum_i \sum_{\sigma\sigma'} U_{iiii} c_{i\sigma}^\dagger c_{i\sigma'}^\dagger c_{i\sigma'} c_{i\sigma} = \sum_i U n_{i\uparrow} n_{i\downarrow}, \quad (1.9)$$

where the particle number operator $n_{i\sigma} = c_{i\sigma}^\dagger c_{i\sigma}$ is introduced. The *on-site* Coulomb interaction is set to $U_{iiii} = U/2$, which leads to a single-band Hamiltonian of the Hubbard model [80–84]:

$$H = -t \sum_{\langle ij \rangle, \sigma} c_{i\sigma}^\dagger c_{j\sigma} + U \sum_i n_{i\uparrow} n_{i\downarrow}, \quad (1.10)$$

where $\langle ij \rangle$ denotes that the sum is taken only over the nearest-neighbor lattice sites.

In this thesis, we mainly focus on the two-dimensional single-band Hubbard model. Let us recall some basic properties of this system in the absence of the Coulomb interaction at half-filling, where the average electronic density at each lattice site is $n = 1$. The chemical potential is set to $\mu = 0$ and the hopping $t = 1$ defines the energy scale of the system. The dispersion of the electrons in the system is following

$$\varepsilon_{\mathbf{k}} = -2[\cos(k_x) + \cos(k_y)], \quad (1.11)$$

which yields the bandwidth $D = 8t$. The momentum dependence of the dispersion along the high-symmetry path is shown in Fig. 1.1 (c). The plateau at the antinodal point $(0, \pi)$ leads to a van Hove singularity in the density of states (DOS) depicted in Fig. 1.1 (b). When we consider the electronic dispersion in the first Brillouin zone shown in Fig. 1.1 (a), we can see that the Fermi surface (black line) has a shape of a diamond leading to a perfect nesting of the momentum vector $\mathbf{q} = (\pi, \pi)$ that connects different points on the Fermi surface (black arrows). Such nesting is responsible for strong antiferromagnetic fluctuations in the system.

Nowadays, the Hubbard model is a standard model to study strongly correlated

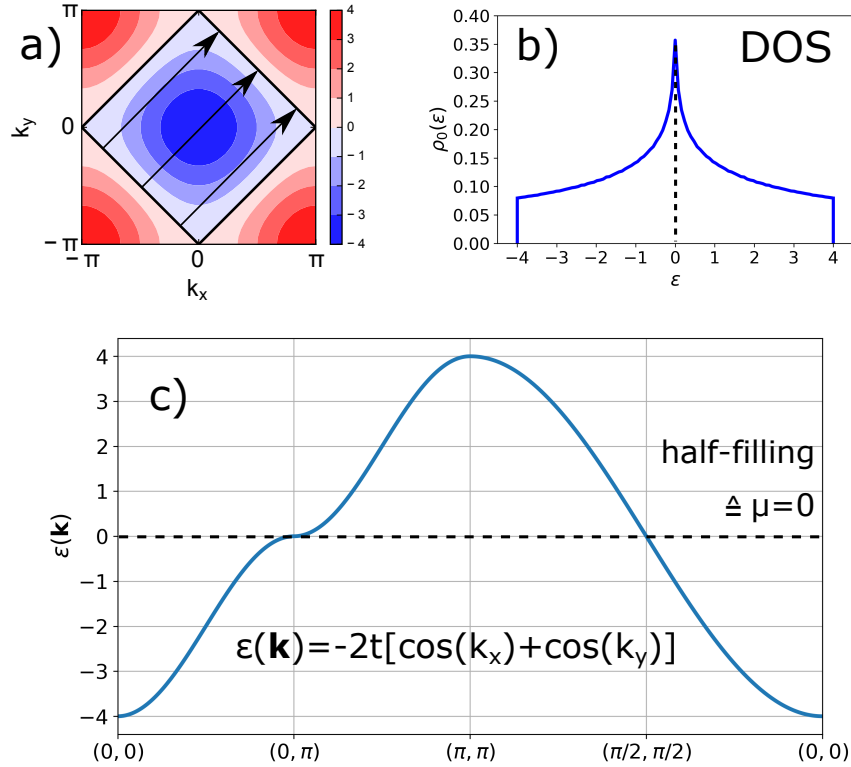


FIGURE 1.1: (a) Electronic dispersion in the first Brillouin zone of the tight-binding model for the square lattice. The hopping parameter is set to $t = 1$. Black solid lines denote the Fermi surface ($\mu = 0$). The arrows show the vector $\mathbf{q} = (\pi, \pi)$ connecting points of the Fermi surface and characterizing perfect nesting. (b) The corresponding density of states $\rho_0(\varepsilon)$ as a function of energy ε . (c) Dispersion along a high symmetry path. At the antinodal point $(0, \pi)$ one can see a plateau leading to the van Hove singularity at the Fermi level shown in (b). The figure is adapted from Ref. [85].

systems. It played a central role in the study of magnetism [86, 87], Mott transition [88, 89], and motion of electrons in high-temperature superconductors [90–92].

However, many features remain not understood. But even though the Hubbard model is rather a simple approximation of realistic systems, it can be realized in experiments of cold atomic gases in optical lattices [93–95].

Similar to the next-nearest-neighbor hopping the Coulomb interaction can also be extended taking into account nonlocal matrix elements in Eq. (1.1). In this case, the Hubbard model is called *extended*.

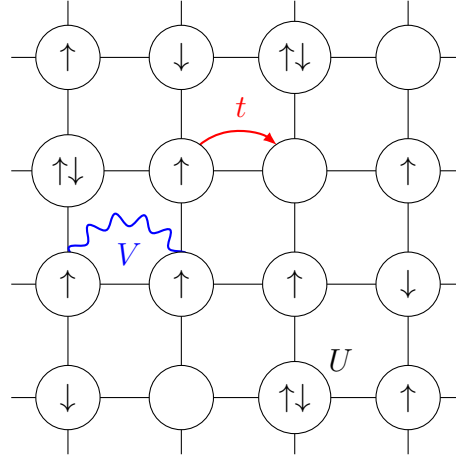


FIGURE 1.2: The schematic representation of the extended Hubbard model (1.12) in the real space for a square lattice. The sites are depicted by cycles and the spin of a particle occupying a site by a black arrow. The next neighbor hopping is indicated by a red arrow and t , the nonlocal interaction by a wiggly blue line and V , and the on-site Coulomb repulsion by U .

Extended Hubbard model

The Hubbard model presented in Eq. (1.10) disregards the nonlocal interaction between electronic densities. In order to properly describe charge fluctuations in the system account for their effect on the electronic dispersion it is necessary to include the inter-site Coulomb interaction. As in the case of the hopping amplitude, we restrict ourselves to nearest-neighbor electronic interactions (in addition to the local one). In this case the Hamiltonian (1.6) takes the following form

$$H = -t \sum_{\langle ij \rangle \sigma} c_{i\sigma}^\dagger c_{j\sigma} + U \sum_i n_{i\uparrow} n_{i\downarrow} + \frac{1}{2} \sum_{\langle ij \rangle} \sum_{\alpha} V_{ij}^{\alpha} \rho_i^{\alpha} \rho_j^{\alpha}, \quad (1.12)$$

where V_{ij}^{α} denotes the nonlocal interactions in the charge ($\alpha = \text{ch}$) and the magnetic ($\alpha = \text{sp} \in \{x, y, z\}$) channels. For convenience, the last term in this expression is written in terms of variables that describe fluctuations of the densities around the average value: $\rho_i^{\alpha} = n_i^{\alpha} - \langle n^{\alpha} \rangle$. Usually, the magnetic exchange interaction term $V_{ij}^{\text{sp}} = -J_{ij}$ is very small and thus can be neglected. The schematic representation of the extended Hubbard model is depicted in Fig. 1.2. On the contrary, the density-density interactions $V_{ij}^{\text{ch}} = V_{ij}$ are sometimes taken into account. In two-dimensional materials, for instance, the nonlocal Coulomb interaction can be weakly screened and long-ranged [10]. This is a direct consequence of the reduced dimensionality [13,

14] and may result in a Coulomb-driven charge density wave (CDW) instability [96, 97].

1.2 Anderson impurity model

The Anderson impurity model (AIM) was first introduced by P.W. Anderson in 1961 [98] to study the formation of local magnetic moments in impurity atoms with partially filled d - or f -shells embedded in a metal, where the interaction between electrons is small and can be modeled by a non-interacting *bath*. The impurity and the bath interact with each other by exchanging electrons. The Hamiltonian of AIM therefore can be divided into three parts as

$$H_{AIM} = H_{imp} + H_{bath} + H_{hyb}, \quad (1.13)$$

where the first term describes the impurity with four eigenstates $\{|0\rangle, |\uparrow\rangle, |\downarrow\rangle, |\uparrow\downarrow\rangle\}$ as

$$H_{imp} = \sum_{\sigma} \varepsilon_{\sigma}^{imp} c_{\sigma}^{\dagger} c_{\sigma} + U n_{\uparrow} n_{\downarrow}, \quad (1.14)$$

where the operator $c_{\sigma}^{(\dagger)}$ annihilates (creates) an electron on the impurity with the spin σ and energy $\varepsilon_{\sigma}^{imp}$. The number of particles with the corresponding spin on the impurity is described by $n_{\sigma} = c_{\sigma}^{\dagger} c_{\sigma}$, and U denotes the Coulomb repulsion between two electrons occupying the impurity simultaneously. As mentioned previously the AIM neglects the mutual interaction of electrons in the bath, so that the Hamiltonian of the bath takes the following simple form,

$$H_{bath} = \sum_{\mathbf{k}\sigma} \varepsilon_{\mathbf{k}} f_{\mathbf{k}\sigma}^{\dagger} f_{\mathbf{k}\sigma}. \quad (1.15)$$

Here $f_{\mathbf{k}\sigma}^{(\dagger)}$ annihilates (creates) an electron in the bath with spin σ , and $\varepsilon_{\mathbf{k}}$ denotes the dispersion of the electrons. The last term in the Hamiltonian describes the hybridization between the impurity and the bath:

$$H_{hyb} = \sum_{\mathbf{k}\sigma} (V_{\mathbf{k}} c_{\sigma}^{\dagger} f_{\mathbf{k}\sigma} + V_{\mathbf{k}}^* f_{\mathbf{k}\sigma}^{\dagger} c_{\sigma}). \quad (1.16)$$

The hopping of electrons between the impurity and the bath is parameterized by the probability amplitude $V_{\mathbf{k}}$.

The Anderson model can be solved numerically exactly by means of, e.g., continuous-time quantum Monte Carlo solvers [99–103] with improved estimators [104–106].

Chapter 2

Concepts

In this section we give an overview over the theoretical concepts used in this thesis. First, the formalism of Matsubara Green's functions on the lattice is introduced. A general comprehensive summary of the Green's functions in the many-body physics would overextend this work. Thus for further details we refer the reader to the literature (see e.g. [76]). For an thorough and systematic analysis of the n-particle Green's function and their properties the reader is also referred to [107, 108] and to the doctoral thesis of G. Rohringer [109]. Further, the Dyson and the Bethe-Salpeter equations are derived. The final part of this chapter about the path integral formalism closely follows the derivation in Ref. [76].

2.1 Matsubara Green's functions

Due to a large number of particles in the system, it is more common to work with Green's functions instead of constructing many-particle wave function of the system from single particle wave functions. The full Green's function contains the full information about the system including all interactions of electrons with each other. But since the solution of the many-body problem can be obtained only approximated, developing Green's functions based methods accordingly means approximating the full Green's functions. In this thesis we focus on single- and two-particle Green's functions.

The single-particle Green's function is directly connected to an experimentally measurable spectral function $A(\mathbf{k}, w) = 1/\pi \text{Im}G(\mathbf{k}, w)$ that can be measured in the angle-resolved photoemission spectroscopy (ARPES) experiments where it is even possible to qualitatively differentiate contribution from different types of interactions [110, 111]. The spectral function provides the spectrum of single-particle excitations in the system.

The two-particle Green's functions in turn are connected to the response of the system to external fields, the susceptibility, and can be measured by the inelastic neutron and X-ray (RIXS) scattering techniques [112–114], or by electron energy loss

spectroscopy (EELS) [115], and nuclear magnetic resonance (NMR) methods [116, 117].

Here, we consider the imaginary time Green's functions defined as the thermodynamic average of time-ordered products of annihilation and creation operators. In particular, the single-particle lattice Green's function is defined as

$$G_{ij\sigma}(\tau) = -\langle \mathcal{T} c_{i\sigma}(\tau) c_{j\sigma}^\dagger(0) \rangle = -\Theta(\tau) \langle c_{i\sigma}(\tau) c_{j\sigma}^\dagger(0) \rangle + \Theta(-\tau) \langle c_{j\sigma}^\dagger(0) c_{i\sigma}(\tau) \rangle, \quad (2.1)$$

where $\tau \in [0, \beta]$ is the imaginary time and $\beta = 1/T$ is the inverse temperature and \mathcal{T} is the time-ordering operator. The Green's function is invariant under time translation and hence depends only on the time difference $G_{ij\sigma}(\tau, \tau') = G_{ij\sigma}(\tau - \tau')$, where the triangular brackets denote the thermodynamic average

$$\langle A \rangle = \frac{1}{Z} \text{Tr}(e^{-\beta\mathcal{H}} A), \quad (2.2)$$

with the partition function

$$Z = \text{Tr}(e^{-\beta\mathcal{H}}), \quad (2.3)$$

where the Hamiltonian $\mathcal{H} = H - \mu N$ describes a grand canonical system with the chemical potential μ and the particle number operator N . And the trace $\text{Tr}(\dots) = \sum_n \langle n | \dots | n \rangle$ denotes a summation over a complete set of states in the Fock space. The creation and annihilation operators are considered in the Heisenberg picture,

$$c_i^{(\dagger)}(\tau) = e^{\tau\mathcal{H}} c_i^{(\dagger)} e^{-\tau\mathcal{H}}. \quad (2.4)$$

Since the many-body problems are typically translationally invariant in space for convenience in this work we consider the Green's functions in the reciprocal space determined by the Fourier transformation

$$G_{\mathbf{k}} = \frac{1}{N} \sum_{ij} G_{ij} e^{i(\mathbf{r}_i - \mathbf{r}_j)\mathbf{k}}, \quad G_{ij} = \frac{1}{N} \sum_{\mathbf{k}} G_{\mathbf{k}} e^{-i(\mathbf{r}_i - \mathbf{r}_j)\mathbf{k}}. \quad (2.5)$$

As a consequence, the Green's function is diagonal in the momentum space. Analogously, the Fourier transformation can be applied to the creation and annihilation operators

$$c_{\mathbf{k}} = \frac{1}{\sqrt{N}} \sum_i c_i e^{i\mathbf{r}_i\mathbf{k}}, \quad c_i = \frac{1}{\sqrt{N}} \sum_{\mathbf{k}} c_{\mathbf{k}} e^{-i\mathbf{r}_i\mathbf{k}}. \quad (2.6)$$

The imaginary time Green's function is related to the Matsubara Green's function through the following transformation

$$G_{ij}(i\nu) = \int_0^\beta d\tau G_{ij}(\tau) e^{i\nu\tau}, \quad G_{ij}(\tau) = \frac{1}{\beta} \sum_{n=-\infty}^{\infty} G_{ij}(i\nu) e^{-i\nu\tau}, \quad (2.7)$$

where $\nu_n = (2n + 1)\pi/\beta$ are the discrete fermionic Matsubara frequencies¹. The discretization arises from the fact that the imaginary time Green's function is anti-periodic with $G(\tau + \beta) = -G(\tau)$ and is defined on the finite interval $\tau \in [0, \beta]$. Furthermore, since in this thesis we are merely considering the paramagnetic case, due to SU(2) symmetry, the Green's function becomes spin independent $G_{\uparrow\uparrow} = G_{\downarrow\downarrow}$.

In order to obtain the observable quantities from the Matsubara Green's functions in terms of real energies one has to perform analytical continuation. Consider as an example again the spectral function and the relation

$$G(i\nu) = \int_{-\infty}^{\infty} d\omega \frac{1}{i\nu - \omega} A(\omega). \quad (2.8)$$

But due to numerical noise in $G(i\nu)$ the solution to this problem is ill-posed. There are infinitely many $A(\omega)$ that approximately satisfy this relation. Naively trying to find one that best approximates the solution by minimizing the deviation in the context of some chosen measure leads to over-fitting and strongly fluctuating result. Thus one needs more sophisticated methods. The ones used in this work are analytical continuation using the maximum entropy method implemented in the `ana_cont` package [118] and stochastic optimization method for analytic continuation (SOM) [119].

The (two-particle) four-point correlation function in the momentum space is defined as [108],

$$G_{\mathbf{k}\mathbf{k}'\mathbf{q}}^{(2),\sigma_1\sigma_2\sigma_3\sigma_4}(\tau_1, \tau_2, \tau_3) = -\langle \mathcal{T} c_{\mathbf{k}\sigma_1}(\tau_1) c_{\mathbf{k}+\mathbf{q}\sigma_2}^\dagger(\tau_2) c_{\mathbf{k}'+\mathbf{q}\sigma_3}(\tau_3) c_{\mathbf{k}'\sigma_4}^\dagger(0) \rangle, \quad (2.9)$$

where one momentum index and one time index was dropped due to the corresponding translational invariance. This representation of the four-point correlation function is called particle-hole notation, since this process can be considered as a scattering between a particle and a hole. This notation is used to investigate charge and spin fluctuations in the system. In the paramagnetic case the four-point correlation function is diagonal in the charge and spin channels. The transformation can

¹Note that the index n is sometimes omitted for sake of simplicity.

be performed using Pauli matrices σ^α as [120],

$$G_{\mathbf{k}\mathbf{k}'\mathbf{q}}^{(2),\alpha}(\tau_1, \tau_2, \tau_3) = -\frac{1}{2} \sum_{\sigma_1\sigma_2\sigma_3\sigma_4} \sigma_{\sigma_1\sigma_2}^\alpha \sigma_{\sigma_3\sigma_4}^\alpha \langle \mathcal{T} c_{\mathbf{k}\sigma_1}(\tau_1) c_{\mathbf{k}+\mathbf{q}\sigma_2}^\dagger(\tau_2) c_{\mathbf{k}'+\mathbf{q}\sigma_3}(\tau_3) c_{\mathbf{k}'\sigma_4}^\dagger(0) \rangle \quad (2.10)$$

The four-point correlation function has $2^4 = 16$ spin components in general. However, spin conservation leads to 6 non-vanishing components. From the 6 only two remain relevant, namely, $\uparrow\uparrow\uparrow\uparrow$ and $\uparrow\uparrow\downarrow\downarrow$. The others can be extracted from them using the SU(2) or the crossing symmetries [109]. The relevant components can be expressed in the shorthand notation $\sigma\sigma'$, where σ describes the first two and σ' the last two spin components. Finally, the four-point correlation function can be transformed to the momentum space due to

$$G_{kk'q}^{(2),\sigma\sigma'} = \int_0^\beta d\tau_1 d\tau_2 d\tau_3 e^{i\nu\tau_1} e^{-i(\nu+\omega)\tau_2} e^{i(\nu'+\omega)\tau_3} G_{\mathbf{k}\mathbf{k}'\mathbf{q}}^{(2),\sigma\sigma'}(\tau_1, \tau_2, \tau_3), \quad (2.11)$$

where compact notations $k = (\mathbf{k}, \nu)$ and $q = (\mathbf{q}, \omega)$ were defined.

2.2 Dyson equation

The Dyson equation can be derived diagrammatically in the framework of perturbation theory. It is a powerful tool where the problem is divided in a exactly solvable reference problem and a small perturbation. The Hamiltonian can then be written as $H = H_0 + H_{int}$ as in the case of the Hubbard Hamiltonian (1.10). Thereby we perform a perturbation expansion around the non-interacting system, i.e. $U = 0$, described by H_0 which can be solved exactly. For a detailed explanation of perturbation theory and Feynman diagrams the reader is referred to [76–78, 121]. In this chapter we will consider only some features which are needed for the derivation of the Dyson equation. There are two basic object needed to construct the diagrams. The first object is the non-interacting (bare) propagator G^0 describing a free propagation of an electron (hole). Note that for the sake of readability we drop the indices. The second object is the interaction U , a dot (dashed line) connecting two incoming and two outgoing lines representing two fermions interacting with each other. There is frequency, momentum and spin conservation at each vertex. In the case of Hubbard interaction both fermions have the opposite spin. Now, using these two objects we can construct any diagram appearing in the perturbation expansion. However, we are interested in the (full) interacting propagator G . It can be calculated by summing over all possible connected diagrams. Let us find a way to collect all the diagrams systematically. To

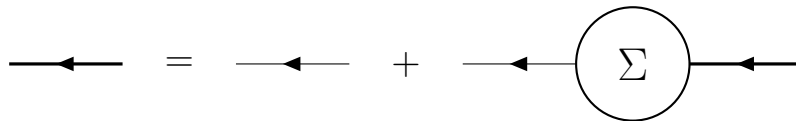


FIGURE 2.1: Diagrammatic depiction of Dyson's equation (2.13). Thin lines denote non-interacting Green's functions, the bold lines denote interacting Green's functions and the circle denotes the self-energy.

do so, first, we define the so-called self-energy *insertions* [78, 122]. Those are any parts of diagrams without external lines. Since the external lines are missing, these diagrams parts can be inserted into any propagator in the diagrammatic series. Such insertions can be classified in two topologically different types. The first class can be divided in two disconnected parts by removing a single propagator line. Those diagrams are called *(one-particle) reducible*. The rest of the diagrams belong to the second class and are called *(one-particle) irreducible*. Using this classification we can define the self-energy Σ diagrammatically as the sum over all possible irreducible self-energy insertions. By connecting all irreducible self-energy insertions with bare propagators, we find a way to collect all possible diagrams systematically. Summing over all contributions leads us to the Dyson equation:

$$G = G^0 + G^0 \Sigma G^0 + G^0 \Sigma G^0 \Sigma G^0 + \dots, \quad (2.12)$$

which can be written in a self-consistent equation as

$$G = G^0 + G^0 \Sigma G. \quad (2.13)$$

Analogously the Dyson equation can be rewritten in the following way

$$\Sigma = [G^0]^{-1} - G^{-1}. \quad (2.14)$$

Since we have found a way to construct diagrams for the interacting Green's function we can reformulate the definition of the self-energy to express it in terms of interacting Green's function which we also call *dressed*. Therefore we first define the so-called *skeleton diagrams* [122]. Those are irreducible self-energy diagrams without any self-energy insertions. The skeleton diagrams can then be dressed by replacing all the bare propagators with the interacting ones. With this Σ can be defined as the sum over all possible dressed skeleton diagrams. This definition of self-energy is called *skeleton-diagram expansion* [122].

The bare Green's function of the Hubbard model can be obtained from

$$G_k^0 = \frac{1}{i\nu - \varepsilon_{\mathbf{k}} + \mu}, \quad (2.15)$$

with dispersion $\varepsilon_{\mathbf{k}}$ and chemical potential μ . To determine the exact solution of the interacting Green's function G is usually not possible because the exact self-energy is unknown, even for simple models such as the Hubbard model. Only for some specific cases the self-energy can be calculated. For this reason, we try to find the best possible approximation for the self-energy Σ . All the information about the electronic correlations of the system is contained in the self-energy. Especially, the momentum dependence of Σ provides information about spatial correlation.

2.3 Bethe-Salpeter equation and the four-point vertex

In this section we consider the diagrammatic derivation of the Bethe-Salpeter equation and of the four-point vertex function. We stick to the notations of [108]. For more details and further derivations as well as for an extensive description of the four-point vertex function and its symmetries the reader is referred to G. Rohringer et al. [107], Bickers et al. [123], and to the doctoral thesis of G. Rohringer [109], F. Krien [120] and H. Hafermann [124].

Considering the diagrammatic extension of the four-point correlation function (2.9), it can be divided into two parts, namely in a disconnected contribution that contains products of two separated single-particle Green's functions which are diagrammatically separated from each other, and a second part containing all connected diagrams. Hence, the four-point correlation function can be written as

$$G_{kk'q}^{(2),\sigma\sigma'} = G_{kk'q}^{(2),\sigma\sigma',con} + G_{kk'q}^{(2),\sigma\sigma',discon}, \quad (2.16)$$

where the disconnected part is given by

$$G_{kk'q}^{(2),\sigma\sigma',discon} = -\beta G_{k\sigma} G_{k'\sigma'} \delta_q + \beta G_{k\sigma} G_{k+q\sigma} \delta_{kk'} \delta_{\sigma\sigma'}, \quad (2.17)$$

and the connected part reads (what about sum here)

$$G_{kk'q}^{(2),\sigma\sigma',con} = G_{k\sigma} G_{k+q\sigma} F_{kk'q}^{\sigma\sigma'} G_{k'\sigma'} G_{k'+q\sigma'}. \quad (2.18)$$

The disconnected part contains the *full* four-point vertex $F_{kk'q}^{\sigma\sigma'}$. The four-point vertex encloses all connected diagrams that also connect the four external Green's functions

with each other (sometimes also referred to as external *legs*).

Considering the non-interacting case ($U = 0$), Wick's theorem applied to the four-point correlation function yields

$$G_{kk'q}^{0,(2),\sigma\sigma'} = -\beta G_{k\sigma}^0 G_{k'\sigma'}^0 \delta_q + \beta G_k^0 G_{k+q}^0 \delta_{kk'} \delta_{\sigma\sigma'}. \quad (2.19)$$

This equation contains *bare* (non-interacting) Green's functions and is similar to the disconnected part of the four-point correlation function with the difference that in Eq. (2.16) we consider *dressed* Green's functions which are dressed by the self-energy through the Dyson equation (2.13).

According to Eq. (2.18), the full four-point vertex function F can be extracted from the four-point correlation function by amputating the external legs. The Feynman diagrams containing the full four-point vertex function can be classified similarly to the concept of the one-particle irreducibility discussed in the previous section. However, to classify the diagrams the concept has to be extended to two-particle irreducible since F does not contain any one-particle reducible diagrams. Diagrams are called two-particle reducible if they can be separated by cutting two internal lines (Green's functions). Therewith, we can separate diagrams that are fully two-particle irreducible from two-particle reducible diagrams. Though compared to the single-particle case, the two-particle diagrams have a more complex structure and hence the class of two-particle reducible diagrams can be further grouped in three different sub-classes usually referred to as channels, namely two-particle reducible in (and only in) the longitudinal particle-hole (ph), transversal particle- (\overline{ph}) or particle-particle (pp) channels. The full four-point vertex can then be written as

$$F_{kk'q}^\alpha = \Lambda_{kk'q}^\alpha + \Phi_{kk'q}^{\alpha,ph} + \Phi_{kk'q}^{\alpha,\overline{ph}} + \Phi_{kk'q}^{\alpha,pp}. \quad (2.20)$$

Note that here F was expressed in terms of charge $\alpha = \text{ch}$ and spin $\alpha = \text{sp} = \{x, y, z\}$ channels using Eq. (2.10) since in the recent theses we are mainly focused on collective charge and magnetic fluctuations. Furthermore, Λ denotes the fully two-particle irreducible contribution and Φ^ϱ the contribution in the corresponding two-particle reducible channel $\varrho = ph, \overline{ph}, pp$. The primary emphasis of this thesis is on the ph channel, which describes scattering processes between a particle and a hole in the system, hence let us take a closer look at this channel. As mentioned before, all components of Eq. (2.20) beside $\Phi_{kk'q}^{\alpha,ph}$ are two-particle irreducible with respect to the ph channel and thus can be combined in quantity namely $\Gamma_{kk'q}^{\alpha,ph}$ which is called the irreducible four-point vertex. The full four-point vertex then can be written as

$$F_{kk'q}^\alpha = \Gamma_{kk'q}^{\alpha,ph} + \Phi_{kk'q}^{\alpha,ph}. \quad (2.21)$$

Similar to the Dyson equation we can then construct a self-consistent equation for F using the irreducible vertex Γ . This yield us the Bethe-Salpeter equation (BSE) for the ph channel

$$F_{kk'q}^\alpha = \Gamma_{kk'q}^{\alpha,ph} + \frac{1}{\beta N} \sum_{k''} \Gamma_{kk''q}^{\alpha,ph} G_{k''} G_{k''+q} F_{k''k'q}^\alpha. \quad (2.22)$$

This type of Feynman diagrams are usually called *ladder* diagrams. They describe scattering processes in the corresponding channel. Of course, the BSE can be constructed in the same way for all three channels. Note that since we are considering the paramagnetic case the vertex F is diagonal in α due to SU(2) symmetry which means that the charge and spin channels do not couple.

In an analog way, we can obtain the BSE for the generalized susceptibility. The generalized susceptibility can be calculated from the four-point correlation function (2.16) by subtracting the trivial contribution of the disconnected part (2.17), namely

$$X_{kk'q}^{\sigma\sigma'} = G_{kk'q}^{(2),\sigma\sigma'} + \beta G_k G_{k'} \delta_q, \quad (2.23)$$

or in the charge and spin channel representation, using Eq. (2.10), as

$$X_{kk'q}^\alpha = G_{kk'q}^{(2),\alpha} + \frac{\beta}{2} \sum_{\sigma\sigma'} \sigma_\sigma^\alpha \sigma_{\sigma'}^\alpha G_{k\sigma} G_{k'\sigma'} \delta_q. \quad (2.24)$$

The connection between both representations is given by

$$X_{kk'q}^{\text{ch}} = X_{kk'q}^{\uparrow\uparrow} + X_{kk'q}^{\uparrow\downarrow}, \quad (2.25)$$

$$X_{kk'q}^{\text{sp}} = X_{kk'q}^{\uparrow\uparrow} - X_{kk'q}^{\uparrow\downarrow}. \quad (2.26)$$

The generalized susceptibility in channel representation can be written as

$$X_{kk'q}^\alpha = X_{kk'q}^{0,\alpha} + \frac{1}{\beta^2 N^2} \sum_{k''k'''} X_{kk''q}^{0,\alpha} F_{k''k'''q}^\alpha X_{k'''k'q}^{0,\alpha}, \quad (2.27)$$

and can be rewritten as the BSE through the irreducible four-point vertex function in the same way as Eq. (2.22),

$$X_{kk'q}^\alpha = X_{kk'q}^{0,\alpha} + \frac{1}{\beta^2 N^2} \sum_{k''k'''} X_{kk''q}^{0,\alpha} \Gamma_{k''k'''q}^\alpha X_{k'''k'q}^\alpha, \quad (2.28)$$

where we define the *bubble* as

$$X_{kk'q}^{0,\alpha} = \beta G_{k\sigma} G_{k+q\sigma} \delta_{kk'}. \quad (2.29)$$

Performing a sum over k and k' in Eq. (2.28) as,

$$X_q^\alpha = \frac{1}{\beta^2 N^2} \sum_{kk'} X_{kk'q}^\alpha = X_q^\alpha = -\langle \rho_{-q}^\alpha \rho_q^\alpha \rangle + \beta \langle \rho^\alpha \rangle \langle \rho^\alpha \rangle \delta_q, \quad (2.30)$$

yields us the response function which we refer to as the susceptibility. Diagrammatically the summation corresponds to a connection of the external legs on each side. The response function describes the linear response of the system to an external perturbation and can be measured in an experiment.

As already mentioned, the full four-point vertex F can be obtained from the BSE using the irreducible four-point vertex Γ^e in each channel. However, practically this turns out to be a very difficult task due to its dependence on several momenta and frequencies. Therefore, approximations for the irreducible four-point vertex are considered. In DMFT, e.g., in the limit of infinite dimensions, the irreducible four-point vertex becomes purely local [6, 50]. In the equivalent dual fermion formulation, the full local vertex of AIM is used [54, 125, 126]. In this case, since only a subset of diagrams is taken into account, the full four-point vertex becomes channel dependent. Throughout the present thesis, as an approximation of the irreducible four-point vertex, we utilize the full local vertex f of the AIM, which can be calculated from the four-point correlation function of the AIM in the same way as F as shown above (for more details see [75]). The full lattice vertex is then calculated from the BSE in the following way

$$F_{\nu\nu'q}^\alpha = f_{\nu\nu'q}^\alpha + \frac{1}{\beta} \sum_{\nu''} f_{\nu\nu''\omega}^\alpha \tilde{X}_{\nu''q}^{0,\alpha} f_{\nu''\nu'q}^\alpha, \quad (2.31)$$

where the bubble of nonlocal propagators is defined as

$$\tilde{X}_{\nu q}^{0,\alpha} = \frac{1}{N} \sum_{\mathbf{k}} \tilde{G}_{k\sigma} \tilde{G}_{k+q\sigma}. \quad (2.32)$$

Thereby, if considering DMFT, we set $\tilde{G}_k = \mathcal{G}_k$ where the nonlocal part of the DMFT Green's function \mathcal{G} is obtained by subtracting the impurity Green's function from the DMFT lattice Green's function ($\mathcal{G}_k = G_k^{DMFT} - g_\nu$). In dual fermion and dual boson approaches the nonlocal part of the DMFT Green's function is additionally dressed in the dual self-energy, $\tilde{G}_k^{-1} = \mathcal{G}_k^{-1} - \tilde{\Sigma}_k$.

Despite the approximation for the four-point vertex function, the computation of the local vertex f usually remains numerical the most expensive part of a calculation

scheme. Especially, when it comes to realistic multi-orbital calculations. Hence, in this thesis, we will present approximations for the full local vertex f of the AIM, which allows us to express the vertex f by means of the (three-point) Hedin vertex [47] and screened interactions. In recent years many works based on this idea were published [38, 61, 69, 70, 72–75, 127–137].

2.4 Coherent state path integral

The following derivation is based on [76].² In single-particle quantum mechanics, the Feynman path integral formalism is represented in terms of coordinate and momentum eigenstates due to the corresponding structure of the Hamiltonian. However, in many-body physics, such representation is not feasible due to a large number of particles. Since in the second quantization the Hamiltonian is represented by means of creation and annihilation operators, it seems reasonable, in analogy to the single-particle case, to find a formulation using eigenstates of these operators. Such states are called *coherent states* and are defined as

$$|\xi\rangle = |\xi_1, \dots, \xi_k\rangle = e^{-\sum_{\alpha} \xi_{\alpha} c_{\alpha}^{\dagger}} |0\rangle = \prod_{\alpha} (1 - \xi_{\alpha} c_{\alpha}^{\dagger}) |0\rangle. \quad (2.33)$$

These are eigenstates of the annihilation operator

$$c_{\alpha} |\xi\rangle = \xi_{\alpha} |\xi\rangle, \quad \langle \xi | c_{\alpha}^{\dagger} = \langle \xi | \xi_{\alpha}^*, \quad (2.34)$$

where the eigenvalues $\xi_{\alpha}^{(*)}$ are Grassmann numbers³ and the adjoint coherent state reads $\langle \xi | = \langle 0 | \prod_{\alpha} (1 + \xi_{\alpha}^* c_{\alpha})$.

Unlike the annihilation operator, the creation operator does not possess any eigenstates since the coherent state contains a superposition of Fock states with a minimum number of particles. A creation operator would increase the minimum number and can therefore not have eigenstates. The fact that for $\alpha \neq \beta$ the fermionic annihilation operators anti-commute implies that their eigenvalues anti-commute:

$$[c_{\alpha}, c_{\beta}]_{+} = 0 \Rightarrow \xi_{\alpha} \xi_{\beta} = -\xi_{\beta} \xi_{\alpha}. \quad (2.35)$$

²We are only considering fermionic systems.

³Note that the Grassmann numbers ξ_{α} and ξ_{α}^* are independent variables and not related through some conjugation.

For this reason, the Grassmann numbers are numbers that square to zero, i.e. $\xi_\alpha^2 = 0$. Furthermore, for consistency of anti-commutation relations, we require that

$$[\xi_\alpha, c_\beta]_+ = 0 \quad (2.36)$$

The coherent states form an overcomplete basis of the generalized Fock space. This can be easily seen considering the overlap of the two states,

$$\langle \xi | \xi' \rangle = e^{\sum_\alpha \xi_\alpha^* \xi'_\alpha} \quad (2.37)$$

so it forms an overcomplete basis of Fock space. Further, the matrix element of a normal-ordered operator $A(c_\alpha^\dagger, c_\alpha)$ between two coherent states is given by

$$\langle \xi | A(c_\alpha^\dagger, c_\alpha) | \xi' \rangle = e^{\sum_\alpha \xi_\alpha^* \xi'_\alpha} A(\xi_\alpha^*, \xi'_\alpha). \quad (2.38)$$

The closure relation is given by

$$\int \prod_\alpha d\xi_\alpha^* d\xi_\alpha e^{-\sum_\alpha \xi_\alpha^* \xi_\alpha} |\xi\rangle \langle \xi| = \mathbb{1} \quad (2.39)$$

with the unity operator $\mathbb{1}$ in the Fock space. Since we are interested in correlation functions which are the thermodynamic average over products of creation and annihilation operators (see eq. (2.2)), let us express the trace over a physical operator A with an even number of annihilation and creation operators in terms of coherent states. Using the fact that for the states $|\psi_i\rangle$ and $|\xi\rangle$ in the Fock space follows due to the anticommutation relations that

$$\langle \psi_i | \xi \rangle \langle \xi | \psi_i \rangle = \langle -\xi | \psi_i \rangle \langle \psi_i | \xi \rangle. \quad (2.40)$$

Therewith and with Eq. (2.39), for the complete set of Fock states $\{|n\rangle\}$ the trace of an operator can be written in the coherent state representation as

$$\text{Tr}(A) = \sum_n \langle n | A | n \rangle = \int \prod_\alpha d\xi_\alpha^* d\xi_\alpha e^{-\sum_\alpha \xi_\alpha^* \xi_\alpha} \langle -\xi | A | \xi \rangle \quad (2.41)$$

where $|n\rangle$ is short for $|n_1, \dots, n_k\rangle$. Using the new representation let us consider the partition function of a grand canonical system:

$$Z = \text{Tr} e^{-\beta \mathcal{H}} = \int \prod_\alpha d\xi_\alpha^* d\xi_\alpha e^{-\sum_\alpha \xi_\alpha^* \xi_\alpha} \langle -\xi | e^{-\beta \mathcal{H}} | \xi \rangle \quad (2.42)$$

The imaginary time interval $(\tau_f - \tau_i) = \beta$ can be divided in M equal steps of the size

$\epsilon = \beta/M$. Then insert the closure relations (2.39) between the exponentials. Finally, taking the limit $M \rightarrow \infty$ or respectively ($\epsilon \rightarrow 0$) the partition function takes the following form

$$Z = \lim_{M \rightarrow \infty} \int \prod_{i=1}^M \prod_{\alpha} d\xi_{\alpha,i}^* d\xi_{\alpha,i} e^{-\sum_i \sum_{\alpha} \xi_{\alpha,i}^* \xi_{\alpha,i}} \prod_{i=1}^M \langle \xi_i | : e^{-\epsilon \mathcal{H}} : + \mathcal{O}(\epsilon^2) | \xi_{i-1} \rangle, \quad (2.43)$$

with the antiperiodic boundary conditions $\xi_{\alpha,0} = \xi_{\alpha}$ and $\xi_{\alpha,M}^* = -\xi_{\alpha}^*$ due to Eq. ((2.42)). We used that $e^{-\epsilon \mathcal{H}}$ is normal ordered up to the second order in ϵ so that

$$e^{-\epsilon \mathcal{H}} =: e^{-\epsilon \mathcal{H}} : + \mathcal{O}(\epsilon^2). \quad (2.44)$$

The normal order is denoted by colons. In the limit $\epsilon \rightarrow 0$ the second term can be neglected. We then use Eq. (2.38) to rewrite

$$\langle \xi_i | : e^{-\beta \mathcal{H}} : | \xi_{i-1} \rangle = e^{-\epsilon \mathcal{H}(\xi_{\alpha,i}^*, \xi_{\alpha,i-1})} e^{\sum_{\alpha} \xi_{\alpha,i}^* \xi_{\alpha,i-1}} + \mathcal{O}(\epsilon^2). \quad (2.45)$$

Therewith, the partition function takes the following form

$$Z = \lim_{M \rightarrow \infty} \int \prod_{i=1}^M \prod_{\alpha} d\xi_{\alpha,i}^* d\xi_{\alpha,i} e^{-\sum_{i=1}^M \sum_{\alpha} \xi_{\alpha,i}^* (\xi_{\alpha,i} - \xi_{\alpha,i-1})} e^{-\epsilon \sum_{i=1}^M (H(\xi_{\alpha,i}^*, \xi_{\alpha,i-1}) + \mu \xi_{\alpha,i}^* \xi_{\alpha,i-1})}. \quad (2.46)$$

And in the continuum limit with boundary condition $\xi_{\alpha,0} = -\xi_{\alpha,M}$

$$Z = \int D[\xi^*(\tau), \xi(\tau)] e^{-\int_0^{\beta} d\tau \sum_{\alpha} \xi_{\alpha}^*(\tau) (\partial_{\tau} - \mu) \xi_{\alpha}(\tau) + H[\xi^*(\tau), \xi(\tau)]} = \int D[\xi^*, \xi] e^{-S[\xi^*, \xi]}, \quad (2.47)$$

where $D[\xi^*(\tau), \xi(\tau)]$ is a symbolic notation of the measure and S is action, which is defined by this equation. Now we can similarly derive the expectation values and write them as

$$\langle A \rangle = \frac{1}{Z} \text{Tr}[e^{-\beta \mathcal{H}} A] = \frac{1}{Z} \int D[\xi^*, \xi] A(\xi^*, \xi) e^{-S[\xi^*, \xi]} \quad (2.48)$$

With this framework correlation functions can be expressed through coherent path formalism as

$$G_{\alpha\beta}(\tau) := -\langle \xi_{\alpha}(\tau) \xi_{\beta}^*(0) \rangle = -\frac{1}{Z} \int D[\xi^*, \xi] \xi_{\alpha}(\tau) \xi_{\beta}^*(0) e^{-S[\xi^*, \xi]}. \quad (2.49)$$

Chapter 3

Methods

In this chapter methods used throughout the thesis are introduced. In the first section, the dynamical mean-field theory is introduced. Sections 3.2 and 3.4 introduce the dual boson and D-TRIELX approaches, respectively. The derivations are based on Refs. [72, 128]. Section 3.3 discusses the partially bosonized approximation for the four-point vertex and is based on [72]. The last Section 3.5 is based on [70, 75] and gives a brief overview of the single-boson exchange decomposition.

3.1 Dynamical mean-field theory

In the last decades, the dynamical mean-field theory (DMFT) has become one of the most used approaches to treat strongly correlated systems [6, 7, 138]. Not only that DMFT was successfully applied to materials where local correlations were dominant, but nowadays it is frequently employed as the basis for diagrammatic extensions that take into account nonlocal correlation effects. DMFT is a self-consistent approach based on a mapping of the (lattice) Hubbard model on a numerically exact solvable AIM. It was shown that this mapping becomes exact in the limit of infinite dimensions providing an exact solution for the Hubbard model in this [139]. Thereby, the self-energy of the lattice becomes purely local. DMFT provides an insight into the local properties of the system via the single-particle Green's function. However, as already mentioned, a computation of momentum-dependent response functions by means of the local vertex function is also possible [107, 109, 125]. In this thesis, the effective local impurity problem of DMFT is used as a reference system for the diagrammatic extension in D-TRILEX and DB. Moreover, we show the importance of the local (three-point) Hedin vertex by means of the DMFT susceptibility using different parametrizations of the local four-point vertex of the AIM[75].

DMFT maps a lattice problem (1.10) onto a single site problem (1.13) called impurity, which is embedded in an effective bath of non-interacting electrons. In the path-integral formalism, the action of the effective (local) impurity problem can be

obtained by integrating out the degrees of freedom of the bath which yields

$$S_{imp} = - \int_0^\beta d\tau \int_0^\beta d\tau' \sum_\sigma c_\sigma^*(\tau) \mathcal{G}^{-1}(\tau - \tau') c_\sigma(\tau') + U \int_0^\beta d\tau n_\uparrow(\tau) n_\downarrow(\tau), \quad (3.1)$$

or in the Matsubara frequency space

$$S_{imp} = \sum_{\nu\sigma} c_{\nu\sigma}^* \mathcal{G}_\nu^{-1} c_{\nu\sigma} + U \sum_\omega n_{-\omega\uparrow} n_{\omega\downarrow}, \quad (3.2)$$

where the inverse of the non-interacting Green's function is defined as

$$\mathcal{G}_\nu^{-1} = i\nu + \mu - \Delta_\nu. \quad (3.3)$$

The hybridization function of problem (1.13) that describes the dynamics of the system (hopping of electrons from the impurity in the bath and back) is given by

$$\Delta_\nu = \sum_{\mathbf{k}} \frac{|V_{\mathbf{k}}|^2}{i\nu - \varepsilon_{\mathbf{k}}}. \quad (3.4)$$

The impurity self-energy can then be obtained from the Dyson equation (2.14):

$$\Sigma_\nu^{imp} = \mathcal{G}_\nu^{-1} - g_\nu^{-1}, \quad (3.5)$$

where the impurity Green's function is calculated numerically exactly as

$$g_{\nu\sigma} \equiv -\langle c_{\nu\sigma} c_{\nu\sigma}^* \rangle_{imp} \quad (3.6)$$

by means of continuous-time quantum Monte Carlo (CT-QMC) solvers [101, 102, 140, 141].

Further, let us consider the lattice model. In general, the self-energy Σ_k is non-local. It depends on frequency and momentum. The lattice Green's function of the Hubbard model can be obtained using the Dyson equation (2.14) and the bare Green's function (2.15) as

$$G_k = \frac{1}{i\nu + \mu - \varepsilon_{\mathbf{k}} - \Sigma_k}. \quad (3.7)$$

In DMFT one neglects all nonlocal correlations by approximating the self-energy in Eq. (3.7) by the impurity self-energy, i.e., $\Sigma_{ij} \simeq \Sigma^{imp} \delta_{ij}$. As already mentioned previously this approximation becomes exact in the limit of infinite dimensions. This

defines the DMFT Green's function

$$G_k^{\text{DMFT}} = \frac{1}{i\nu + \mu - \varepsilon_{\mathbf{k}} - \Sigma_{\nu}^{\text{imp}}}, \quad (3.8)$$

where the momentum dependence arises due to the dispersion $\varepsilon_{\mathbf{k}}$. The local part of the DMFT Green's function is given by summing over momentum,

$$G_{\nu}^{\text{loc}} = \frac{1}{N} \sum_{\mathbf{k}} G_k^{\text{DMFT}}. \quad (3.9)$$

The mapping of the lattice problem to the impurity problem implies that the local part of the lattice Green's function equals the impurity Green's function leading us to the following equation, which determines the hybridization function, namely

$$G_{\nu}^{\text{loc}} = \frac{1}{N} \sum_{\mathbf{k}} \frac{1}{g_{\nu}^{-1} + \Delta_{\nu} - \varepsilon_{\mathbf{k}}}. \quad (3.10)$$

In practice, the self-consistency loop starts with an initial guess for the hybridization function. This can be done, e.g., by setting the self-energy to zero. Then the hybridization can be updated iteratively by means of the following equation

$$\Delta_{\nu}^{\text{new}} = \Delta_{\nu}^{\text{old}} + \xi(g_{\nu}^{-1} - [G_{\nu}^{\text{loc}}]^{-1}), \quad (3.11)$$

with the control parameter ξ which allows controlling the convergence of the self-consistent loop. The impurity problem is fully characterised by Δ_{ν} , U and μ . These parameters are used in the impurity solver to determine the impurity Green's function g_{ν} and with it the impurity self-energy by means of the Dyson equation (3.5). The knowledge of the impurity self-energy is not necessary as can be seen in Eq. (3.10) but can be useful, e.g., to investigate the conservation properties [120, 142]. The local Green's function is then obtained from Eq. (3.8) and Eq. (3.9), or directly from Eq. (3.10). The new hybridization function is then used as an input for the impurity solver. After several iterations, the self-consistent loop converges. A solution is found in the case when the self-consistency condition

$$G_{\nu}^{\text{loc}} = g_{\nu} \quad (3.12)$$

is fulfilled.

Impurity correlation functions

The derivation presented in this chapter can be found in [75]. The exact local four-point correlation function is defined as

$$g_{\nu\nu'\omega}^{(4),\alpha} = -\frac{1}{2} \sum_{\sigma_i} \sigma_{\sigma'_1\sigma_1}^\alpha \sigma_{\sigma'_2\sigma_2}^\alpha \langle c_{\nu\sigma_1} c_{\nu+\omega,\sigma'_1}^* c_{\nu'+\omega,\sigma_2} c_{\nu'\sigma'_2}^* \rangle, \quad (3.13)$$

where $\alpha = \text{ch, sp}$ denotes the charge and spin channel, respectively. As described above, by subtracting the disconnected parts and truncating the *legs* from the four-point correlation function $g^{(4)}$, we obtain the four-point vertex function as

$$f_{\nu\nu'\omega}^\alpha = \frac{g_{\nu\nu'\omega}^{(4),\alpha} - \beta g_\nu g_{\nu+\omega} \delta_{\nu\nu'} + 2\beta g_\nu g_{\nu'} \delta_\omega \delta_{\alpha,\text{ch}}}{g_\nu g_{\nu+\omega} g_{\nu'} g_{\nu'+\omega}}. \quad (3.14)$$

The full local four-point vertex can be obtained from Eq. (2.31). Further, the three-point correlation function is defined as,

$$g_{\nu\omega}^{(3),\alpha} = -\frac{1}{2} \sum_{\sigma\sigma'} \sigma_{\sigma'\sigma}^\alpha \langle c_{\nu\sigma} c_{\nu+\omega,\sigma'}^* \rho_\omega^\alpha \rangle, \quad (3.15)$$

with the charge and spin densities $\rho^{\text{ch}} = n_\uparrow + n_\downarrow$ and $\rho^{\text{sp}} = n_\uparrow - n_\downarrow$, respectively. Similarly, as in the case of the four-point vertex, the Hedin vertex is obtained from $g^{(3)}$ as [143, 144],

$$\lambda_{\nu\omega}^\alpha = \frac{g_{\nu\omega}^{(3),\alpha} + \beta g_\nu \langle n \rangle \delta_\omega \delta_{\alpha,\text{ch}}}{g_\nu g_{\nu+\omega} w_\omega^\alpha / U^\alpha}, \quad (3.16)$$

in the charge and spin channels and as,

$$\lambda_{\nu\omega}^{\text{s}} = \frac{\langle c_{\nu\uparrow} c_{\omega-\nu,\downarrow} \rho_\omega^+ \rangle}{g_\nu g_{\omega-\nu} w_\omega^{\text{s}} / U^{\text{s}}}, \quad (3.17)$$

in the singlet channel. The screened interaction is denoted by w_ω^ϑ and the bare interaction is denoted by U^ϑ in the corresponding channel. The index $\vartheta = \{\alpha, \text{s}\}$ denotes a combined index, where s is the singlet component in the particle-particle channel. Thereby, the bare interaction is defined as,

$$U^{\text{ch}} = +U, \quad U^{\text{sp}} = -U, \quad U^{\text{s}} = +2U. \quad (3.18)$$

The screened interaction is obtained from the susceptibility as,

$$w^\vartheta(\omega) = U^\vartheta + \frac{1}{2}U^\vartheta\chi^\vartheta(\omega)U^\vartheta, \quad (3.19)$$

where the susceptibilities are defined as

$$\chi_\omega^\alpha = -\langle\rho_{-\omega}^\alpha\rho_\omega^\alpha\rangle + \beta\langle n\rangle\langle n\rangle\delta_\omega\delta_{\alpha,\text{ch}}, \quad (3.20)$$

$$\chi_\omega^s = -\langle\rho_{-\omega}^+\rho_\omega^-\rangle. \quad (3.21)$$

3.2 Dual Boson approach

As can be seen from the fact that the self-energy is purely local, DMFT considers only local correlations of the system. One promising way to account for nonlocal correlations is by performing a diagrammatic perturbation expansion around a reference system. This reference system, however, should fulfill two main conditions. On the one hand, the reference system should be exactly solvable, and on the other hand, it should provide a good starting point for the perturbation expansion. For strongly correlated systems DMFT fulfills both criteria. In DMFT the strong local correlations are already taken into account and the weaker spatial correlations can thus be treated perturbatively. The first advanced diagrammatic extensions based on DMFT which account for higher order correlation functions of the local reference system were DF [54] and DGA [50]. In the DF approach, the lattice problem is rewritten in terms of impurities which are coupled through nonlocal degrees of freedom. Applying a Hubbard-Stratonovich (HS) transformation [145, 146] the impurities can be decoupled introducing new auxiliary fields called dual fermions and integrating out the original degrees of freedom transform the original problem into one that depends only on the new fields. The interaction between the dual fermions is then treated perturbatively. If considering nonlocal parts of Coulomb interaction, the DF approach can be generalized by introducing additional auxiliary bosonic fields called dual bosons [58]. The dual boson (DB) approach will be introduced in this chapter. Explicit derivations of the DB method can be found in [58–62, 72]. Note that in the absence of nonlocal interaction and bosonic hybridization the DB scheme reduces to the DF approach.

Usually, the DB approach is derived for taking into account fluctuations in the particle-hole charge and spin channels. In the following, we extend the derivation by additionally considering the particle-particle singlet channel following the derivation in Refs. [72, 128]. We begin the derivation by considering the partition function in

the path integral formalism

$$\mathcal{Z} = \int D[c^*, c] e^{-\mathcal{S}_{\text{latt}}}, \quad (3.22)$$

with c and c^* denoting the Grassmann variables. The action of the extended Hubbard model (1.12) is given by

$$\mathcal{S}_{\text{latt}} = - \sum_{k, \sigma} c_{k\sigma}^* \mathcal{G}_{k\sigma}^{-1} c_{k\sigma} + U \sum_q n_{q\uparrow}^* n_{q\downarrow} + \sum_{q, \vartheta} \xi^\vartheta \left\{ \rho_q^{*\vartheta} V_{\mathbf{q}}^\vartheta \rho_q^\vartheta \right\}, \quad (3.23)$$

where the bare lattice Green's function is defined as $\mathcal{G}_{k\sigma} = [i\nu + \mu - \varepsilon_{\mathbf{k}}]^{-1}$. The index $\vartheta = \{\varsigma, s\}$ denotes different bosonic channels with density ($\varsigma = \text{ch}$) and magnetic ($\varsigma = \text{sp} = \{x, y, z\}$) components in the particle-hole channel ς , and the singlet component s in the particle-particle channel. Note that the triplet particle-particle channel vanishes in the single-band case. The prefactor for the particle-hole and particle-particle channels, respectively, is defined as $\xi^\varsigma = 1/2$ and $\xi^s = 1$.

The variables $\rho_q^\vartheta = n_q^\vartheta - \langle n^\vartheta \rangle$ describe the fluctuations around the average value in the corresponding channel. Thereby, the corresponding densities for the different components are introduced as follows

$$n_q^\varsigma = \sum_{k, \sigma\sigma'} c_{k+q, \sigma}^* \sigma_{\sigma\sigma'}^\varsigma c_{k\sigma'}, \quad (3.24)$$

$$n_q^s = \frac{1}{2} \sum_{k, \sigma\sigma'} c_{q-k, \bar{\sigma}} \sigma_{\sigma\sigma'}^z c_{k\sigma'}, \quad (3.25)$$

$$n_q^{*s} = \frac{1}{2} \sum_{k, \sigma\sigma'} c_{k\sigma}^* \sigma_{\sigma\sigma'}^z c_{q-k, \bar{\sigma}}^*, \quad (3.26)$$

where σ^ς denotes the Pauli matrices and $\bar{\sigma}$ denotes the opposite spin projection to σ . n_q^{*s} is given by the relation $n_q^{*s} = n_{-q}^s$.

In general, the DB approach is a diagrammatic expansion, which can be performed for an arbitrary reference system [57]. The most commonly used reference system is the numerically exactly solvable single-impurity problem of DMFT [6]. Other reference systems based on DMFT are, e.g., isolated impurities [147, 148] or finite cluster problems [8, 15–18, 149] to name a few. However, throughout the thesis, we use the common effective single-impurity problem introduced in Section 1.2

whose action is given as

$$\mathcal{S}_{\text{imp}} = - \sum_{\nu, \sigma} c_{\nu\sigma}^* [i\nu + \mu - \Delta_\nu] c_{\nu\sigma} + U \sum_{\omega} n_{\omega\uparrow}^* n_{\omega\downarrow}, \quad (3.27)$$

Note that we do not consider the bosonic hybridization function, which arises in the framework of extended dynamical mean-field theory (EDMFT) [150–154], since unlike in the case of the fermionic hybridization function no clear method to determine the bosonic hybridization function was found yet. In contrast to the hybridization Δ , which is determined when the self-consistency relation (3.12) is achieved.

By adding and subtracting the fermionic hybridization function within the action of the origin lattice problem (3.23) it can be rewritten in an action consisting of impurity models at each lattice site and a remaining part that couples the impurities mutually. The lattice action (3.23) can then be written as

$$\mathcal{S}_{\text{latt}} = \sum_i \mathcal{S}_{\text{imp}}^{(i)} + \mathcal{S}_{\text{rem}}, \quad (3.28)$$

where the remaining part has the following form

$$\mathcal{S}_{\text{rem}} = - \sum_{k, \sigma} c_{k\sigma}^* [\Delta_\nu - \varepsilon_{\mathbf{k}}] c_{k\sigma} + \sum_{q, \vartheta} \xi^\vartheta \left\{ \rho_q^{*\vartheta} V_{\mathbf{q}}^\vartheta \rho_q^\vartheta \right\}. \quad (3.29)$$

The first term in Eq. (3.28) well describes the isolated atoms in the limit of large interaction U and can be solved numerically exactly. The second term, in contrast, well describes delocalized fermions in the opposite limit. Due to its momentum dependence, the second term can not be solved directly, therefore, we perform a HS transformation to decouple the impurities. The transformation is performed as

follows, introducing new *dual* fermions f and bosons φ ,

$$\exp \left\{ \sum_{k,\sigma} c_{k\sigma}^* [\Delta_\nu - \varepsilon_{\mathbf{k}}] c_{k\sigma} \right\} \quad (3.30)$$

$$= \mathcal{D}_f \int D[f^*, f] \exp \left\{ - \sum_{k,\sigma} (f_{k\sigma}^* g_{\nu\sigma}^{-1} [\Delta_\nu - \varepsilon_{\mathbf{k}}]^{-1} g_{\nu\sigma}^{-1} f_{k\sigma} + f_{k\sigma}^* g_{\nu\sigma}^{-1} c_{k\sigma} + c_{k\sigma}^* g_{\nu\sigma}^{-1} f_{k\sigma}) \right\},$$

$$\exp \left\{ - \sum_{q,\vartheta} \xi^\vartheta (\rho_q^{*\vartheta} V_{\mathbf{q}}^\vartheta \rho_q^\vartheta) \right\} \quad (3.31)$$

$$= \mathcal{D}_\varphi \int D[\varphi^\vartheta] \exp \left\{ \sum_{q,\vartheta} \xi^\vartheta (\varphi_q^{*\vartheta} \alpha_\omega^{\vartheta-1} V_{\mathbf{q}}^{\vartheta-1} \alpha_\omega^{\vartheta-1} \varphi_q^\vartheta - \varphi_q^{*\vartheta} \alpha_\omega^{\vartheta-1} \rho_q^\vartheta - \rho_q^{*\vartheta} \alpha_\omega^{\vartheta-1} \varphi_q^\vartheta) \right\}$$

where g_ν is the full local Green's function of the impurity problem and α_ω^ϑ is given as $\alpha_\omega^\vartheta = w_\omega^\vartheta / U^\vartheta$, where w_ω^ϑ denote the renormalized interaction of the impurity problem in the corresponding bosonic channel. The impurity quantities are defined as

$$g_{\nu\sigma}^{-1} = i\nu + \mu - \Delta_\nu - \Sigma_{\nu\sigma}^{\text{imp}}, \quad (3.32)$$

$$w_\omega^{\vartheta-1} = (U^\vartheta + Y_\omega^\vartheta)^{-1} - \Pi_\omega^{\vartheta \text{ imp}}. \quad (3.33)$$

The determinants $\mathcal{D}_f = \det [g_\nu (\Delta_\nu - \varepsilon_{\mathbf{k}}) g_\nu]$ and $\mathcal{D}_\varphi^{-1} = -\sqrt{\det [\alpha_\omega^\vartheta V_{\mathbf{q}}^\vartheta \alpha_\omega^\vartheta]}$ denote arbitrary matrices which can be neglected when calculating expectation values. To express the interaction part of the transformed action in terms of full local vertex functions of the impurity problem the factors g_ν and α_ω^ϑ were introduced [61].

From the first terms in the exponential of this expressions we see that the fields f and φ are coupled to the ones on other sites in the same way as c and ρ before the transformation. Also we see that the new degrees of freedom f and φ are coupled locally to the original ones c and ρ via g and α . After applying the HS transformation to the partition function the lattice action takes the following form

$$\begin{aligned} \mathcal{S}' = & \sum_i \mathcal{S}_{\text{imp}}^{(i)} + \sum_{k,\sigma} (f_{k\sigma}^* g_{\nu\sigma}^{-1} c_{k\sigma} + c_{k\sigma}^* g_{\nu\sigma}^{-1} f_{k\sigma}) + \sum_{q,\vartheta} \xi^\vartheta (\varphi_q^{*\vartheta} \alpha_\omega^{\vartheta-1} \rho_q^\vartheta + \rho_q^{*\vartheta} \alpha_\omega^{\vartheta-1} \varphi_q^\vartheta) \\ & - \sum_{k,\sigma} f_{k\sigma}^* g_{\nu\sigma}^{-1} [\varepsilon_{\mathbf{k}} - \Delta_\nu]^{-1} g_{\nu\sigma}^{-1} f_{k\sigma} - \sum_{q,\vartheta} \xi^\vartheta \left(\varphi_q^{*\vartheta} [\alpha_\omega^\vartheta V_{\mathbf{q}}^\vartheta \alpha_\omega^\vartheta]^{-1} \varphi_q^\vartheta \right). \end{aligned} \quad (3.34)$$

The impurity problem can be integrated out formally by taking the average over the impurity degrees of freedom as

$$\begin{aligned} & \int D[c^*, c] \exp \left\{ - \sum_i \mathcal{S}_{\text{imp}}^{(i)} - \sum_{k,\sigma} (f_{k\sigma}^* g_{\nu\sigma}^{-1} c_{k\sigma} + c_{k\sigma}^* g_{\nu\sigma}^{-1} f_{k\sigma}) - \sum_{q,\vartheta} \xi^\vartheta (\varphi_q^{*\vartheta} \alpha_\omega^{\vartheta-1} \rho_q^\vartheta + \rho_q^{*\vartheta} \alpha_\omega^{\vartheta-1} \varphi_q^\vartheta) \right\} \\ & = \mathcal{Z}_{\text{imp}} \times \exp \left\{ - \sum_{k,\sigma} f_{k\sigma}^* g_{\nu\sigma}^{-1} f_{k\sigma} - \sum_{q,\vartheta} \xi^\vartheta (\varphi_q^{*\vartheta} \alpha_\omega^{\vartheta-1} \chi_\omega^\vartheta \alpha_\omega^{\vartheta-1} \varphi_q^\vartheta) - \tilde{\mathcal{F}}[f, \varphi] \right\}, \end{aligned} \quad (3.35)$$

where \mathcal{Z}_{imp} denote the impurity partition function and $\chi_\omega^\vartheta = -\langle \rho_\omega^\vartheta \rho_\omega^{\vartheta*} \rangle$ is the susceptibility of the impurity problem. For more details, the reader is referred to [124]. This, together with the remaining terms in Eq. (3.34) leads us to the dual boson action,

$$\tilde{\mathcal{S}} = - \sum_{k,\sigma} f_{k\sigma}^* \tilde{\mathcal{G}}_{k\sigma}^{-1} f_{k\sigma} - \sum_{q,\vartheta} \xi^\vartheta \left\{ \varphi_q^{*\vartheta} \tilde{\mathcal{W}}_q^{\vartheta-1} \varphi_q^\vartheta \right\} + \tilde{\mathcal{F}}[f, \varphi], \quad (3.36)$$

The first term defines the bare fermionic and the second term the bare bosonic propagators of the dual problem as,

$$\tilde{\mathcal{G}}_{k\sigma} = g_{\nu\sigma} \left[[\varepsilon_{\mathbf{k}} - \Delta_\nu]^{-1} - g_{\nu\sigma} \right]^{-1} g_{\nu\sigma} = \check{\mathcal{G}}_{k\sigma} - g_{\nu\sigma}, \quad (3.37)$$

$$\tilde{\mathcal{W}}_q^\vartheta = \alpha_\omega^\vartheta \left[V_{\mathbf{q}}^{\vartheta-1} - \chi_\omega^\vartheta \right]^{-1} \alpha_\omega^\vartheta = \check{\mathcal{W}}_q^\vartheta - w_\omega^\vartheta, \quad (3.38)$$

where $\check{\mathcal{G}}_{k\sigma}$ and $\check{\mathcal{W}}_q^\vartheta$ are the Green's function and renormalized interaction of EDMFT, namely,

$$\check{\mathcal{G}}_{k\sigma}^{-1} = \mathcal{G}_{k\sigma}^{-1} - \Sigma_{\nu\sigma}^{\text{imp}}, \quad (3.39)$$

$$\left[\check{\mathcal{W}}_q^\vartheta \right]^{-1} = (U^\vartheta + V_{\mathbf{q}}^\vartheta)^{-1} - \Pi_\omega^{\vartheta \text{imp}}. \quad (3.40)$$

The interaction part of the action $\tilde{\mathcal{F}}[f, \varphi]$ being truncated to the two-particle level explicitly reads

$$\begin{aligned} \tilde{\mathcal{F}}[f, \varphi] & \simeq \sum_{q,k,\vartheta} \xi^\vartheta \left\{ \Lambda_{\nu\omega}^\vartheta \eta_{q,k}^{*\vartheta} \varphi_q^\vartheta + \Lambda_{\nu\omega}^{*\vartheta} \varphi_q^{*\vartheta} \eta_{q,k}^\vartheta \right\} \\ & + \frac{1}{4} \sum_{q,\{k\},\{\sigma\}} \Gamma_{ph,\nu\nu'\omega}^{\sigma\sigma'\sigma''\sigma'''} f_{k\sigma}^* f_{k+q,\sigma'} f_{k'+q,\sigma'''}^* f_{k'\sigma''}, \end{aligned} \quad (3.41)$$

where, $\eta_{q,k}^\theta$ were defined similar to Eqs. (3.24), (3.25) and (3.26) as

$$\begin{aligned}\eta_{q,k}^s &= \sum_{\sigma\sigma'} f_{k+q,\sigma}^* \sigma_{\sigma\sigma'}^s f_{k\sigma'}, \\ \eta_{q,k}^{\bar{s}} &= \frac{1}{2} \sum_{\sigma\sigma'} f_{q-k,\bar{\sigma}} \sigma_{\sigma\sigma'}^z f_{k\sigma'}, \\ \eta_{q,k}^{*s} &= \frac{1}{2} \sum_{\sigma\sigma'} f_{k\sigma}^* \sigma_{\sigma\sigma'}^z f_{q-k,\bar{\sigma}}^*.\end{aligned}\quad (3.42)$$

The four-point vertex functions in the particle-hole Γ_{ph} and particle-particle Γ_{pp} form are obtained by truncating the legs from the connected part of the four-point correlation function denoted by $\langle \dots \rangle_c$:

$$\begin{aligned}\Gamma_{ph,\nu\nu'\omega}^{\sigma_1\sigma_2\sigma_3\sigma_4} &= \frac{\langle c_{\nu\sigma_1} c_{\nu+\omega,\sigma_2}^* c_{\nu',\sigma_3}^* c_{\nu'+\omega,\sigma_4} \rangle_c}{g_{\nu\sigma_1} g_{\nu+\omega,\sigma_2} g_{\nu'\sigma_3} g_{\nu'+\omega,\sigma_4}}, \\ \Gamma_{pp,\nu\nu'\omega}^{\sigma_1\sigma_2\sigma_3\sigma_4} &= \frac{\langle c_{\nu\sigma_1} c_{\omega-\nu,\sigma_2} c_{\nu',\sigma_3}^* c_{\omega-\nu',\sigma_4}^* \rangle_c}{g_{\nu\sigma_1} g_{\omega-\nu,\sigma_2} g_{\nu'\sigma_3} g_{\omega-\nu',\sigma_4}}.\end{aligned}\quad (3.43)$$

The following relation between two representations holds [109],

$$\Gamma_{pp,\nu\nu'\omega}^{\sigma_1\sigma_2\sigma_3\sigma_4} = \Gamma_{ph,\nu,\omega-\nu',\nu'-\nu}^{\sigma_1\sigma_3\sigma_4\sigma_2} = -\Gamma_{ph,\nu,\nu',\omega-\nu-\nu'}^{\sigma_1\sigma_4\sigma_3\sigma_2}.\quad (3.44)$$

The Density (ch), magnetic (sp), singlet (s), and triplet (t) components of the four-point vertex are defined as

$$\begin{aligned}\Gamma_{\nu\nu'\omega}^{\text{ch/sp}} &= \Gamma_{ph,\nu\nu'\omega}^{\uparrow\uparrow\uparrow\uparrow} \pm \Gamma_{ph,\nu\nu'\omega}^{\uparrow\uparrow\downarrow\downarrow}, \\ \Gamma_{\nu\nu'\omega}^{\text{s/t}} &= \frac{1}{2} \Gamma_{pp,\nu\nu'\omega}^{\uparrow\downarrow\uparrow\downarrow} \mp \frac{1}{2} \Gamma_{pp,\nu\nu'\omega}^{\uparrow\downarrow\downarrow\uparrow}.\end{aligned}\quad (3.45)$$

The three-point vertices in the corresponding channels are defined as follows,

$$\begin{aligned}\Lambda_{\nu\omega}^s &= \frac{\langle c_{\nu\uparrow} c_{\nu+\omega\uparrow}^* \rho_{\omega}^{*s} \rangle}{g_{\nu\uparrow} g_{\nu+\omega\uparrow} \alpha_{\omega}^s}; & \Lambda_{\nu\omega}^{*s} &= \frac{\langle c_{\nu+\omega\uparrow} c_{\nu\uparrow}^* \rho_{\omega}^s \rangle}{g_{\nu+\omega\uparrow} g_{\nu\uparrow} \alpha_{\omega}^s}; \\ \Lambda_{\nu\omega}^{\bar{s}} &= \frac{\langle c_{\nu\uparrow} c_{\omega-\nu\downarrow} \rho_{\omega}^{*\bar{s}} \rangle}{g_{\nu\uparrow} g_{\omega-\nu\downarrow} \alpha_{\omega}^{\bar{s}}}; & \Lambda_{\nu\omega}^{*\bar{s}} &= \frac{\langle c_{\omega-\nu\downarrow} c_{\nu\uparrow}^* \rho_{\omega}^{\bar{s}} \rangle}{g_{\omega-\nu\downarrow} g_{\nu\uparrow} \alpha_{\omega}^{\bar{s}}}.\end{aligned}\quad (3.46)$$

In the particle-hole channel, the three-point vertex obeys the useful relation $\Lambda_{\nu\omega}^{*s} = \Lambda_{\nu+\omega,-\omega}^s$. The three-point vertex in the triplet channel is not introduced, because the composite variable ρ^t is identically zero in the single-band case.

The self-energy and the polarization in the ladder approximation can be obtained from the dual functional [60]. The self-energy then reads

$$\tilde{\Sigma}_{k\sigma}^{\text{LDB}} = \tilde{\Sigma}_{k\sigma}^{\text{LDF}} + \tilde{\Sigma}_{k\sigma}^{\text{mix}}. \quad (3.47)$$

Compared to LDF, in LDB an additional so-called *mixing* term $\tilde{\Sigma}_{k\sigma}^{\text{mix}}$ arises. Before considering the self-energy in more detail, let us introduce the screened three- and four-point vertices in the horizontal particle-hole (charge and spin) and particle-particle (singlet) channels:

$$L_{\nu q}^{\vartheta} = \Lambda_{\nu\omega}^{\vartheta} + \sum_{k_1} P_{\nu\nu_1 q}^{\vartheta} \tilde{X}_{k_1, q}^{0\vartheta} \Lambda_{\nu_1\omega}^{\vartheta} \quad (3.48)$$

$$P_{\nu\nu' q}^{\vartheta} = \Gamma_{\nu\nu'\omega}^{\vartheta} + \sum_{k_1} P_{\nu\nu_1 q}^{\vartheta} \tilde{X}_{k_1, q}^{0\vartheta} \Gamma_{\nu_1\nu'\omega}^{\vartheta} \quad (3.49)$$

Here, we define $\tilde{X}_{k,q}^{0\varsigma} = \tilde{G}_{k\sigma} \tilde{G}_{k+q,\sigma}$ and $\tilde{X}_{k,q}^{0s} = -\tilde{G}_{k\uparrow} \tilde{G}_{q-k,\downarrow}$. The screened vertices in the vertical \bar{P}^{ς} and horizontal P^{ς} particle-hole channels are connected via the relation $\bar{P}_{kk'\omega}^{\varsigma} = -P_{\nu,\nu+\omega,k'-k}^{\varsigma}$. Note that the particle-particle fluctuations in the ladder approximation are negligibly small and therefore are not considered. Hence, the LDB self-energy (3.47) only contains the three- and four-point vertices that are screened in the particle-hole (ς) channel.

The ladder DF self-energy,

$$\tilde{\Sigma}_{k\sigma}^{\text{LDF}} = \tilde{\Sigma}_{k\sigma}^{\text{ladd}} - \tilde{\Sigma}_{k\sigma}^{(2)}, \quad (3.50)$$

is given by the two-particle ladder diagram

$$\tilde{\Sigma}_{k\sigma}^{\text{ladd}} = - \sum_{q,k',\{\sigma\}} \tilde{G}_{k+q,\sigma'} P_{ph,\nu\nu'q}^{\sigma\sigma'\sigma''\sigma'''} \delta_{kk'} \delta_{\sigma\sigma''} \delta_{\sigma'\sigma'''} \quad (3.51)$$

In order to avoid double counting the second-order diagram,

$$\Sigma_{k\sigma}^{(2)} = -\frac{1}{2} \sum_{q,k',\{\sigma\}} \Gamma_{ph,\nu\nu'\omega}^{\sigma\sigma'\sigma''\sigma'''} \tilde{G}_{k',\sigma''} \tilde{G}_{k'+q,\sigma'''} \tilde{G}_{k+q,\sigma'} \Gamma_{ph,\nu'\nu\omega}^{\sigma''\sigma'''\sigma\sigma'}, \quad (3.52)$$

has to be excluded, since it appears twice, as follows from the Schwinger-Dyson equation [124]. The mixed diagram that appears due to the presence of the bosonic

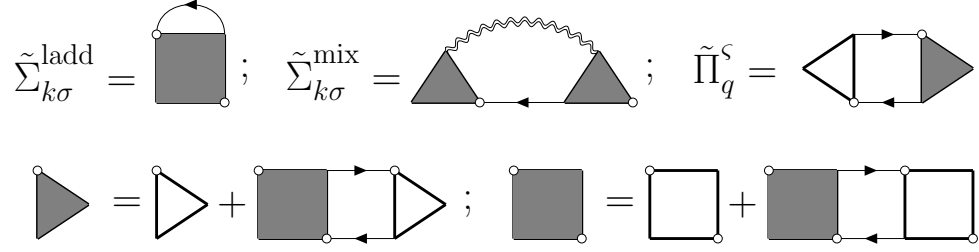


FIGURE 3.1: Diagrammatic representation of dual quantities. Top row: The ladder $\tilde{\Sigma}_{k\sigma}^{\text{ladd}}$ (3.51) and mixed diagram $\tilde{\Sigma}_{k\sigma}^{\text{mix}}$ (3.53) contributions to the LDB self-energy. The LDB polarization operator is denoted by $\tilde{\Pi}_q^\zeta$ (3.56). Bottom row: Screened three-point $L_{\nu q}^\vartheta$ (3.48) (left) and the four-point $P_{\nu\nu'q}^\vartheta$ (3.49) vertex functions in the LDB approximation (right). The figure is adapted from Ref. [128].

propagator \tilde{W}_q^ζ is given as,

$$\tilde{\Sigma}_{k\sigma}^{\text{mix}} = - \sum_{q,\zeta} L_{\nu q}^\zeta \tilde{G}_{q+k,\sigma} \tilde{W}_q^\zeta L_{\nu q}^{*\zeta}. \quad (3.53)$$

The full dual fermionic and bosonic propagators appearing in the self-energy can be obtained from the Dyson equations:

$$\tilde{G}_{k\sigma}^{-1} = \tilde{\mathcal{G}}_{k\sigma}^{-1} - \tilde{\Sigma}_{k\sigma}, \quad (3.54)$$

$$\tilde{W}_q^{\zeta-1} = \tilde{\mathcal{W}}_q^{\zeta-1} - \tilde{\Pi}_q^\zeta, \quad (3.55)$$

where the dual polarization operator in the ladder approximation reads

$$\tilde{\Pi}_q^\zeta = \sum_{k,\sigma} \Lambda_{\nu\omega}^{*\zeta} \tilde{G}_{k\sigma} \tilde{G}_{q+k,\sigma} L_{\nu q}^\zeta. \quad (3.56)$$

The Diagrammatic expressions for the LDB self-energy and polarization operator (top row) together with the screened three- and four-point vertices (bottom row) are shown in Fig. 3.1.

The transformation of the self-energy from the dual space back to the original lattice problem can be performed using the exact relation [58, 60, 61]

$$\Sigma_{k\sigma}^{\text{latt}} = \Sigma_{\omega\sigma}^{\text{imp}} + \frac{\tilde{\Sigma}_{k\sigma}}{1 + g_{\nu\sigma} \tilde{\Sigma}_{k\sigma}}. \quad (3.57)$$

Here, the denominator excludes unphysical terms from the Dyson equation for the lattice Green's function [57]. In practice, however, to reduce the numerical noise, that

arises from the impurity self-energy $\Sigma_{\nu\sigma}^{\text{imp}}$ at high frequencies, it is more convenient to calculate the lattice Green's function from the dual self-energy using an other exact relation that does not involve $\Sigma_{\nu\sigma}^{\text{imp}}$, namely [58, 155]

$$G_{k\sigma}^{-1} = \left[g_{\nu\sigma} + g_{\nu\sigma} \tilde{\Sigma}_{k\sigma} g_{\nu\sigma} \right]^{-1} + \Delta_\nu - \varepsilon_{\mathbf{k}}. \quad (3.58)$$

For more details on back transformation from the dual space, the reader is referred to the thesis of E.G.C.P. van Loon [156].

3.3 Partially bosonized approximation for the four-point vertex

In this section, an approximation for the full local four-point vertex is derived. We begin the derivation by considering the effective sing-impurity action shown in Eq. (3.27) including the bosonic hybridization Y_ω^ζ . Thereby, the term that includes the local interaction is rewritten in terms of variables ρ^ζ as $\frac{1}{2} \sum_\zeta U^\zeta \rho^\zeta \rho^\zeta$. Such a representation is used to partially *bosonize* the leading electronic collective excitations [48, 49, 157]. Note that for the sake of simplicity, in this section, we only consider the channels $\zeta = \{\text{ch}, \text{sp}\}$. Combining this term with the term which contains the bosonic hybridization yield the following effective impurity action:

$$\mathcal{S}_{\text{imp}} = - \sum_{\nu,\sigma} c_{\nu\sigma}^* [i\nu + \mu - \Delta_\nu] c_{\nu\sigma} + \frac{1}{2} \sum_{\omega,\zeta} \mathcal{U}_\omega^\zeta \rho_\omega^\zeta \rho_{-\omega}^\zeta, \quad (3.59)$$

where the bare interaction of the impurity problem in the corresponding bosonic channel is denoted by $\mathcal{U}_\omega^\zeta = U^\zeta + Y_\omega^\zeta$. Thereby, the local Coulomb interaction U can be decoupled arbitrarily, respectively, in the charge and spin channels. Further, the interaction part is antisymmetrized as,

$$\begin{aligned} \mathcal{S}_{\text{imp}} = & - \sum_{\nu,\sigma} c_{\nu\sigma}^* [i\nu + \mu - \Delta_\nu] c_{\nu\sigma} \\ & + \frac{1}{8} \sum_{\nu,\nu',\omega} \sum_{\zeta,\sigma} \Gamma_{\nu\nu'\omega}^{0\zeta} c_{\nu\sigma_1}^* \sigma_{\sigma_1\sigma_2}^\zeta c_{\nu+\omega,\sigma_2} c_{\nu'+\omega,\sigma_3}^* \sigma_{\sigma_3\sigma_4}^\zeta c_{\nu',\sigma_4}. \end{aligned} \quad (3.60)$$

Such antisymmetrization can be performed by interchanging indices of two Grassmann variables c (or c^*) in the interaction term (see, e.g., Section II A in Ref. [158]).

The different components of the vertex functions are given by the following relation:

$$\Gamma_{\nu\nu'\omega}^{0\text{ch}} = 2\mathcal{U}_\omega^{\text{ch}} - \mathcal{U}_{\nu'-\nu}^{\text{ch}} - \mathcal{U}_{\nu'-\nu}^x - \mathcal{U}_{\nu'-\nu}^y - \mathcal{U}_{\nu'-\nu}^z = U + 2Y_\omega^{\text{ch}} - Y_{\nu'-\nu}^{\text{ch}} - 3Y_{\nu'-\nu}^{\text{sp}}, \quad (3.61)$$

$$\Gamma_{\nu\nu'\omega}^{0x} = 2\mathcal{U}_\omega^x - \mathcal{U}_{\nu'-\nu}^x + \mathcal{U}_{\nu'-\nu}^y + \mathcal{U}_{\nu'-\nu}^z - \mathcal{U}_{\nu'-\nu}^{\text{ch}} = -U + 2Y_\omega^{\text{sp}} + Y_{\nu'-\nu}^{\text{sp}} - Y_{\nu'-\nu}^{\text{ch}}, \quad (3.62)$$

$$\Gamma_{\nu\nu'\omega}^{0y} = 2\mathcal{U}_\omega^y - \mathcal{U}_{\nu'-\nu}^y + \mathcal{U}_{\nu'-\nu}^z + \mathcal{U}_{\nu'-\nu}^x - \mathcal{U}_{\nu'-\nu}^{\text{ch}} = -U + 2Y_\omega^{\text{sp}} + Y_{\nu'-\nu}^{\text{sp}} - Y_{\nu'-\nu}^{\text{ch}}, \quad (3.63)$$

$$\Gamma_{\nu\nu'\omega}^{0z} = 2\mathcal{U}_\omega^z - \mathcal{U}_{\nu'-\nu}^z + \mathcal{U}_{\nu'-\nu}^x + \mathcal{U}_{\nu'-\nu}^y - \mathcal{U}_{\nu'-\nu}^{\text{ch}} = -U + 2Y_\omega^{\text{sp}} + Y_{\nu'-\nu}^{\text{sp}} - Y_{\nu'-\nu}^{\text{ch}}. \quad (3.64)$$

Using the exact relation between charge and spin components of the bare Coulomb interaction we find that the expression for the bare four-point vertex $\Gamma^{0\text{c}}$ does not depend on the performed decoupling and contains the contribution of the full U in all considered channels. Therefore, including the main contribution $\pm U$ only in the horizontal contribution $\mathcal{U}_\omega^{\text{c}}$ leads to a unique form of the bare interaction $U^{\text{ch}} = -U^{\text{sp}} = U/2$ that excludes ladderlike irreducible contributions from the full local four-point vertex function of the impurity problem [72]. The approximation of the full four-point vertex is discussed in the following.

The following part (highlighted as bold text) has already been published in APS Journal:

E. A. Stepanov, V. Harkov, A. I. Lichtenstein, “Consistent partial bosonization of the extended Hubbard model”. *Phys. Rev. B* **100**, 205115 (2019) (see Ref. [72]).

We start with the expressions (3.61), (3.62), (3.63) and (3.64) for the bare vertex $\Gamma_{\nu\nu'\omega}^{0\text{c}}$ of the impurity problem (3.60). Using the exact relation between charge and spin components of the bare Coulomb interaction we find that the expression for this bare vertex does not depend on the performed decoupling of the local Coulomb interaction and contains the contribution of the full U in all considered channels. This result is in agreement with the fact that the bare interaction in the Bethe-Salpeter equation for the susceptibility is given by the full local Coulomb interaction [134]. In order to find the origin of the reducible contribution with respect to a bosonic line (hereinafter, we will call this contribution w -reducible) to the fermion-fermion vertex, let us dress the bare vertex in the corresponding “horizontal” particle-hole channel as

$$\bar{\Gamma}_{\nu\nu'\omega}^{\text{c}} = \sum_{\nu'',\nu'''} \Gamma_{\nu\nu''\omega}^{0\text{c}} \chi_{\nu''\nu'''\omega}^{\text{c}} \Gamma_{\nu'''\nu'\omega}^{0\text{c}}, \quad (3.65)$$

where

$$\chi_{\nu\nu'\omega}^S = - \left\langle \left(c_{\nu+\omega,\sigma_1}^* \sigma_{\sigma_1\sigma_2}^S c_{\nu,\sigma_2} \right) \left(c_{\nu'\sigma_3}^* \sigma_{\sigma_3\sigma_4}^S c_{\nu'+\omega,\sigma_4} \right) \right\rangle_{\text{conn}} \quad (3.66)$$

is a generalized susceptibility of the impurity problem in a corresponding channel. After the antisymmetrization, this screened vertex (3.65) together with the bare vertex $\Gamma_{\nu\nu'\omega}^{0\zeta}$ makes up the simplest approximation for the fermion-fermion vertex function of the impurity problem

$$\begin{aligned} \Gamma_{\nu\nu'\omega}^{\text{ch}} &\simeq \Gamma_{\nu\nu'\omega}^{0\text{ch}} + \frac{1}{2}\overline{\Gamma}_{\nu\nu'\omega}^{\text{ch}} - \frac{1}{4}\overline{\Gamma}_{\nu,\nu+\omega,\nu'-\nu}^{\text{ch}} - \frac{3}{4}\overline{\Gamma}_{\nu,\nu+\omega,\nu'-\nu}^{\text{sp}}, \\ \Gamma_{\nu\nu'\omega}^{\text{sp}} &\simeq \Gamma_{\nu\nu'\omega}^{0\text{sp}} + \frac{1}{2}\overline{\Gamma}_{\nu\nu'\omega}^{\text{sp}} + \frac{1}{4}\overline{\Gamma}_{\nu,\nu+\omega,\nu'-\nu}^{\text{sp}} - \frac{1}{4}\overline{\Gamma}_{\nu,\nu+\omega,\nu'-\nu}^{\text{ch}}. \end{aligned} \quad (3.67)$$

Since the bare vertex function does not depend on the decoupling, this approximation is valid for any decomposition of the local Coulomb interaction. In the absence of bosonic hybridizations $Y^\zeta = 0$, the bare fermion-fermion vertex can be simply replaced by the bare Coulomb interaction $\Gamma_{\nu\nu'\omega}^{0\text{ch/sp}} = \pm U$ as derived above. Then, the generalized susceptibility (3.66) in the expression for the screened vertex (3.65) reduces to a bosonic susceptibility χ_ω^S , and the approximation for the full fermion-fermion vertex takes the following simple form:

$$\begin{aligned} \Gamma_{\nu\nu'\omega}^{\text{ch}} &\simeq U + \frac{1}{2}U\chi_\omega^{\text{ch}}U - \frac{1}{4}U\chi_{\nu'\nu}^{\text{ch}}U - \frac{3}{4}U\chi_{\nu'\nu}^{\text{sp}}U, \\ \Gamma_{\nu\nu'\omega}^{\text{sp}} &\simeq -U + \frac{1}{2}U\chi_\omega^{\text{sp}}U + \frac{1}{4}U\chi_{\nu'\nu}^{\text{sp}}U - \frac{1}{4}U\chi_{\nu'\nu}^{\text{ch}}U. \end{aligned} \quad (3.68)$$

This approximation fully coincides with the approximation obtained in the work [159]. The only difference is that here we do not perform a bosonization of collective fluctuations in the particle-particle channel as discussed in the main text. We also note that the susceptibility defined in our work is two times larger than the one introduced in Ref. [159]. Importantly, in the framework of the fermion-boson theory the interaction is introduced as the bosonic propagator. Thus, bare charge and spin interactions that enter the bare fermion-fermion vertex $\Gamma_{\nu\nu'\omega}^{0\zeta}$ have to be considered as ‘‘horizontal’’ U_ω^S and ‘‘vertical’’ bosonic $U_{\nu'-\nu}^S$ lines. In this case, a simple replacement of the bare fermion-fermion vertex by the full local Coulomb interaction is no longer possible. First, let us isolate the w -reducible contribution in the approximation for the fermion-fermion vertex (3.67). If we take only horizontal (ω -dependent) terms U_ω^S from

the bare vertex $\Gamma_{\nu\nu'\omega}^{0\zeta}$ in the expression (3.65), the generalized susceptibility again reduces to the bosonic one, and the w -reducible part of the screened vertex (3.65) becomes $\bar{\Gamma}_{\nu\nu'\omega}^{\zeta} = 4\mathcal{U}_{\omega}^{\zeta} \chi_{\omega}^{\zeta} \mathcal{U}_{\omega}^{\zeta}$. Other w -reducible terms in the screened vertex (3.65) appear from w -reducible contributions to the generalized susceptibility $\chi_{\nu''\nu'''\omega}^{\zeta}$. If the latter contains at least one horizontal bosonic line $\mathcal{U}_{\omega}^{\zeta}$ on which it can be cut into two separate parts, the bare vertex $\Gamma_{\nu\nu'\omega}^{0\zeta}$ in the expression (3.65) does not necessarily have to be w -reducible in order to make the total expression reducible with respect to a bosonic propagator. This leads to an additional fermion-boson vertex correction $\Lambda_{\nu\omega}^{\zeta}$ to the previously derived approximation for the screened vertex

$$\bar{\Gamma}_{\nu\nu'\omega}^{\zeta} = 4\Lambda_{\nu\omega}^{\zeta} \mathcal{U}_{\omega}^{\zeta} \chi_{\omega}^{\zeta} \mathcal{U}_{\omega}^{\zeta} \Lambda_{\nu'+\omega,-\omega}^{\zeta} + 2\Lambda_{\nu\omega}^{\zeta} \mathcal{U}_{\omega}^{\zeta} \Lambda_{\nu'+\omega,-\omega}^{\zeta} - 2\mathcal{U}_{\omega}^{\zeta}. \quad (3.69)$$

The term $2\mathcal{U}_{\omega}^{\zeta}$ is already contained in the bare vertex $\Gamma_{\nu\nu'\omega}^{0\zeta}$ and introduced here to simplify the expression. We note that Eq. (3.67) is only an approximation for the exact charge and spin fermion-fermion vertex functions. The exact w -reducible contribution to the screened fermion-fermion vertex (3.65) is given by the expression

$$\bar{\Gamma}_{\nu\nu'\omega}^{\zeta} = 4\Lambda_{\nu\omega}^{\zeta} w_{\omega}^{\zeta} \Lambda_{\nu'+\omega,-\omega}^{\zeta} - 4\mathcal{U}_{\omega}^{\zeta}, \quad (3.70)$$

where $w_{\omega}^{\zeta} = \mathcal{U}_{\omega}^{\zeta} + \mathcal{U}_{\omega}^{\zeta} \chi_{\omega}^{\zeta} \mathcal{U}_{\omega}^{\zeta}$ is the full renormalized interaction of the impurity problem, and $\Lambda_{\nu\omega}^{\zeta}$ is the exact fermion-boson vertex of the problem. Here, the term $4\mathcal{U}_{\omega}^{\zeta}$ is again excluded from the expression, since it is already contained in the (nonsymmetrized) bare interaction. The remaining part of the generalized susceptibility in the expression (3.67) for the screened vertex is irreducible with respect to the bosonic propagator. Together with vertical lines $\mathcal{U}_{\nu'-\nu}^{\zeta}$ from the bare fermion-fermion vertex $\Gamma_{\nu\nu'\omega}^{0\zeta}$ it makes the w -irreducible contribution to the full fermion-fermion vertex function that is not accounted for by the fermion-boson theory. As discussed in the main text, the ladder-like irreducible contributions to the fermion-fermion vertex function can be fully excluded by a proper choice of the bare interaction $U^{\text{ch}} = -U^{\text{sp}} = U/2$ that has the same value for all $\text{sp} = \{x, y, z\}$ spin components. Since this unique form of the bare interaction cannot be obtained by any of the decoupling of the local Coulomb interaction, we will make separate decouplings for every bosonic channel to keep the bare interaction in the proposed form. Then, coming back to a nonsymmetrized form of the bare fermion-fermion vertex function (3.61), (3.62), (3.63) and (3.64), we get $\Gamma_{\nu\nu'\omega}^{0\zeta} = 2\mathcal{U}_{\omega}^{\zeta} + 2Y_{\omega}^{\zeta}$. Together

with the screened interaction $\bar{\Gamma}_{\nu\nu'\omega}^{\text{S}}$ from (3.70), which is also written in the antisymmetrized form, it makes the total approximation for the nonsymmetrized full fermion-fermion vertex function

$$\frac{1}{8}\Gamma_{\nu\nu'\omega}^{\text{S}} \simeq \frac{1}{2}M_{\nu\nu'\omega}^{\text{S}} = \frac{1}{2}(\Lambda_{\nu\omega}^{\text{S}}w_{\omega}^{\text{S}}\Lambda_{\nu'+\omega,-\omega}^{\text{S}} - U^{\text{S}}/2). \quad (3.71)$$

The term $U^{\text{S}}/2$ appears here, because we use separate mutually exclusive decouplings of the bare Coulomb interaction in different bosonic channels. This term avoids the double counting of the bare Coulomb interaction in the bare vertex $\Gamma_{\nu\nu'\omega}^0$. Note that the same procedure can be performed for the Ising form of the bare interaction $U^{\text{ch}} = -U^z = U/2$ and $U^x = U^y = 0$. Since this form of decoupling is identical for all channels, this does not lead to a double counting of the local Coulomb interaction. Then, the approximation for the fermion-fermion vertex in the antisymmetrized form is given by the expression $M_{\nu\nu'\omega}^{\text{S}} = \Lambda_{\nu\omega}^{\text{S}}w_{\omega}^{\text{S}}\Lambda_{\nu'+\omega,-\omega}^{\text{S}}$.

The final expression for the w -reducible approximation of the full fermion-fermion vertex function can be obtained after antisymmetrizing the expression (3.71)

$$\begin{aligned} \Gamma_{\nu\nu'\omega}^{\text{ch}} &= 2M_{\nu\nu'\omega}^{\text{ch}} - M_{\nu,\nu+\omega,\nu'-\nu}^{\text{ch}} - 3M_{\nu,\nu+\omega,\nu'-\nu}^{\text{sp}}, \\ \Gamma_{\nu\nu'\omega}^{\text{sp}} &= 2M_{\nu\nu'\omega}^{\text{sp}} + M_{\nu,\nu+\omega,\nu'-\nu}^{\text{sp}} - M_{\nu,\nu+\omega,\nu'-\nu}^{\text{ch}}. \end{aligned} \quad (3.72)$$

Note that the w -reducible interaction (3.71), which is introduced to exclude the exact fermion-fermion vertex from the action, does not have a uniform structure due to a presence of the $-U^{\text{S}}/2$ term that does not contain fermion-boson vertex functions. Therefore, the correction $M_{\nu\nu'\omega}^{\text{S}}$ cannot be easily generated performing transformations of the lattice action discussed below. Thus, we make a small additional approximation for the w -reducible fermion-fermion vertex $M_{\nu\nu'\omega}^{\text{S}} \simeq \Lambda_{\nu\omega}^{\text{S}}\bar{w}_{\omega}^{\text{S}}\Lambda_{\nu'+\omega,-\omega}^{\text{S}}$ including the $U^{\text{S}}/2$ term in the propagator $\bar{w}_{\omega}^{\text{S}} = w_{\omega}^{\text{S}} - U^{\text{S}}/2$. After that, the exact (3.70) expression for the reducible contribution to the fermion-fermion vertex function coincides with the approximate one derived in Eq. (3.69). In addition, the last approximation can be motivated by the asymptotic behavior of the fermion-boson vertex function $\Lambda_{\nu\omega} \rightarrow 1$ at large frequencies.

3.4 D-TRILEX approach

In this section, we derive the partially bosonized dual action of the D-TRILEX theory from the dual boson problem (3.36) following Refs. [72, 128]. Therefore, a further

HS transformation is performed in a way that the four-point vertex in the action is nearly canceled using the partially bosonized form of Eq. (3.72). Similar to the DB theory we begin the derivation by adding and subtracting the following term from the dual action (3.36), namely

$$\sum_{q,\vartheta} \xi^\vartheta (\varphi_q^{*\vartheta} \bar{w}_\omega^{\vartheta-1} \varphi_q^\vartheta). \quad (3.73)$$

Similar to the hybridization functions, the quantity \bar{w}_ω^ϑ is arbitrary, however, the proper choice of this quantity will help to exclude the four-point vertex from the action as will be seen below. In the next step, we perform the following HS transformation

$$\begin{aligned} & \exp \left\{ \sum_{q,\vartheta} \xi^\vartheta \varphi_q^{*\vartheta} \left[\tilde{W}_q^{\vartheta-1} + \bar{w}_\omega^{\vartheta-1} \right] \varphi_q^\vartheta \right\} = \\ & \mathcal{D}_b \int D[b^\vartheta] \exp \left\{ - \sum_{q,\vartheta} \xi^\vartheta \left(b_q^{*\vartheta} \bar{w}_\omega^{\vartheta-1} \left[\tilde{W}_q^{\vartheta-1} + \bar{w}_\omega^{\vartheta-1} \right]^{-1} \bar{w}_\omega^{\vartheta-1} b_q^\vartheta - \varphi_q^{*\vartheta} \bar{w}_\omega^{\vartheta-1} b_q^\vartheta - b_q^{*\vartheta} \bar{w}_\omega^{\vartheta-1} \varphi_q^\vartheta \right) \right\}, \end{aligned} \quad (3.74)$$

where we define $\mathcal{D}_b^{-1} = \sqrt{\det \left[\bar{w}_\omega^\vartheta \left(\tilde{W}_q^{\vartheta-1} + \bar{w}_\omega^{\vartheta-1} \right) \bar{w}_\omega^\vartheta \right]}$. After the transformation the dual action (3.36) takes the form:

$$\begin{aligned} \tilde{\mathcal{S}}' = & - \sum_{k,\sigma} f_{k\sigma}^* \tilde{\mathcal{G}}_{k\sigma}^{-1} f_{k\sigma} + \sum_{q,\vartheta} \xi^\vartheta \left\{ b_q^{*\vartheta} \bar{w}_\omega^{\vartheta-1} \left[\tilde{W}_q^{\vartheta-1} + \bar{w}_\omega^{\vartheta-1} \right]^{-1} \bar{w}_\omega^{\vartheta-1} b_q^\vartheta \right\} \\ & + \sum_{q,\vartheta} \xi^\vartheta \left\{ \varphi_q^{*\vartheta} \bar{w}_\omega^{\vartheta-1} \varphi_q^\vartheta - \varphi_q^{*\vartheta} \bar{w}_\omega^{\vartheta-1} b_q^\vartheta - b_q^{*\vartheta} \bar{w}_\omega^{\vartheta-1} \varphi_q^\vartheta \right\} + \tilde{\mathcal{F}}[f, \varphi]. \end{aligned} \quad (3.75)$$

Finally, the dual bosonic fields φ can be integrated out with respect to the new Gaussian part of the dual action as,

$$\begin{aligned} & \int D[\varphi^\vartheta] \exp \left\{ - \sum_{q,k,\vartheta} \xi^\vartheta \left(\varphi_q^{*\vartheta} \bar{w}_\omega^{\vartheta-1} \varphi_q^\vartheta - \varphi_q^{*\vartheta} \left[\bar{w}_\omega^{\vartheta-1} b_q^\vartheta - \Lambda_{\nu\omega}^{*\vartheta} \eta_{q,k}^\vartheta \right] - \left[b_q^{*\vartheta} \bar{w}_\omega^{\vartheta-1} - \eta_{q,k}^{*\vartheta} \Lambda_{\nu\omega}^\vartheta \right] \varphi_q^\vartheta \right) \right\} = \\ & \mathcal{Z}_\varphi \times \exp \left\{ \sum_{q,k,\vartheta} \xi^\vartheta \left(b_q^{*\vartheta} \bar{w}_\omega^{\vartheta-1} b_q^\vartheta - \Lambda_{\nu\omega}^\vartheta \eta_{q,k}^{*\vartheta} b_q^\vartheta - \Lambda_{\nu\omega}^{*\vartheta} b_q^{*\vartheta} \eta_{q,k}^\vartheta + \eta_{q,k}^{*\vartheta} \Lambda_{\nu\omega}^\vartheta \bar{w}_\omega^\vartheta \Lambda_{\nu\omega}^{*\vartheta} \eta_{q,k}^\vartheta \right) \right\}, \end{aligned} \quad (3.76)$$

where \mathcal{Z}_φ is the partition function of the Gaussian part of the bosonic action. The quartic term $\eta_{q,k}^{*\vartheta} \Lambda_{\nu\omega}^\vartheta \bar{w}_\omega \Lambda_{\nu\omega}^{*\vartheta} \eta_{q,k}^\vartheta$ in Eq. (3.76) is the partially bosonized representation for the four-point vertex [72]. This term cancels the four-point vertex in the action after defining \bar{w}_ω^ϑ as

$$\bar{w}_\omega^s = w_\omega^s - U^s/2, \quad (3.77)$$

$$\bar{w}^s = w^s - U^s. \quad (3.78)$$

After integrating out the dual bosonic fields the partially bosonized action of the D-TRILEX theory reads,

$$\begin{aligned} \mathcal{S}_{pb} = & - \sum_{k,\sigma} f_{k\sigma}^* \tilde{\mathcal{G}}_{k\sigma}^{-1} f_{k\sigma} - \sum_{q,\vartheta} \xi^{\vartheta} \left\{ b_q^{*\vartheta} \mathcal{W}_q^{\vartheta-1} b_q^\vartheta \right\} \\ & + \sum_{q,k,\vartheta} \xi^{\vartheta} \left\{ \Lambda_{\nu\omega}^\vartheta \eta_{q,k}^{*\vartheta} b_q^\vartheta + \Lambda_{\nu\omega}^{*\vartheta} b_q^{*\vartheta} \eta_{q,k}^\vartheta \right\}. \end{aligned} \quad (3.79)$$

Here, the bare Green's function $\tilde{\mathcal{G}}_{k\sigma}$ remains the same as in the dual action (3.36), however, the bosonic propagator takes the following form

$$\mathcal{W}_q^s = \check{W}_q^s - U^s/2, \quad (3.80)$$

$$\mathcal{W}_q^s = \check{W}_q^s - U^s. \quad (3.81)$$

The effective four-point interaction in a partially bosonized form (including the singlet channel) is given by

$$\begin{aligned} \Gamma_{\nu\nu'\omega}^{\text{ch}} & \simeq 2M_{\nu\nu'\omega}^{\text{ch}} - M_{\nu,\nu+\omega,\nu'-\nu}^{\text{ch}} - 3M_{\nu,\nu+\omega,\nu'-\nu}^{\text{sp}} + M_{\nu,\nu',\omega+\nu+\nu'}^{\text{s}}, \\ \Gamma_{\nu\nu'\omega}^{\text{sp}} & \simeq 2M_{\nu\nu'\omega}^{\text{sp}} + M_{\nu,\nu+\omega,\nu'-\nu}^{\text{sp}} - M_{\nu,\nu+\omega,\nu'-\nu}^{\text{ch}} - M_{\nu,\nu',\omega+\nu+\nu'}^{\text{s}}, \\ \Gamma_{\nu\nu'\omega}^{\text{s}} & \simeq M_{\nu\nu'\omega}^{\text{s}} + \frac{1}{2} \left(M_{\nu,\nu',\omega-\nu-\nu'}^{\text{ch}} + M_{\nu,\omega-\nu',\nu'-\nu}^{\text{ch}} \right) \\ & \quad - \frac{3}{2} \left(M_{\nu,\nu',\omega-\nu-\nu'}^{\text{sp}} + M_{\nu,\omega-\nu',\nu'-\nu}^{\text{sp}} \right), \end{aligned} \quad (3.82)$$

with

$$M_{\nu\nu'\omega}^\vartheta = \Lambda_{\nu\omega}^\vartheta \bar{w}_\omega^\vartheta \Lambda_{\nu'\omega}^{*\vartheta}. \quad (3.83)$$

Using the analog of the Almladh functional [160] $\Psi[\tilde{G}, W, \Lambda] = \frac{1}{2}\tilde{G}\Lambda^\vartheta W^\vartheta \Lambda^{*\vartheta}\tilde{G}$, which was introduced in the dual space, we can extract the simplest set of diagrams for the self-energy and polarization operator used in the D-TRILEX approach [72]:

$$\tilde{\Sigma}_{k\sigma} = - \sum_{q,\varsigma} \left\{ \Lambda_{\nu\omega}^\varsigma \tilde{G}_{q+k,\sigma} W_q^\varsigma \Lambda_{\nu\omega}^{*\varsigma} - \Lambda_{\nu\omega}^s \tilde{G}_{q-k,\bar{\sigma}} W_q^s \Lambda_{\nu\omega}^{*s} \right\}, \quad (3.84)$$

$$\bar{\Pi}_q^\varsigma = + \sum_{k,\sigma} \Lambda_{\nu\omega}^{*\varsigma} \tilde{G}_{k\sigma} \tilde{G}_{q+k,\sigma} \Lambda_{\nu\omega}^\varsigma, \quad (3.85)$$

$$\bar{\Pi}_q^s = - \sum_k \Lambda_{\nu\omega}^{*s} \tilde{G}_{k\uparrow} \tilde{G}_{q-k\downarrow} \Lambda_{\nu\omega}^s, \quad (3.86)$$

where $\tilde{G}_{k\sigma}$ and W_q^ϑ are the full propagators, which can be obtained using the Dyson equations

$$\tilde{G}_{k\sigma}^{-1} = \tilde{\mathcal{G}}_{k\sigma}^{-1} - \tilde{\Sigma}_{k\sigma}, \quad (3.87)$$

$$W_q^{\vartheta-1} = \mathcal{W}_q^{\vartheta-1} - \bar{\Pi}_q^\vartheta. \quad (3.88)$$

A schematic relation between the simple GW -like diagrams (3.84), (3.85), and (3.86) of the D-TRILEX approach and the DB theory is shown in Fig. 3.2. For an extensive discussion, the reader is referred to Ref. [128]. In the following, for simplicity, we consider the case $V_{\mathbf{q}}^\vartheta = 0$ in which case the DB and DF theories coincide. The dual self-energy $\tilde{\Sigma}^{\text{LDF}}$ in the ladder approximation [56] is given by the Schwinger-Dyson equation [124]. The corresponding diagram is depicted in the upper row of Fig. 3.2. In the same row, the D-TRILEX self-energy (3.84) is depicted in red. As mentioned above, the second-order diagram $\tilde{\Sigma}^{(2)}$ in the ladder (middle row) is subtracted once in order to avoid double-counting. Therefore, a factor “1/2” appear in front of this diagram, which does not appear in front of the higher order diagrams $\tilde{\Sigma}^{(3+)}$ [55] (bottom row). The red insertions show how the D-TRILEX diagrams can be constructed by approximating the four-point vertex in $\tilde{\Sigma}^{\text{LDF}}$ using the longitudinal contributions $M_{\nu\nu'\omega}^\vartheta$ of the partially bosonized representation (3.82). In Ref. [128] we perform an elaborate analysis of different diagrammatic contributions and show that the longitudinal contributions are the main ones. Also, an explicit analytical derivation of the relation between D-TRILEX and ladder DB (LDB) self-energies for the general case is shown. The approximation of the vertex leads to a much simpler diagrammatic structure in the D-TRILEX approach compared to the LDB method. The advantage of D-TRILEX is that on the one hand it does not require the computation of the numerically costly four-point vertex and on the other hand due to the simple diagrammatic structure no inversion of the Bethe-Salpeter equation is

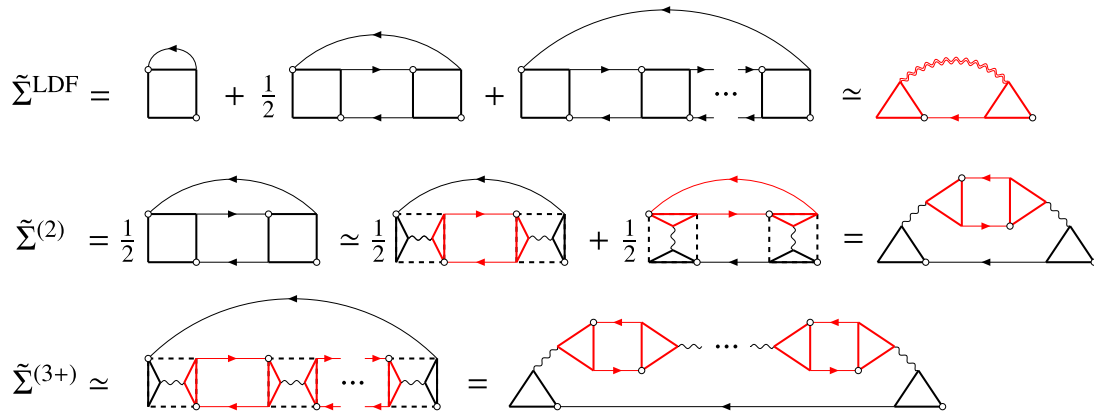


FIGURE 3.2: In the top row, the dual fermion self-energy $\tilde{\Sigma}^{\text{LDF}}$ in the ladder approximation is shown in black. The black square illustrates the four-point vertex Γ and the arrow represents the dressed Green's function. In the same row, the D-TRILEX self-energy is shown in red. The triangle represents the three-point vertex and the wiggly double line denotes the full bosonic propagator. The first term in the ladder is the first-order Hartree-like term. The second term is the second-order diagram $\tilde{\Sigma}^{(2)}$ also shown in the middle row. The third term represents the remaining part of the ladder $\tilde{\Sigma}^{(3+)}$ and is also shown in the bottom row. The four-point vertex is approximated by the longitudinal contribution of the partially bosonized representation. The red parts resulting from the approximation are D-TRILEX polarization operators, which are connected by renormalized interactions (wiggly line). The figure is adapted from Ref. [128].

needed. In the ladder DF/DB theory the inversion of the Bethe-Salpeter equation in the frequency space is required because of the three-frequency dependence of the local vertex function $\Gamma_{\nu\nu'\omega}$.

3.5 Single-boson exchange decomposition for the four-point vertex

In this chapter, we introduce another approximation for the full local four-point vertex of the impurity model. The derivation presented in this section can be found in Ref. [70]. The approximation is based on the decomposition of the four-point vertex in terms of a single-boson exchange (SBE) in the ph , \overline{ph} , and pp channels similar to the parquet decomposition. Thereby, similar to the concept of two-particle reducible and irreducible diagrams, respectively, the SBE is based on the fact that the local full four-point vertex contains two classes of diagrams, namely, the ones which can be divided into two parts by removing a bare interaction U^α where $\alpha = \text{ch, sp, s}$ in the corresponding channel, those diagrams are called U -reducible, and the remaining diagrams which are U -irreducible. While the U -irreducible part of the vertex which is intrinsically a four-point quantity is neglected in the SBE approximation [70, 75], the U -reducible is represented in terms of the (three-point) Hedin vertex and the screened interaction. The new representation reduces the computational effort drastically since it does not require any computation of a four-point object and matrix inversion of the Bethe-Salpeter equation.

Let us discuss the classification of the diagrams contributing to the full vertex in terms of reducibility in more detail. All possible diagrams can be divided into four classes. Each diagram is exclusively either gg -reducible in the horizontal particle-hole (ph), the vertical particle-hole (\overline{ph}), or in the particle-particle (pp) channels. The last class contains fully irreducible (firr) diagrams. We classify a diagram as reducible in the corresponding channel if it can be separated into two parts by cutting a pair of ph -, \overline{ph} - or pp -propagator lines, respectively. Further, let us consider one class of reducible diagrams. A diagram in that class can but not necessarily be also U -reducible in the same channel. For instance, a gg -reducible diagram in the particle-particle channel can also be U -reducible in the particle-particle channel, but not in the other channels. The class of U -reducible diagrams in the particle-particle channel is a subclass of gg -reducible diagram in the particle-particle channel. Accordingly, the same is true for other channels. We classify the U -reducibility of diagrams in the respective channel in a similar fashion as gg -reducibility by removing a bare interaction line U^α in the respective channel. The bare interaction U^α is defined as

$$U^{\text{ch}} = +U, \quad U^{\text{sp}} = -U, \quad U^{\text{s}} = +2U. \quad (3.89)$$

It is important to note that the bare interaction itself U^α is reducible in all three channels. So the bare U^α is a common element in all U -reducible classes. With this

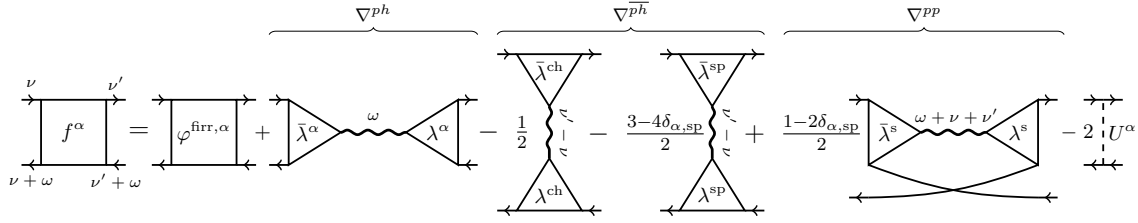


FIGURE 3.3: Diagrammatic representation of the single-boson exchange decomposition of the four-point vertex for $\alpha = \{\text{ch}, \text{sp}\}$. The Hedin vertices are denoted by λ^α and the screened interactions w^α by wiggly lines. The first term in the decomposition is the U -irreducible four-point vertex $\varphi^{\text{firr},\alpha}$. The following diagrams belong to the class of U -reducible diagrams in the corresponding ph , $\bar{p}\bar{h}$ and pp channels. The last term is the double-counting correction that cancels the bare interaction U^α two times which arises in all U -reducible channels. The figure is adapted from Ref. [70].

considerations, we can decompose the full local vertex f in the following way

$$f^\alpha = \varphi^{\text{firr},\alpha} + \nabla_{\nu\nu'\omega}^{\text{SBE},\alpha}, \quad (3.90)$$

where the SBE vertex is defined as

$$\nabla_{\nu\nu'\omega}^{\text{SBE},\alpha} = \nabla_{\nu\nu'\omega}^{ph,\alpha} + \nabla_{\nu\nu'\omega}^{\bar{p}\bar{h},\alpha} + \nabla_{\nu\nu',\omega+\nu+\nu'}^{pp,\alpha} - 2U^\alpha. \quad (3.91)$$

Thereby, the subtraction of $2U^\alpha$ results from the aforementioned fact that U^α is reducible in all three U -reducible channels. So in order to compensate the overcounting we have to subtract it twice.

In the following, we briefly discuss the U -reducible contributions (3.91). The horizontally U -reducible diagrams ∇^{ph} can be derived from the Hedin formalism [47, 69, 161, 162]. Thereby, the Hedin vertex is obtained from the three-point correlation function (3.15). The U -reducible diagrams is then given by,

$$\nabla_{\nu\nu'\omega}^{ph,\alpha} = \lambda_{\nu\omega}^\alpha w_\omega^\alpha \lambda_{\nu'\omega}^\alpha. \quad (3.92)$$

In Fig. 3.3 this diagram is depicted as the second diagram. In the context of the decomposition, we should note that by construction the Hedin vertex λ is irreducible in the U - ph channel [163].

The vertically particle-hole U -reducible diagrams $\nabla^{\bar{p}\bar{h}}$ for the paramagnetic case can be obtained from ∇^{ph} via crossing relations of the four-point vertex [107] and are given by

$$\nabla_{\nu\nu'\omega}^{\bar{p}\bar{h},\alpha} = -\frac{1}{2} \nabla_{\nu,\nu+\omega,\nu'-\nu}^{ph,\text{ch}} - \frac{3-4\delta_{\alpha,\text{sp}}}{2} \nabla_{\nu,\nu+\omega,\nu'-\nu}^{ph,\text{sp}} \quad (3.93)$$

In Fig. 3.3 the vertical particle-hole diagrams are depicted as the third and fourth diagrams. The pp -diagrams we construct in analogy to the ph -diagrams [70]. Accordingly, they are given by

$$\nabla_{\nu\nu'\omega}^{pp,\alpha} = \frac{1 - 2\delta_{\alpha,\text{sp}}}{2} \lambda_{\nu\omega}^s w_{\omega}^s \lambda_{\nu'\omega}^s \quad (3.94)$$

and are depicted as the fifth diagram in Fig. 3.3.

Lastly, we comment that the triplet channel, which consists of two particles with the same spin [107], does not contribute to the full vertex f , since the Hubbard interaction term $U n_{\downarrow} n_{\uparrow}$ only contains particles with opposite spins. As can be seen in Fig. 3.3 diagrammatically the decomposition can be interpreted as processes mediated by the exchange of effective bosons.

The bosonic line is the screened interaction (3.19) in the corresponding channel. The fully irreducible diagrams $\varphi^{f_{irr}}$ can not be described as single-boson exchange but describes multiboson exchange or other processes, which do not involve boson exchanges at all. At last, in the SBE approximation the full four-point vertex f^{α} is approximated by neglecting the fully irreducible part $\varphi^{f_{irr}}$:

$$f_{\nu\nu'\omega}^{\alpha} \approx \nabla_{\nu\nu'\omega}^{\text{SBE},\alpha}. \quad (3.95)$$

By waiving the four-point vertex we also ease the computational effort significantly. As one might expect this approximation performs well in the weak-coupling regime. But more surprisingly, for large interactions SBE captures the dominant scattering processes [70, 75].

Part II

Results

Chapter 4

DB

This chapter is based on the following publications:

T. Schäfer, N. Wentzell, F. Šimkovic, Y.-Y. He, C. Hille, M. Klett, C. J. Eckhardt, B. Arzhang, V. Harkov, F. M. C.-M. Le Régent, A. Kirsch, Y. Wang, A. J. Kim, E. Kozik, E. A. Stepanov, A. Kauch, S. Andergassen, P. Hansmann, D. Rohe, Y. M. Vilc, J. P. F. LeBlanc, S. Zhang, A.-M. S. Tremblay, M. Ferrero, O. Parcollet, A. Georges, “Tracking the Footprints of Spin Fluctuations: A MultiMethod, MultiMessenger Study of the Two-Dimensional Hubbard Model”. *Phys. Rev. X* **11**, 011058 (2021)

M. Vandelli, V. Harkov, E. A. Stepanov, J. Gukelberger, E. Kozik, A. Rubio, A. I. Lichtenstein, “Dual boson diagrammatic Monte Carlo approach applied to the extended Hub-bard model”. *Phys. Rev. B* **102**, 195109 (2020)

4.1 Tracking the Footprints of Spin Fluctuations: A MultiMethod, MultiMessenger Study of the Two-Dimensional Hubbard Model

Despite the simplicity of the Hubbard model, for a long time, an exact solution was only available analytically in one dimension and numerically in the formal limit of infinite dimensions (where the spatial fluctuations can be neglected [138, 139]) in the framework of DMFT by mapping it on an exactly solvable impurity model. However, in the case of two dimensions, where, e.g., the Hubbard-model is known as a prototype model for high-temperature superconducting cuprate compounds [164–167], the Hubbard model holds many open questions.

But owing to new developments in recent years new numerical techniques were presented. Some of them even allow for a numerical exact treatment of the finite-dimensional Hubbard model at certain regimes [85]. Due to the complexity of such techniques the convergence radius usually is restricted, for instance, to high temperatures or regions away from phase boundaries [85, 131, 168, 169]. Nevertheless, such methods provide a perfect testing ground for already established more flexible, and computationally efficient methods or as a benchmark for newly developed methods in future works.

This chapter is based on the study presented in Ref. [85], where all the results of this section were already published. In Ref. [85] different methods are benchmarked against two numerically exact methods, namely diagrammatic Monte Carlo (DiagMC) and determinantal quantum Monte Carlo (DQMC) methods. Thereby, the authors perform a comprehensive study of the weak coupling regime of the two-dimensional Hubbard model which reveals several distinct physical regimes and crossovers between them. In this section of the thesis, we only focus on the results of the DB approach, which were provided by the author of this thesis. For the extensive discussion as well as comparison with other methods the reader is referred to Ref. [85].

The investigation is focused on the weak coupling regime of the single-band Hubbard model on the square lattice. Thereby, the calculations are performed for $U = 2$ at different temperatures at half-filling. The unit of energy for the calculations is set to $t = 1$. Despite the simplicity of the Hubbard model, already in this region, the system reveals nontrivial physical phases with interesting crossover regions between them as the temperature decreases. These features have different origins. First, the ground state of the system is an antiferromagnetic insulator which can be qualitatively explained by the Slater mechanism [170]. However, at any finite temperature, the antiferromagnetic long-range order is destroyed by fluctuations in accord with the Mermin-Wagner theorem [171, 172]. In addition, the van Hove singularity at the antinodal point at $\text{AN}=(\pi, 0)$ leads to a larger scattering probability compared to the nodal point at $\text{N}=(\pi/2, \pi/2)$ which results in the suppression of the coherence of single-particle excitations around this point and with it a nodal/antinodal dichotomy [173–175]. The schematic representation of the physical regimes and the crossover regions are illustrated in Fig. 4.1. The left-hand side shows a schematic $T - U$ phase diagram where the different regimes are illustrated in different colors. The vertical dashed line denotes the considered interaction $U = 2t$ in terms of the hopping t . The right-hand side shows the qualitative behavior of the Matsubara frequency-dependent imaginary part of the self-energy in the corresponding regime. The dots denote the AN and the triangles the N points, respectively. The critical temperatures between the different regions are defined by the change of the slope between the first and second Matsubara frequency at the corresponding \mathbf{k} -point, which

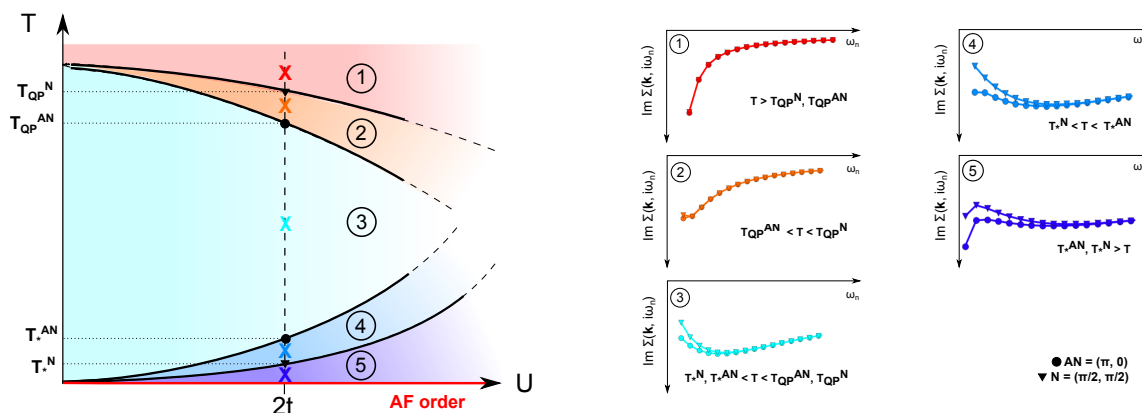


FIGURE 4.1: Schematic representation of the phase diagram for the two-dimensional Hubbard model on the square lattice in dependence of temperature T and coupling U in the weak-coupling regime around $U/t = 2$ (left panel) and qualitative depictions of the imaginary parts of the self-energy in dependence of the Matsubara frequencies ω_n for temperatures marked by \mathbf{X} in the left panel in the corresponding colors (right panel). The upper labels N and AN stand for the nodal $\mathbf{k} = (\pi/2, \pi/2)$ and antinodal points $\mathbf{k} = (\pi, 0)$ respectively, and the lower labels QP and * for the onset of coherence and (pseudo)gap respectively. (The data in the right panel for the self-energy is extracted from D Γ A calculations.) The figure is adapted from Ref. [85].

will be discussed in more detail in the following.

At high temperatures, the system is governed by strong thermal fluctuations. This region ① is depicted in red in Fig. 4.1. These thermal fluctuations suppress the formation of the long-lived single-particle excitations resulting in a divergent behavior in the self-energy at low frequencies. Decreasing the temperature reduces the thermal fluctuations and the long-lived quasiparticles start to develop in the system¹. The increasing coherence in the single-particle spectrum shows itself in the changing behavior of the self-energy. The self-energy at low frequencies increases and the slope between the first two Matsubara frequencies changes. The coherence temperature T_{QP} is therefore defined by the change of the sign in the slope between the first and second frequencies [52, 176, 177]. However, due to the vHS in the AN point the coherence temperature T_{QP}^{N} at the N point is higher than $T_{\text{QP}}^{\text{AN}}$ at the AN point, which defines the crossover region ② denoted by the orange color. In this region, the system becomes coherent at the N point while remaining incoherent close to the AN point. The system becomes metallic ③ when the slope at both points becomes negative. This regime is denoted by the light blue color. Lowering the

¹Note that in the considered system due to the perfect nesting the quasiparticles do not obey Landau's Fermi-Liquid theory. For more details see Ref. [85].

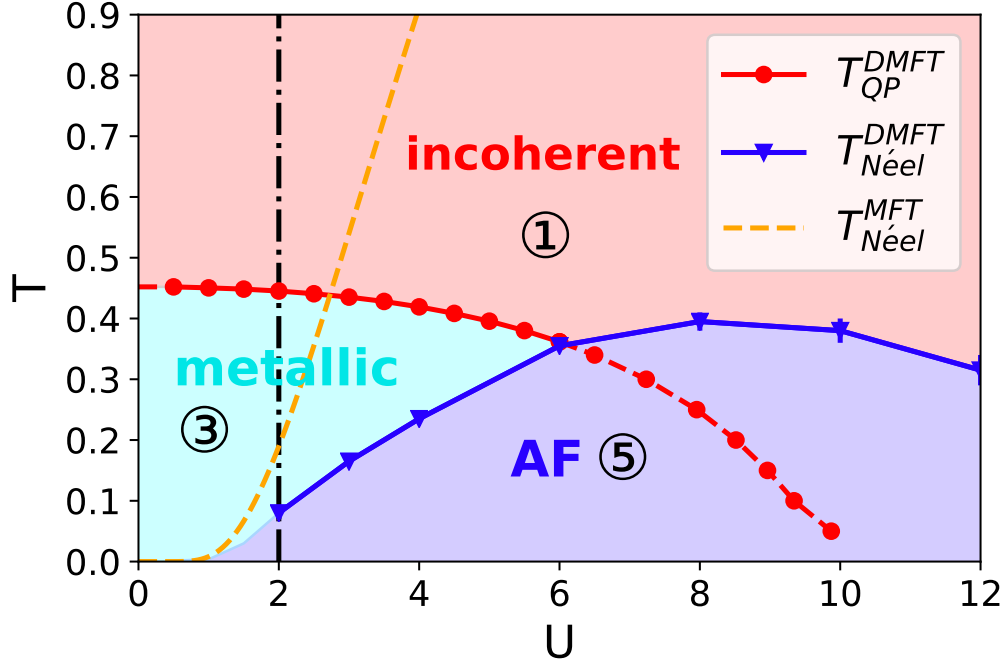


FIGURE 4.2: Phase diagram of the Hubbard model on the square lattice at half filling within the DMFT approach. The red and blue lines denote the quasiparticle coherence temperature and the antiferromagnetic (AF) transition temperatures, respectively. For comparison, the orange line indicates the Néel transition temperature according to the mean-field theory. The figure is adapted from Ref. [85].

temperature suppresses the thermal fluctuations, which further increases the lifetime of the quasiparticles until AFM fluctuations start to develop in the system reaching the long-range AFM order at $T = 0$. Their correlation length increases exponentially. The scattering rate of the quasiparticles increases due to the development of the AFM order and a pseudogap develops at the Fermi surface in the single-particle spectrum. This leads to a decrease of the self-energy at low frequencies defining the crossover temperature T_* again with the change of the sign of the slope in the opposite way compared to the coherence temperature. T_* denotes the temperature where the coherence is suppressed and the pseudogap begins to develop. The pseudogap first appears at the AN point at T_*^{AN} and with the temperature decreasing it propagates along the Fermi surface until it opens at the N point at T_*^N . This crossover region ④ with a partially gapped Fermi surface is depicted in blue. The region ⑤, drawn in purple, is governed by long-ranged AFM fluctuations and the pseudogap occurs everywhere on the Fermi surface.

DMFT

Since in the DB approach we have performed a diagrammatic extension of DMFT to account for nonlocal correlations, DMFT can be considered as the zero-order approximation. Therefore, before discussing the results of the DB approach let us consider the $T - U$ phase diagram within DMFT. The phase diagram is shown in Fig. 4.2. Since the DMFT self-energy is local, no crossover appears in the phase diagram. At $U = 2$ DMFT shows a good agreement with the local part of the exact results obtained from DiagMC (not shown) up to temperature $T \simeq 0.1$ [85]. The coherence temperature $T_{\text{QP}}^{\text{DMFT}}$ denoting the crossover to the metallic regime is obtained in the same way as discussed above. The red line in Fig. 4.2 denotes this crossover temperature. At $U = 2$ the transition occurs at $T_{\text{QP}}^{\text{DMFT}} \simeq 0.45$. The exact shows a transition at $T_{\text{QP}}^{\text{N}} \simeq 0.42$ and $T_{\text{QP}}^{\text{AN}} \simeq 0.35$ [85]. The DMFT result lies within the error bars of the exact result at the N point, however, shows a larger mismatch compared to the AN point due to the absence of momentum dependence. The DMFT Néel temperature is used as the estimation of T_*^{DMFT} . Due to the absence of the nonlocal correlations which destroy the AFM order an actual phase transition to the AFM ordered phase appears in DMFT at finite temperatures. T_*^{DMFT} is depicted in Fig. 4.2 as the blue line. The DMFT Néel temperature exhibits a large crossover region with a maximum at $U = 8$ between the weak coupling regime where the Néel temperature behaves exponentially and the strong coupling regime where the Néel is proportional to the superexchange $J = 4t^2/U$ and the Hubbard model can be mapped on the effective Heisenberg model. For comparison, the Néel temperature T_*^{MFT} of the static mean-field theory (MFT) is depicted in orange. At $U = 2$ the DMFT Néel temperature lies around $T_*^{\text{DMFT}} \simeq 0.08$. For comparison, the numerically exact results is around $T_*^{\text{AN}} \simeq 0.065$ and $T_*^{\text{N}} \simeq 0.0625$, respectively [85].

DB

In the following the results of the DB approach are discussed. To this end we first consider a part of a text which has been already published in the APS Journal:

T. Schäfer, N. Wentzell, F. Šimkovic, Y.-Y. He, C. Hille, M. Klett, C. J. Eckhardt, B. Arzhang, V. Harkov, F. M. C.-M. Le Régent, A. Kirsch, Y. Wang, A. J. Kim, E. Kozik, E. A. Stepanov, A. Kauch, S. Andergassen, P. Hansmann, D. Rohe, Y. M. Vilc, J. P. F. LeBlanc, S. Zhang, A.-M. S. Tremblay, M. Ferrero, O. Parcollet, A. Georges, “Tracking the Footprints of Spin Fluctuations: A MultiMethod, MultiMessenger Study of the Two-Dimensional Hubbard Model”. *Phys. Rev. X* **11**, 011058 (2021) (see Ref. [85]).

The dual boson (DB) approach [58–60] is an extension of the DF approach that, additionally to the local Coulomb interaction, accounts for

the effect of nonlocal interactions in different bosonic channels (ς). Within the DB approach, local electronic correlations are considered exactly in the framework of the (extended) dynamical mean-field theory [21, 178]. Nonlocal collective fluctuations are treated diagrammatically beyond the EDMFT level. For this aim, dual-boson fields φ^ς are introduced in addition to dual-fermion variables $f^{(*)}$ that are already present in the DF approach. The DB theory is derived analytically using a path-integral formalism, so many existing EDMFT-based approaches can be obtained as a certain approximation of the DB [60, 72]. Also, the DB theory fulfills the Mermin-Wagner theorem, which allows us to avoid unphysical phase transitions in two dimensions [62].

The action of the DB theory is as follows:

$$\tilde{S} = - \sum_{\mathbf{k}, \omega, \sigma} f_{\mathbf{k}\omega\sigma}^* \tilde{\mathcal{G}}_{\mathbf{k}\omega\sigma}^{-1} f_{\mathbf{k}\omega\sigma} - \frac{1}{2} \sum_{\mathbf{q}, \Omega, \varsigma} \phi_{\mathbf{q}\Omega}^\varsigma \tilde{\mathcal{W}}_{\mathbf{q}\Omega}^{\varsigma-1} \phi_{-\mathbf{q}, -\Omega}^\varsigma + \tilde{\mathcal{F}}. \quad (4.1)$$

Here, the bare fermion $\tilde{\mathcal{G}}_{\mathbf{k}, \nu, \sigma}$ and boson $\tilde{\mathcal{W}}_{\mathbf{q}, \Omega}^\varsigma$ propagators are given by nonlocal parts of the EDMFT Green function and renormalized interaction [60], respectively. The interaction part $\tilde{\mathcal{F}}[f^*, f, \varphi]$ of the dual action contains all possible, exact, local fermion-fermion and fermion-boson vertex functions of the impurity problem. Here, as well as in most of the DB approximations, we restrict ourselves to the lowest-order (two-particle) interaction terms that are given by the four-leg fermion-fermion and three-leg fermion-boson vertex functions. This truncation of the interaction allows us to describe collective charge [134, 179] and spin [133, 180] degrees of freedom in a conserving way using the ladder DB approximation [58–60, 125].

In the main part of the text, only single-shot ladder dual-boson results are discussed. These calculations are performed on the basis of the converged DMFT solution of the problem, where the bosonic hybridization function is equal to zero. Importantly, in the latter case, the DB theory fully coincides with the DF approach if only the local Coulomb interaction is considered. The corresponding local impurity problem is solved using the open-source CT-HYB solver [181, 182] based on the ALPS libraries [183]. This solution requires $N_{\text{cycles}} = 8.1 \times 10^7$ Monte Carlo steps. After that, we calculate the dual self-energy and polarization operator diagrammatically and perform only the inner self-consistency loop in order to obtain the dressed Green function and renormalized interaction using the Dyson equation. For this purpose, we use a momentum grid with a maximum linear mesh size of $N_k = 128$, with the number of fermionic and

bosonic Matsubara frequencies being $N_{i\omega} = 256$ and $N_{i\Omega} = 64$, respectively. The expression for the lattice self-energy of the DB approach coincides with the one of the DF theory in Eq. (D8)². The lattice polarization function can be found using a similar expression [61]:

$$\Pi(\mathbf{q}, i\Omega_n) = \frac{\tilde{\Pi}(\mathbf{q}, i\Omega_n)}{1 + \mathcal{W}(i\Omega_n)\tilde{\Pi}(\mathbf{q}, i\Omega_n)} + \Pi^{\text{EDMFT}}(i\Omega_n). \quad (4.2)$$

The fully self-consistent DB calculations can be performed as follows. To obtain the fermionic hybridization of the effective impurity problem, we use the outer self-condition that equates the local part of the lattice Green function and local impurity Green function $\sum_{\mathbf{k}} G_{\mathbf{k}\omega\sigma} = g_{\omega\sigma}$. Regarding the bosonic hybridization function, there is no clear method for how this quantity has to be determined. Here, we investigate two different self-consistency schemes that fix the bosonic hybridization. For the X-self-consistent (Xsc) result, the local part of the lattice susceptibility is equated to the corresponding local susceptibility of the impurity problem $\sum_{\mathbf{q}} X_{\Omega}^{\zeta} = \chi_{\Omega}^{\zeta}$. The other self-consistency can be imposed on a renormalized (screened) interaction (Wsc) $\sum_{\mathbf{q}} W_{\Omega}^{\zeta} = w_{\Omega}^{\zeta}$. The renormalized interaction W of the lattice problem can be defined as

$$W^{\zeta-1}(\mathbf{q}, i\Omega_n) = U^{\zeta-1} - \Pi^{\zeta}(\mathbf{q}, i\Omega_n), \quad (4.3)$$

where $U^{\text{ch/sp}} = \pm U/2$ [72]. The EDMFT renormalized interaction can be obtained by neglecting the dual contribution to the polarization operator in Eq. 4.3, so that $\Pi^{\zeta}(\mathbf{q}, i\Omega_n) = \Pi^{\zeta\text{EDMFT}}(i\Omega_n)$. The renormalized interaction of the impurity problem can be found as

$$w^{\zeta-1}(i\Omega_n) = (U^{\zeta} + Y^{\zeta}(i\Omega_n))^{-1} - \Pi^{\zeta\text{EDMFT}}(i\Omega_n), \quad (4.4)$$

where $Y^{\zeta}(i\Omega_n)$ is the bosonic hybridization function. Corresponding results are shown in Figs. 4.3, 4.6, 4.5 and 4.4. We note, as well, that the comparisons between self-consistent DB and self-consistent DF schemes are in good agreement, but they differ from the exact result. As we point out in the main text, the single-shot DB approach correctly reproduces exact DiagMC results at almost all temperatures. Surprisingly, we observe that the Xsc DB calculations strongly deviate from the exact result presented in both figures. At the same time, we find that the Wsc DB result for the self-energy agrees with DiagMC calculations even better than the

²See Eq. (3.57).

single-shot DB one. However, two-particle quantities, such as the lattice susceptibility and double occupancy, get worse when the self-consistency on the renormalized interaction is utilized. This observation can be explained by the fact that the considered bosonic self-consistencies cannot fix all desired single-and two-particle quantities at the same time. Therefore, the question of a good self-consistency for the bosonic hybridization function remains open.

In the following, the results of the DB calculations will be discussed in more detail. We begin the discussion by comparing the single-shot DB results with the results of the DiagMC approach. Note that by *single-shot* we do not mean that the bare Green's function is used to calculate the self-energy. In DF and DB a full (or outer) self-consistency cycle can be performed. Thereby, after obtaining the lattice quantities the hybridization function Δ_ν is updated imposing the self-consistency condition $\sum_{\mathbf{k}} \tilde{G}_k = 0$ [54, 124]. The new hybridization function is then used as a new initial guess for the impurity solver. In this case, the DMFT is not viewed as the reference system. Hence, the full self-consistency cycle is not used in our calculation and we refer to our results as single-shot calculations.

In Fig. 4.3 we show the comparison between the numerical exact DiagMC (on the left) and the single-shot DB (on the right) methods. The upper row shows the Matsubara frequency dependent imaginary part of the self-energy at the AN point. The lower row shows same results for the N point. Since for single-particle quantities DiagMC and DQMC are in agreement within error bars, we only show the results obtained within DiagMC. For the considered interaction strength both methods are able to be converged until $T \approx 0.063$ due to different reasons [85]. The different temperatures (and colors) of the DiagMC result correspond to the different regimes shown in Fig. 4.1. This does not hold for the right hand side. Note that the same colors on both sides do not always correspond to the same temperature.

At high temperatures (red and orange) DB shows a good agreement to the exact result. It correctly reproduces the incoherent behaviour and correctly predicts the coherence temperature $T_{\text{QP}}^{\text{N}} \simeq 0.42$ and $T_{\text{QP}}^{\text{AN}} \simeq 0.35$ at both N and AN points, respectively (not shown) [85]. However, DB shows a deviation at low temperature. Even though the tendency towards a pseudogap is clearly visible, the temperature T_* could not be reached due to convergence problems. The results show, that single-shot DB underestimate the scattering rate. This underestimation arises due to missing transverse contributions in the ladder approximation [131, 168, 169].

In Fig. 4.4 we show results obtained from DB calculations which take into account the bosonic hybridization function Y^ζ obtained from to different self-consistency conditions [156]. The main difference between the obtained hybridization functions is that the one obtained from the self-consistency condition of the screened interaction goes to zero for large frequencies. Beside an additional self-consistency condition,

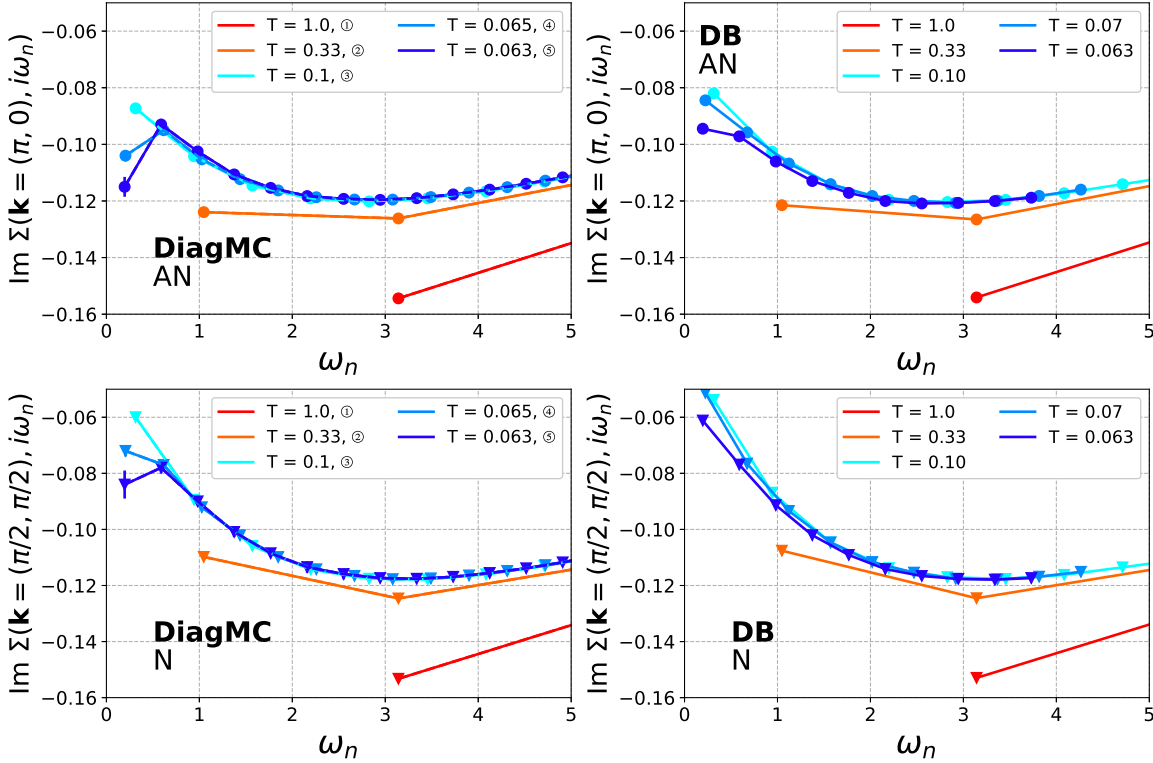


FIGURE 4.3: Comparison of the imaginary part of the Matsubara self-energy at the antinodal $\mathbf{k} = (\pi, 0)$ (upper row) and nodal $\mathbf{k} = (\pi/2, \pi/2)$ (lower row) points between the diagrammatic Monte Carlo (DiagMC) (left column) and dual boson (DB) (right column) methods for different temperatures. (Note the slight difference in the lower temperatures.) The figure is adapted from Ref. [85].

taking the bosonic hybridization function into account leads to a more complex dramatic structure. For this reason, achieving convergence becomes more difficult. In case of Xsc DB, e.g. the convergence could be achieved only up to $T = 0.1$ as shown on the left hand side of Fig. 4.4. Additionally, the results for Xsc DB shows the largest deviation to the exact results at all temperatures compared to the other presented DB schemes. Obviously, in this regime the considered self-consistency condition does not provide a good bosonic hybridization function. In contrast, the results for Wsc DB are very similar to single-shot DB results. For temperatures up to $T = 0.1$ Wsc DB shows a good agreement with the exact results and shows even a larger tendency towards the pseudogap formation than single-shot DB. However, in the following we will see that for the considered parameters quantities on the two-particle level, such as lattice susceptibility and double occupancy, show a larger deviation from the exact result if the bosonic hybridization function is not zero.

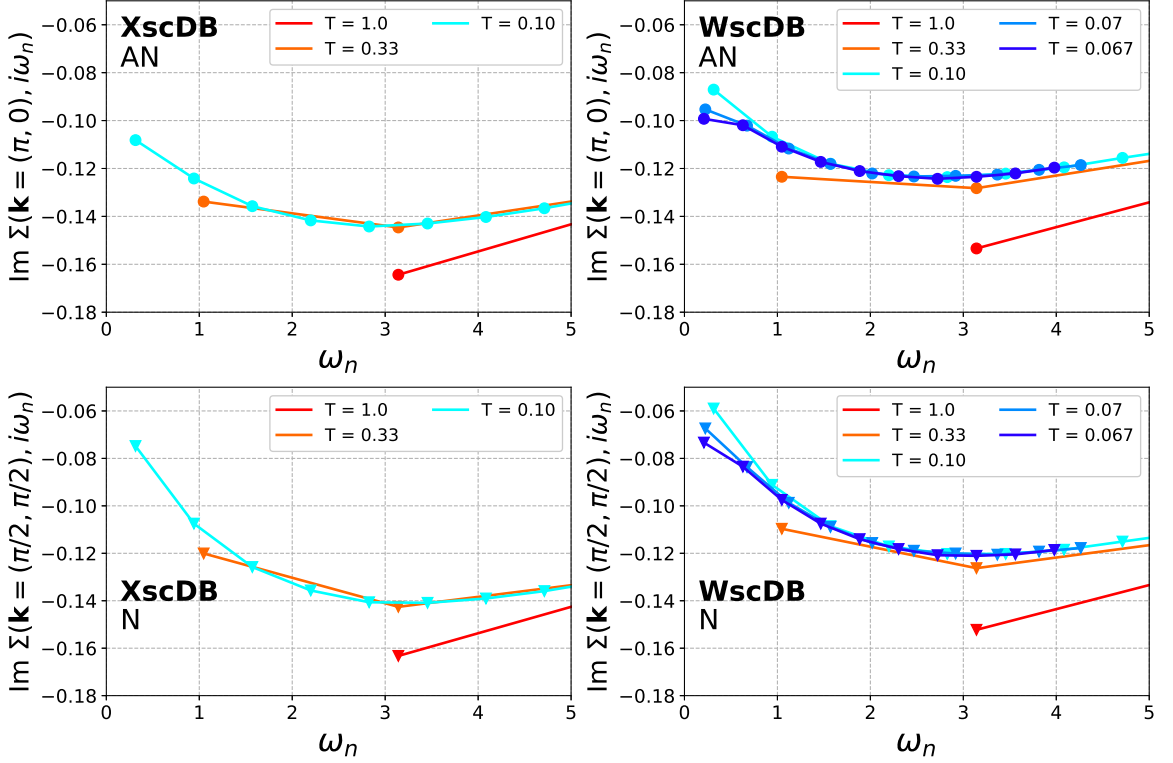


FIGURE 4.4: Comparison of the imaginary part of the Matsubara self-energy at the antinodal $\mathbf{k} = (\pi, 0)$ (upper row) and nodal $\mathbf{k} = (\pi/2, \pi/2)$ (lower row) points between the alternative DB schemes, self-consistent (XscDB) (left column) and W-self-consistent (WscDB) (right column) for different temperatures. The figure is adapted from Ref. [85].

To investigate magnetic correlations in the system we consider the static spin susceptibility at $\mathbf{q} = (\pi, \pi)$ and $i\Omega_n = 0$ as well as the correlation length ξ at different temperatures. The real part of the susceptibility (left) and ξ (right) are depicted in Fig. 4.5. For comparison, MFT (orange) and DMFT (gray) results are shown with the Néel temperature denoted by a vertical dashed line. Here, $\mathbf{q} = (\pi, \pi)$ is of particular interest because of the strong enhancement of the susceptibility at this point due to the perfect nesting of this moment vector. At high temperature where the magnetic fluctuations are weak, the magnetism can be described by the Curie law where $\chi_{sp}(\mathbf{q} = (\pi, \pi), i\Omega_n = 0) \propto T^{-1}$. However, at lower temperatures, when the AFM correlation becomes large, the susceptibility and the correlation length grows exponentially. The correlation length is extracted by a fitting procedure using the Ornstein-Zernik form [85].

At small temperatures up to $T \approx T_{\text{Néel}}^{\text{MFT}}$ all DB schemes are in good agreement

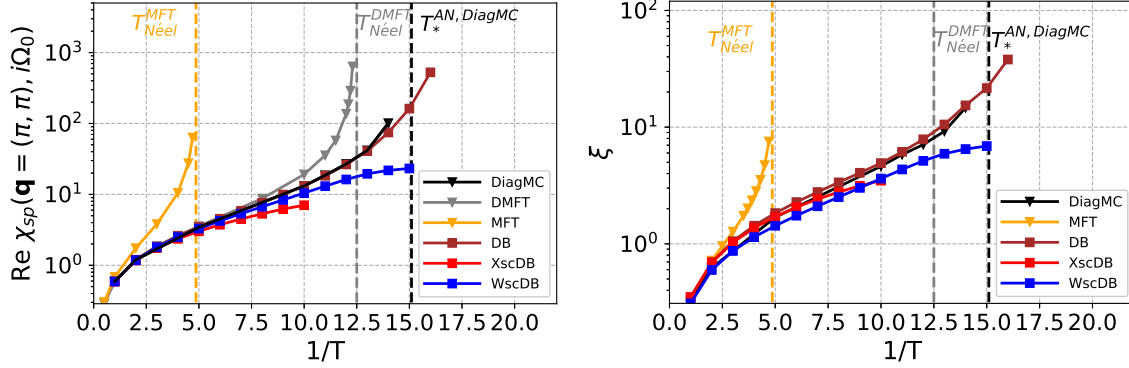


FIGURE 4.5: Real part of the spin susceptibility (left panel) at $\mathbf{q} = (\pi, \pi)$ and the first Matsubara frequency $i\Omega_0$ and correlation length ξ (right panel) in dependence of the inverse temperature for various methods on the logarithmic scale. The figure is adapted from Ref. [85].

with the DiagMC (black) result. At higher temperatures, the results start deviating. Xsc DB (red) performs the worst. Wsc DB (blue) shows a better performance, however, the method does not capture the second exponential regime at low temperatures. The single-shot DB (brown) shows good agreement in the first exponential (metallic) regime at intermediate temperatures between $T_{\text{Néel}}^{\text{MFT}}$ and $T_{\text{Néel}}^{\text{DMFT}}$. Furthermore, at low temperatures, it captures the second exponential regime qualitatively. Quantitatively single-shot DB lies slightly below the benchmark at low T . This shows again, as discussed above, that at low temperatures the ladder approximation underestimates the AFM fluctuations. The correlation length shows qualitatively the same results.

As the final result we discuss the temperature dependence of the double occupancy,

$$D = \langle n_{\uparrow} n_{\downarrow} \rangle. \quad (4.5)$$

The DB double occupancy is obtained from the local part of the lattice susceptibility [184]. The results are illustrated in Fig. 4.6. First, let us consider the DiagMC result in more detail. At high temperatures, the double occupancy is rather high due to the thermal fluctuations and decreases with cooling until at $T \simeq 1$ a minimum is reached. Further decreasing the temperature leads to an increase of D . This behavior can be qualitatively understood considering the entropy of the system since the main part of this region lies within the metallic regime [85]. The increase of D is followed by a sudden drop at low temperature due to a gain in potential energy because of increasing AFM fluctuations [85].

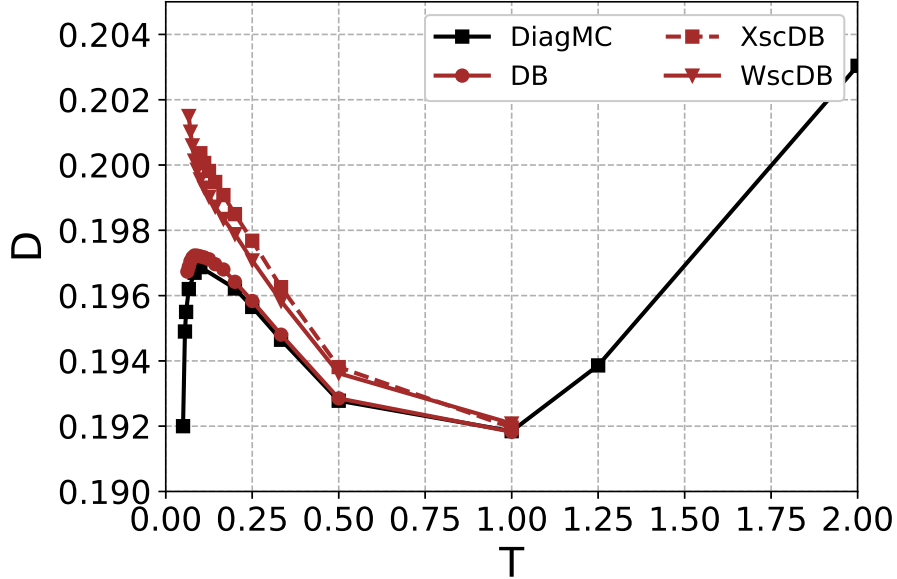


FIGURE 4.6: Comparison of the double occupancy D between diagrammatic Monte Carlo (diagMC) and alternative DB schemes, single-shot (DB), self-consistent (XscDB), and W-self-consistent (WscDB). The figure is adapted from Ref. [85].

We find that all DB calculation scheme shows a good agreement at high temperatures up to $T \simeq 1$ (not shown). Xsc (squares) and Wsc (triangles) DB captures the increasing of the double occupancy below $T = 1$ qualitatively but fails to capture the drop of D at low temperatures due to the large underestimation of AFM fluctuations in this region. In contrast, single-shot DB (dots) show an accurate quantitative agreement with the benchmark at all accessible temperatures.

To summarize, we have investigated the weak coupling regime of the two-dimensional single-band Hubbard model at half filling. Despite the simplicity of this regime, the model reveals interesting physical regimes and crossover regions with characteristic properties. Single-shot DB captures qualitatively all the regimes and the crossovers between them. The method reproduces very accurately the exact benchmark results for single- and two-particle quantities up to low temperatures where the AFM fluctuation becomes large. In this regime, however, the results show small deviations, since the ladder approximation underestimates the AFM fluctuations due to the missing transversal contributions. Additionally, we find that the inclusion of the bosonic hybridization function using different self-consistency conditions leads to a larger deviation from the benchmark and complicates the convergence due to a more complex diagrammatic structure.

4.2 Dual boson diagrammatic Monte Carlo approach applied to the extended Hubbard model

In the next study [131] the dual boson diagrammatic Monte Carlo (DiagMC@DB) technique for strongly correlated systems is introduced which is an extension of a previous diagrammatic Monte Carlo scheme based on the DF approach [168, 169]. However, since the author of the current thesis provided the ladder DB results for this study, we consider the work [131] from the perspective of investigating the accuracy of the ladder approximation by comparing it to the numerical exact DiagMC@DB solution of the dual boson problem. The DiagMC@DB method allows one to sample all possible Feynman diagrams on the level of the four-point impurity vertex function. We perform calculations for the half-filled extended Hubbard model (1.12) on a square lattice for different strengths of the local U and non-local V electronic interactions. The inverse temperature is set to $\beta = 4$ for $U \leq 4$ and to $\beta = 2$ for $U > 4$. We find that the ladder DB approach performs very accurately in the regime of small to moderate local Coulomb interaction U up to half of the bandwidth, which can be explained due to the perturbation nature of electronic correlations in this regime. But also for other interaction strengths, the deviation from the exact solution remains within $\delta_M = 8\%$ errorbar. Moreover, we observe that the deviation is the largest around $U = 7$, which means that in this regime the diagrammatic contributions beyond the ladder become important. Further increase of the coupling leads to a decrease in the mismatch. Additionally, the mismatch between the results decreases with increasing V due to larger charge fluctuations in the longitudinal channel which are captured in the ladder approximation. Finally, we find that both methods yield a good agreement in predicting charge density wave (CDW) phase transition for considered control parameters justifying the argument that the ladder contribution is the leading one.

Dual boson diagrammatic Monte Carlo approach applied to the extended Hubbard modelM. Vandelli ^{1,2,3} V. Harkov ^{2,4} E. A. Stepanov ² J. Gukelberger,⁵ E. Kozik,⁶ A. Rubio,^{3,7,8} and A. I. Lichtenstein^{2,4,1}¹*The Hamburg Centre for Ultrafast Imaging, Luruper Chaussee 149, 22761 Hamburg, Germany*²*Institute of Theoretical Physics, Department of Physics, University of Hamburg, Jungiusstrasse 9, 20355 Hamburg, Germany*³*Max Planck Institute for the Structure and Dynamics of Matter, Center for Free Electron Laser Science, 22761 Hamburg, Germany*⁴*European X-Ray Free-Electron Laser Facility, Holzkoppel 4, 22869 Schenefeld, Germany*⁵*Microsoft Quantum, One Microsoft Way Redmond, Washington 98052, USA*⁶*Department of Physics, King's College London, Strand, London WC2R 2LS, United Kingdom*⁷*Center for Computational Quantum Physics, Flatiron Institute, 162 5th Avenue, New York, New York 10010, USA*⁸*Nano-Bio Spectroscopy Group and ETSF, Universidad del País Vasco, 20018 San Sebastián, Spain*

(Received 9 July 2020; revised 19 October 2020; accepted 20 October 2020; published 5 November 2020)

In this work we introduce the dual boson diagrammatic Monte Carlo technique for strongly interacting electronic systems. This method combines the strength of dynamical mean-field theory for nonperturbative description of local correlations with the systematic account of nonlocal corrections in the dual boson theory by the diagrammatic Monte Carlo approach. It allows us to get a numerically exact solution of the dual boson theory at the two-particle local vertex level for the extended Hubbard model. We show that it can be efficiently applied to description of single-particle observables in a wide range of interaction strengths. We compare our exact results for the self-energy with the ladder dual boson approach and determine a physical regime, where the description of collective electronic effects requires more accurate consideration beyond the ladder approximation. Additionally, we find that the order-by-order analysis of the perturbative diagrammatic series for the single-particle Green's function allows to estimate the transition point to the charge density wave phase.

DOI: [10.1103/PhysRevB.102.195109](https://doi.org/10.1103/PhysRevB.102.195109)**I. INTRODUCTION**

Strongly correlated systems represent a formidable challenge in condensed matter physics. For this reason, the study of model systems can allow us to investigate the effects of strong interactions and analyze the effects of different approximations. Among these models, the Hubbard model [1] has been extensively studied in the past decades due to its capacity of successfully describing the emerging physics of some classes of strongly correlated materials, where local interactions are assumed to be much stronger than nonlocal ones. A major breakthrough in the solution of the Hubbard model was made by dynamical mean-field theory (DMFT) [2]. This method becomes exact in the limit of infinite spacial dimensions or connectivity of the lattice [3], and serves as an accurate approximation for single-particle quantities in finite dimensions [4].

At the same time, many real materials exhibit interesting physical effects, such as a charge density wave (CDW) phase, that cannot be described by a local Hubbard interaction term alone. To consider these phenomena, nonlocal interactions

have to be taken into account. For this aim, in analogy with DMFT, an extended dynamical mean-field theory (EDMFT) has been developed [5–9]. However, in this approach the self-energy and polarization operator are local, meaning that they are frequency dependent, but not momentum dependent. Extensions of EDMFT, such as the *GW* + EDMFT [10–16], the dual boson (DB) [17–20], the triply irreducible local expansion (TRILEX) [21–23], and the dual TRILEX (D-TRILEX) [24] approaches have been developed to cope with this issue. In particular, the DB and D-TRILEX techniques are based on the exact transformation that allows to rewrite the initial action of the extended Hubbard model in terms of the local impurity problem, which can be solved numerically exactly [25–29], and a diagrammatic series around the impurity. Since the effective impurity problem already includes the main contribution coming from local correlations, this looks to be a naturally convenient starting point for perturbation theory and approximate approaches.

So far, calculations in the framework of the dual boson approach have been performed only in the ladder approximation [30–34]. This approach is based on the calculation of a specific sub-set of diagrams that, in principle, can be justified by physical considerations only in the regime of developed collective electronic fluctuations [35,36]. However, the ladder DB approximation provides remarkably good results in comparison with other advanced methods, as, for instance, dynamical cluster approximation (DCA) [37,38]. An alternative approach that involves solution of parquet equations based on dual theories was recently proposed in Ref. [39]. A

Published by the American Physical Society under the terms of the Creative Commons Attribution 4.0 International license. Further distribution of this work must maintain attribution to the author(s) and the published article's title, journal citation, and DOI. Open access publication funded by the Max Planck Society.

comparison between various methods based on extensions of (E)DMFT can be found in Ref. [40].

Another route to study strongly correlated systems has recently been attempted—the use of unbiased methods based on the combination of diagrammatic approaches with Markov chain Monte Carlo [41]. In particular, the bare diagrammatic Monte Carlo (DiagMC) method has been successfully applied to the Hubbard model at weak and moderate Coulomb interactions [42]. This method starts from an expansion in terms of the Hubbard coupling U and constructs all Feynman diagrams up to some finite but high order in U . The algorithm allows to sample all possible diagrams without any restriction to specific topologies. Efficient algorithms that express all connected diagrams of the perturbative expansion up to a given order by means of determinants [43] have been developed for various observables and correlation functions [44–47], significantly reducing the computational cost of the calculation. Approaches based on a small-coupling expansion work very well in the regime of small to moderate couplings, but start to fail when U is of the order of half of the bandwidth [4,48]. These failures are related to the finite convergence radius of the diagrammatic series and can be improved using resummation techniques [44].

To allow for a nonperturbative treatment of strong correlation effects, a diagrammatic Monte Carlo scheme based on the dual fermion (DF) approach [49] was proposed in Refs. [50,51]. The advantage of this method in comparison with diagrammatic expansions in terms of the bare Coulomb interaction U is that the impurity problem already accounts for the main effects of local correlations, which strongly screen the bare interaction U . The expansion is thus performed in terms of the renormalized local interaction vertex function, which appears to be naturally more convenient at the moderate and strongly interacting regime. Additionally, the diagrams are sampled continuously in the momentum space without the discretization of the Brillouin zone. Hence, the result of the calculation is not influenced by any finite-size effects.

In this paper we generalize this approach to the extended Hubbard model, performing an additional dual transformation that introduces effective bosonic fields related to nonlocal interactions. Our dual boson diagrammatic Monte Carlo (DiagMC@DB) method combines the advantages of DMFT, because it already accounts for the screened local interaction in the impurity problem, with the capability of sampling all the possible Feynman diagrams without any restriction. The result is an efficient diagrammatic Monte Carlo algorithm that naturally incorporates the nonlocal Coulomb interaction in the original DiagMC@DF approach [51].

II. DUAL BOSON THEORY

Our starting point is the extended Hubbard model in the action formalism

$$\mathcal{S} = - \sum_{\mathbf{k}, \nu, \sigma} c_{\mathbf{k}\nu\sigma}^* [i\nu + \mu - \varepsilon_{\mathbf{k}}] c_{\mathbf{k}\nu\sigma} + U \sum_{\mathbf{q}, \omega} n_{-\mathbf{q}, -\omega, \uparrow} n_{\mathbf{q}\omega, \downarrow} + \frac{1}{2} \sum_{\mathbf{q}, \omega, \zeta} V_{\mathbf{q}}^{\zeta} \rho_{-\mathbf{q}, -\omega}^{\zeta} \rho_{\mathbf{q}\omega}^{\zeta}. \quad (1)$$

Here, $c_{\mathbf{k}\nu\sigma}^{(*)}$ are Grassman variables corresponding to the annihilation (creation) of electrons with momentum \mathbf{k} , fermionic Matsubara frequency ν , and spin σ . We also introduced the electronic dispersion $\varepsilon_{\mathbf{k}}$ and chemical potential μ . The model additionally includes an on-site Coulomb interaction of strength U in terms of the electron density $n_{\mathbf{q}\omega\sigma}$ at momentum \mathbf{q} and bosonic Matsubara frequency ω , as well as a nonlocal interaction $V_{\mathbf{q}}^{\zeta}$, where the index ζ represents charge ($\zeta = \text{ch}$) or spin ($\zeta = \text{sp} = \{x, y, z\}$) degrees of freedom. Variables $\rho_{\mathbf{q}\omega}^{\zeta} = n_{\mathbf{q}\omega}^{\zeta} - \langle n^{\zeta} \rangle$ are expressed in terms of composite quantities $n_{\mathbf{q}\omega}^{\zeta} = \sum_{\mathbf{k}\nu, \sigma, \sigma'} c_{\mathbf{k}+\mathbf{q}, \nu+\omega, \sigma}^* \sigma_{\sigma\sigma'}^{\zeta} c_{\mathbf{k}, \omega, \sigma'}$. In the previous expression $\sigma^{\text{ch}} = \mathbb{1}$, and $\sigma^{x,y,z}$ is the corresponding Pauli matrix in spin space. The general idea of dual theories is to split the action into two parts: a local impurity problem that contains the full local interaction and a nonlocal part that can be treated perturbatively. Instead of directly applying a perturbation theory to the nonlocal part, a transformation that introduces new variables is performed. This allows to dress the nonlocal part with the local impurity quantities. An additional important consideration is that, once the DMFT impurity is chosen, the dual theories represent a diagrammatic expansion around the DMFT solution. This starting point for the perturbation theory looks appealing since the DMFT already accounts for local many-body effects, which allows to correctly reproduce both the small and large U limits. To perform this transformation, we add and subtract an arbitrary fermionic hybridization function Δ_{ν} , so that we can isolate a local impurity part of the action. With this fermionic hybridization function the action reads $\mathcal{S} = \sum_i \mathcal{S}_{\text{imp}}^{(i)} + \mathcal{S}_{\text{nonloc}}$, where the impurity part is

$$\mathcal{S}_{\text{imp}}^{(i)} = - \sum_{\nu, \sigma} c_{\nu\sigma}^* [i\nu + \mu - \Delta_{\nu}] c_{\nu\sigma} + U \sum_{\omega} n_{-\omega, \uparrow} n_{\omega, \downarrow}, \quad (2)$$

and the nonlocal part reads

$$\mathcal{S}_{\text{nonloc}} = - \sum_{\mathbf{k}, \nu, \sigma} c_{\mathbf{k}\nu\sigma}^* [\Delta_{\nu} - \varepsilon_{\mathbf{k}}] c_{\mathbf{k}\nu\sigma} + \frac{1}{2} \sum_{\mathbf{q}, \omega, \zeta} V_{\mathbf{q}}^{\zeta} \rho_{-\mathbf{q}, -\omega}^{\zeta} \rho_{\mathbf{q}\omega}^{\zeta}. \quad (3)$$

In the following, $\langle \dots \rangle_{\text{imp}}$ denotes the average with respect to the local action (2). The impurity problem of Eq. (2) can be solved exactly using continuous-time quantum Monte Carlo solvers [25–29]. In the same way we could include a bosonic hybridization function [17–19]. However, this step would require an additional discussion of the self-consistency condition needed to determine it. Therefore, we exclude the bosonic hybridization from the current discussion to reduce the number of external parameters in the system. The hybridization function can be defined in an arbitrary way, but some choices are more convenient than others. In the rest of the paper we will use Δ_{ν} obtained from the single-site DMFT impurity problem.

The dual boson transformation amounts to perform a fermionic and a bosonic Hubbard-Stratonovich transformations over the nonlocal part of the action $\mathcal{S}_{\text{nonloc}}$, which introduces new dual fermionic variables f, f^* , and bosonic ϕ^{ζ} fields. The action obtained after this transformation is quadratic in the electronic operators $c^{(*)}$, so we can integrate them out [32]. The original problem of interacting electrons is then recast into a new problem in terms of the dual degrees

of freedom only. Single- and two-particle observables of the original electron system can be exactly related to dual correlation functions, as shown for example in Ref. [32]. The result for the dual action reads (see Ref. [24] for the derivation)

$$\begin{aligned} \tilde{S} = & - \sum_{\mathbf{k}, \nu, \sigma} f_{\mathbf{k}\nu\sigma}^* \tilde{\mathcal{G}}_{\mathbf{k}\nu\sigma}^{-1} f_{\mathbf{k}\nu\sigma} \\ & - \frac{1}{2} \sum_{\mathbf{q}, \omega, \zeta} \phi_{-\mathbf{q}, -\omega}^{\zeta} \tilde{W}_{\mathbf{q}\omega}^{\zeta} \phi_{\mathbf{q}\omega}^{\zeta} + \tilde{\mathcal{F}}[f, \phi]. \end{aligned} \quad (4)$$

The bare dual propagators are defined as

$$\tilde{\mathcal{G}}_{\mathbf{k}\nu\sigma} = [g_{\nu}^{-1} + \Delta_{\nu} - \epsilon_{\mathbf{k}}]^{-1} - g_{\nu} = G_{\mathbf{k}\nu\sigma}^{\text{EDMFT}} - g_{\nu\sigma}, \quad (5)$$

$$\tilde{W}_{\mathbf{q}\omega}^{\zeta} = \alpha_{\omega}^{\zeta} [V_{\mathbf{q}}^{\zeta}{}^{-1} - \chi_{\omega}^{\zeta}]^{-1} \alpha_{\omega}^{\zeta} = W_{\mathbf{q}\omega}^{\zeta \text{EDMFT}} - w_{\omega}^{\zeta}, \quad (6)$$

where g_{ν} and w_{ω}^{ζ} are the Green's function and renormalized interaction of the auxiliary impurity problem, respectively, and the impurity susceptibility $\chi_{\omega}^{\zeta} = -\langle \rho_{-\omega}^{\zeta} \rho_{\omega}^{\zeta} \rangle_{\text{imp}}$. Additionally, $\alpha_{\omega}^{\zeta} = 1 + U^{\zeta} \chi_{\omega}^{\zeta}$ with $U^{\text{ch/sp}} = \pm U/2$. The choice of the Matsubara frequency space is natural in this case because in Eq. (5) the $\sim \nu^{-1}$ part of the tail in $G_{\mathbf{k}\nu\sigma}^{\text{EDMFT}}$ is exactly canceled by g_{ν} . This means that the dual fermion Green's function decays as fast as $\sim \nu^{-2}$, and there are no convergence issues related to summations over Matsubara frequencies. The interaction term truncated at the two-particle level is given by

$$\begin{aligned} \tilde{\mathcal{F}}[f, \phi] = & \sum_{\substack{\mathbf{q}, \mathbf{k}, \omega, \nu \\ \zeta, \sigma, \sigma'}} \Lambda_{\nu\omega}^{\zeta} f_{\mathbf{k}\nu\sigma}^* \sigma_{\sigma'}^{\zeta} f_{\mathbf{k}+\mathbf{q}, \nu+\omega, \sigma'} \phi_{\mathbf{q}\omega}^{\zeta} \\ & + \frac{1}{4} \sum_{\substack{\mathbf{q}, \omega \\ \{\mathbf{k}, \nu, \sigma\}}} \Gamma_{\nu\nu'\omega}^{\sigma\sigma'\sigma''\sigma'''} f_{\mathbf{k}\nu\sigma}^* \\ & \times f_{\mathbf{k}+\mathbf{q}, \nu+\omega, \sigma'} f_{\mathbf{k}'+\mathbf{q}, \nu'+\omega, \sigma''} f_{\mathbf{k}'\nu'\sigma''}, \end{aligned} \quad (7)$$

where $\Lambda_{\nu\omega}^{\zeta}$ and $\Gamma_{\nu\nu'\omega}^{\sigma\sigma'\sigma''\sigma''}'$ are the impurity fermion-boson and fermion-fermion vertex functions, respectively. These quantities are defined in the particle-hole form as in Ref. [24], that in terms of impurity variables explicitly read

$$\Lambda_{\nu\omega}^{\zeta} = \frac{\langle c_{\nu\uparrow} c_{\nu+\omega, \uparrow}^* \rho_{-\omega}^{\zeta} \rangle_{\text{imp}}}{g_{\nu} g_{\nu+\omega} \alpha_{\omega}^{\zeta}}, \quad (8)$$

$$\Gamma_{\nu\nu'\omega}^{\sigma\sigma'\sigma''\sigma''}' = \frac{\langle c_{\nu\sigma} c_{\nu+\omega, \sigma'}^* c_{\nu'\sigma''}^* c_{\nu'+\omega, \sigma'''} \rangle_{\text{c, imp}}}{g_{\nu} g_{\nu+\omega} g_{\nu'} g_{\nu'+\omega}}. \quad (9)$$

In general, the interaction term also contains all the higher-order vertices that conserve the number of dual fermions, but we will limit our study to the two-particle interaction terms only. Terms beyond this approximation were shown to lead to very small corrections in many regimes [52]. As a matter of fact, dual theories with only two-particle vertex functions show a rather good agreement with other unbiased methods, and it is still under debate if deviations with other methods are due to higher-order vertices or to different effects [50–54]. Additionally, the inclusion of higher-order vertices would enormously increase the complexity of the diagrammatic Monte Carlo scheme. In light of all these considerations, we exclude them from our calculations.

In our case, the solution of the impurity problem is obtained using a continuous-time Monte Carlo solver based on

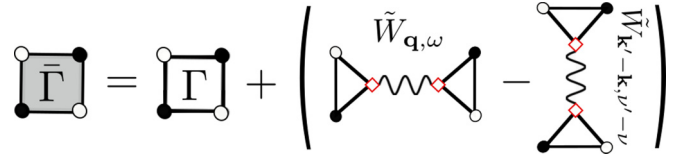


FIG. 1. Schematic diagrammatic interpretation of Eq. (12). The full antisymmetrized fermion-fermion interaction $\bar{\Gamma}$ (gray box) is a combination of the impurity vertex Γ (white box) and processes involving a boson exchange (wiggly line). The full vertex acquires a momentum dependence due to the presence of the bosonic lines. White and black dots represent incoming and outgoing particles, respectively. Triangles represent $\Lambda_{\nu\omega}$ vertices. The exact dependence on the channel indices and prefactors is shown in Eq. (12).

hybridization expansion (CT-HYB) [29]. This gives an access to all the impurity observables needed for the construction of the dual boson diagrammatics. In particular, we compute Δ_{ν} , g_{ν} , and χ_{ω} for the construction of bare propagators, as well as the fermion-fermion vertex $\Gamma_{\nu\nu'\omega}^{\sigma\sigma'\sigma''\sigma''}'$ and the fermion-boson vertex $\Lambda_{\nu\omega}^{\zeta}$. Within this approximation, the dual action (4) with the interaction (7) is quadratic in the bosonic fields. This means that it is possible to integrate dual bosonic degrees of freedom out exactly and obtain a fully fermionic action. The bosonic Hubbard-Stratonovich transformation is necessary for decoupling of the nonlocal interaction term that otherwise would prevent the integration of the local impurity action out. Moreover, the introduction of the bosonic variables dresses the interaction in terms of the impurity quantities, so that the bosonic propagator is already partially screened. To construct a form of the full fermion-fermion vertex after the integration of the bosons, it is useful to decompose the impurity fermion-fermion vertex (9) in channel representation as

$$\Gamma^{\sigma\sigma'\sigma''\sigma''}' = \frac{1}{2} \sum_{\zeta} \Gamma^{\zeta} \sigma_{\sigma'}^{\zeta} \sigma_{\sigma''}^{\zeta} \sigma_{\sigma'''}^{\zeta}. \quad (10)$$

The result is a modified dual fermion action

$$\begin{aligned} \tilde{S} = & - \sum_{\mathbf{k}, \nu, \sigma} f_{\mathbf{k}\nu\sigma}^* \tilde{\mathcal{G}}_{\mathbf{k}\nu\sigma}^{-1} f_{\mathbf{k}\nu\sigma} \\ & + \frac{\xi}{8} \sum_{\substack{\mathbf{q}, \omega, \zeta \\ \{\mathbf{k}, \nu, \sigma\}}} \bar{\Gamma}_{\nu\nu'\omega}^{\zeta, \mathbf{k}\mathbf{k}'\mathbf{q}} f_{\mathbf{k}\nu\sigma}^* \sigma_{\sigma'}^{\zeta} \\ & \times f_{\mathbf{k}+\mathbf{q}, \nu+\omega, \sigma'} f_{\mathbf{k}'+\mathbf{q}, \nu'+\omega, \sigma''} \sigma_{\sigma''}^{\zeta} f_{\mathbf{k}'\nu'\sigma''}, \end{aligned} \quad (11)$$

where ξ is a formal expansion parameter, which must be set to unity ($\xi = 1$) in the actual calculations and keeps track of the expansion order. Importantly, we introduced a new momentum-dependent fermion-fermion vertex that combines the vertex function of the local impurity problem and the non-local interaction between fermions mediated by dual bosonic fields

$$\begin{aligned} \bar{\Gamma}_{\nu\nu'\omega}^{\text{ch}, \mathbf{k}\mathbf{k}'\mathbf{q}} &= \Gamma_{\nu\nu'\omega}^{\text{ch}} + 2\tilde{M}_{\nu, \nu', \omega}^{\text{ch}, \mathbf{q}} - \tilde{M}_{\nu, \nu+\omega, \nu'-\nu}^{\text{ch}, \mathbf{k}'-\mathbf{k}} - 3\tilde{M}_{\nu, \nu+\omega, \nu'-\nu}^{\text{sp}, \mathbf{k}'-\mathbf{k}}, \\ \bar{\Gamma}_{\nu\nu'\omega}^{\text{sp}, \mathbf{k}\mathbf{k}'\mathbf{q}} &= \Gamma_{\nu\nu'\omega}^{\text{sp}} + 2\tilde{M}_{\nu, \nu', \omega}^{\text{sp}, \mathbf{q}} + \tilde{M}_{\nu, \nu+\omega, \nu'-\nu}^{\text{sp}, \mathbf{k}'-\mathbf{k}} - \tilde{M}_{\nu, \nu+\omega, \nu'-\nu}^{\text{ch}, \mathbf{k}'-\mathbf{k}}. \end{aligned} \quad (12)$$

Here, $\tilde{M}_{\nu,\nu',\omega}^{\xi,\mathbf{q}} = \Lambda_{\nu,\omega}^{\xi} \tilde{W}_{\mathbf{q}\omega}^{\xi} \Lambda_{\nu'+\omega,-\omega}^{\xi}$. Since Eq. (10) holds for both vertices $\Gamma_{\nu\nu'\omega}$ and $\bar{\Gamma}_{\nu\nu'\omega}^{\mathbf{k}\mathbf{k}'\mathbf{q}}$, it is possible to switch easily between the two representations using the relations

$$\Gamma^{\text{ch}} = \Gamma^{\uparrow\uparrow\uparrow\uparrow} + \Gamma^{\uparrow\uparrow\downarrow\downarrow}, \quad \Gamma^{\text{sp}} = \Gamma^{\uparrow\uparrow\uparrow\uparrow} - \Gamma^{\uparrow\uparrow\downarrow\downarrow}. \quad (13)$$

Additionally, all the other nonzero components can be simply obtained by applying the SU(2) symmetry in Eq. (10)

$$\Gamma^{\uparrow\downarrow\uparrow\downarrow} = \Gamma^{\uparrow\uparrow\uparrow\uparrow} - \Gamma^{\uparrow\uparrow\downarrow\downarrow} = \Gamma^{\text{sp}} \quad (14)$$

or by exploiting the fact that a simultaneous flipping of all the spins leads to the same result in the paramagnetic case. We note that the structure of the new fermion-fermion vertex function (12) shown in Fig. 1 is reminiscent of the D-TRILEX theory [24], and appears due to the antisymmetrized form of the interaction. Integrating out of bosonic fields is very important for the calculation of diagrams because it allows to eliminate the bosonic degrees of freedom from the theory analytically and to avoid their sampling in diagrammatic Monte Carlo.

In our implementation we compute the dual self-energy. To obtain the single-particle observables of the lattice problem, we can use the standard equation that relates the dual self-energy to the lattice self-energy $\Sigma_{\mathbf{k}\nu}$,

$$\Sigma_{\mathbf{k}\nu} = \Sigma_{\nu}^{\text{imp}} + \bar{\Sigma}_{\mathbf{k}\nu}, \quad (15)$$

with $\bar{\Sigma}_{\mathbf{k}\nu} = \frac{\tilde{\Sigma}_{\mathbf{k}\nu}}{1+g_{\nu}\tilde{\Sigma}_{\mathbf{k}\nu}}$, where $\Sigma_{\nu}^{\text{imp}}$ is the self-energy of the impurity problem, as shown, for example, in Ref. [32]. The lattice Green's function can be obtained via the usual Dyson equation from the lattice self-energy or using its relation with the dual Green's function [32].

III. DIAGRAMMATIC MONTE CARLO SCHEME

The algorithm tested in this paper is an extension of the DiagMC@DF method proposed in Refs. [50,51]. Our DiagMC algorithm computes numerically exactly the coefficients $a_n(\mathbf{k}, \nu)$ in the expansion of the dual self-energy

$$\tilde{\Sigma}_{\mathbf{k}\nu}(\xi) = \sum_n a_n(\mathbf{k}, \nu) \xi^n, \quad (16)$$

for the action (11) up to some maximum order N_{max} . The value of the dual self-energy can be recovered by setting $\xi = 1$. We will call it diagrammatic Monte Carlo for dual bosons (DiagMC@DB). In the same way as the original algorithm, our method is based on bare diagrammatic Monte Carlo approach [55]. This algorithm allows to construct all the Feynman diagrams up to any finite order and to sum over them using Markov chain Monte Carlo. According to the authors of Refs. [41,56], any correlation function O can be expressed as a sum of diagrams as follows:

$$\begin{aligned} O(y) &= \lim_{N_{\text{max}} \rightarrow +\infty} \sum_{n=0}^{N_{\text{max}}} \sum_{\{x_i\}} O_{C_n}(\{x_i\}, y) \\ &= \lim_{N_{\text{max}} \rightarrow +\infty} \sum_{n=0}^{N_{\text{max}}} \sum_{\{x_i\}} \text{sgn}[O_{C_n}(\{x_i\}, y)] \cdot |O_{C_n}(\{x_i\}, y)|, \end{aligned} \quad (17)$$

where y is a combined index that contains all the dependence on external points, n indicates the number of vertices that appear in the diagram, C_n are the topologies, and O_{C_n} is the value of a specific diagram. Additionally x_i is shorthand notation for the internal degrees of freedom $(\mathbf{k}, \nu, \sigma)_i$ corresponding to momentum, Matsubara frequency, and spin that originate from the presence of loops of Green's functions. This statement is true provided that the limit in Eq. (17) is well defined and convergent for the chosen parameters as $N_{\text{max}} \rightarrow +\infty$. Divergencies of the diagrammatic series are often related to physical instabilities, as we show in Sec. IV, or to some unphysical behavior of the starting point, for example, the antiferromagnetic phase transition of DMFT [51].

The summation over the perturbation order n , topologies, and internal degrees of freedom is performed using a Metropolis-Hastings scheme [55], where the function to be sampled is the $\text{sgn}(O)$, and the probability distribution is given by the amplitude $|O|$ to respect the requirement of positive weight function. This approach automatically satisfies the detailed balance condition for the Markov chain (see Ref. [57]), given that the acceptance probability to go from a configuration C to another configuration \bar{C} is constructed as

$$R_{C \rightarrow \bar{C}} = \min \left\{ 1, \frac{\mathcal{P}_{\bar{C}}}{\mathcal{P}_C} \cdot \frac{|O_{\bar{C}}|}{|O_C|} \right\}, \quad (18)$$

where \mathcal{P}_C and $\mathcal{P}_{\bar{C}}$ are the probabilities of the initial and final configurations, respectively. There are no substantial changes from DiagMC@DF in the acceptance-rejection scheme adopted, except for the fact that in our case the bare fermion-fermion vertex function (12) is momentum dependent. Each contribution to the series expansion (17) can be written as a combination of two kinds of diagrammatic elements: fermionic lines that represent dual Green's functions \tilde{G} (called also propagator lines) and vertices $\bar{\Gamma}$ described in Eq. (12). Each vertex is attached to four propagator lines, two incoming and two outgoing. The terms at order n in the expansion are represented in terms of Feynman diagrams with n vertices connected by lines in all the possible combinations.

These diagrams give an intuitive and efficient picture that allows us to design the updates so that all the contributions to the expansion (17) can be generated by changing how the vertices are connected to each other by means of the propagator lines. In particular, we use the same worm algorithm described in Ref. [51] to update the diagram topologies. The aim of the worm algorithm is to enforce momentum conservation, which is a nonlocal property of the diagram, by means of updates that act locally on few elements of a diagram. The worm algorithm introduces a set of unphysical updates that allow the transition between all the different possible topologies contributing to the dual self-energy $\tilde{\Sigma}_{\mathbf{k}\nu}$. This means that we sample all the diagrams with one incoming and one outgoing line that are also irreducible with respect to a cut of a fermionic line. This can be practically implemented by the condition that no internal line can carry the same momentum and frequency dependence of the external lines. All the subtleties and details related to the implementation are discussed in detail in Ref. [51].

Each configuration is identified by an ordered set of vertices, where each vertex is stored together with the incoming

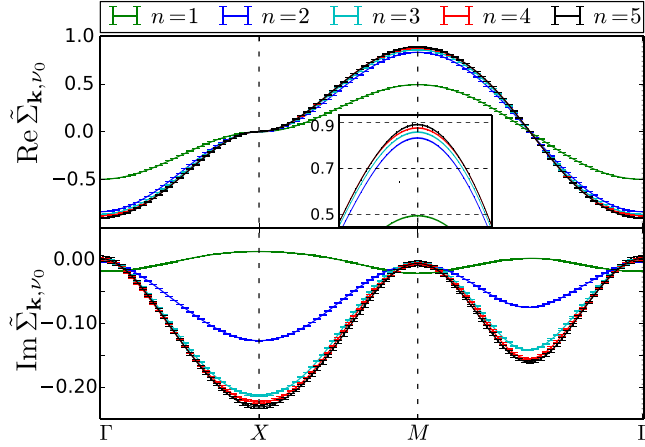


FIG. 2. Convergence of the real (top panel) and imaginary (bottom panel) parts of the dual self-energy $\tilde{\Sigma}_{\mathbf{k}, \nu}$ obtained for the zeroth Matsubara frequency ν_0 . The result is plotted along the high-symmetry path in momentum space \mathbf{k} as a function of the expansion order n . The parameters are $U = 5$, $V = 1.25$, and $\beta = 2$ in the units of the hopping amplitude. The inset shows the convergence of the real part around the $M = \{\pi, \pi\}$ point.

and outgoing frequencies, momenta, spins, and the connections with the other vertices. The original implementation found in Ref. [51] works with unsymmetrized diagrams to avoid topology-dependent prefactors. However, the local vertex Γ itself has an antisymmetric form in spin space, and we find it convenient to introduce also the nonlocal vertex corrections $\tilde{M}_{\nu, \nu' \omega}^{s, q}$ in the antisymmetrized form shown in Eq. (12). The corresponding vertex in the unsymmetrized diagrammatic theory can be obtained by simply dividing this vertex by 2 [51].

The simultaneous sampling of contributions coming from the fermion-fermion scattering and boson exchange processes efficiently reduces the number of topologies. On the other hand, we do not distinguish between local and nonlocal diagrams, so that we cannot exclude local diagrams from the beginning simply by a proper choice of the DMFT self-consistency condition, as it was done in DiagMC@DF calculations. However, in the spirit of Refs. [42,58], we can reduce the diagrammatic space and thereby increase the efficiency of DiagMC sampling by self-consistently eliminating all diagrams that contain insertions of the topology $\Sigma^{(1)}$ depicted in Fig. 3. This is accomplished by the so-called “semi-bold” DiagMC scheme of Ref. [59], in which the bare Green’s function in all diagrams is replaced with $\tilde{\mathcal{G}}_{\text{sb}}$ that is dressed by the first-order self-energy, found as the self-consistent solution of the Dyson equation $\tilde{\mathcal{G}}_{\text{sb}}^{-1} = \tilde{\mathcal{G}}_0^{-1} - \Sigma^{(1)}[\tilde{\mathcal{G}}_{\text{sb}}]$. Here $\Sigma^{(1)}[\tilde{\mathcal{G}}_{\text{sb}}]$ is the first-order diagram where the bare propagator is replaced by the self-consistently calculated one $\tilde{\mathcal{G}}_{\text{sb}}$. This formal transformation of the series is exact in the sense that it does not change the final result [59], although the convergence properties of the semi-bold series are generally different [60]. Using the Metropolis-Hastings scheme allows us to compute observables up to a normalization factor. To keep track of the normalization, we sample the absolute value of an additional diagram that we can calculate explicitly

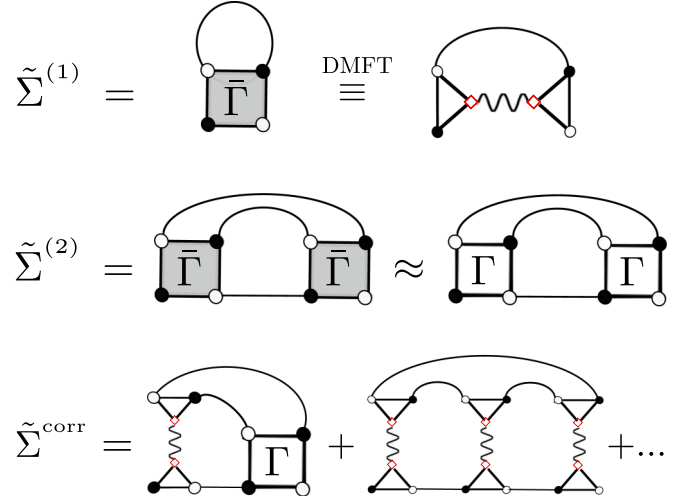


FIG. 3. Most important self-energy diagrams. Top row shows the only nonzero contribution to the first order diagram, taking into account that we cannot connect two slots of the same local vertex with a propagator line due to DMFT self-consistency condition. The middle row shows the second-order diagrams $\tilde{\Sigma}^{(2)}$. If V is small compared to $U/4$, it can be approximated by the second-order dual fermion diagram on the right-hand side. The last term $\tilde{\Sigma}^{\text{corr}}$ shows few diagrams that enter $\tilde{\Sigma}$ in our calculations, but are not included in the ladder DB.

outside Monte Carlo and we store its value in a suitable accumulator N_{norm} . The chosen diagram is simply a single vertex with unitary value with the upper corners connected by a single bare dual Green’s function. Its value is given by

$$\mathcal{N} = \sum_{\mathbf{k}\nu} |\tilde{\mathcal{G}}_{\mathbf{k}\nu}|, \quad (19)$$

which is computed directly from the analytical expression for the bare dual propagator $\tilde{\mathcal{G}}$. The normalized dual self-energy $\tilde{\Sigma}_{\mathbf{k}\nu}$ is then straightforwardly computed from the normalization accumulator N_{norm} using the following equation:

$$\tilde{\Sigma}_{\mathbf{k}\nu} = \frac{\mathcal{N}}{N_{\text{norm}}} \langle \tilde{\Sigma}_{\mathbf{k}\nu} \rangle_{\text{MC}}. \quad (20)$$

IV. RESULTS

A. Computational details

We perform our calculations on a two-dimensional (2D) square lattice with the nearest-neighbor hopping amplitude $t = 1$ that fixes the energy units. The chemical potential μ is set to $U/2$, ensuring that the system is at half-filling. To avoid the low temperature issues related to the DMFT Néel transition discussed in details in Ref. [51], all the calculations are performed at $\beta = 4$ when $U \leq 4$ and at $\beta = 2$ for $U > 4$. We would like to stress that this is not a limitation of the method, which works with any dispersion and with a general form of the interaction as a function of momentum. We start from the description of the output of the calculation, namely the dual self-energy $\tilde{\Sigma}_{\mathbf{k}\nu}$, obtained within the bare diagrammatic Monte Carlo scheme. The only obvious difference between a bare and semi-bold run is that the $\Sigma^{(1)}[\tilde{\mathcal{G}}_{\text{sb}}]$ is computed in advance and added to the DiagMC result. Since the DiagMC

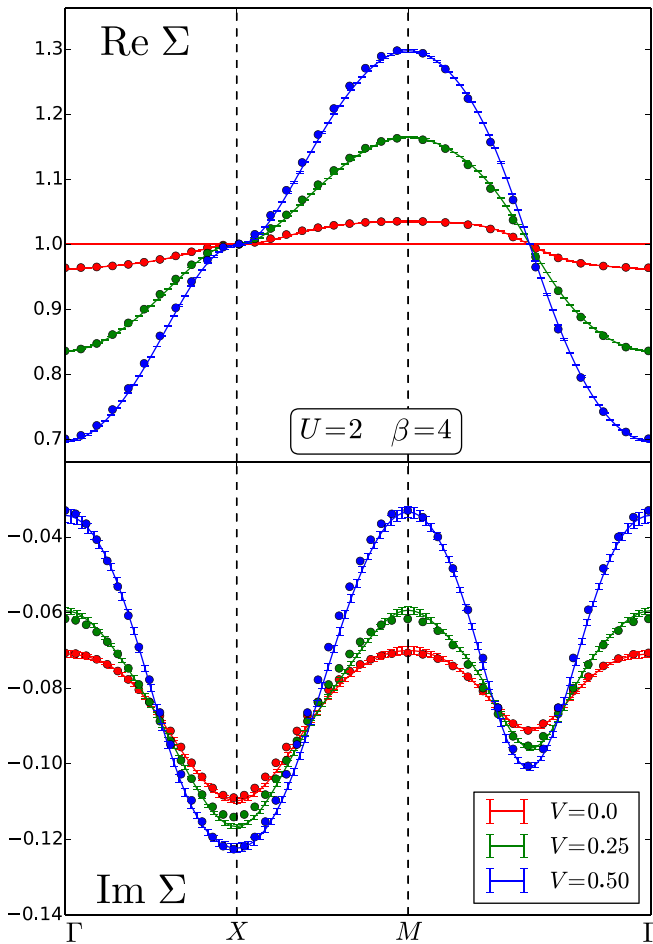


FIG. 4. Comparison between DiagMC@DB (solid lines with error bars) and ladder DB (dots) results for the real (top panel) and imaginary (bottom panel) parts of the lattice self-energy $\Sigma_{\mathbf{k}\nu_0}$. The result is obtained for $U = 2$, $\beta = 4$, and different values of the nonlocal Coulomb interaction V specified in the legend of the bottom panel.

result sums diagrams up to a given order, one has to check that the result is converged with respect to the order. In Fig. 2 we show a converged output of our calculations. In particular, the result for the maximum order of the diagrammatic expansion, order 5, differs from order 4 of $\sim 1\%$, hence we consider the result converged. Practically, this means that the performed calculation can be considered converged already at order 4. This is the case for most of the presented calculations.

Far away from instabilities, it is not possible to observe any improvement in going beyond the fifth order of the diagrammatic expansion, and the computation necessary to achieve convergence at the order 6 increases significantly. Thus, a standard DiagMC@DB computation requires around 12 hours with a hundred parallel runs to obtain a converged result at the fifth order. Instead, for a converged result at the sixth order, the required computational time increases to more than 24 hours to reach a reasonable accuracy. For this reason, all results presented in this work are calculated up to the fifth order of expansion, except the ones that are used for the analysis of the phase transition.

An important remark is that the contribution coming from the nonlocal interaction can be quite large, even up to val-

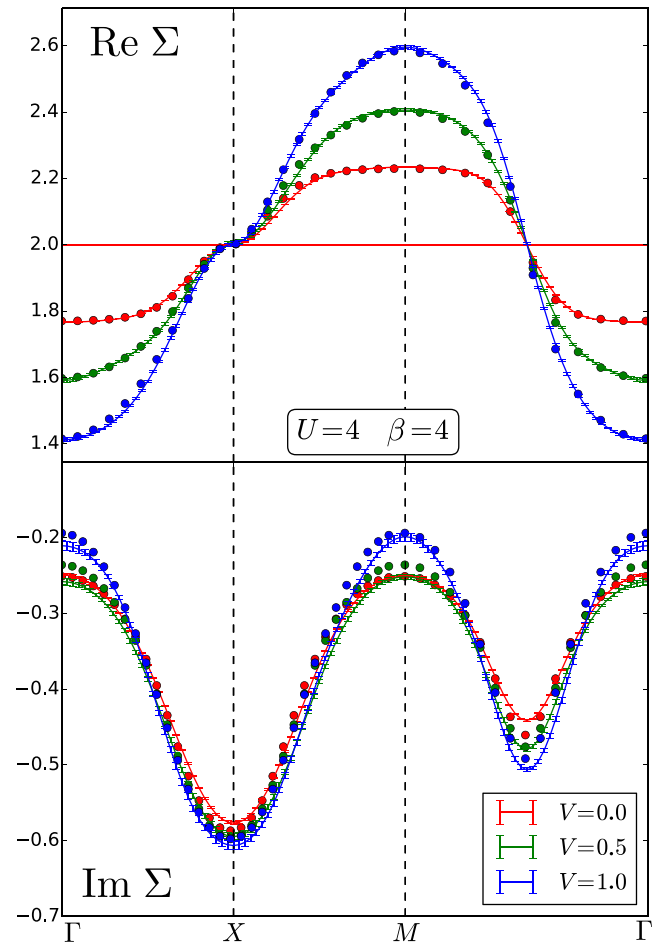


FIG. 5. Comparison between DiagMC@DB (solid lines with error bars) and ladder DB (dots) results for the real (top panel) and imaginary (bottom panel) parts of the lattice self-energy $\Sigma_{\mathbf{k}\nu_0}$. The result is obtained for $U = 4$, $\beta = 4$, and different values of the nonlocal Coulomb interaction V specified in the legend of the bottom panel.

ues around $U = 6t$. Additionally, we observe that the main contribution to the real part of the self-energy comes from two kind of diagrams that are shown in Fig. 3. The first is the single boson diagram $\tilde{\Sigma}^{(1)}$ that contains only one factor $\tilde{M}_{\nu,\nu'}^{\mathbf{q}}$, which is the only nonzero contribution at the first order of the diagrammatic expansion in terms of the vertex function. This can be already seen in Fig. 2, where the first-order contribution accounts for around 50% of the real part of the dual self-energy. The second important contribution is the second-order dual fermion diagram $\tilde{\Sigma}^{(2)}$ that contains two fermion-fermion vertices connected to each other. At values of V far away from the CDW instability, other contributions to $\text{Re}\tilde{\Sigma}$ are rather small compared to these ones. On the other hand, the imaginary part of the self-energy is much more sensitive to higher-order corrections. In Fig. 2 we can see that the second order is way off compared to the third order, accounting for only around 50% of the contributions to $\text{Im}\tilde{\Sigma}$. Interestingly, the third order already accounts for most of the contributions. We deduce that the inclusions of third-order diagrams in our expansion that contain multiple fermion-fermion scattering and bosonic exchanges are important for the imaginary

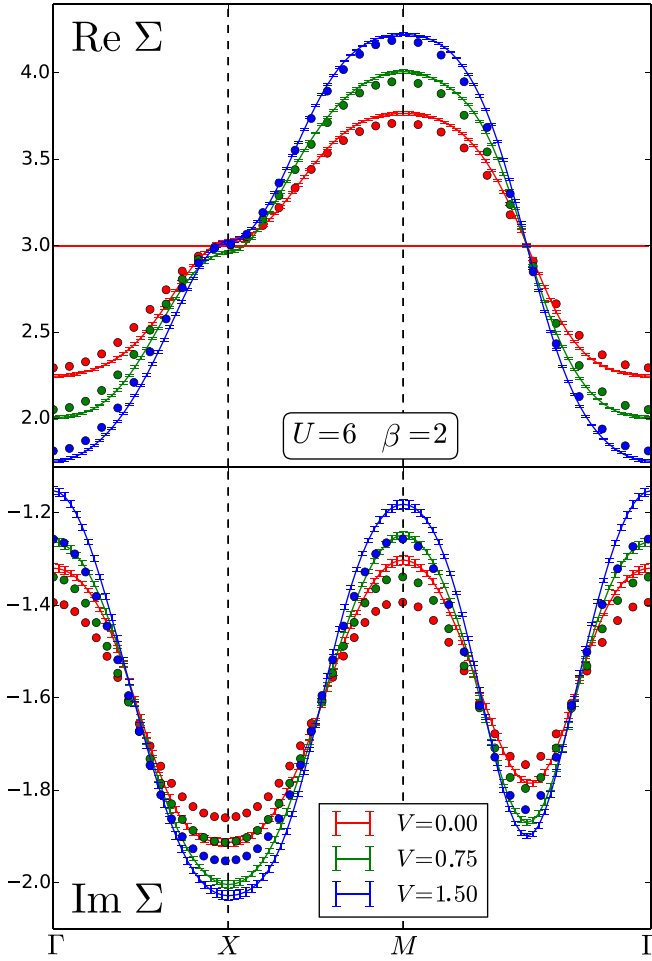


FIG. 6. Comparison between DiagMC@DB (solid lines with errorbars) and ladder DB (dots) results for the real (top panel) and imaginary (bottom panel) parts of the lattice self-energy $\Sigma_{\mathbf{k}\nu_0}$. The result is obtained for $U = 6$, $\beta = 2$, and different values of the nonlocal Coulomb interaction V specified in the legend of the bottom panel.

part of the self-energy. These diagrams contribute to around 40% of $\text{Im}\tilde{\Sigma}$ at high symmetry points for $U = 5$, and their impact on dual quantities becomes even more important at larger U . Orders larger than the third typically amount to a correction of less than 10% of $\text{Im}\tilde{\Sigma}$ at high symmetry points.

However, the overall momentum dependence of the lattice self-energy is still dominated by $\text{Re}\tilde{\Sigma}$ in the regimes where $U \leq 4$ or $U \geq 8$ because of the denominator in Eq. (15), as shown also in Ref. [51]. The most important corrections to the lattice self-energy coming from $\text{Im}\tilde{\Sigma}$ appear exactly in the regime between half of the bandwidth and the bandwidth, where it can account for around 40% of the difference with DMFT solution at high symmetry points. Even though second order is thought to already account for the most important contributions far away from instabilities, as shown in Ref. [4], the inclusion of two-boson exchanges and third-order corrections in fermion-fermion vertices can lead to significant quantitative improvements over second-order calculations.

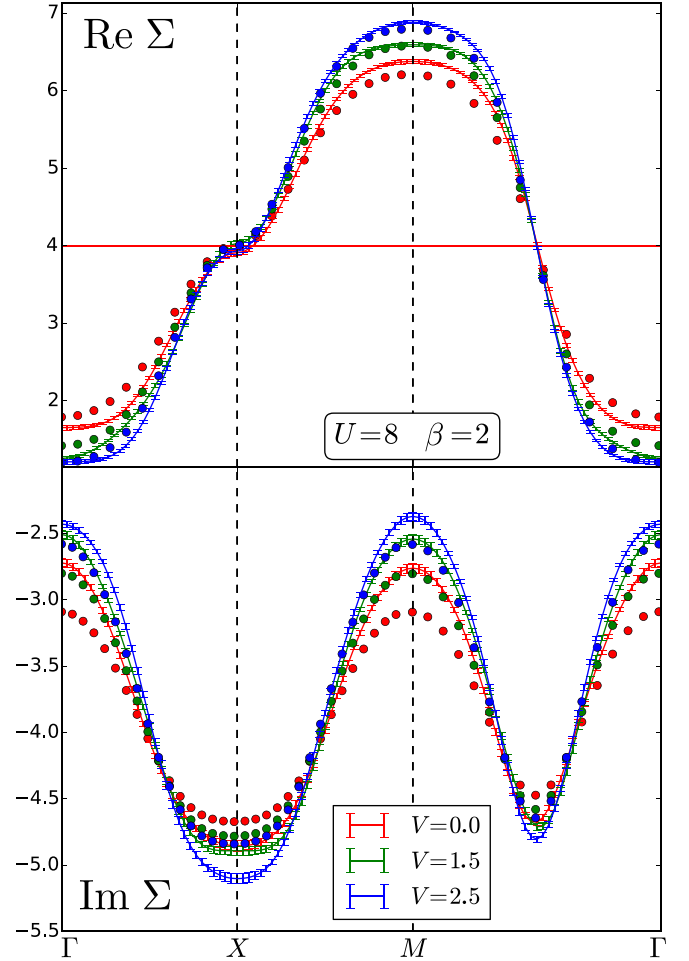


FIG. 7. Comparison between DiagMC@DB (solid lines with errorbars) and ladder DB (dots) results for the real (top panel) and imaginary (bottom panel) parts of the lattice self-energy $\Sigma_{\mathbf{k}\nu_0}$. The result is obtained for $U = 8$, $\beta = 2$, and different values of the nonlocal Coulomb interaction V specified in the legend of the bottom panel.

B. Comparison with the ladder DB approach

Figures 4 to 7 show a comparison of the DiagMC@DB and ladder DB calculations for different values of the local U and nonlocal $V_{\mathbf{q}}^{\text{ch}}$ Coulomb interactions. In all the figures we show the result of the calculation at the fifth order. In particular, we show results from a quarter of the bandwidth $U = 2$ up to the bandwidth $U = 8$. We note that the agreement between these two methods is substantially exact up to a half of the bandwidth for all considered values of the nonlocal interaction. In fact, in this regime the ladder DB result for the lattice self-energy lies inside the error bars of the DiagMC@DB calculation. For larger values of the on-site Coulomb interaction exceeding the half of the bandwidth, the difference between two theories is more noticeable, especially for small strength of the nonlocal interaction V . To quantify the difference between these two methods, we look at the $M = (\pi, \pi)$ point in the momentum space and calculate the following quantity

$$\delta_M = \text{Re} \left[\frac{\overline{\Sigma}_{M,\nu_0}^{\text{DiagMC}} - \overline{\Sigma}_{M,\nu_0}^{\text{ladd.}}}{\overline{\Sigma}_{M,\nu_0}^{\text{DiagMC}}} \right], \quad (21)$$

where $\bar{\Sigma}_{M,\nu_0}$ is the difference between the self-energy in the specified method and the DMFT self-energy $\Sigma_{\nu_0}^{\text{imp}}$ (15), and ν_0 is the lowest positive Matsubara frequency. We measure differences with respect to DMFT self-energy because this last is constant in momentum space and quite large. If we want to resolve relatively small differences in momentum space, we have to exclude its contribution. Additionally, we choose the M point because it shows the largest difference between the two curves in the Brillouin zone. In this way, we are sure that the δ_M parameter contains information only about the maximum mismatch coming from the dual corrections. The reason for taking the real part of this quantity comes from the fact that the imaginary part of the dual self-energy $\text{Im}\bar{\Sigma}$ shows a systematic shift already at $V = 0$, i.e., at the dual fermion level (see Ref. [51]). Here, we aim to assess the behavior of the self-energy as a function of the nonlocal V rather than to investigate this aspect.

The result for the mismatch parameter δ_M is summarized in a tentative phase diagram shown in Fig. 8. We can conclude that the difference between DiagMC@DB and ladder DB approaches is negligible at small U below the half of the bandwidth and further increases with the local interaction. This behavior can be explained considering that for small local Coulomb interaction U the regime is still perturbative in the dual boson theory, so we expect all the methods to give quantitatively similar results. This finding is also in agreement with the result of DiagMC@DF calculations [51] obtained for the zero nonlocal Coulomb interaction. On the other hand, we observe that the mismatch is more severe at $V = 0$ and decreases as V increases. Indeed, when the nonlocal Coulomb interaction is large, charge fluctuations in the horizontal channel are expected to give the main contribution to physical observables such as self-energy and susceptibility [36] because the system lies close to the charge density wave (CDW) phase. Ladder DB approach accounts for this kind of fluctuations by construction, and for this reason the mismatch δ_M decreases. From Fig. 8, we find that the values of U at which the largest mismatch occurs (red area) lie in the region where the phase transition to the Mott-insulating state was predicted by cluster DMFT [61] and dual fermion [62] calculations at lower temperature. This means that in this regime contributions not included in the ladder approximation cease to be negligible. These contributions correspond to bosonic lines in a direction orthogonal to the ladder direction (see, e.g., $\bar{\Sigma}^{\text{corr}}$ in Fig. 2), which are included in DiagMC@DB. It means that the correct description of this phase transition, especially at $V = 0$ would require advanced approaches beyond the ladder approximation. Another consideration that emerges from this analysis as a function of U and V is that up to a half the bandwidth a momentum dependence of the real part of the self-energy at $V = U/4$ is dominated by the nonlocal interaction V . It plays a very important role even for $U = 6$, where we would expect the local interaction to give the most important contribution.

C. Monitoring the CDW phase transition from single-particle observables

In the current implementation, the DiagMC@DB theory is based on a solution of a single-site impurity problem,

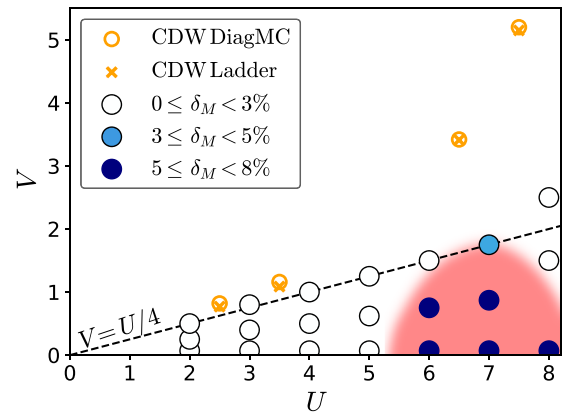


FIG. 8. Summary of the results of our calculations as a function of the local U and nonlocal V Coulomb interactions. Results for $U \leq 4$ were obtained at $\beta = 4$, while for $U > 4$ they were calculated at $\beta = 2$. The mismatch parameter δ_M is depicted by color. Points correspond to physical parameters for which calculations are performed. The red area highlights the region where the mismatch parameter is larger. Transition points between the normal and CDW phases obtained in DiagMC@DB and ladder DB calculations are depicted by an orange circle and cross, respectively. The dashed black line $V = U/4$ represents an estimation of the phase boundary predicted by mean-field arguments.

which does not allow for a description of broken-symmetry phases. A practical example of the failure of an expansion based on single-site DMFT is given by the strong anti-ferromagnetic fluctuations arising in the Hubbard model at low temperature, as discussed in detail in Ref. [51] for the DiagMC@DF. In particular, this results in a divergence of the infinite diagrammatic expansion in terms of bare dual quantities at the phase transition [18,20,32,36,51]. The most interesting phase of the extended Hubbard model that is associated with the presence of the nonlocal Coulomb interaction is the charge density wave phase, i.e., a checkerboard configuration in the real space with alternating empty sites and doubly occupied sites. The phase transition to this state occurs when V is large enough to overcome the effect of the on-site Coulomb repulsion that favors a single-electron occupation of lattice sites. A perturbative expansion at small values of U predicts the onset of the CDW phase to be located at $V \simeq U/8 + \text{const.}$ [63]. A mean-field estimate based on random phase approximation (RPA) or GW theories gives the transition point at $V \simeq U/4$ [16]. This behavior is reproduced at moderate interaction strength by DCA calculations [38,64]. Finally, as we shall see below, for large values of U and large temperatures the position of the onset of the CDW phase appears to shift towards the value $V \simeq U$ that can be found, for example, using the Peierls-Feynman-Bogoliubov variational principle [65]. Dual boson calculations are in good agreement with the DCA results and reproduce all these different trends in the different regimes [18,32].

The description of the system inside the CDW state requires an inclusion of symmetry breaking terms in the theory. However, the instability can be identified already in the normal phase studying the charge susceptibility [18,20,32]. In particular, we expect the susceptibility to show a very sharp

peak when the instability occurs. This trend can be seen in the upper right panel of Fig. 9, where the inverse of the charge susceptibility linearly decreases. Our ladder dual boson calculations predict a transition point V_{CDW} at $V = 0.77$ for $U = 2.5$ and $V = 1.09$ for $U = 3.5$ at inverse temperature $\beta = 4$. In the strongly correlated regime, the transition points evaluated with this method are $V = 3.41$ for $U = 6.5$ and $V = 5.15$ for $U = 7.5$ at $\beta = 2$.

However, the critical value V_{CDW} for the CDW phase transition can also be found in a controlled way from the analytic structure of the dual self-energy $\tilde{\Sigma}$ as a function of the complex expansion parameter ξ . Since the dual action (11) is explicitly constructed for the translationally symmetric phase, the critical point $V = V_{\text{CDW}}$ is marked by a singularity appearing in the function $\tilde{\Sigma}(\xi)$ at $\xi = 1$. When V is increased beyond V_{CDW} in the symmetry-broken phase, this singularity must move along the real axis towards the origin for the physical $\tilde{\Sigma}(\xi = 1)$ to remain inaccessible by its power-series expansion (16). The method introduced in Ref. [66] and routinely applied in the context of DiagMC [44] allows to accurately evaluate the specific location of the singularity ξ_s . It assumes a generic power-law behavior near the singularity, which is typical for a continuous phase transition, $\tilde{\Sigma}(\xi) \propto (\xi_s - \xi)^\eta$ for $|\xi - \xi_s| \ll 1$ with some real number η , and extracts ξ_s from the behavior of the series coefficients a_n in Eq. (16). As shown in Ref. [44], ξ_s can be found from a finite number of coefficients $\{a_n\}$ with a reliable error bar that includes both the systematic and statistical (Monte Carlo) error. The result of this procedure for different values of V is shown in the bottom right panel of Fig. 9, where $\xi_s(V)$ is obtained from $\{\text{Re } a_n(\mathbf{k}, \nu_0)\}$, for $n = 1, \dots, N_{\text{max}} = 6$ projected on the first A_{1g} -symmetric harmonic $\psi_{(1,0)}^s(\mathbf{k}) = \cos(k_x) + \cos(k_y)$ to produce a numerical series from the functional one. The condition $\xi_s(V) = 1$ then gives the critical value V_{CDW} . To study the behavior of the series close to the phase transition, it is crucial to get very well-converged coefficients and to achieve high orders in the expansion. For this reason the calculations of the phase boundary were performed using the semi-bold scheme described in Sec. III up to the sixth order. The critical values V_{CDW} obtained with this method are $V = 0.81(1)$ at $U = 2.5$ and $\beta = 4$. In the same fashion we can estimate the transition to occur at $V = 1.15(1)$ for $U = 3.5$, $V = 3.42(1)$ for $U = 6.5$ and $V = 5.20(2)$ for $U = 7.5$. These points are highlighted in orange in Fig. 8.

In combination with this controlled method, we propose an additional empirical way to obtain the instability point. It is important to notice that the checkerboard configuration of electrons is insulating. This means that strong charge fluctuations create a pseudogap in the electronic spectrum, which can be detected calculating the spectral function. In particular, the spectral function at the Fermi energy is directly connected to the local Green's function $G(\beta/2)$ calculated at imaginary time $\tau = \beta/2$ by the relation $A(E_F) \approx -\beta G(\beta/2)/\pi$ (see, for example, Ref. [18]), without the need of analytical continuation from Matsubara to real frequencies. This situation is conceptually similar to the antiferromagnetic pseudogap, but the analysis in the framework of our theory is very different. In fact, the divergence of the dual fermion series is not associated with a true physical instability, as discussed previously, hence the divergence of the diagrammatic series in terms of the

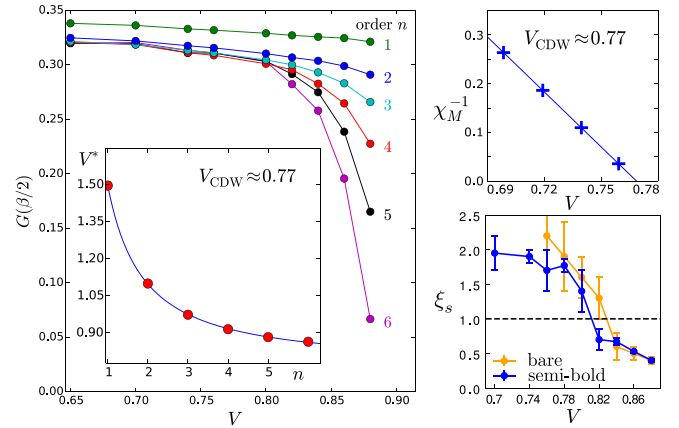


FIG. 9. Left panel: $G_{\text{loc}}(\tau = \beta/2)$ as a function of nonlocal interaction V for the various perturbation orders in the bare DiagMC scheme at $U = 2.5$ and $\beta = 4$. In the inset it is shown the estimated V of the CDW transition as a function of the order. An additional fitting of the curve with the function $f(n) = C_0 + C_1 n^{-C_2}$, where C_0 , C_1 , and C_2 are fitting parameters, allows to extrapolate the value at infinite order $V_{\text{CDW}} = C_0 = 0.77(2)$. Upper right panel: The inverse of the charge susceptibility at the $M = \{\pi, \pi\}$ point obtained by ladder dual boson calculations as a function of V for the same U and β . The value V_{CDW} can be obtained by a linear fitting of the data and checking where the fitting line crosses zero. Lower right panel: Position ξ_s of the singularity on the real axis obtained within the method presented in Ref. [66] for the bare and semi-bold DiagMC schemes. The phase transition occurs when ξ_s crosses $\xi = 1$. This analysis predicts the transition at $V_{\text{CDW}} = 0.82(1)$ for the bare series and $V_{\text{CDW}} = 0.81(1)$ for the semi-bold series.

local interaction does not have a clear physical interpretation. On the contrary, the nonlocal interaction V enters only the effective fermion-fermion vertex function of Eq. (12) in a trivial form through the dual boson propagator, which up to a local prefactor is proportional to [32]

$$\tilde{W}_{\mathbf{q}\omega}^s \sim \frac{V_{\mathbf{q}}^s}{1 - \chi_{\omega}^s V_{\mathbf{q}}^s}. \quad (22)$$

We consider the local Green's function obtained by replacing the dual self-energy up to order n into the Dyson equation $G^{(n)}(\beta/2)$ as a function of the nonlocal interaction V , keeping the local interaction U fixed. If we inspect left panel of Fig. 9, the behavior of this function resembles a Fermi function

$$G_V^{(n)}(\beta/2) \approx \frac{G_{V=0}^{(n)}(\beta/2)}{\exp[\alpha_n(V - V_n^*)] + 1}, \quad (23)$$

where V_n^* is the critical value of the nonlocal interaction at which the function shows a steep drop, and α_n is a numerical value that defines the broadening of the Fermi function at order n . From these empirical and physical considerations, we expect that $V_n^* \rightarrow V_{\text{CDW}}$ as the order $n \rightarrow +\infty$, which means that, if we extrapolate the central point of the Fermi function as a function of n , we expect it to converge to the value V_{CDW} . Results based on this analysis for the bare series are plotted in the left panel of Fig. 9, and the expected behavior is clearly visible in the figure. Fitting the value of V^* as a function of the order n allows to extrapolate the value of V_{CDW} by letting the order go to infinity. In the case of the semi-bold series, there is

a redistribution of weight between the various orders and the extrapolation to infinite order from the first six coefficients based on the same fitting function described in the caption of Fig. 9 is not as accurate as in the bare case. The inset in the left panel of Fig. 9 clearly shows the convergence of the values of V_n^* to a finite value as the order increases. We compared the extrapolated values from the bare series with the susceptibility at $M = (\pi, \pi)$ calculated from ladder calculations. With this simple analysis we obtained values for V_{CDW} compatible with the ladder results. The specific values are $V_{\text{CDW}} = 0.77(2)$ at $U = 2.5$ and $V_{\text{CDW}} = 1.09(2)$ at $U = 3.5$ with $\beta = 4$.

The methods presented in this section show how order-by-order or cumulative analysis of the series allows for an accurate extrapolation of results in the limit of infinite order of perturbation expansion. Our results for $U = 2.5$ show a very good agreement with the value obtained with $GW + \text{DMFT}$ in Ref. [16]. Additionally there is a good agreement with previous dual boson [18,32,36] and DCA calculations [37,64].

V. CONCLUSIONS AND OUTLOOK

Even though the method presented in the previous sections is not exact because higher-order impurity vertices are neglected, the DiagMC@DB scheme allows to include contributions coming from all the possible diagrams with no restriction on a particular class of topologies. In other words, DiagMC@DB is the exact solution of the dual boson action truncated at the level of two-particle scattering. Due to this consideration, the results provided by DiagMC@DB are based on theoretically much more stable grounds than other approximations based on partial resummation of specific diagrams, as in the case of the ladder dual boson. Additionally, there are no finite-size effects since we worked in momentum space and Matsubara frequencies directly.

In our calculations we observed a very accurate agreement between DiagMC@DB and ladder calculations for U up to half of the bandwidth. Even above this value of U , the ladder dual boson seems to capture the main contributions and the difference between the two methods is quite small. In fact, we never observed a value of the δ_M parameter bigger than 8% in the region of the parameter space where the series converges. This offers a further validation of the ladder dual boson technique over a very wide range of interaction strengths. The presence of strong nonlocal interaction V enhances nonlocal bosonic excitations in the charge channel that are accounted for in ladder approximation. This can be captured by looking

at the real part of the self-energy, which coincides for the two methods at large values of V .

The advantage of the DiagMC@DB is that it allows to consider diagrams order by order and investigate the convergence properties of the series in an unbiased and systematic way. In particular, starting from DMFT impurity, the solution is a series in terms of a complicated function of V . Since V does not enter the impurity, it is possible to use resummation techniques to estimate the value of V at which the charge order occurs already from the study of single-particle quantities. Different choices of the hybridization functions, obtained, for instance, from ladder dual boson calculations, could, in principle, extend the convergence radius of the series at lower temperatures (see Ref. [51]).

Another strategy that could improve the efficiency of sampling could be the formulation of the series in terms of the semi-bold Green's function, in which some diagrams are included in the bare dual propagator from the very beginning, or the fully bold Green's function, substantially reducing the configuration space. It is expected that both approaches could improve the convergence properties as well, but a systematic study is required. In our calculations for the phase diagram, we observe that the computational time needed for a converged result at the sixth order is typically decreased by an order of magnitude if the first order diagram is included in the semi-bold Green's function. At the same time, this choice of the semi-bold scheme consistently gives results compatible with the bare series in the whole parameter space investigated in this study.

We are currently working in the direction of extending this method to calculate also two-particle observables in two-dimensional heterostructures. In addition, the inclusion of a checkerboard configuration with two nonequivalent sublattices (impurity problems) can allow to study the extended Hubbard model inside the broken symmetry phases, as the CDW phase or the antiferromagnetic phase.

ACKNOWLEDGMENTS

We acknowledge financial support from the European Research Council (ERC-2015-AdG-694097). This work is funded by the Cluster of Excellence ‘‘CUI: Advanced Imaging of Matter’’ of the Deutsche Forschungsgemeinschaft (DFG) - EXC 2056 - project ID 390715994. Additional support by the Max Planck Institute, the North-German Supercomputing Alliance (HLRN) under the Project No. hhp00042, and the Simons Foundation is also acknowledged. The Flatiron Institute is a division of the Simons Foundation.

-
- [1] J. Hubbard, Electron correlations in narrow energy bands, *Proc. R. Soc. Lond. A* **276**, 238 (1963).
 [2] A. Georges, G. Kotliar, W. Krauth, and M. J. Rozenberg, Dynamical mean-field theory of strongly correlated fermion systems and the limit of infinite dimensions, *Rev. Mod. Phys.* **68**, 13 (1996).
 [3] W. Metzner and D. Vollhardt, Correlated Lattice Fermions in $d = \infty$ Dimensions, *Phys. Rev. Lett.* **62**, 324 (1989).

- [4] J. Gukelberger, L. Huang, and P. Werner, On the dangers of partial diagrammatic summations: Benchmarks for the two-dimensional Hubbard model in the weak-coupling regime, *Phys. Rev. B* **91**, 235114 (2015).
 [5] A. M. Sengupta and A. Georges, Non-Fermi-liquid behavior near a $T=0$ spin-glass transition, *Phys. Rev. B* **52**, 10295 (1995).

- [6] Q. Si and J. L. Smith, Kosterlitz-Thouless Transition and Short Range Spatial Correlations in an Extended Hubbard Model, *Phys. Rev. Lett.* **77**, 3391 (1996).
- [7] J. L. Smith and Q. Si, Spatial correlations in dynamical mean-field theory, *Phys. Rev. B* **61**, 5184 (2000).
- [8] R. Chitra and G. Kotliar, Effect of Long Range Coulomb Interactions on the Mott Transition, *Phys. Rev. Lett.* **84**, 3678 (2000).
- [9] R. Chitra and G. Kotliar, Effective-action approach to strongly correlated fermion systems, *Phys. Rev. B* **63**, 115110 (2001).
- [10] P. Sun and G. Kotliar, Extended dynamical mean-field theory and GW method, *Phys. Rev. B* **66**, 085120 (2002).
- [11] S. Biermann, F. Aryasetiawan, and A. Georges, First-Principles Approach to the Electronic Structure of Strongly Correlated Systems: Combining the *GW* Approximation and Dynamical Mean-Field Theory, *Phys. Rev. Lett.* **90**, 086402 (2003).
- [12] T. Ayral, P. Werner, and S. Biermann, Spectral Properties of Correlated Materials: Local Vertex and Nonlocal Two-Particle Correlations from Combined *GW* and Dynamical Mean Field Theory, *Phys. Rev. Lett.* **109**, 226401 (2012).
- [13] T. Ayral, S. Biermann, and P. Werner, Screening and non-local correlations in the extended Hubbard model from self-consistent combined *GW* and dynamical mean field theory, *Phys. Rev. B* **87**, 125149 (2013).
- [14] L. Huang, T. Ayral, S. Biermann, and P. Werner, Extended dynamical mean-field study of the Hubbard model with long-range interactions, *Phys. Rev. B* **90**, 195114 (2014).
- [15] L. Boehnke, F. Nilsson, F. Aryasetiawan, and P. Werner, When strong correlations become weak: Consistent merging of *GW* and DMFT, *Phys. Rev. B* **94**, 201106(R) (2016).
- [16] T. Ayral, S. Biermann, P. Werner, and L. Boehnke, Influence of Fock exchange in combined many-body perturbation and dynamical mean field theory, *Phys. Rev. B* **95**, 245130 (2017).
- [17] A. N. Rubtsov, M. I. Katsnelson, and A. I. Lichtenstein, Dual boson approach to collective excitations in correlated fermionic systems, *Ann. Phys. (NY)* **327**, 1320 (2012).
- [18] E. G. C. P. van Loon, A. I. Lichtenstein, M. I. Katsnelson, O. Parcollet, and H. Hafermann, Beyond extended dynamical mean-field theory: Dual boson approach to the two-dimensional extended Hubbard model, *Phys. Rev. B* **90**, 235135 (2014).
- [19] E. A. Stepanov, E. G. C. P. van Loon, A. A. Katanin, A. I. Lichtenstein, M. I. Katsnelson, and A. N. Rubtsov, Self-consistent dual boson approach to single-particle and collective excitations in correlated systems, *Phys. Rev. B* **93**, 045107 (2016).
- [20] L. Peters, E. G. C. P. van Loon, A. N. Rubtsov, A. I. Lichtenstein, M. I. Katsnelson, and E. A. Stepanov, Dual boson approach with instantaneous interaction, *Phys. Rev. B* **100**, 165128 (2019).
- [21] T. Ayral and O. Parcollet, Mott physics and spin fluctuations: A unified framework, *Phys. Rev. B* **92**, 115109 (2015).
- [22] T. Ayral and O. Parcollet, Mott physics and spin fluctuations: A functional viewpoint, *Phys. Rev. B* **93**, 235124 (2016).
- [23] T. Ayral, J. Vučićević, and O. Parcollet, Fierz Convergence Criterion: A Controlled Approach to Strongly Interacting Systems with Small Embedded Clusters, *Phys. Rev. Lett.* **119**, 166401 (2017).
- [24] E. A. Stepanov, V. Harkov, and A. I. Lichtenstein, Consistent partial bosonization of the extended Hubbard model, *Phys. Rev. B* **100**, 205115 (2019).
- [25] A. N. Rubtsov, V. V. Savkin, and A. I. Lichtenstein, Continuous-time quantum Monte Carlo method for fermions, *Phys. Rev. B* **72**, 035122 (2005).
- [26] P. Werner, A. Comanac, L. de' Medici, M. Troyer, and A. J. Millis, Continuous-Time Solver for Quantum Impurity Models, *Phys. Rev. Lett.* **97**, 076405 (2006).
- [27] P. Werner and A. J. Millis, Dynamical Screening in Correlated Electron Materials, *Phys. Rev. Lett.* **104**, 146401 (2010).
- [28] E. Gull, A. J. Millis, A. I. Lichtenstein, A. N. Rubtsov, M. Troyer, and P. Werner, Continuous-time Monte Carlo methods for quantum impurity models, *Rev. Mod. Phys.* **83**, 349 (2011).
- [29] H. Hafermann, P. Werner, and E. Gull, Efficient implementation of the continuous-time hybridization expansion quantum impurity solver, *Comput. Phys. Commun.* **184**, 1280 (2013).
- [30] E. G. C. P. van Loon, H. Hafermann, A. I. Lichtenstein, A. N. Rubtsov, and M. I. Katsnelson, Plasmons in Strongly Correlated Systems: Spectral Weight Transfer and Renormalized Dispersion, *Phys. Rev. Lett.* **113**, 246407 (2014).
- [31] H. Hafermann, E. G. C. P. van Loon, M. I. Katsnelson, A. I. Lichtenstein, and O. Parcollet, Collective charge excitations of strongly correlated electrons, vertex corrections, and gauge invariance, *Phys. Rev. B* **90**, 235105 (2014).
- [32] E. A. Stepanov, A. Huber, E. G. C. P. van Loon, A. I. Lichtenstein, and M. I. Katsnelson, From local to nonlocal correlations: The dual boson perspective, *Phys. Rev. B* **94**, 205110 (2016).
- [33] E. G. C. P. van Loon, M. Rösner, G. Schönhoff, M. I. Katsnelson, and T. O. Wehling, Competing Coulomb and electron-phonon interactions in NbS₂, *npj Quantum Mater.* **3**, 32 (2018).
- [34] E. A. Stepanov, L. Peters, I. S. Krivenko, A. I. Lichtenstein, M. I. Katsnelson, and A. N. Rubtsov, Quantum spin fluctuations and evolution of electronic structure in cuprates, *npj Quantum Mater.* **3**, 54 (2018).
- [35] E. A. Stepanov, S. Brener, F. Krien, M. Harland, A. I. Lichtenstein, and M. I. Katsnelson, Effective Heisenberg Model and Exchange Interaction for Strongly Correlated Systems, *Phys. Rev. Lett.* **121**, 037204 (2018).
- [36] E. A. Stepanov, A. Huber, A. I. Lichtenstein, and M. I. Katsnelson, Effective Ising model for correlated systems with charge ordering, *Phys. Rev. B* **99**, 115124 (2019).
- [37] H. Terletska, T. Chen, and E. Gull, Charge ordering and correlation effects in the extended Hubbard model, *Phys. Rev. B* **95**, 115149 (2017).
- [38] H. Terletska, T. Chen, J. Paki, and E. Gull, Charge ordering and nonlocal correlations in the doped extended Hubbard model, *Phys. Rev. B* **97**, 115117 (2018).
- [39] G. V. Astretsov, G. Rohringer, and A. N. Rubtsov, Dual parquet scheme for the two-dimensional Hubbard model: Modeling low-energy physics of high-*T_c* cuprates with high momentum resolution, *Phys. Rev. B* **101**, 075109 (2020).
- [40] G. Rohringer, H. Hafermann, A. Toschi, A. A. Katanin, A. E. Antipov, M. I. Katsnelson, A. I. Lichtenstein, A. N. Rubtsov, and K. Held, Diagrammatic routes to nonlocal correlations beyond dynamical mean field theory, *Rev. Mod. Phys.* **90**, 025003 (2018).

- [41] N. V. Prokof'ev and B. V. Svistunov, Polaron Problem by Diagrammatic Quantum Monte Carlo, *Phys. Rev. Lett.* **81**, 2514 (1998).
- [42] E. Kozik, K. Van Houcke, E. Gull, L. Pollet, N. Prokof'ev, B. Svistunov, and M. Troyer, Diagrammatic Monte Carlo for correlated fermions, *Europhys. Lett.* **90**, 10004 (2010).
- [43] R. Rossi, Determinant Diagrammatic Monte Carlo Algorithm in the Thermodynamic Limit, *Phys. Rev. Lett.* **119**, 045701 (2017).
- [44] F. Šimkovic and E. Kozik, Determinant Monte Carlo for irreducible Feynman diagrams in the strongly correlated regime, *Phys. Rev. B* **100**, 121102(R) (2019).
- [45] A. Moutenet, W. Wu, and M. Ferrero, Determinant monte carlo algorithms for dynamical quantities in fermionic systems, *Phys. Rev. B* **97**, 085117 (2018).
- [46] R. Rossi, Direct sampling of the self-energy with Connected Determinant Monte Carlo, [arXiv:1802.04743](https://arxiv.org/abs/1802.04743).
- [47] A. J. Kim, F. Simkovic, and E. Kozik, Spin and Charge Correlations across the Metal-to-Insulator Crossover in the Half-Filled 2D Hubbard Model, *Phys. Rev. Lett.* **124**, 117602 (2020).
- [48] J. P. F. LeBlanc, A. E. Antipov, F. Becca, I. W. Bulik, Garnet Kin-Lic Chan, Chia-Min Chung, Y. Deng, M. Ferrero, T. M. Henderson, C. A. Jiménez-Hoyos, E. Kozik, X.-W. Liu, A. J. Millis, N. V. Prokof'ev, M. Qin, G. E. Scuseria, H. Shi, B. V. Svistunov, L. F. Tocchio, I. S. Tupitsyn, S. R. White, S. Zhang, B.-X. Zheng, Z. Zhu, and E. Gull (Simons Collaboration on the Many-Electron Problem), Solutions of the Two-Dimensional Hubbard Model: Benchmarks and Results from a Wide Range of Numerical Algorithms, *Phys. Rev. X* **5**, 041041 (2015).
- [49] A. N. Rubtsov, M. I. Katsnelson, and A. I. Lichtenstein, Dual fermion approach to nonlocal correlations in the Hubbard model, *Phys. Rev. B* **77**, 033101 (2008).
- [50] S. Isakov, A. E. Antipov, and E. Gull, Diagrammatic monte carlo for dual fermions, *Phys. Rev. B* **94**, 035102 (2016).
- [51] J. Gukelberger, E. Kozik, and H. Hafermann, Diagrammatic Monte Carlo approach for diagrammatic extensions of dynamical mean-field theory: Convergence analysis of the dual fermion technique, *Phys. Rev. B* **96**, 035152 (2017).
- [52] H. Hafermann, G. Li, A. N. Rubtsov, M. I. Katsnelson, A. I. Lichtenstein, and H. Monien, Efficient Perturbation Theory for Quantum Lattice Models, *Phys. Rev. Lett.* **102**, 206401 (2009).
- [53] S. Isakov, H. Terletska, and E. Gull, Momentum-space cluster dual-fermion method, *Phys. Rev. B* **97**, 125114 (2018).
- [54] T. Ribic, P. Gunacker, S. Isakov, M. Wallerberger, G. Rohringer, A. N. Rubtsov, E. Gull, and K. Held, Role of three-particle vertex within dual fermion calculations, *Phys. Rev. B* **96**, 235127 (2017).
- [55] N. Prokof'ev and B. Svistunov, Fermi-polaron problem: Diagrammatic Monte Carlo method for divergent sign-alternating series, *Phys. Rev. B* **77**, 020408(R) (2008).
- [56] F. Šimkovic, Understanding electron correlations through advances in diagrammatic Monte Carlo, Ph.D. thesis, King's College, London, 2018.
- [57] W. K. Hastings, Monte Carlo sampling methods using Markov chains and their applications, *Biometrika* **57**, 97 (1970).
- [58] K. V. Houcke, E. Kozik, N. Prokof'ev, and B. Svistunov, Diagrammatic Monte Carlo, *Phys. Procedia* **6**, 95 (2010), Computer Simulations Studies in Condensed Matter Physics XXI.
- [59] R. Rossi, F. Werner, N. Prokof'ev, and B. Svistunov, Shifted-action expansion and applicability of dressed diagrammatic schemes, *Phys. Rev. B* **93**, 161102(R) (2016).
- [60] W. Wu, M. Ferrero, A. Georges, and E. Kozik, Controlling feynman diagrammatic expansions: Physical nature of the pseudogap in the two-dimensional hubbard model, *Phys. Rev. B* **96**, 041105(R) (2017).
- [61] H. Park, K. Haule, and G. Kotliar, Cluster Dynamical Mean Field Theory of the Mott Transition, *Phys. Rev. Lett.* **101**, 186403 (2008).
- [62] A. Tanaka, Metal-insulator transition in the two-dimensional Hubbard model: Dual fermion approach with Lanczos exact diagonalization, *Phys. Rev. B* **99**, 205133 (2019).
- [63] A. A. Katanin, Extended dynamical mean field theory combined with the two-particle irreducible functional renormalization-group approach as a tool to study strongly correlated systems, *Phys. Rev. B* **99**, 115112 (2019).
- [64] J. Paki, H. Terletska, S. Isakov, and E. Gull, Charge order and antiferromagnetism in the extended Hubbard model, *Phys. Rev. B* **99**, 245146 (2019).
- [65] M. Schüler, M. Rösner, T. O. Wehling, A. I. Lichtenstein, and M. I. Katsnelson, Optimal Hubbard Models for Materials with Nonlocal Coulomb Interactions: Graphene, Silicene, and Benzene, *Phys. Rev. Lett.* **111**, 036601 (2013).
- [66] G. A. Baker, Jr., Application of the Padé Approximant Method to the Investigation of Some Magnetic Properties of the Ising Model, *Phys. Rev.* **124**, 768 (1961).

Chapter 5

D-TRILEX

This chapter is based on the following publications:

E. A. Stepanov, V. Harkov, A. I. Lichtenstein, “Consistent partial bosonization of the extended Hubbard model”. *Phys. Rev. B* **100**, 205115 (2019)

V. Harkov, M. Vandelli, S. Brener, A. I. Lichtenstein, E. A. Stepanov, “Impact of partially bosonized collective fluctuations on electronic degrees of freedom”. *Phys. Rev. B* **103**, 245123 (2021)

E. A. Stepanov, V. Harkov, M. Rösner, A. I. Lichtenstein, M. I. Katsnelson, A. N. Rudenko, “Coexisting charge density wave and ferromagnetic instabilities in monolayer InSe”. *npj Computational Materials* **8**, 118 (2022)

5.1 Consistent partial bosonization of the extended Hubbard model

Description of various many-body effects in condensed matter theory is usually done in the context of mean-field theory performing a partial bosonization of collective fermionic fluctuations in leading (charge, spin, etc.) channels of instability. However, a simultaneous account for different bosonic channels in this framework gives rise to a so-called Fierz ambiguity problem related to the decomposition of the local Coulomb interaction into considered channels, which drastically affects the final result of the calculation. This issue remains yet unsolved for all mean-field-based theories, although many of them, such as *GW* or *GW*+EDMFT, are intensively used for the solution of realistic problems in and out of equilibrium.

In Ref. [72], we introduce a consistent partial bosonization of the fermionic model that solves the Fierz ambiguity problem. We apply our method to the extended

Hubbard model and derive an effective theory that is formulated in terms of dual fermionic degrees of freedom, new bosonic fields, and an effective fermion-boson interaction. Moreover, we perform a parametrization of the full local four-point vertex¹ of the auxiliary Anderson impurity model which allow us to express the vertex in terms of the fermion-boson (three-point) vertex and screened interactions w and show that the local four-point vertex can be safely excluded from the model action, which results in a very simple and efficient approximation that inherits the high performance of more elaborate dual methods. However, the action can be also used in more complex calculation schemes like, e.g., diagrammatic Monte Carlo as it was done in [128]. The new efficient approach is called dual triply irreducible local expansion (D-TRILEX)² for the partially bosonized theory. The structure of the self-energy (3.84) and polarization operators (3.85) and diagrams (3.86) in D-TRILEX is reminiscent of GW +DMFT and TRILEX approaches, but accounts for the exact local three-point vertex function in a symmetric way. The importance of a symmetric inclusion of the vertex is discussed in Ref. [61].

In Ref. [72], the derived D-TRILEX approach is applied to the half-filled Hubbard model on a square lattice. Calculations are performed at temperature $T = 0.1$. Note that the energy scale is set to half of the bandwidth $D = 4t = 1$. The results are shown for the Coulomb interactions $U = 0.5, 1.0, 1.5$. We find that the dual self-energy D-TRILEX provides a very accurate agreement compared to the ladder DF results at moderate interaction strength $U = 1.0$. A small mismatch appears due to the missing transversal contributions. This effect is even more pronounced at weak coupling. The largest deviation we observe at $U = 1.5$. Finally, we show that D-TRILEX provides a qualitatively good estimation of the metal-to-Mott-insulator transition by predicting it at smaller interaction strength than DMFT similar to cluster DMFT [187] and second-order DF [188].

¹Similar parametrizations were introduced in [69, 133, 134]. Simpler parametrizations based on a weak coupling perturbation expansion can be found in [159, 185, 186].

²Note that previously (in Ref. [72]) the method was called TRILEX².

Consistent partial bosonization of the extended Hubbard model

E. A. Stepanov,^{1,2} V. Harkov,^{1,3} and A. I. Lichtenstein^{1,2,3}

¹*Institute of Theoretical Physics, University of Hamburg, 20355 Hamburg, Germany*

²*Theoretical Physics and Applied Mathematics Department, Ural Federal University, Mira Street 19, 620002 Ekaterinburg, Russia*

³*European X-Ray Free-Electron Laser Facility, Holzkoppel 4, 22869 Schenefeld, Germany*



(Received 25 July 2019; revised manuscript received 11 October 2019; published 11 November 2019)

We design an efficient and balanced approach that captures major effects of collective electronic fluctuations in strongly correlated fermionic systems using a simple diagrammatic expansion on a basis of dynamical mean-field theory. For this aim we perform a partial bosonization of collective fermionic fluctuations in leading channels of instability. We show that a simultaneous account for different bosonic channels can be done in a consistent way that allows to avoid the famous Fierz ambiguity problem. The present method significantly improves a description of an effective screened interaction W in both charge and spin channels, and has a great potential for application to realistic GW -like calculations for magnetic materials.

DOI: [10.1103/PhysRevB.100.205115](https://doi.org/10.1103/PhysRevB.100.205115)

I. INTRODUCTION

Mean-field theory is a simple and transparent method that is used for a description of collective fermionic excitations in a broad range of physical problems from condensed matter physics to quantum field theory. It allows to capture both magnetic and superconducting fluctuations in Hubbard [1,2] and t - J [3,4] models, as well as spontaneous symmetry breaking and formation of various condensates in Nambu–Jona-Lasinio and Gross-Neveu models [5–13]. The underlying idea of the method is based on a partial bosonization of collective fermionic fluctuations in leading channels of instability in the system [14–16]. This allows a simple diagrammatic solution of the initial problem in terms of original fermionic and effective new bosonic fields in a GW fashion [17–19].

Theoretical description of many-body effects in a regime of strong electronic interactions requires more advanced approaches that are usually based on (extended) dynamical mean-field theory (EDMFT) [20–25]. DMFT provides an exact solution of the problem in the limit of infinite dimension [26] and is found to be a good approximation for single-particle quantities [27], especially when properties of the system are dominated by local correlations. However, collective electronic fluctuations are essentially nonlocal. For this reason, a number of proposed approaches that treat many-body excitations beyond DMFT grow as fast as a degree of their complexity [28]. These new methods provide a very accurate solution of model (single-band) problems, but are numerically very expensive for realistic multiband calculations [29–34].

Following the mean-field idea, a partially bosonized description of collective electronic effects in strongly correlated systems can also be performed on a basis of EDMFT. Research in this direction resulted in GW +EDMFT [35–41] and TRILEX [42–44] methods. Although the GW -like extension of EDMFT is an efficient and inexpensive numerical approach, it has a significant drawback that is common for every

partially bosonized theory. This severe problem is known as the Fierz ambiguity [14–16]. It appears when two or more different bosonic channels are considered simultaneously. Then, the theory becomes drastically dependent on the way how these channels are introduced. Surprisingly, this issue remains unsolved even for a standard mean-field theory, let alone the GW +EDMFT method that is actively used for solution of realistic multiband [36,45–49] and time-dependent problems [50,51].

Recently, the authors of TRILEX approach showed that the effect of the Fierz ambiguity can be reduced using a cluster extension of the theory [44]. However, this approach is much more time consuming numerically than its original single-site version and, in fact, breaks a translational symmetry of the initial lattice problem. Indeed, the nonlocal in space self-energy obtained within the cluster becomes different from the corresponding one between two clusters. All above discussions suggest that there is no reliable simple theory that can accurately describe an interacting fermionic system in the regime of coexisting strong bosonic fluctuations in different channels.

In this work we introduce a consistent partial bosonization of an extended Hubbard model that solves the famous Fierz ambiguity problem without a complicated cluster extension of the method. We show that the resulting action of the problem contains only an effective fermion-boson vertex function, while a fermion-fermion interaction can be safely excluded from the theory. The derived approach combines a simplicity of a mean-field approximation with an efficiency of much more advanced EDMFT-based methods. This allows to improve many existing extensions of GW method and include an effect of magnetic fluctuations in a standard GW scheme in a consistent way. Although the introduced theory is discussed in a context of an extended Hubbard model, it is not restricted only to this particular single-band model, and can be applied to other fermionic problems from different areas of physics.

II. PARTIAL BOSONIZATION OF A FERMION MODEL

A. Fierz ambiguity

We start the derivation of a partially bosonized theory for strongly correlated electrons with the following action of extended Hubbard model:

$$S_{\text{latt}} = - \sum_{\mathbf{k}, \nu, \sigma} c_{\mathbf{k}\nu\sigma}^* [i\nu + \mu - \varepsilon_{\mathbf{k}}] c_{\mathbf{k}\nu\sigma} + U \sum_{\mathbf{q}, \omega} n_{\mathbf{q}\omega\uparrow} n_{-\mathbf{q}, -\omega\downarrow} + \frac{1}{2} \sum_{\mathbf{q}, \omega, \zeta} V_{\mathbf{q}}^{\zeta} \rho_{\mathbf{q}\omega}^{\zeta} \rho_{-\mathbf{q}, -\omega}^{\zeta}. \quad (1)$$

Here, $c_{\mathbf{k}\nu\sigma}^{(*)}$ is a Grassmann variable corresponding to annihilation (creation) of an electron with momentum \mathbf{k} , fermionic Matsubara frequency ν_n , and spin projection $\sigma = \uparrow, \downarrow$. We also introduce following bilinear combinations of fermionic variables $\rho_{\mathbf{q}\omega}^{\zeta} = n_{\mathbf{q}\omega}^{\zeta} - \langle n^{\zeta} \rangle$ that correspond to charge ($\zeta = c$) and spin ($\zeta = \{x, y, z\}$) degrees of freedom with momentum \mathbf{q} and bosonic frequency ω_m . $n_{\mathbf{q}\omega}^{\zeta} = \sum_{\mathbf{k}, \nu, \sigma, \sigma'} c_{\mathbf{k}\nu\sigma}^* \sigma_{\sigma\sigma'}^{\zeta} c_{\mathbf{k}+\mathbf{q}, \nu+\omega, \sigma'}$, $\sigma^c = \mathbb{1}$, and $\sigma^{x,y,z}$ are Pauli matrices in the spin space. U corresponds to a local Coulomb interaction, $V_{\mathbf{q}}^{\zeta}$ describes a nonlocal Coulomb and direct exchange interactions in the charge and spin channels, respectively. Dispersion relation $\varepsilon_{\mathbf{k}}$ can be obtained via a Fourier transform of hopping matrix elements t_{ij} between lattice sites i and j . All numerical calculations in this work are performed for a half-filled two-dimensional Hubbard model ($V_{\mathbf{q}}^{\zeta}, Y_{\omega}^{\zeta} = 0$) on a square lattice with a nearest-neighbor hopping amplitude t . The half of the bandwidth $D = 4t = 1$ sets the energy scale. The temperature is $T = 0.1$.

For a simplified description of many-body effects in the system, leading collective electronic excitations can be partially *bosonized* [14–16]. For this aim, the local interaction term $Un_{\uparrow}n_{\downarrow}$ has to be rewritten in terms of bilinear combinations of fermionic variables as $\frac{1}{2} \sum_{\zeta} U^{\zeta} \rho^{\zeta} \rho^{\zeta}$. This allows to introduce an effective bosonic field for every bilinear combination using the Hubbard-Stratonovich transformation for the total (local and nonlocal) interaction part of the problem [52,53]. It should be noted, however, that the decoupling of the local Coulomb interaction U into different channels can be done almost arbitrary. As discussed, for instance, in Ref. [42], a free choice for the bare interaction U^c in the charge channel immediately fixes the $U^s = (U^c - U)/3$ value of the spin interaction if all three $s = \{x, y, z\}$ spin channels are introduced simultaneously. The Ising decoupling with $U^z = U^c - U$ corresponds to the case when only the z component of the spin is considered. Then, if the initial problem (1) is solved exactly, the result does not depend on the way how the decoupling of U is performed. However, an approximate (mean-field or *GW*-like) solution of the problem dramatically depends on the decoupling [44]. This issue is known as Fierz ambiguity [14–16].

B. Collective electronic effects beyond EDMFT

As follows from the above discussions, the Fierz ambiguity problem can be avoided if the local interaction term $Un_{\uparrow}n_{\downarrow}$ stays undecoupled in its original form. However, this form of the interaction prevents any Hubbard-Stratonovich transformation. Nevertheless, in this case we still can benefit from

the idea of (extended) dynamical mean-field theory (EDMFT) [20–26], where all local correlations are treated *exactly* via an effective local impurity problem

$$S_{\text{imp}}^{(i)} = - \sum_{\nu, \sigma} c_{\nu\sigma}^* [i\nu + \mu - \Delta_{\nu}] c_{\nu\sigma} + U \sum_{\omega} n_{\omega\uparrow} n_{-\omega\downarrow} + \frac{1}{2} \sum_{\omega, \zeta} Y_{\omega}^{\zeta} \rho_{\omega}^{\zeta} \rho_{-\omega}^{\zeta}. \quad (2)$$

The latter is a local part of the lattice action (1), where a dispersion relation and nonlocal interaction are replaced by local fermionic ($\varepsilon_{\mathbf{k}} \rightarrow \Delta_{\nu}$) and bosonic ($V_{\mathbf{q}}^{\zeta} \rightarrow Y_{\omega}^{\zeta}$) hybridization functions that effectively account for nonlocal single- and two-particle fluctuations, respectively. In the absence of these hybridizations, EDMFT reduces to a static mean-field approximation. Since the impurity model is solved numerically exactly using, e.g., continuous-time quantum Monte Carlo solvers [54–57], the Fierz ambiguity problem on the local level is absent by construction.

Further, we integrate out the impurity problem in order to exactly account for all local fluctuations in the effective lattice model. As shown in the dual fermion (DF) approach [58], this can be done after the nonlocal part of the lattice action is rewritten in terms of new fermionic variables $c^{(*)} \rightarrow f^{(*)}$. In addition, we perform a partial bosonization $\rho^{\zeta} \rightarrow \varphi^{\zeta}$ of the nonlocal interaction following the dual boson (DB) scheme [59,60], which does not lead to the Fierz ambiguity either. Then, the initial problem (1) transforms to a dual action (see Ref. [61] and Appendix B)

$$\tilde{S} = - \sum_{\mathbf{k}, \nu, \sigma} f_{\mathbf{k}\nu\sigma}^* \tilde{G}_{\mathbf{k}\nu\sigma}^{-1} f_{\mathbf{k}\nu\sigma} - \frac{1}{2} \sum_{\mathbf{q}, \omega, \zeta} \varphi_{\mathbf{q}\omega}^{\zeta} \tilde{W}_{\mathbf{q}\omega}^{\zeta-1} \varphi_{-\mathbf{q}, -\omega}^{\zeta} + \tilde{\mathcal{F}}. \quad (3)$$

After the impurity problem is integrated out, bare fermion $\tilde{G}_{\mathbf{k}\nu\sigma} = G_{\mathbf{k}\nu\sigma}^{\text{EDMFT}} - g_{\nu\sigma}$ and boson $\tilde{W}_{\mathbf{q}\omega}^{\zeta} = W_{\mathbf{q}\omega}^{\zeta \text{EDMFT}} - w_{\omega}^{\zeta}$ propagators are given by nonlocal parts of EDMFT Green's function and renormalized interaction [61], respectively. Thus, they already account for local single- and two-particle fluctuations in the system via an exact local self-energy $\Sigma_{\nu\sigma}^{\text{imp}}$ and polarization operator $\Pi_{\omega}^{\zeta \text{imp}}$ of the effective impurity problem, respectively. Here, $g_{\nu\sigma}$ and w_{ω}^{ζ} are the full local Green's function and renormalized interaction of the impurity problem.

The interaction part $\tilde{\mathcal{F}}[f, \varphi]$ of the dual action (3) contains all possible fully screened local fermion-fermion and fermion-boson vertex functions of the impurity problem [59,60]. Here, as well as in most of DB approximations, we restrict ourselves to the lowest-order (two-particle) interaction terms that are given by the fermion-fermion $\Gamma_{\nu\nu'\omega}$ and fermion-boson $\Lambda_{\nu\omega}$ vertex functions

$$\Gamma_{\nu\nu'\omega} = \begin{array}{c} \nu \\ \square \\ \nu + \omega \quad \nu' + \omega \end{array}, \quad \Lambda_{\nu\omega} = \begin{array}{c} \nu \\ \triangle \\ \nu + \omega \end{array} \omega. \quad (4)$$

Exact definition of these quantities can be found in Appendix B. The dual theory with only two-particle interaction terms has been tested against exact benchmark results showing a good performance of the theory in a broad regime of model parameters [62–64]. Moreover, the fact that the screened

six-fermion vertex function has only a minor effect on the self-energy of the Hubbard model has been observed in [65].

In the absence of the interaction part $\tilde{\mathcal{F}}[f, \varphi]$ the dual theory (3) reduces to EDMFT [59,60]. However, an account for vertex corrections beyond the dynamical mean-field solution is desirable [66–68]. Especially, it is an important problem for description of spin fluctuations and magnetic polarization in realistic systems [69,70] as they are not captured by a standard $GW+DMFT$ scheme [35–41]. While the use of the fermion-boson vertex in a diagrammatic solution of multiband problems is possible [44], an inclusion of the fermion-fermion vertex in realistic calculations is extremely challenging and time consuming numerically [29–34]. The fermion-fermion vertex describes the full (renormalized) local fermion-fermion interaction, so it cannot be simply discarded.

It would be extremely helpful to find an additional transformation of the problem (3) in which the full local fermion-fermion vertex $\Gamma_{\nu\nu'\omega}$ vanishes from the effective action. Then, the resulting theory will be written in terms of fermion and boson propagators, and the remaining fermion-boson interaction $\Lambda_{\nu\omega}$. An effective fermion-fermion vertex function in this theory appears only after bosonic fields are integrated out. Such a fermion-fermion vertex is by definition reducible with respect to a bosonic propagator and serves as an approximation for the original fermion-fermion vertex function $\Gamma_{\nu\nu'\omega}$. Since irreducible contributions are not contained in this approximation, the effective fermion-fermion vertex of the resulting fermion-boson theory becomes drastically dependent on the way how bosonic fields are introduced. This fact again leads to the Fierz ambiguity problem.

C. Approximation for the fermion-fermion vertex

We have found a unique form of the bare interaction in every considered bosonic channel that almost fully suppresses the effect of missing irreducible diagrams. As a consequence, an effective reducible fermion-fermion interaction almost exactly coincides with the full local fermion-fermion vertex $\Gamma_{\nu\nu'\omega}$, which automatically solves the Fierz ambiguity problem. This unique form of the bare interaction can be found by analyzing the bare fermion-fermion vertex of the impurity problem. Let us arbitrarily decouple the local Coulomb interaction U of the impurity problem (2) into charge U^c and spin U^s parts. This leads to the following bare interaction $\mathcal{U}_{\omega}^s = U^s + Y_{\omega}^s$ in a corresponding bosonic channel. Then, we rewrite the interaction part of the impurity problem in an antisymmetrized form of the bare fermion-fermion vertex $\Gamma_{\nu\nu'\omega}^0$:

$$\begin{aligned} S_{\text{imp}}^{(i)} = & - \sum_{\nu, \sigma} c_{\nu\sigma}^* [i\nu + \mu - \Delta_{\nu}] c_{\nu\sigma} \\ & + \frac{1}{8} \sum_{\nu, \nu', \omega} \sum_{\zeta, \sigma(\zeta')} \Gamma_{\nu\nu'\omega}^0 \zeta_{\sigma\sigma'}^* c_{\nu+\omega, \sigma'} c_{\nu'+\omega, \sigma''}^* \sigma_{\sigma''\sigma'''}^{\zeta} c_{\nu', \sigma'''} \cdot \end{aligned} \quad (5)$$

This procedure can be performed in a standard way (see, for instance, Sec. II A in Ref. [71]) interchanging indices of two creation (or annihilation) Grassmann variables in the interaction term. Charge and spin “z” components of the bare

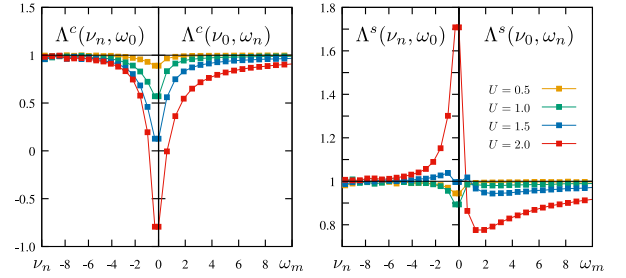


FIG. 1. Fermion-boson vertex function $\Lambda_{\nu\omega}$ in the charge (left) and spin (right) channels as a function of fermionic ν_n and bosonic ω_m frequencies. The result is obtained for different values of the local Coulomb interaction.

fermion-fermion vertex are given by the expressions

$$\begin{aligned} \Gamma_{\nu\nu'\omega}^{0c} &= 2\mathcal{U}_{\omega}^c - \mathcal{U}_{\nu'-\nu}^c - \mathcal{U}_{\nu'-\nu}^x - \mathcal{U}_{\nu'-\nu}^y - \mathcal{U}_{\nu'-\nu}^z \\ &= U + 2Y_{\omega}^c - Y_{\nu'-\nu}^c - Y_{\nu'-\nu}^x - Y_{\nu'-\nu}^y - Y_{\nu'-\nu}^z, \\ \Gamma_{\nu\nu'\omega}^{0z} &= 2\mathcal{U}_{\omega}^z - \mathcal{U}_{\nu'-\nu}^z + \mathcal{U}_{\nu'-\nu}^x + \mathcal{U}_{\nu'-\nu}^y - \mathcal{U}_{\nu'-\nu}^c \\ &= -U + 2Y_{\omega}^z - Y_{\nu'-\nu}^z + Y_{\nu'-\nu}^x + Y_{\nu'-\nu}^y - Y_{\nu'-\nu}^c, \end{aligned} \quad (6)$$

and spin “x” and “y” components can be obtained by a circle permutation of spin $\{x, y, z\}$ indices in the second equation.

As can be seen from Eq. (6), the ladderlike irreducible contributions to the fermion-fermion vertex $\Gamma_{\nu\nu'\omega}^s$ of the impurity problem originate from the presence of “vertical” bosonic lines $\mathcal{U}_{\nu'-\nu}^s$ in the bare vertex. Dressed by a two-particle ladder they become irreducible with respect to the (“horizontal”) bosonic line \mathcal{U}_{ω}^s and will not be included in the reducible approximation. As the second line in Eq. (6) shows, the bare vertex $\Gamma_{\nu\nu'\omega}^{0s}$ does not depend on the way how the decoupling of the local Coulomb interaction is performed. This fact follows from the exact relation between bare interactions U^s in different bosonic channels. Therefore, let us include the main contribution $\pm U$ of the charge/spin bare vertex only to the horizontal line \mathcal{U}_{ω}^s . This immediately leads to a unique form of the bare interaction $U^c = -U^s = U/2$ with the same value for all $s = \{x, y, z\}$ spin components that excludes ladderlike irreducible contributions from the full local fermion-fermion vertex function. If more complicated nonladder irreducible contributions to the fermion-fermion vertex become important, they cannot be completely excluded from the theory, but are still strongly suppressed by our choice of the bare interaction. Importantly, this result for the bare interaction *cannot* be obtained by any decoupling of the Coulomb interaction U discussed above. Note that the fermion-boson vertex is by definition irreducible with respect to the bosonic propagator, the inclusion of the full local Coulomb interaction U in the horizontal line leads to a correct asymptotic behavior of this vertex $\Lambda_{\nu\omega}^{c/s} \rightarrow 1$ at large frequencies as shown in Fig. 1.

The best possible decoupling-based approximation for the fermion-fermion vertex can be obtained for the Ising form of the bare interaction $U^c = -U^z = U/2$ and $U^x, U^y = 0$. This approximation still reproduces the “ $-U$ ” contribution to the bare vertex $\Gamma_{\nu\nu'\omega}^{0x/y}$ via U^c and U^z terms, but neglects the screening of this vertex by two-particle fluctuations in x and y channels. Note that the Ising decoupling leads to a correct Hartree-Fock saddle point in the mean-field description

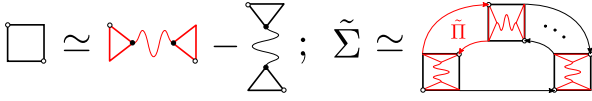


FIG. 2. The sketch of the approximation for the full local fermion-fermion vertex function $\Gamma_{\nu\nu'\omega}$ introduced in Eq. (7) (left). The illustration of the TRILEX² approximation of the nonlocal self-energy $\tilde{\Sigma}$ of the ladder dual theory that accounts only for the horizontal (shown in red) contribution to the fermion-fermion vertex function (right).

of spin fluctuations [72]. Moreover, the Ising decoupling provides the best possible result for a single-site TRILEX approach [44]. However, as we show below, the result for physical observables, such as the self-energy, can be drastically improved using our unique form of the bare interaction, which is not based on the decoupling ideology.

After all, a final result for the reducible approximation of the full fermion-fermion vertex function of the impurity problem can be written in the following form (see Fig. 2):

$$\begin{aligned}\Gamma_{\nu\nu'\omega}^c &= 2M_{\nu\nu'\omega}^c - M_{\nu,\nu+\omega,\nu'-\nu}^c - 3M_{\nu,\nu+\omega,\nu'-\nu}^s, \\ \Gamma_{\nu\nu'\omega}^s &= 2M_{\nu\nu'\omega}^s + M_{\nu,\nu+\omega,\nu'-\nu}^s - M_{\nu,\nu+\omega,\nu'-\nu}^c,\end{aligned}\quad (7)$$

where

$$M_{\nu\nu'\omega}^s = \Lambda_{\nu\omega}^s W_{\omega}^s \Lambda_{\nu'+\omega,-\omega}^s - U^s/2 = \text{Diagram}, \quad (8)$$

and the term $U^s/2$ excludes a double counting of the bare Coulomb interaction between different channels. Note that in the case of Ising decoupling of the Coulomb interaction, the term $U^s/2$ does not appear in Eq. (8) because this form of the decoupling is identical for every bosonic channel and does not lead to a double counting. A detailed derivation of these expressions can be found in Appendix A.

A simpler parametrization of the fermion-fermion vertex, which is based on a weak coupling perturbation expansion, has been derived in Refs. [73–75]. A more advanced approximation that additionally accounts for fermion-boson vertex corrections $\Lambda_{\nu,\omega}^s$ has been later introduced in [76,77]. There, a decomposition of the local Coulomb interaction in only one (spin or charge) channel has been considered. Note also that in these two works the approximation for the fermion-fermion vertex appears in a nonsymmetrized form that contains only a horizontal contribution $M_{\nu\nu'\omega}^s$ (8). However, it can be *identically* rewritten in the antisymmetrized form of Eq. (7) that has both horizontal $M_{\nu\nu'\omega}^s$ and vertical $M_{\nu,\nu+\omega,\nu'-\nu}^s$ components.

Our present parametrization (7) improves the idea of Refs. [76,77] and exploits a unique multiple-channel decomposition of the fermion-fermion vertex. We find that this approximation (7) is in a good agreement with the exact result not only in the weakly interacting regime $U = 0.5$, but also at much larger values of the local Coulomb interaction

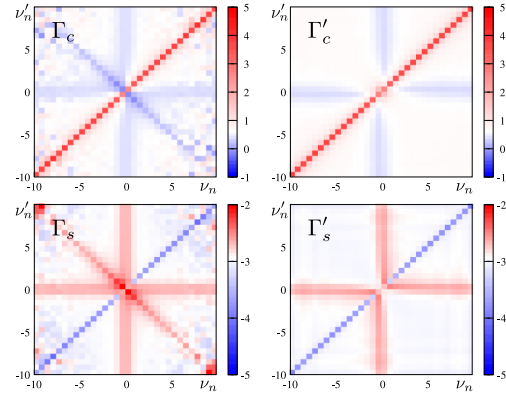


FIG. 3. Charge and spin components of the exact ($\Gamma_{\nu,\nu'\omega}$) and approximate ($\Gamma'_{\nu,\nu'\omega}$) fermion-fermion vertex functions at zeroth bosonic frequency ω_0 . The result is obtained for $U = 1.0$.

$U = 1.0$ and 1.5 . For this reason, Fig. 3 shows the result for the exact and approximate vertex functions only for $U = 1.0$, which were obtained for the same impurity problem of dynamical mean-field theory. Note that the contribution from the particle-particle channel, which at ω_0 is located along the $\nu_n = -\nu'_n$ line [78,79], is not considered in our approximation. Although this contribution to the fermion-fermion vertex is not small itself, it has a minor effect on physical observables, such as a self-energy, at general fillings [80]. The exclusion of a particle-particle channel from the approximation of the vertex greatly simplifies the theory as it does not require the calculation of the “anomalous” fermion-boson vertex function with two incoming or two outgoing fermionic lines. However, if a certain physical problem needs an account for the particle-particle channel, the latter can be introduced in the theory in the same way as it is done for the particle-hole (charge and spin) channel. We have noticed that a similar decomposition of the fermion-fermion vertex is proposed in [81]. In contrast, our derivation of an approximate fermion-fermion vertex aims to explain why irreducible contributions are almost fully suppressed by the unique choice of the bare interaction. This is a key ingredient for our study that allows to exclude the fermion-fermion vertex function from the theory.

Figure 4 shows the cut of the fermion-fermion vertex function $\Gamma_{\nu,\nu'\omega}$ obtained for $U = 0.5$ (top row), $U = 1.0$ (middle row), and $U = 1.5$ (bottom row) at zeroth bosonic frequency ω_0 in two most important directions. We find that the frequency dependence of the exact vertex along ν'_0 (left column) and $\nu_n = \nu'_n$ (right column) lines is captured reasonably well by the horizontal $M_{\nu\nu'\omega}^s$ and vertical $M_{\nu,\nu+\omega,\nu'-\nu}^s$ diagrams, respectively. A neglected particle-particle contribution results in a mismatch between the approximate and exact results for the fermion-fermion vertex in a small region around the ν_{-1} point. Since the particle-particle contribution has a minor effect on the $\uparrow\uparrow$ component of the vertex [75], our approximation provides a reasonably good result for $\Gamma_{\nu\nu'\omega}^{\uparrow\uparrow} = (\Gamma_{\nu,\nu'\omega}^c + \Gamma_{\nu,\nu'\omega}^s)/2$.

D. Effective fermion-boson model

Further, we make an additional approximation for the reducible fermion-fermion vertex $M_{\nu\nu'\omega}^s \simeq \Lambda_{\nu\omega}^s \bar{w}_{\omega}^s \Lambda_{\nu'+\omega,-\omega}^s$

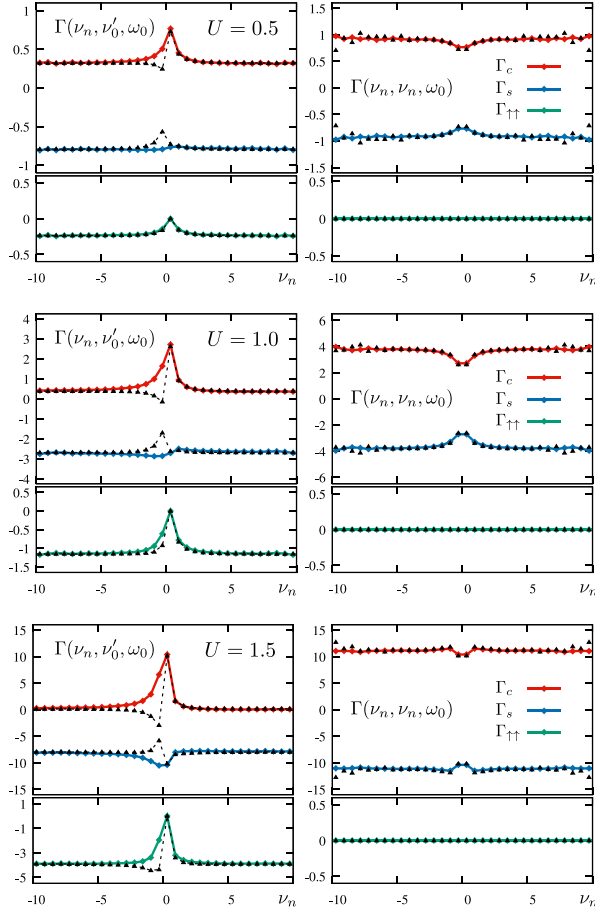


FIG. 4. Frequency dependence of charge, spin, and $\uparrow\uparrow$ components of the exact (black triangles) and approximate (lines with diamonds) fermion-fermion vertex function $\Gamma_{\nu_n, \nu'_0, \omega_0}$ along ν'_0 (left column) and $\nu_n = \nu'_n$ (right column) lines at zeroth bosonic frequency ω_0 . Results are obtained for $U = 0.5$ (top row), $U = 1.0$ (middle row), and $U = 1.5$ (bottom row).

including the term $U^S/2$ in the propagator $\bar{w}_\omega^S = w_\omega^S - U^S/2$. Without this step it would be impossible to find a simple transformation of the problem (3) that generates the $M_{\nu\nu'}^S$ correction in order to cancel the full local vertex function $\Gamma_{\nu\nu'}^S$ from the theory. This approximation is justified in the high-frequency limit where the fermion-boson vertex function $\Lambda_{\nu\omega}$ is equal to unity (Fig. 1), and also by a good agreement of the resulting theory with much more elaborate approaches discussed below. Following recent works [76,77], the $M_{\nu\nu'}^S$ correction can be obtained with the help of an additional Hubbard-Stratonovich transformation over bosonic variables $\varphi^S \rightarrow b^S$ (for details, see Appendix B). As a result, we get the final expression for the action of the effective fermion-boson model

$$\begin{aligned} \mathcal{S}_{f-b} = & - \sum_{\mathbf{k}, \nu, \sigma} f_{\mathbf{k}\nu\sigma}^* \tilde{\mathcal{G}}_{\mathbf{k}\nu\sigma}^{-1} f_{\mathbf{k}\nu\sigma} - \frac{1}{2} \sum_{\mathbf{q}, \omega, \zeta} b_{\mathbf{q}\omega}^{\zeta} \mathcal{W}_{\mathbf{q}\omega}^{\zeta} b_{-\mathbf{q}, -\omega}^{\zeta} \\ & + \sum_{\mathbf{k}, \mathbf{q}} \sum_{\nu, \omega} \sum_{\zeta, \sigma, \sigma'} \Lambda_{\nu\omega}^{\zeta} f_{\mathbf{k}\nu\sigma}^* \sigma_{\sigma\sigma'}^{\zeta} f_{\mathbf{k}+\mathbf{q}, \nu+\omega, \sigma'} b_{-\mathbf{q}, -\omega}^{\zeta}. \end{aligned} \quad (9)$$

The bare Green's function $\tilde{\mathcal{G}}_{\mathbf{k}\nu\sigma}$ remains unchanged during the last transformation, and the bare bosonic propagator becomes

equal to $\mathcal{W}_{\mathbf{q}\omega}^S = W_{\mathbf{q}\omega}^{\text{EDMFT}} - U^S/2$. Note that if the local Coulomb interaction is considered in the Ising decoupling form, the bare bosonic propagator of the new fermion-boson theory coincides with the renormalized interaction of EDMFT $\mathcal{W}_{\mathbf{q}\omega}^S = W_{\mathbf{q}\omega}^{\text{EDMFT}}$ as discussed in Appendix B.

The simplest set of diagrams for the self-energy and polarization operator has the following form:

$$\begin{aligned} \tilde{\Sigma}_{\mathbf{k}\nu\sigma} &= - \sum_{\mathbf{q}, \omega, \zeta} \Lambda_{\nu+\omega, -\omega}^{\zeta} \tilde{\mathcal{G}}_{\mathbf{k}+\mathbf{q}, \nu+\omega, \sigma'} W_{\mathbf{q}\omega}^{\zeta} \Lambda_{\nu, \omega}^{\zeta} = \text{Diagram 1} \\ \tilde{\Pi}_{\mathbf{q}\omega}^S &= \sum_{\mathbf{k}, \nu, \sigma(\zeta)} \Lambda_{\nu+\omega, -\omega}^{\zeta} \tilde{\mathcal{G}}_{\mathbf{k}+\mathbf{q}, \nu+\omega, \sigma'} \tilde{\mathcal{G}}_{\mathbf{k}\nu\sigma'} \Lambda_{\nu, \omega}^{\zeta} = \text{Diagram 2} \end{aligned} \quad (10)$$

Here, $\tilde{\mathcal{G}}_{\mathbf{k}\nu\sigma}$ and $W_{\mathbf{q}\omega}^S$ are full propagators of the derived fermion-boson problem (9). We prefer to keep fermions in the dual space, which results in the following connection between dual and lattice self-energies $\Sigma_{\mathbf{k}\nu\sigma}^{\text{latt}} = \Sigma_{\nu}^{\text{imp}} + \Sigma'_{\mathbf{k}\nu\sigma}$, where $\Sigma'_{\mathbf{k}\nu} = \tilde{\Sigma}_{\mathbf{k}\nu} (1 + g_{\nu} \tilde{\Sigma}_{\mathbf{k}\nu})^{-1}$, as derived in Refs. [59–61]. The last expression excludes the double counting between contributions of the local $\Sigma_{\nu}^{\text{imp}}$ and nonlocal $\tilde{\Sigma}_{\mathbf{k}\nu}$ self-energies to the lattice Green's function $G_{\mathbf{k}\nu}$ that arise in the Dyson equation. Here, g_{ν} is the full local Green's function of the impurity problem. Although the introduced diagram for the nonlocal self-energy has a very simple form (10), it effectively contains the leading “horizontal” part of the two-particle ladder contribution that is present in much more advanced DF [58] and DB [54,55] theories (see Fig. 2). Moreover, an account for this contribution does not require an inversion of the Bethe-Salpeter equation, which is a big advantage for numerical calculations.

At first glance, nonlocal diagrams introduced in Eq. (10) do not obey the Hedin form [17], where the full lattice fermion-boson vertex function appears only at one side of the diagram. However, in the resulting action (9) the full local fermion-boson vertex $\Lambda_{\nu\omega}^S$ is the *bare* interaction vertex for an effective lattice problem that consequently enters diagrams for the self-energy and polarization operator from both sides. The importance to have the local vertex function at both sides of dual diagrams has been discussed in details in Ref. [61].

The present approach immediately suggests an improvement for already existing partially bosonized theories. Indeed, if two or one fermion-boson vertices in Eq. (10) are replaced by unity, our method reduces to GW +DMFT or TRILEX approaches, respectively, but with a more accurate Fierz-ambiguity-free form of the bosonic propagator. Thus, we will call the introduced set of diagrams (10) for the self-energy and polarization operator that contains a double-triangular fermion-boson vertex correction as the TRILEX² approximation of the partially bosonized theory.

III. RESULTS

A. Nonlocal self-energy

The performance of the TRILEX² approach can be tested against a more elaborate ladder DF method, which is accurate enough in the regime of strong interactions U not exceeding the bandwidth ($U \leq 2.0$) [62–64]. Figure 5 shows the nonlocal self-energy $\tilde{\Sigma}_{\mathbf{k}\nu}$ at zero Matsubara frequency

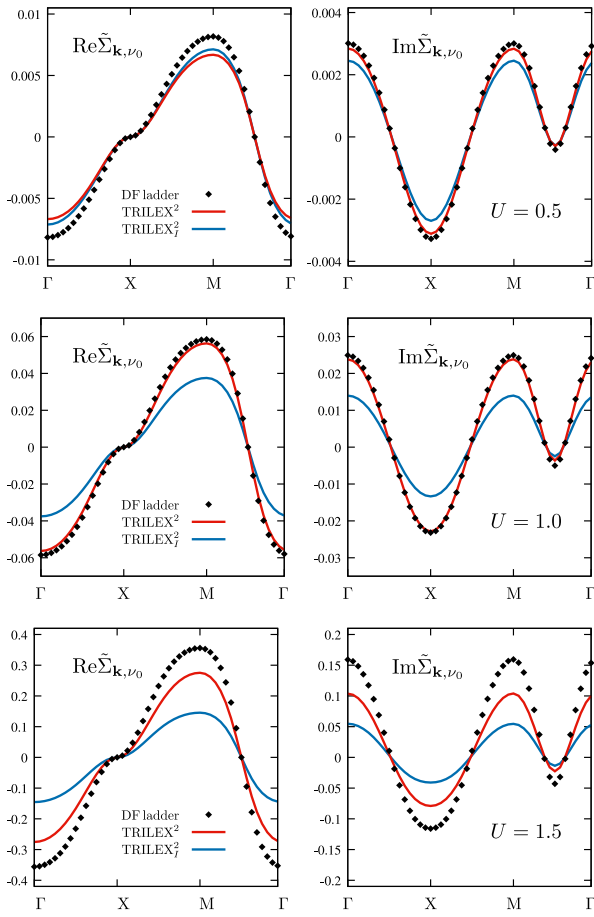


FIG. 5. Real and imaginary parts of the nonlocal self-energy $\tilde{\Sigma}_{\mathbf{k}\nu}$ at the first fermionic Matsubara frequency ν_0 obtained for the ladder dual fermion and TRILEX² (for the “unique” and Ising form of the bare interaction) approaches. Results are calculated for $U = 0.5$ (top row), $U = 1.0$ (middle row), and $U = 1.5$ (bottom row).

ν_0 for different approaches. The result is obtained within a single-shot calculation performed on top of the converged DMFT solution, so that the local self-energy Σ_ν^{imp} has the same value for all compared theories. For numerical solution of the impurity problem we used the open source CT-HYB solver [82,83] based on ALPS libraries [84].

We find that the result for the self-energy of the TRILEX² approximation is in a very good agreement with the one of the ladder DF approach even in the strongly interacting $U = 1.0$ regime. A small mismatch between these two results appears because the TRILEX² theory does not account for “vertical” contributions $M_{\nu,\nu+\omega,\nu'-\nu}^S$ to the fermion-fermion vertex that are present in the DF approach. The absence of these corrections only slightly modifies the result, but greatly simplifies numerical calculations. The effect of neglected contribution of vertical diagrams is more visible in the weakly correlated regime ($U = 0.5$). This can be explained by the fact that the horizontal contribution to the vertex function becomes leading when collective fluctuations in the corresponding channel are strong [76,77]. In the regime of $U = 0.5$, charge and spin fluctuations only start to develop, which results in a larger mismatch with the exact result for the self-energy. However, the value of the nonlocal self-energy in this regime

is relatively small, so this inconsistency should not lead to a serious problem for calculation of physical observables. At larger value of the interaction ($U = 1.5$) the contribution of vertical diagrams becomes more important. As expected, the TRILEX² result, which is based on the Ising decoupling, provides a less accurate result due to missing diagrams in x and y spin channels.

B. Metal-to-Mott-insulator phase transition

The present approach also shows a qualitatively good estimation for a metal-to-Mott-insulator phase transition. The corresponding phase boundary can be obtained from the behavior of the local Green’s function at imaginary time $\tau = \beta/2$, which approximates the quasiparticle density of states at the Fermi level [85]. For this aim we perform a fully self-consistent TRILEX² calculation using a standard self-consistency condition on the local part of the lattice Green’s function $\sum_{\mathbf{k}} G_{\mathbf{k}\nu} = g_\nu$ to determine the fermionic hybridization function Δ_ν of the impurity problem. We find that in our case, the phase transition occurs at much smaller values of the local Coulomb interaction $U \simeq 1.7$ compared to the DMFT result [86]. The same trend and qualitatively similar results were previously reported for cluster DMFT [86] and second-order DF [87] calculations. Surprisingly, the elimination of one fermion-boson vertex in diagrams (10), as originally proposed in the TRILEX approach [42–44], drastically changes the metal-to-Mott-insulator transition point and shifts it to a larger value of the local Coulomb interaction compared even to the DMFT result [43]. This can be attributed to the fact that the fermion-boson vertex at low frequencies considerably deviates from unity in the strongly interacting regime as shown in Fig. 1.

IV. CONCLUSIONS

To conclude, the derived fermion-boson theory is a powerful tool for description of many-body effects beyond the dynamical mean-field level. The main advantage is that the method does not suffer from the Fierz ambiguity problem, which is present in all partially bosonized theories. The TRILEX² approximation of the theory combines a simplicity of mean-field and GW -like diagrammatic descriptions of collective excitations with a high performance of the method comparable to much more elaborate approaches. A rigorous account for spin fluctuations in this approach provides an opportunity for a solution of a challenging problem of realistic magnetic GW -based calculations [69,70]. Finally, it is worth noting that the derived formalism is not restricted only to diagrams for the self-energy and polarization operator introduced in Eq. (10), respectively. The effective fermion-boson action (9) also allows for a more advanced solution of the problem using, for example, functional renormalization group (fRG) [88–93], parquet [94–97], or diagrammatic Monte Carlo [62,63] methods.

ACKNOWLEDGMENTS

The authors thank F. Krien and S. Brener for valuable comments on the work. The authors also thank M. Katsnelson and A. Rubtsov for inspiring discussions and long-term

collaboration. The work of E.A.S. was supported by the Russian Science Foundation, Grant No. 17-72-20041. This work was partially supported by the Cluster of Excellence ‘‘Advanced Imaging of Matter’’ of the Deutsche Forschungsgemeinschaft (DFG)-EXC 2056- Project No. ID390715994, and by North-German Supercomputing Alliance (HLRN) under the Project No. hhp00042.

APPENDIX A: APPROXIMATION FOR THE FERMION-FERMION VERTEX

In this Appendix we derive an approximation for the full local fermion-fermion vertex. We start with the expression (6) for the bare vertex $\Gamma_{\nu\nu'\omega}^{0\zeta}$ of the impurity problem (5). Using the exact relation between charge and spin components of the bare Coulomb interaction we find that the expression for this bare vertex does not depend on the performed decoupling of the local Coulomb interaction and contains the contribution of the full U in all considered channels. This result is in agreement with the fact that the bare interaction in the Bethe-Salpeter equation for the susceptibility is given by the full local Coulomb interaction [77]. In order to find the origin of the reducible contribution with respect to a bosonic line (hereinafter, we will call this contribution w reducible) to the fermion-fermion vertex, let us dress the bare vertex in the corresponding ‘‘horizontal’’ particle-hole channel as

$$\bar{\Gamma}_{\nu\nu'\omega}^{\zeta} = \sum_{\nu'',\nu'''} \Gamma_{\nu\nu''\omega}^{0\zeta} \chi_{\nu''\nu'''\omega}^{\zeta} \Gamma_{\nu'''\nu'\omega}^{0\zeta}, \quad (\text{A1})$$

where

$$\chi_{\nu\nu'\omega}^{\zeta} = -\left((c_{\nu+\omega,\sigma_1}^* \sigma_{\sigma_1\sigma_2}^{\zeta} c_{\nu,\sigma_2}) (c_{\nu'\sigma_3}^* \sigma_{\sigma_3\sigma_4}^{\zeta} c_{\nu'+\omega,\sigma_4}) \right)_{\text{conn}} \quad (\text{A2})$$

is a generalized susceptibility of the impurity problem in a corresponding channel. After the antisymmetrization, this screened vertex (A1) together with the bare vertex $\Gamma_{\nu\nu'\omega}^{0\zeta}$ makes up the simplest approximation for the fermion-fermion vertex function of the impurity problem

$$\begin{aligned} \Gamma_{\nu\nu'\omega}^c &\simeq \Gamma_{\nu\nu'\omega}^{0c} + \frac{1}{2}\bar{\Gamma}_{\nu\nu'\omega}^c - \frac{1}{4}\bar{\Gamma}_{\nu,\nu+\omega,\nu'-\nu}^c - \frac{3}{4}\bar{\Gamma}_{\nu,\nu+\omega,\nu'-\nu}^s, \\ \Gamma_{\nu\nu'\omega}^s &\simeq \Gamma_{\nu\nu'\omega}^{0s} + \frac{1}{2}\bar{\Gamma}_{\nu\nu'\omega}^s + \frac{1}{4}\bar{\Gamma}_{\nu,\nu+\omega,\nu'-\nu}^s - \frac{1}{4}\bar{\Gamma}_{\nu,\nu+\omega,\nu'-\nu}^c. \end{aligned} \quad (\text{A3})$$

Since the bare vertex function does not depend on the decoupling, this approximation is valid for any decomposition of the local Coulomb interaction. In the absence of bosonic hybridizations $Y^{\zeta} = 0$, the bare fermion-fermion vertex can be simply replaced by the bare Coulomb interaction $\Gamma_{\nu\nu'\omega}^{0c/s} = \pm U$ as derived above. Then, the generalized susceptibility (A2) in the expression for the screened vertex (A1) reduces to a bosonic susceptibility χ_{ω}^{ζ} , and the approximation for the full fermion-fermion vertex takes the following simple form:

$$\begin{aligned} \Gamma_{\nu\nu'\omega}^c &\simeq U + \frac{1}{2}U\chi_{\omega}^c U - \frac{1}{4}U\chi_{\nu'-\nu}^c U - \frac{3}{4}U\chi_{\nu'-\nu}^s U, \\ \Gamma_{\nu\nu'\omega}^s &\simeq -U + \frac{1}{2}U\chi_{\omega}^s U + \frac{1}{4}U\chi_{\nu'-\nu}^s U - \frac{1}{4}U\chi_{\nu'-\nu}^c U. \end{aligned} \quad (\text{A4})$$

This approximation fully coincides with the approximation obtained in the work [75]. The only difference is that here we do not perform a bosonization of collective fluctuations in the particle-particle channel as discussed in the main text.

We also note that the susceptibility defined in our work is two times larger than the one introduced in Ref. [75].

Importantly, in the framework of the fermion-boson theory the interaction is introduced as the bosonic propagator. Thus, bare charge and spin interactions that enter the bare fermion-fermion vertex $\Gamma_{\nu\nu'\omega}^{0\zeta}$ have to be considered as ‘‘horizontal’’ $\mathcal{U}_{\omega}^{\zeta}$ and ‘‘vertical’’ bosonic $\mathcal{U}_{\nu'-\nu}^{\zeta}$ lines. In this case, a simple replacement of the bare fermion-fermion vertex by the full local Coulomb interaction is no longer possible. First, let us isolate the w -reducible contribution in the approximation for the fermion-fermion vertex (A3). If we take only horizontal (ω -dependent) terms $\mathcal{U}_{\omega}^{\zeta}$ from the bare vertex $\Gamma_{\nu\nu'\omega}^{0\zeta}$ in the expression (A1), the generalized susceptibility again reduces to the bosonic one, and the w -reducible part of the screened vertex (A1) becomes $\bar{\Gamma}_{\nu\nu'\omega}^{\zeta} = 4\mathcal{U}_{\omega}^{\zeta} \chi_{\omega}^{\zeta} \mathcal{U}_{\omega}^{\zeta}$. Other w -reducible terms in the screened vertex (A1) appear from w -reducible contributions to the generalized susceptibility $\chi_{\nu'\nu''\omega}^{\zeta}$. If the latter contains at least one horizontal bosonic line $\mathcal{U}_{\omega}^{\zeta}$ on which it can be cut into two separate parts, the bare vertex $\Gamma_{\nu\nu'\omega}^{0\zeta}$ in the expression (A1) does not necessarily have to be w reducible in order to make the total expression reducible with respect to a bosonic propagator. This leads to an additional fermion-boson vertex correction $\Lambda_{\nu\omega}^{\zeta}$ to the previously derived approximation for the screened vertex

$$\begin{aligned} \bar{\Gamma}_{\nu\nu'\omega}^{\zeta} &= 4\Lambda_{\nu\omega}^{\zeta} \mathcal{U}_{\omega}^{\zeta} \chi_{\omega}^{\zeta} \mathcal{U}_{\omega}^{\zeta} \Lambda_{\nu'+\omega,-\omega}^{\zeta} \\ &\quad + 2\Lambda_{\nu\omega}^{\zeta} \mathcal{U}_{\omega}^{\zeta} \Lambda_{\nu'+\omega,-\omega}^{\zeta} - 2\mathcal{U}_{\omega}^{\zeta}. \end{aligned} \quad (\text{A5})$$

The term $2\mathcal{U}_{\omega}^{\zeta}$ is already contained in the bare vertex $\Gamma_{\nu\nu'\omega}^{0\zeta}$ and introduced here to simplify the expression. We note that Eq. (A3) is only an approximation for the exact charge and spin fermion-fermion vertex functions. The exact w -reducible contribution to the screened fermion-fermion vertex (A1) is given by the expression

$$\bar{\Gamma}_{\nu\nu'\omega}^{\zeta} = 4\Lambda_{\nu\omega}^{\zeta} w_{\omega}^{\zeta} \Lambda_{\nu'+\omega,-\omega}^{\zeta} - 4\mathcal{U}_{\omega}^{\zeta}, \quad (\text{A6})$$

where $w_{\omega}^{\zeta} = \mathcal{U}_{\omega}^{\zeta} + \mathcal{U}_{\omega}^{\zeta} \chi_{\omega}^{\zeta} \mathcal{U}_{\omega}^{\zeta}$ is the full renormalized interaction of the impurity problem, and $\Lambda_{\nu\omega}^{\zeta}$ is the exact fermion-boson vertex of the problem. Here, the term $4\mathcal{U}_{\omega}^{\zeta}$ is again excluded from the expression since it is already contained in the (nonsymmetrized) bare interaction.

The remaining part of the generalized susceptibility in the expression (A3) for the screened vertex is irreducible with respect to the bosonic propagator. Together with vertical lines $\mathcal{U}_{\nu'-\nu}^{\zeta}$ from the bare fermion-fermion vertex $\Gamma_{\nu\nu'\omega}^{0\zeta}$ it makes the w -irreducible contribution to the full fermion-fermion vertex function that is not accounted for by the fermion-boson theory. As discussed in the main text, the ladderlike irreducible contributions to the fermion-fermion vertex function can be fully excluded by a proper choice of the bare interaction $U^c = -U^s = U/2$ that has the same value for all $s = \{x, y, z\}$ spin components. Since this unique form of the bare interaction cannot be obtained by any of the decoupling of the local Coulomb interaction, we will make separate decouplings for every bosonic channel to keep the bare interaction in the proposed form. Then, coming back to a nonsymmetrized form of the bare fermion-fermion vertex function (6), we get $\Gamma_{\nu\nu'\omega}^{0\zeta} = 2\mathcal{U}_{\omega}^{\zeta} + 2Y_{\omega}^{\zeta}$. Together with the screened interaction $\bar{\Gamma}_{\nu\nu'\omega}^{\zeta}$ from (A6), which is also written

in the antisymmetrized form, it makes the total approximation for the nonsymmetrized full fermion-fermion vertex function

$$\frac{1}{8}\Gamma_{\nu\nu'\omega}^{\zeta} \simeq \frac{1}{2}M_{\nu\nu'\omega}^{\zeta} = \frac{1}{2}(\Lambda_{\nu\omega}^{\zeta} w_{\omega}^{\zeta} \Lambda_{\nu'+\omega,-\omega}^{\zeta} - U^{\zeta}/2). \quad (\text{A7})$$

The term $U^{\zeta}/2$ appears here because we use separate mutually exclusive decouplings of the bare Coulomb interaction in different bosonic channels. This term avoids the double counting of the bare Coulomb interaction in the bare vertex $\Gamma_{\nu\nu'\omega}^0$. Note that the same procedure can be performed for the Ising form of the bare interaction $U^c = -U^z = U/2$ and $U^x = U^y = 0$. Since this form of decoupling is identical for all channels, this does not lead to a double counting of the local Coulomb interaction. Then, the approximation for the fermion-fermion vertex in the antisymmetrized form is given by the expression $M_{\nu\nu'\omega}^{\zeta} = \Lambda_{\nu\omega}^{\zeta} w_{\omega}^{\zeta} \Lambda_{\nu'+\omega,-\omega}^{\zeta}$.

The final expression for the w -reducible approximation of the full fermion-fermion vertex function can be obtained after

antisymmetrizing the expression (A7):

$$\begin{aligned} \Gamma_{\nu\nu'\omega}^c &= 2M_{\nu\nu'\omega}^c - M_{\nu,\nu+\omega,\nu'-\nu}^c - 3M_{\nu,\nu+\omega,\nu'-\nu}^s, \\ \Gamma_{\nu\nu'\omega}^s &= 2M_{\nu\nu'\omega}^s + M_{\nu,\nu+\omega,\nu'-\nu}^s - M_{\nu,\nu+\omega,\nu'-\nu}^c. \end{aligned} \quad (\text{A8})$$

Note that the w -reducible interaction (A7), which is introduced to exclude the exact fermion-fermion vertex from the action, does not have a uniform structure due to a presence of the $-U^{\zeta}/2$ term that does not contain fermion-boson vertex functions. Therefore, the correction $M_{\nu\nu'\omega}^{\zeta}$ cannot be easily generated performing transformations of the lattice action discussed below. Thus, we make a small additional approximation for the w -reducible fermion-fermion vertex $M_{\nu\nu'\omega}^{\zeta} \simeq \Lambda_{\nu\omega}^{\zeta} \bar{w}_{\omega}^{\zeta} \Lambda_{\nu'+\omega,-\omega}^{\zeta}$ including the $U^{\zeta}/2$ term in the propagator $\bar{w}_{\omega}^{\zeta} = w_{\omega}^{\zeta} - U^{\zeta}/2$. After that, the exact (A6) expression for the reducible contribution to the fermion-fermion vertex function coincides with the approximate one derived in Eq. (A5). In addition, the last approximation can be motivated by the asymptotic behavior of the fermion-boson vertex function $\Lambda_{\nu\omega} \rightarrow 1$ at large frequencies.

APPENDIX B: DERIVATION OF THE EFFECTIVE FERMION-BOSON PROBLEM

In this Appendix we derive an effective fermion-boson problem. We start with two Hubbard-Stratonovich transformations of the nonlocal part of the lattice action of the extended Hubbard model (1):

$$\begin{aligned} & \exp \left\{ \sum_{\mathbf{k},\nu,\sigma} c_{\mathbf{k}\nu\sigma}^* [\Delta_{\nu\sigma} - \varepsilon_{\mathbf{k}}] c_{\mathbf{k}\nu\sigma} \right\} \\ &= D_f \int D[f^*, f] \exp \left\{ - \sum_{\mathbf{k},\nu,\sigma} (f_{\mathbf{k}\nu\sigma}^* g_{\nu\sigma}^{-1} [\Delta_{\nu\sigma} - \varepsilon_{\mathbf{k}}]^{-1} g_{\nu\sigma}^{-1} f_{\mathbf{k}\nu\sigma} + c_{\mathbf{k}\nu\sigma}^* g_{\nu\sigma}^{-1} f_{\mathbf{k}\nu\sigma} + f_{\mathbf{k}\nu\sigma}^* g_{\nu\sigma}^{-1} c_{\mathbf{k}\nu\sigma}) \right\}, \\ & \exp \left\{ \sum_{\mathbf{q},\omega,\zeta} \frac{1}{2} \rho_{\mathbf{q}\omega}^{\zeta} [Y_{\omega}^{\zeta} - V_{\mathbf{q}}^{\zeta}] \rho_{-\mathbf{q},-\omega}^{\zeta} \right\} \\ &= D_{\varphi} \int D[\phi^{\zeta}] \exp \left\{ - \sum_{\mathbf{q},\omega,\zeta} \left(\frac{1}{2} \varphi_{\mathbf{q}\omega}^{\zeta} \alpha_{\omega}^{\zeta -1} [Y_{\omega}^{\zeta} - V_{\mathbf{q}}^{\zeta}]^{-1} \alpha_{\omega}^{\zeta -1} \varphi_{-\mathbf{q},-\omega}^{\zeta} + \varphi_{\mathbf{q}\omega}^{\zeta} \alpha_{\omega}^{\zeta -1} \rho_{-\mathbf{q},-\omega}^{\zeta} \right) \right\}, \end{aligned} \quad (\text{B1})$$

where terms $D_f = \det[g_{\nu}(\Delta_{\nu\sigma} - \varepsilon_{\mathbf{k}})g_{\nu}]$ and $D_{\varphi}^{-1} = \sqrt{\det[\alpha_{\omega}^{\zeta}(Y_{\omega}^{\zeta} - V_{\mathbf{q}}^{\zeta})\alpha_{\omega}^{\zeta}]}$ can be neglected when calculating expectation values. Here, g_{ν} is the full local Green's function of the impurity problem. $\mathcal{U}_{\omega}^{\zeta} = U^{\zeta} + Y_{\omega}^{\zeta}$, and w_{ω}^{ζ} are the bare and renormalized interactions of the local impurity interaction in the corresponding bosonic channel. Factors g_{ν} and $\alpha_{\omega}^{\zeta} = w_{\omega}^{\zeta}/\mathcal{U}_{\omega}^{\zeta}$ in the Hubbard-Stratonovich transformations are introduced for the special reason to express the interaction part of the transformed action in terms of full local vertex function of the impurity problem [61]. After these transformations, the action takes the following form:

$$\begin{aligned} S' &= \sum_i S_{\text{imp}}^{(i)} + \sum_{\mathbf{k},\nu,\sigma} [c_{\mathbf{k}\nu\sigma}^* g_{\nu\sigma}^{-1} f_{\mathbf{k}\nu\sigma} + f_{\mathbf{k}\nu\sigma}^* g_{\nu\sigma}^{-1} c_{\mathbf{k}\nu\sigma}] + \sum_{\mathbf{q},\omega,\zeta} \varphi_{\mathbf{q}\omega}^{\zeta} \alpha_{\omega}^{\zeta -1} \rho_{-\mathbf{q},-\omega}^{\zeta} \\ & - \sum_{\mathbf{k},\nu,\sigma} f_{\mathbf{k}\nu\sigma}^* g_{\nu\sigma}^{-1} [\varepsilon_{\mathbf{k}} - \Delta_{\nu\sigma}]^{-1} g_{\nu\sigma}^{-1} f_{\mathbf{k}\nu\sigma} - \frac{1}{2} \sum_{\mathbf{q},\omega,\zeta} \varphi_{\mathbf{q}\omega}^{\zeta} \alpha_{\omega}^{\zeta -1} [V_{\mathbf{q}}^{\zeta} - Y_{\omega}^{\zeta}]^{-1} \alpha_{\omega}^{\zeta -1} \varphi_{-\mathbf{q},-\omega}^{\zeta}. \end{aligned} \quad (\text{B2})$$

The above introduced transformations allow to integrate out the impurity part of the problem as

$$\begin{aligned} & \int D[c^*, c] \exp \left\{ - \sum_i S_{\text{imp}}^{(i)} - \sum_{\mathbf{k},\nu,\sigma} [c_{\mathbf{k}\nu\sigma}^* g_{\nu\sigma}^{-1} f_{\mathbf{k}\nu\sigma} + f_{\mathbf{k}\nu\sigma}^* g_{\nu\sigma}^{-1} c_{\mathbf{k}\nu\sigma}] - \sum_{\mathbf{q},\omega,\zeta} \varphi_{\mathbf{q}\omega}^{\zeta} \alpha_{\omega}^{\zeta -1} \rho_{-\mathbf{q},-\omega}^{\zeta} \right\} \\ &= \mathcal{Z}_{\text{imp}} \times \exp \left\{ - \sum_{\mathbf{k},\nu,\sigma} f_{\mathbf{k}\nu\sigma}^* g_{\nu\sigma}^{-1} f_{\mathbf{k}\nu\sigma} - \frac{1}{2} \sum_{\mathbf{q},\omega,\zeta} \varphi_{\mathbf{q}\omega}^{\zeta} \alpha_{\omega}^{\zeta -1} \chi_{\omega}^{\zeta} \alpha_{\omega}^{\zeta -1} \varphi_{-\mathbf{q},-\omega}^{\zeta} - \tilde{\mathcal{F}}[f, \varphi] \right\}, \end{aligned} \quad (\text{B3})$$

where \mathcal{Z}_{imp} is a partition function of the impurity problem. Here, the interaction part of the action $\tilde{\mathcal{F}}[f, \varphi]$ contains an infinite series of full vertex functions of impurity problem as discussed in [59,60]. The lowest-order interaction terms are

$$\tilde{\mathcal{F}}[f, \varphi] \simeq \sum_{\mathbf{k}, \mathbf{k}', \mathbf{q}} \sum_{v, v', \omega} \sum_{\zeta, \sigma(\zeta')} \left(\Lambda_{v\omega}^{\zeta} f_{\mathbf{k}v\sigma}^* f_{\mathbf{k}+\mathbf{q}, v+\omega, \sigma'} \varphi_{-\mathbf{q}, -\omega}^{\zeta} + \frac{1}{4} \Gamma_{vv'\omega}^{\sigma\sigma'\sigma''\sigma'''} f_{\mathbf{k}v\sigma}^* f_{\mathbf{k}+\mathbf{q}, v+\omega, \sigma'} f_{\mathbf{k}'+\mathbf{q}, v'+\omega, \sigma''} f_{\mathbf{k}'v'\sigma'''}^* \right), \quad (\text{B4})$$

where the fermion-fermion and fermion-boson vertices have the following form:

$$\Gamma_{vv'\omega} = \frac{\langle c_{v\sigma} c_{v+\omega, \sigma'}^* c_{v'\sigma''}^* c_{v'+\omega, \sigma'''} \rangle_{\text{c imp}}}{g_{v\sigma} g_{v+\omega, \sigma'} g_{v'+\omega, \sigma''} g_{v'\sigma'''}} , \quad \Lambda_{v\omega}^{\zeta} = \frac{\langle c_{v\sigma} c_{v+\omega, \sigma'}^* \rho_{\omega}^{\zeta} \rangle_{\text{imp}}}{g_{v\sigma} g_{v+\omega, \sigma'} \alpha_{\omega}^{\zeta}} . \quad (\text{B5})$$

Then, the initial lattice problem transforms to the following *dual* action:

$$\tilde{\mathcal{S}} = - \sum_{\mathbf{k}, v, \sigma} f_{\mathbf{k}v\sigma}^* \tilde{\mathcal{G}}_{\mathbf{k}v\sigma}^{-1} f_{\mathbf{k}v\sigma} - \frac{1}{2} \sum_{\mathbf{q}, \omega, \zeta} \varphi_{\mathbf{q}\omega}^{\zeta} \tilde{\mathcal{W}}_{\mathbf{q}\omega}^{\zeta -1} \varphi_{-\mathbf{q}, -\omega}^{\zeta} + \tilde{\mathcal{F}}[f, \varphi]. \quad (\text{B6})$$

Here, bare propagators $\tilde{\mathcal{G}}_{\mathbf{k}v\sigma} = G_{\mathbf{k}v\sigma}^{\text{EDMFT}} - g_{v\omega}$ and $\tilde{\mathcal{W}}_{\mathbf{q}\omega}^{\zeta} = W_{\mathbf{q}\omega}^{\zeta \text{EDMFT}} - w_{\omega}^{\zeta}$ are nonlocal parts of the Green's function $G_{\mathbf{k}v\sigma}^{\text{EDMFT}}$ and renormalized interaction $W_{\mathbf{q}\omega}^{\zeta \text{EDMFT}}$ of EDMFT defined as

$$G_{\mathbf{k}v\sigma}^{\text{EDMFT} -1} = iv + \mu - \varepsilon_{\mathbf{k}} - \Sigma_{v\sigma}^{\text{imp}} , \quad W_{\mathbf{q}\omega}^{\zeta \text{EDMFT} -1} = (U^{\zeta} + V_{\mathbf{q}}^{\zeta})^{-1} - \Pi_{\omega}^{\zeta \text{imp}} . \quad (\text{B7})$$

Here, g_v and w_{ω}^{ζ} are the full local impurity Green's function and renormalized interaction of the impurity problem

$$g_{v\sigma}^{-1} = iv + \mu - \Delta_v - \Sigma_{v\sigma}^{\text{imp}} , \quad w_{\omega}^{\zeta -1} = (U^{\zeta} + Y_{\omega}^{\zeta})^{-1} - \Pi_{\omega}^{\zeta \text{imp}} . \quad (\text{B8})$$

The second transformation of bosonic variables that excludes the fermion-fermion vertex function from the dual action can be performed as follows. Let us add and subtract the term $\frac{1}{2} \sum_{\mathbf{q}, \omega, \zeta} \varphi_{\mathbf{q}\omega}^{\zeta} \bar{w}_{\omega}^{\zeta -1} \varphi_{-\mathbf{q}, -\omega}^{\zeta}$ in the dual action

$$\begin{aligned} \tilde{\mathcal{S}} = & - \sum_{\mathbf{k}, v, \sigma} f_{\mathbf{k}v\sigma}^* \tilde{\mathcal{G}}_{\mathbf{k}v\sigma}^{-1} f_{\mathbf{k}v\sigma} + \frac{1}{2} \sum_{\mathbf{q}, \omega, \zeta} \varphi_{\mathbf{q}\omega}^{\zeta} \bar{w}_{\omega}^{\zeta -1} \varphi_{-\mathbf{q}, -\omega}^{\zeta} + \tilde{\mathcal{F}}[f, \varphi] \\ & - \frac{1}{2} \sum_{\mathbf{q}, \omega, \zeta} \varphi_{\mathbf{q}\omega}^{\zeta} \alpha_{\omega}^{\zeta -1} \{ [V_{\mathbf{q}}^{\zeta} - Y_{\omega}^{\zeta}]^{-1} - \chi_{\omega}^{\zeta} + \alpha_{\omega}^{\zeta} \bar{w}_{\omega}^{\zeta -1} \alpha_{\omega}^{\zeta} \} \alpha_{\omega}^{\zeta -1} \varphi_{-\mathbf{q}, -\omega}^{\zeta} . \end{aligned} \quad (\text{B9})$$

Then, we can perform the following Hubbard-Stratonovich transformation:

$$\begin{aligned} & \exp \left\{ \frac{1}{2} \sum_{\mathbf{q}, \omega, \zeta} \varphi_{\mathbf{q}\omega}^{\zeta} \alpha_{\omega}^{\zeta -1} \{ [V_{\mathbf{q}}^{\zeta} - Y_{\omega}^{\zeta}]^{-1} - \chi_{\omega}^{\zeta} + \alpha_{\omega}^{\zeta} \bar{w}_{\omega}^{\zeta -1} \alpha_{\omega}^{\zeta} \} \alpha_{\omega}^{\zeta -1} \varphi_{-\mathbf{q}, -\omega}^{\zeta} \right\} \\ & = D_b \int D[b^{\zeta}] \exp \left\{ - \sum_{\mathbf{q}, \omega, \zeta} \left(\frac{1}{2} b_{\mathbf{q}\omega}^{\zeta} \bar{w}_{\omega}^{-1} \alpha_{\omega}^{\zeta} \{ [V_{\mathbf{q}}^{\zeta} - Y_{\omega}^{\zeta}]^{-1} - \chi_{\omega}^{\zeta} + \alpha_{\omega}^{\zeta} \bar{w}_{\omega}^{\zeta -1} \alpha_{\omega}^{\zeta} \}^{-1} \alpha_{\omega}^{\zeta} \bar{w}_{\omega}^{-1} b_{-\mathbf{q}, -\omega}^{\zeta} - \varphi_{\mathbf{q}\omega}^{\zeta} \bar{w}_{\omega}^{-1} b_{-\mathbf{q}, -\omega}^{\zeta} \right) \right\} . \end{aligned} \quad (\text{B10})$$

The action transforms to

$$\begin{aligned} \tilde{\mathcal{S}}' = & - \sum_{\mathbf{k}, v, \sigma} f_{\mathbf{k}v\sigma}^* \tilde{\mathcal{G}}_{\mathbf{k}v\sigma}^{-1} f_{\mathbf{k}v\sigma} + \frac{1}{2} \sum_{\mathbf{q}, \omega, \zeta} b_{\mathbf{q}\omega}^{\zeta} \bar{w}_{\omega}^{-1} \alpha_{\omega}^{\zeta} \{ [V_{\mathbf{q}}^{\zeta} - Y_{\omega}^{\zeta}]^{-1} - \chi_{\omega}^{\zeta} + \alpha_{\omega}^{\zeta} \bar{w}_{\omega}^{\zeta -1} \alpha_{\omega}^{\zeta} \}^{-1} \alpha_{\omega}^{\zeta} \bar{w}_{\omega}^{-1} b_{-\mathbf{q}, -\omega}^{\zeta} \\ & + \frac{1}{2} \sum_{\mathbf{q}, \omega, \zeta} \varphi_{\mathbf{q}\omega}^{\zeta} \bar{w}_{\omega}^{\zeta -1} \varphi_{-\mathbf{q}, -\omega}^{\zeta} - \sum_{\mathbf{q}, \omega, \zeta} \varphi_{\mathbf{q}\omega}^{\zeta} \bar{w}_{\omega}^{-1} b_{-\mathbf{q}, -\omega}^{\zeta} + \tilde{\mathcal{F}}[f, \varphi]. \end{aligned} \quad (\text{B11})$$

Finally, bosonic fields φ^ζ can be integrated out with respect to the Gaussian bosonic part of the dual action as

$$\begin{aligned} \int D[\varphi^\zeta] \exp \left\{ -\frac{1}{2} \sum_{\mathbf{q}, \omega, \zeta} \varphi_{\mathbf{q}\omega}^\zeta \bar{w}_\omega^{\zeta-1} \varphi_{-\mathbf{q}, -\omega}^\zeta + \sum_{\mathbf{q}, \omega, \zeta} \varphi_{\mathbf{q}\omega}^\zeta \bar{w}_\omega^{\zeta-1} b_{-\mathbf{q}, -\omega}^\zeta - \tilde{\mathcal{F}}[f, \varphi] \right\} \\ = \mathcal{Z}_\varphi \times \exp \left\{ \frac{1}{2} \sum_{\mathbf{q}, \omega, \zeta} b_{\mathbf{q}\omega}^\zeta \bar{w}_\omega^{\zeta-1} b_{-\mathbf{q}, -\omega}^\zeta - \mathcal{F}[f, b] \right\}, \end{aligned} \quad (\text{B12})$$

where \mathcal{Z}_φ is a partition function of the Gaussian part of the bosonic action. The integration of dual bosonic fields modifies the interaction that now has the following form:

$$\begin{aligned} \mathcal{F}[f, b] = \sum_{\mathbf{k}, \mathbf{q}} \sum_{v, \omega} \sum_{\zeta, \sigma, \sigma'} \Lambda_{v\omega}^\zeta f_{\mathbf{k}v\sigma}^* \sigma_{\sigma\sigma'}^\zeta f_{\mathbf{k}+\mathbf{q}, v+\omega, \sigma'} b_{-\mathbf{q}, -\omega}^\zeta \\ + \frac{1}{8} \sum_{\mathbf{k}, \mathbf{k}', \mathbf{q}} \sum_{v, v', \omega} \sum_{\zeta, \sigma(\ell)} (\Gamma_{vv'\omega}^\zeta - 4M_{vv'\omega}^\zeta) f_{\mathbf{k}v\sigma}^* \sigma_{\sigma\sigma'}^\zeta f_{\mathbf{k}+\mathbf{q}, v+\omega, \sigma'} f_{\mathbf{k}'+\mathbf{q}, v'+\omega, \sigma''}^* \sigma_{\sigma''\sigma'''}^\zeta f_{\mathbf{k}'v'\sigma'''} \end{aligned} \quad (\text{B13})$$

The $4M_{vv'\omega}^\zeta$ term that was introduced in (A7) is exactly the approximation that excludes the full fermion-fermion vertex $\Gamma_{vv'\omega}^\zeta$. After collecting and simplifying all terms, the action (B11) takes a very compact form

$$\mathcal{S}_{f-b} = - \sum_{\mathbf{k}, v, \sigma} f_{\mathbf{k}v\sigma}^* \tilde{\mathcal{G}}_{\mathbf{k}v\sigma}^{-1} f_{\mathbf{k}v\sigma} - \frac{1}{2} \sum_{\mathbf{q}, \omega, \zeta} b_{\mathbf{q}\omega}^\zeta \mathcal{W}_{\mathbf{q}\omega}^{\zeta-1} b_{-\mathbf{q}, -\omega}^\zeta + \sum_{\mathbf{k}, \mathbf{q}} \sum_{v, \omega} \sum_{\zeta, \sigma, \sigma'} \Lambda_{v\omega}^\zeta f_{\mathbf{k}v\sigma}^* \sigma_{\sigma\sigma'}^\zeta f_{\mathbf{k}+\mathbf{q}, v+\omega, \sigma'} b_{-\mathbf{q}, -\omega}^\zeta, \quad (\text{B14})$$

where the bare bosonic propagator is equal to $\mathcal{W}_{\mathbf{q}\omega}^\zeta = \tilde{\mathcal{W}}_{\mathbf{q}\omega}^\zeta + \bar{w}_\omega^{\zeta-1}$, which can also be rewritten as $\mathcal{W}_{\mathbf{q}\omega}^\zeta = W_{\mathbf{q}\omega}^{\zeta \text{EDMFT}} - U^\zeta/2$ for our choice $U^{c/s} = \pm U/2$ of the bare interaction. Since for the Ising decoupling $\bar{w}_\omega^\zeta = w_\omega^\zeta$, the bare bosonic propagator coincides with the renormalized interaction of EDMFT $\mathcal{W}_{\mathbf{q}\omega}^\zeta = W_{\mathbf{q}\omega}^{\zeta \text{EDMFT}}$.

Remarkably, for our unique choice of the bare interaction U^ζ the renormalized interaction of EDMFT can be identically rewritten in the form using in FLEX approach [71,98]

$$W_{\mathbf{q}\omega}^{\zeta \text{EDMFT}} = \frac{1}{2} \hat{U}_{\mathbf{q}}^\zeta [1 - \hat{\Pi}_\omega^{\zeta \text{imp}} \hat{U}_{\mathbf{q}}^\zeta]^{-1}, \quad (\text{B15})$$

where $\hat{U}_{\mathbf{q}}^{c/s} = \pm U + 2V_{\mathbf{q}}^{c/s}$ and $\hat{\Pi}_\omega^{\zeta \text{imp}} = \Pi_\omega^{\zeta \text{imp}}/2$ are the bare interaction and local polarization operator in FLEX notations. Thus, the introduced theory can be seen as an efficient combination of FLEX approach for local degrees of freedom with *GW*-like description of nonlocal fluctuations beyond the EDMFT level and additionally accounts for the fermion-boson vertex corrections.

-
- [1] E. Fradkin, *Field Theories of Condensed Matter Systems* (Westview Press, Oxford, 1997).
- [2] D. Sénéchal, A. M. Tremblay, and C. Bourbonnais, *Theoretical Methods for Strongly Correlated Electrons* (Springer, New York, 2006).
- [3] E. Dagotto, Correlated electrons in high-temperature superconductors, *Rev. Mod. Phys.* **66**, 763 (1994).
- [4] G. Kotliar and J. Liu, Superexchange mechanism and d-wave superconductivity, *Phys. Rev. B* **38**, 5142 (1988).
- [5] Y. Nambu and G. Jona-Lasinio, Dynamical Model of Elementary Particles Based on an Analogy with Superconductivity. I, *Phys. Rev.* **122**, 345 (1961).
- [6] Y. Nambu and G. Jona-Lasinio, Dynamical model of elementary particles based on an analogy with superconductivity. II, *Phys. Rev.* **124**, 246 (1961).
- [7] D. Bailin and A. Love, Superfluidity and superconductivity in relativistic fermion systems, *Phys. Rep.* **107**, 325 (1984).
- [8] M. Alford, K. Rajagopal, and F. Wilczek, QCD at finite baryon density: nucleon droplets and color superconductivity, *Phys. Lett. B* **422**, 247 (1998).
- [9] J. Berges and K. Rajagopal, Color superconductivity and chiral symmetry restoration at non-zero baryon density and temperature, *Nucl. Phys. B* **538**, 215 (1999).
- [10] M. Alford, K. Rajagopal, and F. Wilczek, Color-flavor locking and chiral symmetry breaking in high density QCD, *Nucl. Phys. B* **537**, 443 (1999).
- [11] T. Schäfer and F. Wilczek, Continuity of Quark and Hadron Matter, *Phys. Rev. Lett.* **82**, 3956 (1999).
- [12] D. J. Gross and A. Neveu, Dynamical symmetry breaking in asymptotically free field theories, *Phys. Rev. D* **10**, 3235 (1974).
- [13] V. C. Zhukovsky and E. A. Stepanov, Effective (2+1)-dimensional field theory of fermions: Fermion mass generation with Kaluza-Klein fermions and gauge field, *Phys. Lett. B* **718**, 597 (2012).
- [14] J. Jaeckel and C. Wetterich, Flow equations without mean field ambiguity, *Phys. Rev. D* **68**, 025020 (2003).
- [15] T. Baier, E. Bick, and C. Wetterich, Temperature dependence of antiferromagnetic order in the Hubbard model, *Phys. Rev. B* **70**, 125111 (2004).
- [16] J. Jaeckel, Understanding the fierz ambiguity of partially bosonized theories, [arXiv:hep-ph/0205154](https://arxiv.org/abs/hep-ph/0205154).
- [17] L. Hedin, New method for calculating the one-particle green's function with application to the electron-gas problem, *Phys. Rev.* **139**, A796 (1965).
- [18] F. Aryasetiawan and O. Gunnarsson, The *GW* method, *Rep. Prog. Phys.* **61**, 237 (1998).

- [19] L. Hedin, On correlation effects in electron spectroscopies and the *GW* approximation, *J. Phys.: Condens. Matter* **11**, R489 (1999).
- [20] A. Georges, G. Kotliar, W. Krauth, and M. J. Rozenberg, Dynamical mean-field theory of strongly correlated fermion systems and the limit of infinite dimensions, *Rev. Mod. Phys.* **68**, 13 (1996).
- [21] A. M. Sengupta and A. Georges, Non-Fermi-liquid behavior near a $T=0$ spin-glass transition, *Phys. Rev. B* **52**, 10295 (1995).
- [22] Q. Si and J. L. Smith, Kosterlitz-Thouless Transition and Short Range Spatial Correlations in an Extended Hubbard Model, *Phys. Rev. Lett.* **77**, 3391 (1996).
- [23] J. L. Smith and Q. Si, Spatial correlations in dynamical mean-field theory, *Phys. Rev. B* **61**, 5184 (2000).
- [24] R. Chitra and G. Kotliar, Effect of Long Range Coulomb Interactions on the Mott Transition, *Phys. Rev. Lett.* **84**, 3678 (2000).
- [25] R. Chitra and G. Kotliar, Effective-action approach to strongly correlated fermion systems, *Phys. Rev. B* **63**, 115110 (2001).
- [26] W. Metzner and D. Vollhardt, Correlated Lattice Fermions in $d = \infty$ Dimensions, *Phys. Rev. Lett.* **62**, 324 (1989).
- [27] J. Gukelberger, L. Huang, and P. Werner, On the dangers of partial diagrammatic summations: Benchmarks for the two-dimensional hubbard model in the weak-coupling regime, *Phys. Rev. B* **91**, 235114 (2015).
- [28] G. Rohringer, H. Hafermann, A. Toschi, A. A. Katanin, A. E. Antipov, M. I. Katsnelson, A. I. Lichtenstein, A. N. Rubtsov, and K. Held, Diagrammatic routes to nonlocal correlations beyond dynamical mean field theory, *Rev. Mod. Phys.* **90**, 025003 (2018).
- [29] H. Park, K. Haule, and G. Kotliar, Magnetic Excitation Spectra in BaFe_2As_2 : A Two-Particle Approach within a Combination of the Density Functional Theory and the Dynamical Mean-Field Theory Method, *Phys. Rev. Lett.* **107**, 137007 (2011).
- [30] L. Boehnke and F. Lechermann, Competing orders in Na_xCoO_2 from strong correlations on a two-particle level, *Phys. Rev. B* **85**, 115128 (2012).
- [31] A. Galler, P. Thunström, P. Gunacker, J. M. Tomczak, and K. Held, *Ab initio* dynamical vertex approximation, *Phys. Rev. B* **95**, 115107 (2017).
- [32] L. Boehnke, P. Werner, and F. Lechermann, Multi-orbital nature of the spin fluctuations in Sr_2RuO_4 , *Europhys. Lett.* **122**, 57001 (2018).
- [33] S. Acharya, D. Pashov, C. Weber, H. Park, L. Sponza, and M. van Schilfgaarde, Evening out the spin and charge parity to increase T_c in unconventional superconductors Sr_2RuO_4 , [arXiv:1811.05143](https://arxiv.org/abs/1811.05143).
- [34] H. U. R. Strand, M. Zingl, N. Wentzell, O. Parcollet, and A. Georges, Magnetic response of Sr_2RuO_4 : Quasi-local spin fluctuations due to Hund's coupling, *Phys. Rev. B* **100**, 125120 (2019).
- [35] P. Sun and G. Kotliar, Extended dynamical mean-field theory and *GW* method, *Phys. Rev. B* **66**, 085120 (2002).
- [36] S. Biermann, F. Aryasetiawan, and A. Georges, First-Principles Approach to the Electronic Structure of Strongly Correlated Systems: Combining the *GW* Approximation and Dynamical Mean-Field Theory, *Phys. Rev. Lett.* **90**, 086402 (2003).
- [37] T. Ayral, P. Werner, and S. Biermann, Spectral Properties of Correlated Materials: Local Vertex and Nonlocal Two-Particle Correlations from Combined *GW* and Dynamical Mean Field Theory, *Phys. Rev. Lett.* **109**, 226401 (2012).
- [38] T. Ayral, S. Biermann, and P. Werner, Screening and non-local correlations in the extended Hubbard model from self-consistent combined *GW* and dynamical mean field theory, *Phys. Rev. B* **87**, 125149 (2013).
- [39] L. Huang, T. Ayral, S. Biermann, and P. Werner, Extended dynamical mean-field study of the Hubbard model with long-range interactions, *Phys. Rev. B* **90**, 195114 (2014).
- [40] L. Boehnke, F. Nilsson, F. Aryasetiawan, and P. Werner, When strong correlations become weak: Consistent merging of *GW* and DMFT, *Phys. Rev. B* **94**, 201106(R) (2016).
- [41] T. Ayral, S. Biermann, P. Werner, and L. Boehnke, Influence of Fock exchange in combined many-body perturbation and dynamical mean field theory, *Phys. Rev. B* **95**, 245130 (2017).
- [42] T. Ayral and O. Parcollet, Mott physics and spin fluctuations: A unified framework, *Phys. Rev. B* **92**, 115109 (2015).
- [43] T. Ayral and O. Parcollet, Mott physics and spin fluctuations: A functional viewpoint, *Phys. Rev. B* **93**, 235124 (2016).
- [44] T. Ayral, J. Vučković, and O. Parcollet, Fierz Convergence Criterion: A Controlled Approach to Strongly Interacting Systems with Small Embedded Clusters, *Phys. Rev. Lett.* **119**, 166401 (2017).
- [45] A. van Roekeghem, T. Ayral, J. M. Tomczak, M. Casula, N. Xu, H. Ding, M. Ferrero, O. Parcollet, H. Jiang, and S. Biermann, Dynamical Correlations and Screened Exchange on the Experimental Bench: Spectral Properties of the Cobalt Pnictide BaCo_2As_2 , *Phys. Rev. Lett.* **113**, 266403 (2014).
- [46] J. M. Tomczak, M. Casula, T. Miyake, F. Aryasetiawan, and S. Biermann, Combined *GW* and dynamical mean-field theory: Dynamical screening effects in transition metal oxides, *Europhys. Lett.* **100**, 67001 (2012).
- [47] C. Taranto, M. Kaltak, N. Parragh, G. Sangiovanni, G. Kresse, A. Toschi, and K. Held, Comparing quasiparticle *GW*+DMFT and LDA+DMFT for the test bed material SrVO_3 , *Phys. Rev. B* **88**, 165119 (2013).
- [48] R. Sakuma, P. Werner, and F. Aryasetiawan, Electronic structure of SrVO_3 within *GW*+DMFT, *Phys. Rev. B* **88**, 235110 (2013).
- [49] J. M. Tomczak, M. Casula, T. Miyake, and S. Biermann, Asymmetry in band widening and quasiparticle lifetimes in SrVO_3 : Competition between screened exchange and local correlations from combined *GW* and dynamical mean-field theory *GW* + DMFT, *Phys. Rev. B* **90**, 165138 (2014).
- [50] H. Aoki, N. Tsuji, M. Eckstein, M. Kollar, T. Oka, and P. Werner, Nonequilibrium dynamical mean-field theory and its applications, *Rev. Mod. Phys.* **86**, 779 (2014).
- [51] D. Golež, L. Boehnke, H. U. R. Strand, M. Eckstein, and P. Werner, Nonequilibrium *GW* + EDMFT: Antiscreening and Inverted Populations from Nonlocal Correlations, *Phys. Rev. Lett.* **118**, 246402 (2017).
- [52] R. L. Stratonovich, On a method of calculating quantum distribution functions, *Sov. Phys. Dokl.* **2**, 416 (1957).
- [53] J. Hubbard, Calculation of Partition Functions, *Phys. Rev. Lett.* **3**, 77 (1959).
- [54] A. N. Rubtsov, V. V. Savkin, and A. I. Lichtenstein, Continuous-time quantum Monte Carlo method for fermions, *Phys. Rev. B* **72**, 035122 (2005).

- [55] P. Werner, A. Comanac, L. de' Medici, M. Troyer, and A. J. Millis, Continuous-Time Solver for Quantum Impurity Models, *Phys. Rev. Lett.* **97**, 076405 (2006).
- [56] P. Werner and A. J. Millis, Dynamical Screening in Correlated Electron Materials, *Phys. Rev. Lett.* **104**, 146401 (2010).
- [57] E. Gull, A. J. Millis, A. I. Lichtenstein, A. N. Rubtsov, M. Troyer, and P. Werner, Continuous-time monte carlo methods for quantum impurity models, *Rev. Mod. Phys.* **83**, 349 (2011).
- [58] A. N. Rubtsov, M. I. Katsnelson, and A. I. Lichtenstein, Dual fermion approach to nonlocal correlations in the hubbard model, *Phys. Rev. B* **77**, 033101 (2008).
- [59] A. N. Rubtsov, M. I. Katsnelson, and A. I. Lichtenstein, Dual boson approach to collective excitations in correlated fermionic systems, *Ann. Phys.* **327**, 1320 (2012).
- [60] E. A. Stepanov, E. G. C. P. van Loon, A. A. Katanin, A. I. Lichtenstein, M. I. Katsnelson, and A. N. Rubtsov, Self-consistent dual boson approach to single-particle and collective excitations in correlated systems, *Phys. Rev. B* **93**, 045107 (2016).
- [61] E. A. Stepanov, A. Huber, E. G. C. P. van Loon, A. I. Lichtenstein, and M. I. Katsnelson, From local to nonlocal correlations: The Dual Boson perspective, *Phys. Rev. B* **94**, 205110 (2016).
- [62] J. Gukelberger, E. Kozik, and H. Hafermann, Diagrammatic monte carlo approach for diagrammatic extensions of dynamical mean-field theory: Convergence analysis of the dual fermion technique, *Phys. Rev. B* **96**, 035152 (2017).
- [63] S. Isakov, A. E. Antipov, and E. Gull, Diagrammatic Monte Carlo for dual fermions, *Phys. Rev. B* **94**, 035102 (2016).
- [64] S. Isakov, H. Terletska, and E. Gull, Momentum-space cluster dual-fermion method, *Phys. Rev. B* **97**, 125114 (2018).
- [65] H. Hafermann, G. Li, A. N. Rubtsov, M. I. Katsnelson, A. I. Lichtenstein, and H. Monien, Efficient Perturbation Theory for Quantum Lattice Models, *Phys. Rev. Lett.* **102**, 206401 (2009).
- [66] F. Nilsson, L. Boehnke, P. Werner, and F. Aryasetiawan, Multi-tier self-consistent $GW + EDMFT$, *Phys. Rev. Mater.* **1**, 043803 (2017).
- [67] J. M. Tomczak, M. van Schilfgaarde, and G. Kotliar, Many-Body Effects in Iron Pnictides and Chalcogenides: Nonlocal Versus Dynamic Origin of Effective Masses, *Phys. Rev. Lett.* **109**, 237010 (2012).
- [68] K. Zantout, S. Backes, and R. Valentí, Effect of non-local correlations on the electronic structure of LiFeAs, [arXiv:1906.11853](https://arxiv.org/abs/1906.11853).
- [69] F. Aryasetiawan and S. Biermann, Generalized Hedin's Equations for Quantum Many-Body Systems with Spin-Dependent Interactions, *Phys. Rev. Lett.* **100**, 116402 (2008).
- [70] L. Sponza, P. Pisanti, A. Vishina, D. Pashov, C. Weber, M. van Schilfgaarde, S. Acharya, J. Vidal, and G. Kotliar, Self-energies in itinerant magnets: A focus on Fe and Ni, *Phys. Rev. B* **95**, 041112(R) (2017).
- [71] A. I. Lichtenstein and M. I. Katsnelson, *Ab initio* calculations of quasiparticle band structure in correlated systems: LDA++ approach, *Phys. Rev. B* **57**, 6884 (1998).
- [72] H. J. Schulz, Effective Action for Strongly Correlated Fermions from Functional Integrals, *Phys. Rev. Lett.* **65**, 2462 (1990).
- [73] C. Husemann and M. Salmhofer, Efficient parametrization of the vertex function, Ω scheme, and the t, t' hubbard model at van hove filling, *Phys. Rev. B* **79**, 195125 (2009).
- [74] S. Friederich, H. C. Krahl, and C. Wetterich, Four-point vertex in the Hubbard model and partial bosonization, *Phys. Rev. B* **81**, 235108 (2010).
- [75] O. Gunnarsson, T. Schäfer, J. P. F. LeBlanc, E. Gull, J. Merino, G. Sangiovanni, G. Rohringer, and A. Toschi, Fluctuation Diagnostics of the Electron Self-Energy: Origin of the Pseudogap Physics, *Phys. Rev. Lett.* **114**, 236402 (2015).
- [76] E. A. Stepanov, S. Brener, F. Krien, M. Harland, A. I. Lichtenstein, and M. I. Katsnelson, Effective Heisenberg Model and Exchange Interaction for Strongly Correlated Systems, *Phys. Rev. Lett.* **121**, 037204 (2018).
- [77] E. A. Stepanov, A. Huber, A. I. Lichtenstein, and M. I. Katsnelson, Effective Ising model for correlated systems with charge ordering, *Phys. Rev. B* **99**, 115124 (2019).
- [78] G. Rohringer, A. Valli, and A. Toschi, Local electronic correlation at the two-particle level, *Phys. Rev. B* **86**, 125114 (2012).
- [79] N. Wentzell, G. Li, A. Tagliavini, C. Taranto, G. Rohringer, K. Held, A. Toschi, and S. Andergassen, High-frequency asymptotics of the vertex function: diagrammatic parametrization and algorithmic implementation, [arXiv:1610.06520](https://arxiv.org/abs/1610.06520).
- [80] C.-H. Pao and N. E. Bickers, Renormalization-group acceleration of self-consistent field solutions: Two-dimensional hubbard model, *Phys. Rev. B* **49**, 1586 (1994).
- [81] F. Krien, A. Valli, and M. Capone, Single-boson exchange decomposition of the vertex function, [arXiv:1907.03581](https://arxiv.org/abs/1907.03581).
- [82] H. Hafermann, P. Werner, and E. Gull, Efficient implementation of the continuous-time hybridization expansion quantum impurity solver, *Comput. Phys. Commun.* **184**, 1280 (2013).
- [83] H. Hafermann, Self-energy and vertex functions from hybridization-expansion continuous-time quantum monte carlo for impurity models with retarded interaction, *Phys. Rev. B* **89**, 235128 (2014).
- [84] B. Bauer, L. D. Carr, H. G. Evertz, A. Feiguin, J. Freire, S. Fuchs, L. Gamper, J. Gukelberger, E. Gull, S. Guertler, A. Hehn, R. Igarashi, S. V. Isakov, D. Koop, P. N. Ma, P. Mates, H. Matsuo, O. Parcollet, G. Pawłowski, J. D. Picon *et al.*, The ALPS project release 2.0: Open source software for strongly correlated systems, *J. Stat. Mech.: Theory Exp.* (2011) P05001.
- [85] E. G. C. P. van Loon, A. I. Lichtenstein, M. I. Katsnelson, O. Parcollet, and H. Hafermann, Beyond extended dynamical mean-field theory: Dual boson approach to the two-dimensional extended Hubbard model, *Phys. Rev. B* **90**, 235135 (2014).
- [86] H. Park, K. Haule, and G. Kotliar, Cluster Dynamical Mean Field Theory of the Mott Transition, *Phys. Rev. Lett.* **101**, 186403 (2008).
- [87] E. G. C. P. van Loon, M. I. Katsnelson, and H. Hafermann, Second-order dual fermion approach to the Mott transition in the two-dimensional Hubbard model, *Phys. Rev. B* **98**, 155117 (2018).
- [88] W. Metzner, M. Salmhofer, C. Honerkamp, V. Meden, and K. Schönhammer, Functional renormalization group approach to correlated fermion systems, *Rev. Mod. Phys.* **84**, 299 (2012).
- [89] C. Platt, W. Hanke, and R. Thomale, Functional renormalization group for multi-orbital fermi surface instabilities, *Adv. Phys.* **62**, 453 (2013).
- [90] C. Taranto, S. Andergassen, J. Bauer, K. Held, A. Katanin, W. Metzner, G. Rohringer, and A. Toschi, From Infinite to Two Dimensions Through the Functional Renormalization Group, *Phys. Rev. Lett.* **112**, 196402 (2014).

- [91] N. Wentzell, C. Taranto, A. Katanin, A. Toschi, and S. Andergassen, Correlated starting points for the functional renormalization group, *Phys. Rev. B* **91**, 045120 (2015).
- [92] A. A. Katanin, Extended dynamical mean field theory combined with the two-particle irreducible functional renormalization-group approach as a tool to study strongly correlated systems, *Phys. Rev. B* **99**, 115112 (2019).
- [93] A. Tagliavini, C. Hille, F. B. Kugler, S. Andergassen, A. Toschi, and C. Honerkamp, Multiloop functional renormalization group for the two-dimensional Hubbard model: Loop convergence of the response functions, *SciPost Phys.* **6**, 9 (2019).
- [94] V. Yu. Irkhin, A. A. Katanin, and M. I. Katsnelson, Effects of van hove singularities on magnetism and superconductivity in the $t - t'$ hubbard model: A parquet approach, *Phys. Rev. B* **64**, 165107 (2001).
- [95] A. Valli, T. Schäfer, P. Thunström, G. Rohringer, S. Andergassen, G. Sangiovanni, K. Held, and A. Toschi, Dynamical vertex approximation in its parquet implementation: Application to hubbard nanorings, *Phys. Rev. B* **91**, 115115 (2015).
- [96] G. Li, N. Wentzell, P. Pudleiner, P. Thunström, and K. Held, Efficient implementation of the parquet equations: Role of the reducible vertex function and its kernel approximation, *Phys. Rev. B* **93**, 165103 (2016).
- [97] O. Gunnarsson, T. Schäfer, J. P. F. LeBlanc, J. Merino, G. Sangiovanni, G. Rohringer, and A. Toschi, Parquet decomposition calculations of the electronic self-energy, *Phys. Rev. B* **93**, 245102 (2016).
- [98] N. E. Bickers and D. J. Scalapino, Conserving approximations for strongly fluctuating electron systems. I. Formalism and calculational approach, *Ann. Phys.* **193**, 206 (1989).

5.2 Impact of partially bosonized collective fluctuations on electronic degrees of freedom

In the previous work, the D-TRILEX approach was introduced as an approximation of the DB theory. To this aim, we performed an additional Hubbard-Stratonovich transformation for the dual action and introduced a simple action of the partially bosonized dual theory (PBDT). This action can be used not only to construct diagrams for the simple D-TRILEX theory but also allows for the exact solution using diagrammatic Monte Carlo methods [128]. In this work, we investigate the validity of the D-TRILEX method in a broad range of parameters by comparing it to different methods. In addition, we compare methods with different diagrammatic structures in order to study the impact of different diagrammatic contributions on the single-particle properties of the system. To this aim, we compare the numerically exact DiagMC@DF and the ladder DF approximation, which use the full four-point impurity vertex, with the DiagMC@PBDT and D-TRILEX, where the vertex is approximated.

Since the work [128] is focused on the applicability of D-TRILEX let us consider the workflow of the method, which is illustrated in Fig. 5.1, in more detail in the following. The calculation can be divided into two main parts. In the first part, depicted in red, the reference system, which in our case is the Anderson impurity problem, is solved numerically exactly as already discussed in section 3.1 (DMFT). The solver, in the first step, takes some control parameters and computes the correlation functions from the first guess of the hybridization function. These are in turn

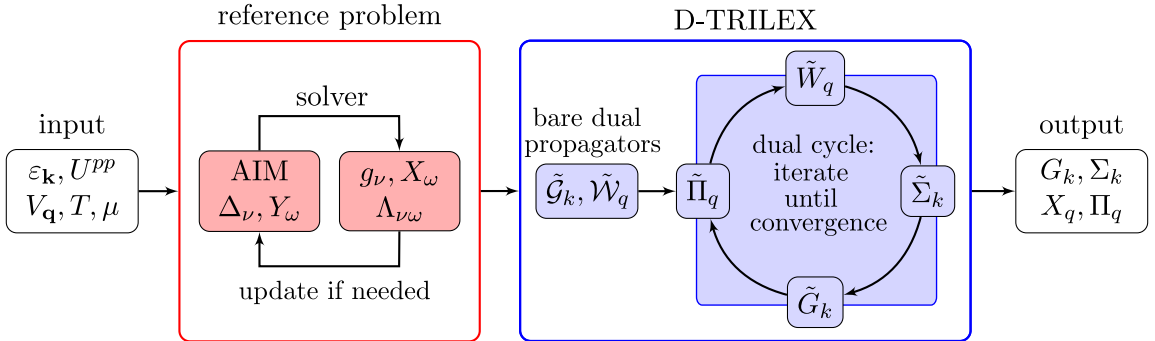


FIGURE 5.1: Schematic representation of the D-TRILEX workflow. The solver takes the control parameter of the system as an input and solves the reference problem (the Anderson impurity model in our case) self-consistently. The correlation functions are then used to contract the diagrams in D-TRILEX. The dual self-consistency cycle is performed until convergence is reached. The lattice quantities are obtained in the last step from the converged result. The figure is adapted from Ref. [73].




used to provide a new hybridization function for the solver (3.11). This procedure is repeated until the self-consistency condition is reached (3.12). Subsequently, the extracted correlation functions are used as building blocks to construct the diagrams of D-TRILEX. The second part starts with computing the bare dual propagators $\tilde{\mathcal{G}}_k$ from Eq. (3.37) and $\tilde{\mathcal{W}}_q$ from Eq. (3.80) and Eq. (3.81). Including the Green's function in Eq. (3.85) and Eq. (3.86) together with the vertex function, we obtain the dual polarization, which can be used in Eq. (3.88) to compute the renormalized interaction \tilde{W}_q . The dual self-energy is then obtained from the renormalized interaction and the bare dual Green's function using Eq. (3.84) and is used to dress the bare Green's function by means of the Dyson equation (3.87). The cycle is repeated until the result for the Green's function converges and the single- and two-particle quantities of the lattice problem are obtained from Eq. (3.57) and Eq. (3.58).

In the following study, we perform calculations for the Hubbard model on a square lattice at half-filling, where the unit of energy is determined by the nearest-neighbor hopping $t = 1$. First, we compare the self-energies obtained from different methods at different interaction strengths to investigate the impact of different diagrammatic contributions. In Table I. of [128] we summarise different forms of the four-point vertex and types of diagrams used in the considered methods. Comparing different methods we find that the irreducible part of the vertex can be safely excluded in a wide range of model parameters. Its contribution enhances in regions where AFM fluctuations increase. At weak to moderate interaction strength, the diagrams apart of the ladder remain small. At large interactions, these contributions are nearly canceled by transverse singlet fluctuations. Furthermore, we find that the longitudinal singlet bosonic modes are negligibly small for all parameters. The main finding of the analysis is that the longitudinal particle-hole bosonic modes can be considered as the main contribution for a broad range of considered parameters, which leads to the assumption that the efficient D-TRILEX method provides a promising tool for solving a broad class of interacting electronic problems.

Further, we show that D-TRILEX yields good results at weak and moderate couplings even below the DMFT Néel temperature where the AFM fluctuations become strong. However, at $U = 2$, in the Slater regime of magnetic fluctuations [170] D-TRILEX, similar to other ladder approximations, underestimates the strong magnetic fluctuations, due to their anharmonic behaviour [189] and shows a formation of the pseudo gap at a lower temperature compared to the exact result.

In addition, we apply the D-TRILEX method on the hole-doped $t - t'$ Hubbard model at $U = 5.6$, $\beta = 5$, and 4% hole-doping and compare our results to exact DiagMC results recently presented in Ref. [175]. We find that in this regime the DMFT does not provide an accurate starting point which results in a mismatch in the local part of the self-energy. On the contrary, D-TRILEX provides a reasonably accurate result for the nonlocal part of the self-energy.

Impact of partially bosonized collective fluctuations on electronic degrees of freedom

V. Harkov ^{1,2} M. Vandelli ^{1,3,4} S. Brener^{1,3} A. I. Lichtenstein^{1,2,3} and E. A. Stepanov ^{5,*}

¹*Institute of Theoretical Physics, University of Hamburg, Jungiusstrasse 9, 20355 Hamburg, Germany*

²*European X-Ray Free-Electron Laser Facility, Holzkoppel 4, 22869 Schenefeld, Germany*

³*The Hamburg Centre for Ultrafast Imaging, Luruper Chaussee 149, 22761 Hamburg, Germany*

⁴*Max Planck Institute for the Structure and Dynamics of Matter, Center for Free Electron Laser Science, 22761 Hamburg, Germany*

⁵*CPHT, CNRS, Ecole Polytechnique, Institut Polytechnique de Paris, F-91128 Palaiseau, France*



(Received 10 February 2021; revised 19 May 2021; accepted 20 May 2021; published 14 June 2021)

In this work we present a comprehensive analysis of collective electronic fluctuations and their effect on single-particle properties of the Hubbard model. Our approach is based on a standard dual fermion and boson scheme with the interaction truncated at the two-particle level. Within this framework we compare various approximations that differ in the set of diagrams (ladder vs exact diagrammatic Monte Carlo), and/or in the form of the four-point interaction vertex (exact vs partially bosonized). This allows to evaluate the effect of all components of the four-point vertex function on the electronic self-energy. In particular, we observe that contributions that are not accounted for by the partially bosonized approximation for the vertex have only a minor effect on electronic degrees of freedom in a broad range of model parameters. In addition, we find that in the regime, where the ladder dual fermion approximation provides an accurate solution of the problem, the leading contribution to the self-energy is given by the longitudinal bosonic modes. This can be explained by the fact that contributions of transverse particle-hole and particle-particle modes partially cancel each other. Our results justify the applicability of the recently introduced dual triply irreducible local expansion (D-TRILEX) method that represents one of the simplest consistent diagrammatic extensions of the dynamical mean-field theory. We find that the self-consistent D-TRILEX approach is reasonably accurate also in challenging regimes of the Hubbard model, even where the dynamical mean-field theory does not provide the optimal local reference point (impurity problem) for the diagrammatic expansion.

DOI: [10.1103/PhysRevB.103.245123](https://doi.org/10.1103/PhysRevB.103.245123)

I. INTRODUCTION

Long-range correlations play a crucial role in strongly interacting electronic systems. They are responsible for various phenomena as, for instance magnetism, charge density waves, and superconductivity. A consistent treatment of non-local collective electronic fluctuations often appears to be a challenging task. It is important for an accurate description not only of these effective bosonic modes themselves, but also of their influence on the single-particle characteristics of the system.

A consistent model description of strongly correlated materials should be able to identify leading collective instability channels governing physical processes in the system. Apart from giving physical insight, this often drastically diminishes technical efforts required for solving the problem. The Hubbard model is a minimal model that accounts for the interplay between kinetic energy and Coulomb interaction of electrons. For infinite number of spatial dimensions, the Hubbard model can be solved exactly by means of the dynamical mean-field theory (DMFT) [1], where the self-energy becomes purely local [2]. DMFT is a nonperturbative method that accurately accounts for local correlations by mapping the original lattice

model onto an auxiliary local impurity problem, which can be solved numerically exactly. In finite dimensions DMFT turns out to be a good approximation for single-particle quantities, in particular when local correlations are strong [3,4]. However, DMFT reaches its limits when spatial fluctuations become large [5].

Further, cluster extensions of DMFT [6–12] have been introduced to consider nonlocal correlation effects. However, the range of spatial correlations captured by these methods is limited by the size of the cluster. For this reason, long-range collective fluctuations are usually described by various diagrammatic extensions of DMFT [13]. Some of these approaches, such as the GW +DMFT [14–20], the triply irreducible local expansion (TRILEX) [21–23], and the dynamical vertex approximation (D Γ A) [24,25], as well as most applications of the dual fermion (DF) [26–29] and the dual boson (DB) [30–34] theories, take into account only a particular subset of diagrams corresponding to certain channels of instability. Others are based on the exact diagrammatic Monte Carlo (DiagMC) method [35,36], which allows to consider all diagrammatic contributions [37–39].

GW +DMFT is a simple method that is widely used for calculating properties of realistic materials [40–44]. However, among various long-range fluctuations this approach considers only collective charge excitations and does not account for vertex corrections. The latter are important for an accurate

*evgeny.stepanov@polytechnique.edu

description of magnetic, optical, and transport properties of the system [45–55]. More elaborate theories like DF, DB, and D Γ A, which address all leading collective fluctuations on equal footing, account for vertex corrections and appear to be in a good agreement with numerically exact methods [4,37–39,56]. However, the use of the renormalized local four-point vertex makes all these methods numerically expensive for application to realistic materials [57–59]. At the same time, this vertex cannot be simply neglected because it represents the screened local interaction between electrons. Therefore, a consistent description of the long-range collective fluctuations requires a theory that combines the simplicity of the GW+DMFT diagrammatic scheme with vertex corrections and the equal-footing description of the leading collective modes provided by more elaborate approaches.

To resolve this issue, a simple consistent diagrammatic extension of DMFT, dubbed “dual TRILEX” (D-TRILEX), has recently been proposed in Ref. [60]. This method is a derivative of the DB approach and is based on a set of Hubbard-Stratonovich transformations of fermionic and bosonic variables. This allows to consider local correlation effects exactly within the impurity problem of DMFT, and nonlocal effects perturbatively. The resulting approach considers all leading collective electronic fluctuations on equal footing without any limitation on the range. Unlike the DB method, the D-TRILEX approach relies on a partially bosonized representation for the renormalized local four-point vertex [60] that uncovers explicit contributions of different collective modes. A single (spin or charge) mode approximation of the vertex can be found in prior works [33,61,62]. Similar approximations for the four-point vertex have also been discussed in Refs. [63–66]. However, only the special form of the partially bosonized approximation introduced in Ref. [60] allows to derive the D-TRILEX theory that with a low computational complexity comparable to GW+DMFT or TRILEX methods reproduces the result of the much more elaborate DB theory even in the strongly interacting regime. Additionally, unlike the TRILEX method, the D-TRILEX approach accounts for vertex corrections for both lattice sites that are involved in nonlocal diagrams for the self-energy and the polarization operator. For instance, this allows to preserve the correct orbital structure of considered diagrams [67]. Furthermore, the D-TRILEX approach does not suffer from the famous Fierz ambiguity problem [68–70], which plagues many theories that perform a partially bosonized description of collective modes.

The D-TRILEX theory was introduced only recently [60], and although it has already been extended to a multiorbital case [67], its limits of applicability have not been studied in details so far. In this work we address this important question and justify the validity of the theory in a broad range of physical parameters. To this aim we consider a two-dimensional (2D) Hubbard model on a square lattice and compare the performance of the D-TRILEX approach with its parental DB method and the numerically exact DiagMC theory. Note that in this case the absence of the nonlocal interaction and the bosonic hybridization function identically reduces the DB theory to the DF approach. To evaluate the impact of different collective fluctuations on the self-energy, we exploit a partially bosonized representation of the full local four-point

vertex and obtain the exact solution of the dual problem with the DiagMC@DF method [38,39], as well as the approximate ladder DF solution of the problem. In particular, we explicitly investigate the effect of particle-particle fluctuations that enter the four-point vertex function since they are believed to be negligibly small at standard fillings [71]. As the result, we show that exclusion of the irreducible part and transverse contributions from the four-point vertex function often does not lead to a noticeable change of the result, but significantly reduces costs of numerical calculations.

The paper is organized as follows: Section II contains a brief derivation of the D-TRILEX theory presented in Ref. [60]. In Sec. III we compare the D-TRILEX self-energy with the ladder DF, the DiagMC@DF, and the exact DiagMC results in a broad range of temperatures and local interactions. Finally, Sec. IV is devoted to conclusions.

II. THEORY

In this section we highlight the key points of the derivation of the D-TRILEX method. We begin with the extended Hubbard model described by the following lattice action:

$$\begin{aligned} S_{\text{latt}} = & - \sum_{k,\sigma} c_{k\sigma}^* \mathcal{G}_{k\sigma}^{-1} c_{k\sigma} + U \sum_q n_{q\uparrow}^* n_{q\downarrow} \\ & + \sum_{q,\vartheta} \xi^{\vartheta} \{ \rho_q^{*\vartheta} V_q^{\vartheta} \rho_q^{\vartheta} \}. \end{aligned} \quad (1)$$

Here, the Grassmann variable $c_{k\sigma}^{(*)}$ with the combined index $k = \{\mathbf{k}, \nu\}$ describes the annihilation (creation) of an electron with momentum \mathbf{k} , fermionic Matsubara frequency ν , and spin $\sigma = \{\uparrow, \downarrow\}$. $\mathcal{G}_{k\sigma} = [i\nu + \mu - \varepsilon_{\mathbf{k}}]^{-1}$ is the bare lattice Green’s function, where $\varepsilon_{\mathbf{k}}$ is the dispersion of electrons, and μ is the chemical potential. U describes the onsite Coulomb interaction between electron densities $n_{q\sigma} = \sum_k c_{k+q,\sigma}^* c_{k\sigma}$ that depend on momentum \mathbf{q} and bosonic Matsubara frequency ω through the combined index $q = \{\mathbf{q}, \omega\}$. For the sake of generality, we also introduce a nonlocal interaction V_q in different bosonic channels $\vartheta = \{\zeta, s\}$, where “ ζ ” denotes the particle-hole channel with density ($\zeta = d$) and magnetic ($\zeta = m = \{x, y, z\}$) components, and “ s ” labels the particle-particle singlet channel. For numerical calculations we restrict ourselves to the Hubbard model and set these nonlocal interactions to zero at the end of the derivation. To shorten the expression for the action we introduce the prefactor ξ^{ϑ} that for the particle-hole and particle-particle channels, respectively, reads as $\xi^d = \frac{1}{2}$ and $\xi^s = 1$. Corresponding composite bosonic variables $\rho_q^{\vartheta} = n_q^{\vartheta} - \langle n^{\vartheta} \rangle$ are introduced as follows:

$$n_q^{\zeta} = \sum_{k,\sigma\sigma'} c_{k+q,\sigma}^* \sigma_{\sigma\sigma'}^{\zeta} c_{k\sigma'}, \quad (2)$$

$$n_q^s = \frac{1}{2} \sum_{k,\sigma\sigma'} c_{q-k,\bar{\sigma}} \sigma_{\sigma\sigma'}^z c_{k\sigma'}, \quad (3)$$

$$n_q^{*s} = \frac{1}{2} \sum_{k,\sigma\sigma'} c_{k\sigma}^* \sigma_{\sigma\sigma'}^z c_{q-k,\bar{\sigma}'}, \quad (4)$$

where $\sigma^{x,y,z}$ are Pauli matrices in the spin space, σ^d is the identity matrix in the same space, and $\bar{\sigma}$ is the opposite spin projection to σ . The variable n_q^{*s} can be found from the

relation $n_q^{*\zeta} = n_{-q}^\zeta$, and is introduced to unify notations. Note that in the single-band case considered here the composite bosonic variables for the triplet channel are identically equal to zero.

The D-TRILEX approach, as well as its parental DB theory, performs a diagrammatic expansion around a reference system [29], which in this particular work is given by the exactly solvable effective local impurity problem of DMFT [1]:

$$\mathcal{S}_{\text{imp}} = - \sum_{\nu, \sigma} c_{\nu\sigma}^* [i\nu + \mu - \Delta_\nu] c_{\nu\sigma} + U \sum_{\omega} n_{\omega\uparrow}^* n_{\omega\downarrow}. \quad (5)$$

Here, we introduce the fermionic hybridization function Δ_ν that aims to describe the screening effect of “bath” electrons that surround the given lattice site, which plays a role of the local impurity. Note that in this work we do not consider the bosonic hybridization function, which is usually introduced for the impurity problem of the extended dynamical mean-field theory (EDMFT) [72–76]. In DMFT the fermionic hybridization is determined self-consistently demanding that the local part of the dressed lattice Green’s function $G_{k\sigma}$ is equal to the Green’s function $g_{\nu\sigma}$ of the impurity problem (5). To be consistent, the same hybridization function Δ_ν has to be subtracted from the remaining part of the lattice action $\mathcal{S}_{\text{rem}} = \mathcal{S}_{\text{latt}} - \sum_i \mathcal{S}_{\text{imp}}$ so that the original lattice problem (1) remains unchanged.

The impurity problem (5) can be solved numerically exactly using, e.g., continuous-time quantum Monte Carlo (CTQMC) solvers [77–80]. This allows to obtain not only the single-particle Green’s function $g_{\nu\sigma}$ and the corresponding self-energy $\Sigma_{\nu\sigma}^{\text{imp}}$, but also the two-particle quantities in all bosonic channels ϑ of interest. The latter include the susceptibility χ_ω , the renormalized interaction w_ω , and the polarization operator Π_ω^{imp} , as well as the renormalized local four-point $\Gamma_{\nu\nu'\omega}$ and three-point $\Lambda_{\nu\omega}^{(*)}$ vertex functions. The remaining part of the lattice action \mathcal{S}_{rem} cannot be taken into account exactly. Instead, it is treated diagrammatically performing an expansion around the impurity problem (5). In a consistent way, this procedure can be carried out with the help of a Hubbard-Stratonovich transformation. The latter allows to rewrite the \mathcal{S}_{rem} in terms of new fermionic f and bosonic φ fields that are dual to original electronic c and composite ρ variables. After that, the impurity problem (5) with all original variables can be integrated out, which excludes the possibility of the double counting between \mathcal{S}_{imp} and \mathcal{S}_{rem} parts of the lattice problem. This yields the dual boson action (see Ref. [60] and Appendix A)

$$\tilde{\mathcal{S}} = - \sum_{k, \sigma} f_{k\sigma}^* \tilde{\mathcal{G}}_{k\sigma}^{-1} f_{k\sigma} - \sum_{q, \vartheta} \xi^\vartheta \{ \varphi_q^{*\vartheta} \tilde{\mathcal{W}}_q^{\vartheta-1} \varphi_q^\vartheta \} + \tilde{\mathcal{F}}[f, \varphi]. \quad (6)$$

Here, the bare dual fermion $\tilde{\mathcal{G}}_{k\sigma} = \check{G}_{k\sigma} - g_{\nu\sigma}$ and boson $\tilde{\mathcal{W}}_q^\vartheta = \check{W}_q^\vartheta - w_\omega^\vartheta$ propagators are given by the difference between corresponding EDMFT and impurity quantities. To prevent misunderstanding, by the EDMFT Green’s function $\check{G}_{k\sigma}$ and the renormalized interaction \check{W}_q^ϑ we understand the bare lattice Green’s function and the bare interaction that are

dressed, respectively, in the local impurity self-energy and polarization operator via Dyson equations

$$\check{G}_{k\sigma}^{-1} = \mathcal{G}_{k\sigma}^{-1} - \Sigma_{\nu\sigma}^{\text{imp}}, \quad (7)$$

$$[\check{W}_q^\vartheta]^{-1} = (U^\vartheta + V_q^\vartheta)^{-1} - \Pi_\omega^{\vartheta \text{imp}}. \quad (8)$$

In this way, bare dual quantities that describe spatial fluctuations already take into account the effect of local correlations. Note that in the dual problem (6) the bare local interaction U^ϑ is introduced as a fictitious quantity that does not affect the result for physical observables (see Appendix A). This directly follows from the fact that the DB theory is free from the Fierz ambiguity in decoupling of the local Coulomb interaction U into different channels (see, e.g., Ref. [60]).

For actual numerical calculations, the dual interaction $\tilde{\mathcal{F}}[f, \varphi]$ is truncated at the two-particle level, which contains only the four-point $\Gamma_{\nu\nu'\omega}$ and three-point $\Lambda_{\nu\omega}^{(*)}$ vertices of the impurity problem (5). These quantities are explicitly defined in Appendix A. With this approximation the theory shows a good agreement with the exact benchmark results [4,37–39,56]. However, it still remains relatively complex due to the presence of the four-point vertex function $\Gamma_{\nu\nu'\omega}$. The latter depends on three frequencies, so calculating and using it in realistic multiorbital simulations, which involve the inversion of the Bethe-Salpeter equation in the frequency-orbital space, becomes time consuming numerically [57–59]. To cope with this problem, one can make use of yet another Hubbard-Stratonovich transformation over bosonic variables $\varphi \rightarrow b$ that generates an effective four-point interaction in a partially bosonized form

$$\begin{aligned} \Gamma_{\nu\nu'\omega}^{\text{d}} &\simeq 2M_{\nu\nu'\omega}^{\text{d}} - M_{\nu, \nu+\omega, \nu'-\nu}^{\text{d}} - 3M_{\nu, \nu+\omega, \nu'-\nu}^{\text{m}} + M_{\nu, \nu', \omega+\nu+\nu'}^{\text{s}}, \\ \Gamma_{\nu\nu'\omega}^{\text{m}} &\simeq 2M_{\nu\nu'\omega}^{\text{m}} + M_{\nu, \nu+\omega, \nu'-\nu}^{\text{m}} - M_{\nu, \nu+\omega, \nu'-\nu}^{\text{d}} - M_{\nu, \nu', \omega+\nu+\nu'}^{\text{s}}, \\ \Gamma_{\nu\nu'\omega}^{\text{s}} &\simeq M_{\nu\nu'\omega}^{\text{s}} + \frac{1}{2} (M_{\nu, \nu', \omega-\nu-\nu'}^{\text{d}} + M_{\nu, \omega-\nu', \nu'-\nu}^{\text{d}}) \\ &\quad - \frac{3}{2} (M_{\nu, \nu', \omega-\nu-\nu'}^{\text{m}} + M_{\nu, \omega-\nu', \nu'-\nu}^{\text{m}}). \end{aligned} \quad (9)$$

This approximation uncovers the underlying structure of the vertex, which consists of all possible collective electronic fluctuations

$$M_{\nu\nu'\omega}^\vartheta = \Lambda_{\nu\omega}^\vartheta \bar{w}_\omega^\vartheta \Lambda_{\nu'\omega}^{*\vartheta} \quad (10)$$

that behave as bosonic modes

$$\bar{w}_\omega^\zeta = w_\omega^\zeta - U^\zeta/2, \quad (11)$$

$$\bar{w}^{\text{s}} = w_\omega^{\text{s}} - U^{\text{s}}. \quad (12)$$

As Ref. [60] shows, the partially bosonized representation (9) for the four-point vertex can be fine tuned in such a way that it nearly cancels the exact four-point vertex from the dual action. Indeed, this approximation does not take into account contributions to the vertex function that cannot be reduced to a single boson propagator. However, this irreducible part can be completely excluded on the level of the ladder approximation for the vertex by a special choice of bare local interactions in different channels $U^{\text{d/m}} = \pm U/2$ and $U^{\text{s}} = U$. The precise effect of nonladder irreducible contributions on the electronic

self-energy is investigated below. As a consequence, this specific choice for the bare interactions U^ϑ provides the most accurate partially bosonized approximation for the four-point vertex function given by Eq. (9). In addition, it also leads to a correct high-frequency ($\nu \rightarrow \infty$ or $\omega \rightarrow \infty$) asymptotic behavior of the three-point vertex $\Lambda_{\nu\omega}^{(*)} \rightarrow 1$ [60].

At the same time, it should be noted that this special choice of the bare interaction U^ϑ cannot be obtained by any decoupling of the local Coulomb interaction U into different bosonic channels [60]. Therefore, it results in a double counting of U in the vertex function, which is explicitly subtracted from the renormalized interaction w_ω^ϑ of the impurity problem in Eqs. (11) and (12). As follows from these equations and the fact that $w^\vartheta(\omega \rightarrow \infty) = U^\vartheta$, we prefer to keep the bare Coulomb interaction U only in the particle-hole channel. In this way, it does not contribute to the renormalized singlet interaction \bar{w}_ω^s (12), and becomes equally distributed between density and magnetic channels. The reason for such decomposition lies in the fact that the renormalization of the bare interaction in the particle-particle channel is believed to be negligibly small at standard fillings [71]. Therefore, the corresponding singlet contribution M^s , which in the considered form (12) does not contain the bare interaction U^s , can be excluded from the theory, as it was consciously done in the previous work [60]. To clarify this statement, we explicitly introduce and investigate the effect of singlet terms in this work. Note that although the bare interaction is (partially or fully) subtracted from the local renormalized interactions (11) and (12), the partially bosonized approximation (9) for the four-point vertex has a correct asymptotic behavior at high frequencies $\Gamma^{d/m} \rightarrow \pm U$ and $\Gamma^s \rightarrow U$. This follows from the fact that the four-point function does not depend on the way how the onsite Coulomb interaction U is distributed between different bosonic channels [60]. For example, although the singlet bosonic mode \bar{w}^s does not contain the constant contribution U^s , the latter is still present in the singlet vertex function Γ^s (9) due to transverse charge and spin fluctuations.

After the last Hubbard-Stratonovich transformation the dual problem (6) reduces to a simple action of a partially bosonized dual theory (PBDT) written in terms of fermion f and boson b variables, and the local three-point interaction vertex $\Lambda_{\nu\omega}^{(*)}$ only [60]:

$$\begin{aligned} S_{pb} = & - \sum_{k,\sigma} f_{k\sigma}^* \tilde{G}_{k\sigma}^{-1} f_{k\sigma} - \sum_{q,\vartheta} \xi^\vartheta \{ b_q^{*\vartheta} \mathcal{W}_q^{\vartheta-1} b_q^\vartheta \} \\ & + \sum_{q,k,\vartheta} \xi^\vartheta \{ \Lambda_{\nu\omega}^\vartheta \eta_{q,k}^{*\vartheta} b_q^\vartheta + \Lambda_{\nu\omega}^{*\vartheta} b_q^{*\vartheta} \eta_{q,k}^\vartheta \}, \end{aligned} \quad (13)$$

where, similarly to Eqs. (2), (3), and (4), we define

$$\eta_{q,k}^s = \sum_{\sigma\sigma'} f_{k+q,\sigma}^* \sigma_{\sigma\sigma'}^s f_{k\sigma'}, \quad (14)$$

$$\eta_{q,k}^s = \frac{1}{2} \sum_{\sigma\sigma'} f_{q-k,\bar{\sigma}} \sigma_{\sigma\sigma'}^z f_{k\sigma'}, \quad (15)$$

$$\eta_{q,k}^{*s} = \frac{1}{2} \sum_{\sigma\sigma'} f_{k\sigma}^* \sigma_{\sigma\sigma'}^z f_{q-k,\bar{\sigma}'}. \quad (16)$$

The bare Green's function $\tilde{G}_{k\sigma}$ of this new problem (13) remains unchanged, and the bare bosonic propagators become

$$\mathcal{W}_q^s = \tilde{W}_q^s - U^s/2, \quad (17)$$

$$\mathcal{W}_q^s = \tilde{W}_q^s - U^s, \quad (18)$$

where the same exclusion of the double counting between different bosonic channels as in Eqs. (11) and (12) takes place.

The simplest set of diagrams for the self-energy and polarization operator used in the D-TRILEX approach [60]

$$\tilde{\Sigma}_{k\sigma} = - \sum_{q,s} \{ \Lambda_{\nu\omega}^s \tilde{G}_{q+k,\sigma} \mathcal{W}_q^s \Lambda_{\nu\omega}^{*s} - \Lambda_{\nu\omega}^s \tilde{G}_{q-k,\bar{\sigma}} \mathcal{W}_q^s \Lambda_{\nu\omega}^{*s} \}, \quad (19)$$

$$\bar{\Pi}_q^s = + \sum_{k,\sigma} \Lambda_{\nu\omega}^{*s} \tilde{G}_{k\sigma} \tilde{G}_{q+k,\sigma} \Lambda_{\nu\omega}^s, \quad (20)$$

$$\bar{\Pi}_q^s = - \sum_k \Lambda_{\nu\omega}^{*s} \tilde{G}_{k\uparrow} \tilde{G}_{q-k\downarrow} \Lambda_{\nu\omega}^s \quad (21)$$

can be obtained from the analog of the Almladh functional [81] $\Psi[\tilde{G}, W, \Lambda] = \frac{1}{2} \tilde{G} \Lambda^\vartheta W^\vartheta \Lambda^{*\vartheta} \tilde{G}$ introduced in the dual space. This ensures the consistency between single- and two-particle quantities produced by the theory. Here, $\tilde{G}_{k\sigma}$ and W_q^ϑ are full propagators of the fermion-boson problem (13) given by Dyson equations

$$\tilde{G}_{k\sigma}^{-1} = \tilde{G}_{k\sigma}^{-1} - \tilde{\Sigma}_{k\sigma}, \quad (22)$$

$$W_q^{\vartheta-1} = \mathcal{W}_q^{\vartheta-1} - \bar{\Pi}_q^\vartheta. \quad (23)$$

This simple GW -like diagrammatics (19), (20), and (21) of the D-TRILEX approach can also be related to its parental DB theory. For simplicity, the main text of the paper contains only a sketch of this derivation presented in Fig. 1. Also, here we only consider the case when the nonlocal interaction is discarded ($V_q^\vartheta = 0$). Then, the DB theory (6) identically coincides with the DF approach, and the dual self-energy in the ladder approximation takes the form of $\tilde{\Sigma}^{\text{LDF}}$ [28] displayed in the first line of Fig. 1. This expression can be obtained using the Schwinger-Dyson equation for the dual self-energy [82]. As the result, the second-order contribution $\tilde{\Sigma}^{(2)}$ has a “ $\frac{1}{2}$ ” prefactor that does not appear for the rest of the ladder self-energy $\tilde{\Sigma}^{(3+)}$ [27]. As two subsequent lines in Fig. 1 show, if one uses the partially bosonized representation (9) for every vertex function that enters $\tilde{\Sigma}^{\text{LDF}}$ and keeps only longitudinal contributions in this approximation, the dual self-energy immediately reduces to the D-TRILEX form (19). By longitudinal contributions we understand $M_{\nu\nu'}^\vartheta$ terms, where the bosonic propagator \bar{w}_ω^ϑ carries the main bosonic frequency ω . The exclusion of transverse particle-hole and particle-particle fluctuations from the four-point vertex can be motivated by the fact that their contributions to the self-energy partially cancel each other, which is demonstrated in Sec. III B. The explicit analytical derivation of the relation between D-TRILEX and ladder DB (LDB) self-energies for the general case when the nonlocal interaction is not neglected is shown in Appendix C. This result demonstrates the important advantage of the D-TRILEX theory over its parental LDB method, which drastically reduces costs of numerical calculations. Thus, although the D-TRILEX approach accounts for the main longitudinal

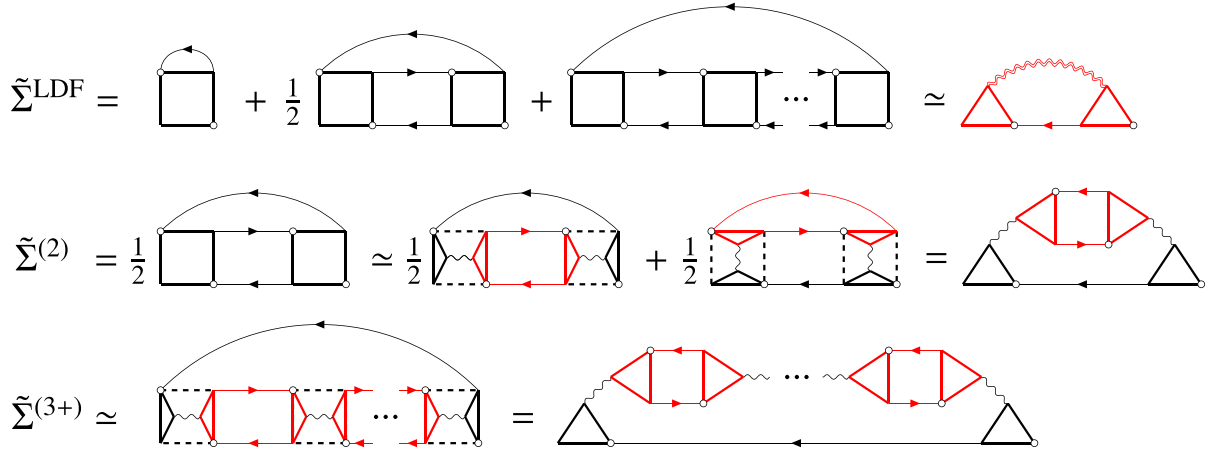


FIG. 1. Top row shows the ladder dual fermion self-energy $\tilde{\Sigma}^{\text{LDF}}$, which consists of the first-order Hartree-type term, second-order diagram $\tilde{\Sigma}^{(2)}$, and the rest of the ladder $\tilde{\Sigma}^{(3+)}$. Keeping only longitudinal modes of the partially bosonized representation for the four-point vertex Γ (black squares), the LDF self-energy reduces to the self-energy of the D-TRILEX approach (red diagram at the end of the top row). For $\tilde{\Sigma}^{(2)}$ and $\tilde{\Sigma}^{(3+)}$ the result of this approximation is explicitly shown in the middle and bottom rows, respectively. Red parts of these diagrams that consist of two triangles (three-point vertices) connected by two solid lines (dual Green's functions) is the polarization operator of the D-TRILEX theory. Wiggly line corresponds to the renormalized interaction.

part of the full two-particle ladder fluctuation, the calculation of the self-energy (19) and polarization operators (20) and (21) does not require the inversion of the Bethe-Salpeter equation in the momentum-frequency space. In the ladder DF/DB theory the inversion of the Bethe-Salpeter equation in the frequency space cannot be avoided due to a three-frequency dependence of the local vertex function $\Gamma_{vv'\omega}$.

We note that the diagrammatic expansion in DF, DB, and D-TRILEX methods is performed in the dual space. The self-energy of the original lattice problem (1) can be obtained from the following exact relation [30,32,33]:

$$\Sigma_{k\sigma}^{\text{latt}} = \Sigma_{\omega\sigma}^{\text{imp}} + \frac{\tilde{\Sigma}_{k\sigma}}{1 + g_{v\sigma} \tilde{\Sigma}_{k\sigma}}. \quad (24)$$

Here, the dual contribution to the lattice self-energy comes with the denominator $(1 + g_{v\sigma} \tilde{\Sigma}_{k\sigma})$ that excludes unphysical terms from the Dyson equation for the lattice Green's function [29]. Note that the expression (24) requires the explicit calculation of the impurity self-energy that cannot be measured directly as a single-particle correlation function. Instead, $\Sigma_{v\sigma}^{\text{imp}}$ is usually obtained by inverting the Dyson equation for the full impurity Green's function $g_{v\sigma}$, which makes the result noisy at high frequencies. The noise in the self-energy can be reduced using the improved estimators method that, however, requires the measurement of higher-order correlations functions [83–85]. Therefore, for calculation of the lattice Green's function it is more convenient to use another exact relation that does not involve $\Sigma_{v\sigma}^{\text{imp}}$ [30,86]:

$$G_{k\sigma}^{-1} = [g_{v\sigma} + g_{v\sigma} \tilde{\Sigma}_{k\sigma} g_{v\sigma}]^{-1} + \Delta_v - \varepsilon_{\mathbf{k}}. \quad (25)$$

This expression for the dressed lattice Green's function $G_{k\sigma}$ completes the derivation of the D-TRILEX approach.

III. RESULTS

A. Comparing different methods

In this section we consistently investigate the effect of different contributions that make up the renormalized local four-point vertex on the electronic self-energy. To this aim we consider a two-dimensional (2D) Hubbard model on a square lattice with the nearest-neighbor hopping amplitude $t = 1$ and different values of the onsite Coulomb potential U . Numerical calculations are performed at half-filling unless the other filling is explicitly specified. All nonlocal interactions are set to zero $V_{\mathbf{q}}^{\beta} = 0$. Note that in this case the renormalized interaction of EDMFT $\check{W}_{\mathbf{q}}^{\beta}$ (8) coincides with the impurity w_{ω}^{β} , and the dual boson propagator $\check{W}_{\mathbf{q}}^{\beta}$ becomes zero. As

TABLE I. Summary of considered methods that specifies the form of the local four-point vertex and types of diagrams that are used for the diagrammatic expansion. The square corresponds to the exact four-point vertex $\Gamma_{vv'\omega}$ of the impurity problem. Longitudinal and transverse components $M_{vv'\omega}$ that enter the partially bosonized approximation for the vertex (9) are depicted by two triangles connected by the wavy line placed horizontally and vertically. The “-” sign in front of the transverse contribution corresponds to the antisymmetric form of the vertex (9). The DiagMC@PBDT-s approximation can be obtained from the DiagMC@PBDT method by excluding the singlet contribution $M_{v,v',\omega+v+v'}^s$ from the partially bosonized vertex (9).

Method	Four-point vertex	Types of diagrams
D-TRILEX		ladder
LDF		ladder
DiagMC@DF		all
DiagMC@PBDT		all

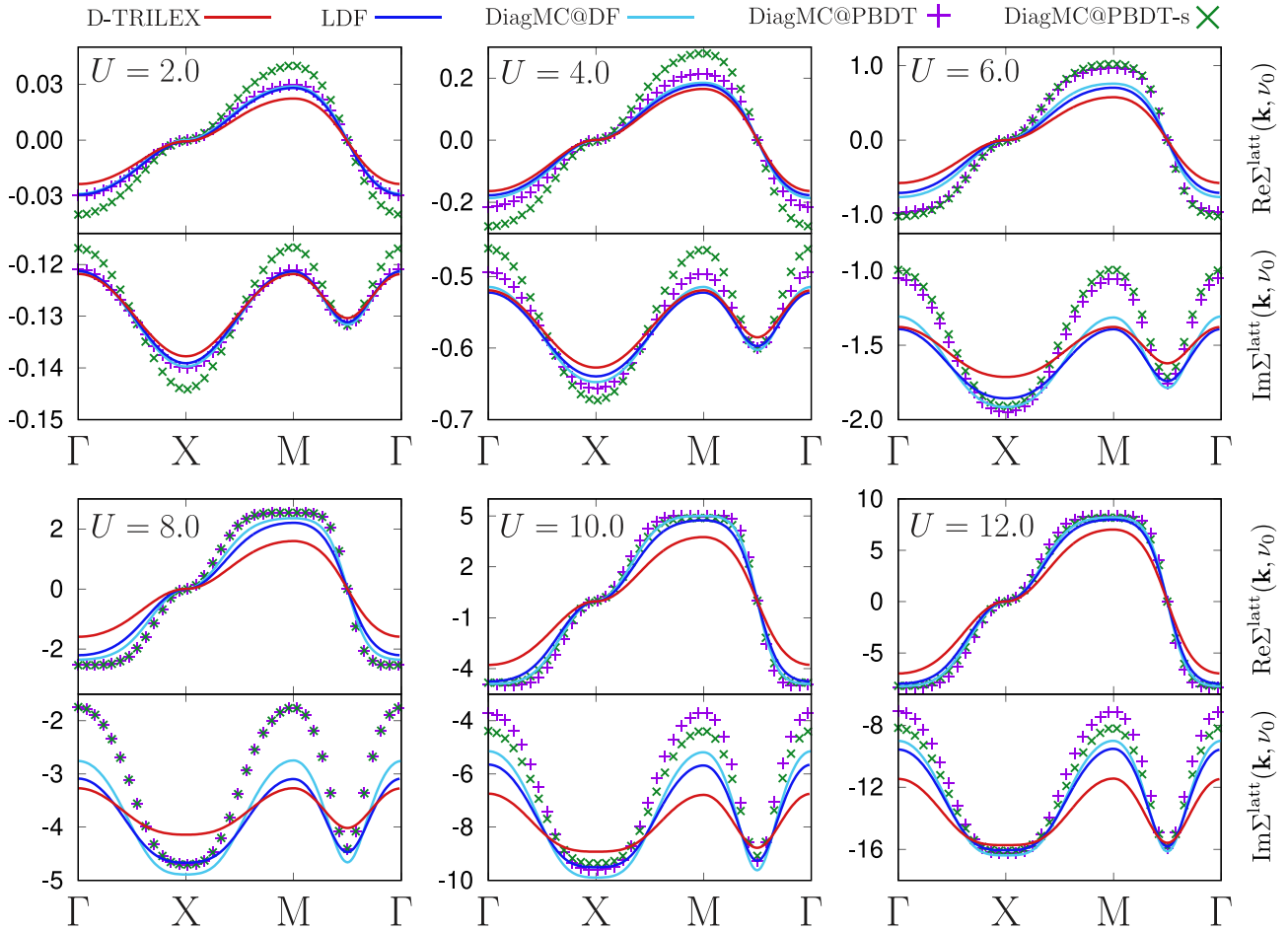


FIG. 2. The lattice self-energy $\Sigma_{\mathbf{k},\nu_0}^{\text{latt}}$ obtained for the first Matsubara frequency $\nu_0 = \pi/\beta$ for the inverse temperature $\beta = 2$ along the high-symmetry path in momentum space \mathbf{k} . The value of the onsite Coulomb potential U for which the calculation was performed is specified in panels. Upper and lower parts of each panel correspond to real and imaginary parts of the self-energy, respectively. Results are obtained using D-TRILEX (red line), LDF (dark blue line), DiagMC@DF (light blue line), DiagMC@PBDT (purple crosses), and DiagMC@PBDT-s (green crosses) methods.

a consequence, the DB action (6) reduces to the DF problem [26]. Restricting the interaction $\tilde{\mathcal{F}}[f]$ to the four-point vertex function $\Gamma_{\nu\nu'\omega}$, the dual problem (6) can be solved numerically exactly within the diagrammatic Monte Carlo method for dual fermions (DiagMC@DF) [37–39]. In this work we perform DiagMC@DF calculations on the basis of the converged DMFT solution of the lattice problem (1). The corresponding single-site impurity problem of DMFT (5) is solved numerically exactly using the open source CT-HYB solver [87,88] based on ALPS libraries [89]. After that, the calculated bare dual Green’s function $\hat{G}_{k\sigma}$ and the local four-point vertex function $\Gamma_{\nu\nu'\omega}$ are used as building blocks for a diagrammatic expansion. A detailed description of the DiagMC@DF method can be found in Ref. [38]. For physical parameters considered in this work, the converged result for the dual self-energy is achieved at the fifth order of expansion.

Different levels of approximation for the four-point vertex can be investigated to reveal the effect of contributions that are not accounted for in the D-TRILEX theory. In particular, the contribution to the self-energy that stems from the irreducible part of the four-point vertex function can be identified by comparing the exact DiagMC@DF solution of the dual problem

(6) with the result of another DiagMC calculation, where the exact local vertex $\Gamma_{\nu\nu'\omega}$ is replaced by its partially bosonized approximation (9). Hereinafter this method is referred to as DiagMC@PBDT and corresponds to the exact evaluation of the self-energy of the partially bosonized dual theory (13). The next level of approximation that allows to observe the effect of collective fluctuations in the singlet channel can be achieved by performing DiagMC calculations with the partially bosonized vertex (9) where all M^s terms are neglected. This calculation is referred to as DiagMC@PBDT-s.

We note that the DiagMC@DF method does not distinguish between longitudinal and transverse components of the four-point vertex because the Monte Carlo sampling considers all possible topologies of diagrams. As has been discussed in the Sec. II, the contribution of these modes can be disentangled comparing the self-energy of the ladder dual fermion (LDF) approach, which exploits the exact local four-point vertex, with the result of the D-TRILEX theory, where only longitudinal modes are taken into account. These calculations are also performed on the basis of the converged DMFT solution, so that the local impurity problem remains the same for all compared theories. Note that the LDF and D-TRILEX

results for the self-energy are obtained within the self-consistent scheme in terms of dressed fermionic (22) and bosonic (23) propagators. When possible, we compare our results with the exact DiagMC solution [90–92] of the lattice problem (1) that was kindly provided by the authors of Refs. [4,93]. All methods are summarized in Table I.

B. Effect of the local interaction

First, we make a scan over a broad range of local Coulomb interactions U at a fixed temperature. We note that in two dimensions DMFT predicts the Néel transition at a finite temperature. This transition is forbidden by Mermin-Wagner theorem [94] and thus is an artifact of the DMFT theory. However, since the DiagMC@DF method uses the DMFT impurity problem as a starting point for the diagrammatic expansion, the DiagMC@DF theory shows difficult convergence or even divergent result close to the DMFT Néel point [37,38]. For this reason, calculations are performed at the inverse temperature $\beta = 2$, so that the DiagMC results are not affected by any convergence issue. Figure 2 shows the lattice self-energy (24) calculated for all above-mentioned approaches (see Sec. III A). Note that the self-energy does not contain the constant Hartree part that is equal to $U/2$ at half-filling. The results are obtained for the first Matsubara frequency $\nu_0 = \pi/\beta$ along the high-symmetry path that connects $\Gamma = (0, 0)$, $X = (0, \pi)$, and $M = (\pi, \pi)$ points in momentum space $\mathbf{k} = (k_x, k_y)$.

Let us first consider the effect of the irreducible part of the four-point vertex comparing the self-energy of DiagMC@DF (light blue line) and DiagMC@PBDT (purple crosses) approaches shown in Fig. 2. We find that at $U = 2$ both methods produce identical results, which means that in a weakly correlated regime the irreducible contributions to the vertex do not affect the self-energy. Upon increasing the local interaction, the discrepancy between these two methods also increases and is noticeable the most in the strongly correlated regime at $U = 8$, which is equal to the bandwidth. After that, at very large interactions $U = 10$ and 12 the real part of the DiagMC@PBDT self-energy again nearly coincides with the one of the DiagMC@DF approach. The agreement in the imaginary part of the self-energy also improves, but the discrepancy between these two methods remains noticeable.

To quantify the difference of the given self-energy from the reference DiagMC@DF result we calculate the following normalized deviation:

$$\delta = \sum_{\mathbf{k}} \left| \frac{\Sigma_{\mathbf{k}, \nu_0}^{\text{ref}} - \Sigma_{\mathbf{k}, \nu_0}}{\Sigma_{\mathbf{k}, \nu_0}^{\text{ref}}} \right|. \quad (26)$$

A similar quantity but for only one \mathbf{k} -point was introduced in Ref. [39]. The corresponding result for all considered approaches is presented in Fig. 3. We find that the normalized deviation of the DiagMC@PBDT method reaches its maximum value $\delta = 15\%$ at $U = 8$. As has been pointed out in the Sec. II, the irreducible part can be excluded from the renormalized four-point vertex only in the ladder approximation. In the strongly correlated regime nonladder diagrams become important [37–39], which is also confirmed by the increase of the normalized deviation of the LDF approach (blue line in Fig. 3). Consequently, the contribution of the irre-

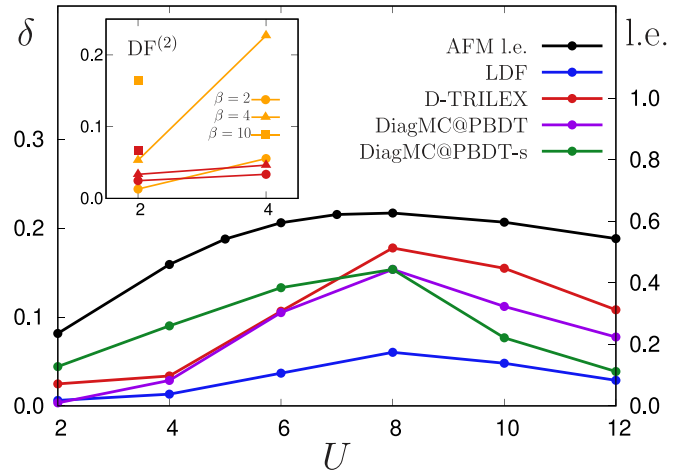


FIG. 3. The normalized deviation δ calculated for LDF (blue), D-TRILEX (red), DiagMC@PBDT (purple), and DiagMC@PBDT-s (green) approximations with respect to the reference Diag@DF result. The black line shows the leading eigenvalue (l.e.) of AFM fluctuations. The vertical left axis shows the scale for the normalized deviation, while the vertical right axis displays values for the leading eigenvalue. The inset compares δ obtained for D-TRILEX and second-order DF ($DF^{(2)}$, orange) approaches for different inverse temperatures $\beta = 2$ (circles), $\beta = 4$ (triangles), and $\beta = 10$ (squares).

ducible part of the vertex to the electronic self-energy also becomes noticeable. We would like to emphasize that by the strength of electronic correlations we mean not only the strength of the interaction, but also the proximity of the system to an instability. The latter can be estimated by the leading eigenvalue (l.e.) of the Bethe-Salpeter equation of the LDF theory [28,95] (black line in Fig. 3), which in our case indicates the strength of antiferromagnetic (AFM) fluctuations.

In the next step we investigate the effect of an additional exclusion of all singlet contributions from the partially bosonized four-point vertex (9). At small ($U = 2$) and moderate ($U = 4$) interactions this immediately leads to a large discrepancy between DiagMC@PBDT-s (green crosses) and DiagMC@PBDT (purple crosses) results for the self-energy presented in Fig. 2. In addition, from Fig. 3 we find that for these values of the interaction the DiagMC@PBDT-s strongly differs from the reference result, while the DiagMC@PBDT performs reasonably well. Therefore, one can conclude that singlet fluctuations play an important role in weakly and moderately correlated regime. At a first glance this observation is in a contradiction with the statement that particle-particle fluctuations are believed to be negligibly small at standard fillings [71]. This point is clarified below when we discuss the result of the D-TRILEX approach. Increasing the interaction to $U = 6$ makes the discrepancy between DiagMC@PBDT and DiagMC@PBDT-s results rapidly decrease, and in the strongly correlated regime ($U = 8$) both methods produce identical results. Remarkably, for $U = 10$ and 12 the DiagMC@PBDT-s method shows the best agreement with the DiagMC@DF result among all considered DiagMC-based approximations. This result suggests that in the regime of very large interactions contributions to the

self-energy that stem from the irreducible and singlet parts of the renormalized four-point vertex, which are not considered in the DiagMC@PBDT-s theory, nearly cancel each other.

Finally, let us consider the D-TRILEX method that can be obtained from the LDF theory excluding the irreducible part and neglecting transverse particle-hole and particle-particle fluctuations from the exact local impurity four-point vertex. As Fig. 2 shows, the best agreement between the D-TRILEX (red line) and the reference DiagMC@DF (light blue line) results for the imaginary part of the self-energy occurs at $U = 2$. At small and moderate values of U , the D-TRILEX self-energy seems to be pinned to the LDF result (dark blue line) at Γ and M points. Therefore, the difference between these two methods is mostly visible around local minima located at antinodal AN = $(0, \pi)$ and nodal N = $(\pi/2, \pi/2)$ points. This difference increases with the interaction, and the observed trend persists up to $U = 6$. At larger interactions, when the value of the self-energy at local minima becomes similar, the D-TRILEX result shifts downwards, and at $U = 12$ becomes pinned to the LDF result at N and AN points.

The discrepancy between the D-TRILEX and the reference results for the real part of the self-energy also increases with the interaction up to $U = 8$, and after that decreases again for very large interaction strengths. However, here the best agreement with the exact result is achieved at $U = 4$ (see red line in Fig. 2). It can be explained by the fact, that in the perturbative regime of small interactions ($U = 2$) and high temperatures ($\beta = 2$) the second-order dual self-energy $\tilde{\Sigma}^{(2)}$ gives the main contribution to the nonlocal part of the total self-energy [3,37–39]. The D-TRILEX theory is not based on a perturbation expansion because it takes into account only a particular (*GW*-like) subset of diagrams. For this reason, this simple theory does not fully reproduce the second-order self-energy $\tilde{\Sigma}^{(2)}$, which leads to a slight underestimation of the result as discussed in Appendix C. On the contrary, the D-TRILEX approach correctly accounts for the screening of the interaction that is represented by longitudinal part of the infinite two-particle ladder in all bosonic channels. At lower temperatures and/or larger interactions, when the system enters the correlated regime, these types of diagrams become more important than the second-order self-energy. To illustrate this point, we also obtained the normalized deviation for the D-TRILEX approach for $\beta = 4$ (for $U = 2$ and 4) and $\beta = 10$ (for $U = 2$), and compared it with δ calculated for the second-order DF ($\text{DF}^{(2)}$) approximation that considers only $\tilde{\Sigma}^{(2)}$ contribution to the dual self-energy. The corresponding result is shown in the inset of Fig. 3. As expected, the accuracy of the $\text{DF}^{(2)}$ approximation rapidly decreases with the temperature and becomes $\delta = 16.5\%$ (for $\beta = 10$ and $U = 2$) and $\delta = 22.5\%$ (for $\beta = 4$ and $U = 4$) in the regime, which is yet above the DMFT Néel point $\beta_N \simeq 12.5$ for $U = 2$ and $\beta_N \simeq 4.3$ for $U = 4$. At the same time, the D-TRILEX theory remains in a reasonable agreement with the reference result.

Figure 3 shows that in the regime of weak and moderate interactions the D-TRILEX self-energy is relatively close to the DiagMC@DF result ($\delta = 2\%$ for $U = 2$ and $\delta = 3\%$ for $U = 4$). This fact looks paradoxical at a first glance because the D-TRILEX method does not take into account singlet fluctuations that were found to be important in this regime of interactions. To explain this result, let us first note that at $U \leq$

4 the LDF method is in a very good agreement with the DiagMC@DF theory. Therefore, in the weakly and moderately correlated regime ladder diagrams provide the most important contribution to the self-energy. This fact allows for a direct comparison of the self-energies produced by ladder DF and D-TRILEX methods with the result of DiagMC@ methods that account for all diagrammatic contributions. Note, however, that all DiagMC-based schemes tend to overestimate the reference result, while ladderlike approaches underestimate it. Therefore, the normalized deviation presented in Fig. 3 should be compared cautiously. Figure 2 shows that D-TRILEX and DiagMC@PBDT self-energies obtained at $U = 2$ and 4 are very close to the reference result. Both methods do not take into account the irreducible part of the four-point vertex function, but the D-TRILEX approach additionally neglects all transverse particle-hole and particle-particle modes. Keeping in mind that for these interaction strengths the exclusion of only singlet fluctuations leads to a large overestimation of the self-energy, we can conclude that transverse particle-hole and particle-particle fluctuations partially screen each other. This means that the exclusion of both types of vertical insertions in diagrams, as it is done in the D-TRILEX theory, turns out to be a good approximation in the weakly and moderately correlated regimes. On the other hand, excluding only one channel leaves the other channel unscreened, which results in a large contribution to the self-energy.

Remarkably, the normalized deviation for all considered approximations shown in Fig. 3 resembles the behavior of the leading eigenvalue of the magnetic channel (black line). For instance, the D-TRILEX and LDF methods show the largest discrepancy with the DiagMC@DF result exactly in the region where the l.e. is maximal. As has been pointed out in Ref. [5], approaching an instability leads to collective fluctuations becoming strongly anharmonic, which cannot be captured by simple diagrammatic theories. Consequently, in this regime transverse momentum-dependent fluctuations are expected to be important. At $U = 10$ and 12 the agreement of the D-TRILEX theory with the DiagMC@DF result improves again. Above we have found that at very large interaction strengths contributions to the self-energy that stem from singlet and irreducible parts of the vertex partially cancel each other. This result suggests that the effect of remaining transverse particle-hole fluctuations becomes weaker at very large interactions, which again justifies the applicability of the D-TRILEX theory.

We would like to note that the largest discrepancy between the D-TRILEX and reference DiagMC@DF result $\delta = 18\%$ corresponds to the most correlated regime ($U = 8$). At small and moderate interactions the normalized difference does not exceed 3.5% ($U = 4$). At the same time, the maximal difference from the parental LDF is only around 10% ($U = 8$), which can be considered as relatively good result for such a simple theory. Finally, we looked at the contribution of the longitudinal particle-particle fluctuations to the D-TRILEX self-energy (19) and, as expected, found it to be negligibly small. Indeed, the renormalized singlet interaction in the D-TRILEX form (18) does not contain the bare constant interaction U^s and therefore describes only the screening of the Coulomb interaction by particle-particle fluctuations. As the result, we observe that the part of the self-energy that

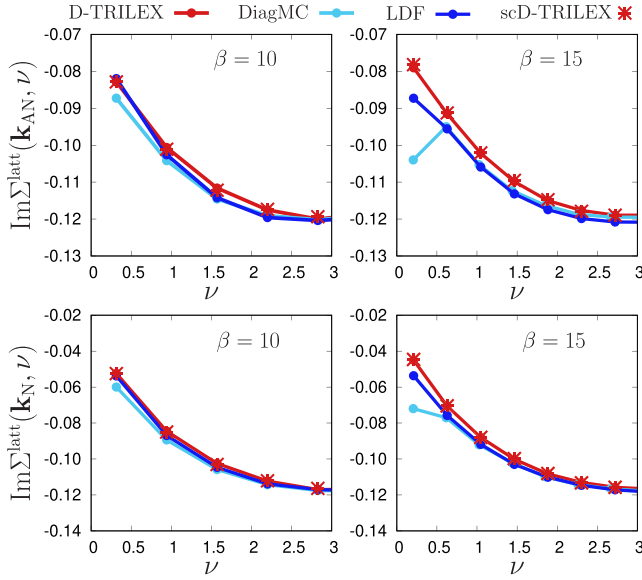


FIG. 4. Imaginary part of the lattice self-energy as the function of Matsubara frequency ν obtained for $U = 2$ at the antinodal AN $= (0, \pi)$ (top row) and nodal N $= (\pi/2, \pi/2)$ (bottom row) points. Results are calculated at the inverse temperature $\beta = 10$ (left column) and $\beta = 15$ (right column) using D-TRILEX (red line), scD-TRILEX (red stars), and LDF (dark blue line) approaches. The DiagMC results (light blue line) are provided by the authors of Ref. [4].

stems from the singlet bosonic mode makes only 3% of the D-TRILEX self-energy at $U = 2$, and does not exceed 1% for other interaction strength. Taking into account all above discussions, this result confirms that all particle-particle fluctuations can indeed be safely excluded from the simple D-TRILEX theory, which, however, does not hold for every diagrammatic approach.

C. Low-temperature regime

In the previous section we considered only the high-temperature regime ($\beta = 2$), where AFM fluctuations are not very strong especially at $U = 2$ and 4. As the next step, we perform calculations at substantially lower temperatures

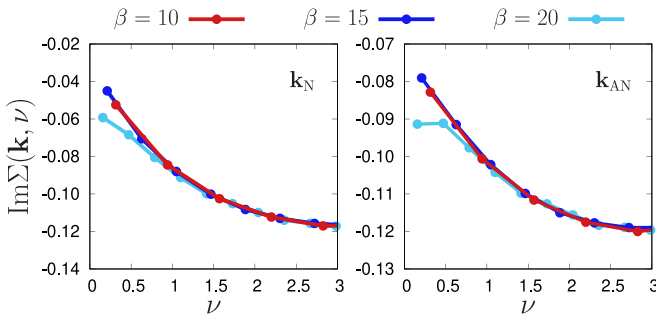


FIG. 5. Imaginary part of the D-TRILEX self-energy as the function of Matsubara frequency ν obtained for $U = 2$ at the nodal N $= (\pi/2, \pi/2)$ (left panel) and antinodal AN $= (0, \pi)$ (right panel) points for different inverse temperatures $\beta = 10$ (red line), $\beta = 15$ (dark blue line), and $\beta = 20$ (light blue line).

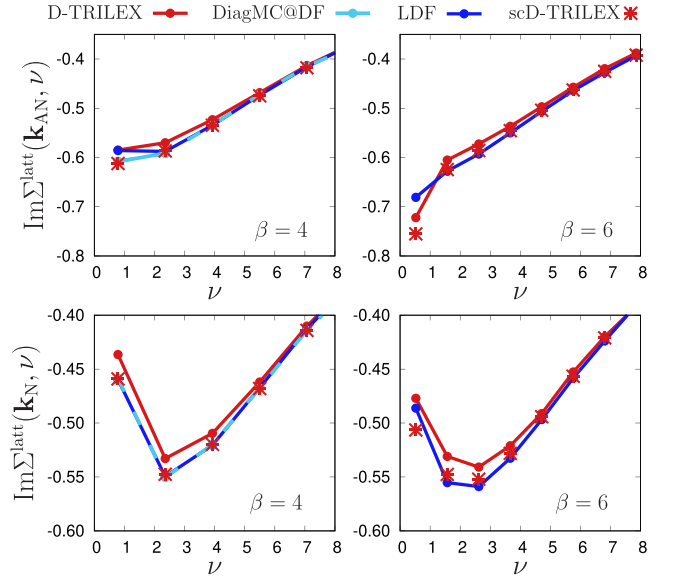


FIG. 6. Imaginary part of the lattice self-energy as the function of Matsubara frequency ν obtained for $U = 4$ at the AN (top row) and N (bottom row) points. Results are calculated at the inverse temperature $\beta = 4$ (left column) and $\beta = 6$ (right column) using D-TRILEX (red line), scD-TRILEX (red stars), and LDF (dark blue line) approaches. The reference DiagMC@DF result (light blue line) is presented only for $\beta = 4$ and is reproduced by the scD-TRILEX method.

around the DMFT Néel point for the interaction strengths up to a half of the bandwidth ($U \leq 4$). A detailed investigation of the Hubbard model for $U = 2$ and different temperatures has been performed in the recent work [4]. This allows for a direct comparison of LDF and D-TRILEX results with the exact DiagMC solution of the lattice problem (1) presented in that paper. For $U = 4$ we consider only the LDF, the D-TRILEX, and the DiagMC@DF methods due to the lack of the lattice DiagMC reference data. The LDF, the D-TRILEX, and the DiagMC@DF results are obtained on the basis of the converged DMFT solution in the same way as in the previous section. In addition, we also performed fully self-consistent (sc) D-TRILEX calculations, for which the fermionic hybridization function Δ_ν of the impurity problem was updated imposing the following self-consistency condition on the local part of the dual Green's function $\sum_{\mathbf{k}} \tilde{G}_{\mathbf{k}\nu} = 0$ (see, e.g., Ref. [26]).

As has been demonstrated in Ref. [4], upon lowering the temperature even a weakly interacting system goes from a metallic regime, which is characterised by the imaginary part of the self-energy extrapolating to zero at low Matsubara frequencies, to a correlated regime where a pseudogap opens. The latter can be explained by a Slater mechanism [96] associated with the increase of long-range AFM fluctuations of itinerant electrons. The pseudogap opens first at the AN point, which can be detected by the change of the sign in the slope of the self-energy between the first and the second Matsubara frequency. This N/AN dichotomy appears due to additional suppression of the coherence of single-particle excitations due to the presence of the van Hove singularity at the AN point.

Figure 4 shows that despite a small mismatch at the first Matsubara frequency the LDF and D-TRILEX methods

correctly reproduce the DiagMC result at $U = 2$ and $\beta = 10$ above the DMFT Néel point ($\beta_N \simeq 12.5$). Moreover, both D-TRILEX approaches provide identical results for the self-energy, which almost exactly coincides with the one of the LDF approach. Below the DMFT Néel point at $\beta = 15$ the DiagMC self-energy already shows the formation of a pseudogap at the AN point, while the D-TRILEX and the LDF still exhibit a metallic behavior. However, for all other frequencies than the first one the LDF self-energy remains in a very good agreement with the exact result. In its turn, the D-TRILEX self-energy starts to deviate from the LDF result, and this discrepancy is more visible at the AN point. We recall that close to the AFM instability collective fluctuations become strongly anharmonic [5]. In particular, this anharmonicity is significant in the Slater regime of weak interactions, where the magnetic fluctuations are formed by itinerant electrons. As a consequence, one can expect that in this regime the transverse modes start to play an important role [37–39]. We note that in the D-TRILEX method these transverse contributions are fully discarded, while the LDF approach at least accounts for them in the local four-point vertex function of the impurity problem. This fact explains why the LDF shows the formation of the pseudogap at the AN point at a bit lower temperature $T_*^{\text{AN}} = 0.059$ ($\beta = 17$, see Ref. [97]) than the one of the DiagMC method $T_*^{\text{AN}} = 0.065$ [4], and the D-TRILEX approach captures it at $T_*^{\text{AN}} = 0.050$ ($\beta = 20$, see Fig. 5). This also explains the result that the most noticeable deviation of the self-energy from the exact result corresponds to the D-TRILEX method and appears at the AN point where the pseudogap opens first.

Now we increase the strength of the interaction to $U = 4$ (Fig. 6) and find that at $\beta = 4$ slightly above the DMFT Néel point ($\beta_N \simeq 4.3$) the D-TRILEX self-energy is in a good agreement with the LDF result for the AN point and shows the beginning of the formation of a pseudogap. In its turn, the LDF approach agrees with the DiagMC@DF theory for all frequencies except for the first one. At the N point the LDF self-energy lies on top of the DiagMC@DF curve, but the deviation of the D-TRILEX method from the reference result is more visible. However, the fully self-consistent calculation strongly improves the D-TRILEX self-energy, which now perfectly agrees with the DiagMC@DF result. At $\beta = 6$ below the DMFT Néel point the DiagMC@DF result suffers from the convergence issue [37,38] and is not shown here. All other considered methods show an insulating self-energy at the AN point, while the N point remains metallic. This result confirms the N/AN dichotomy in the formation of a pseudogap. Also, this result suggests that at moderate interactions collective magnetic fluctuations are less anharmonic in contrast to the weakly interacting regime. This fact can be attributed to a more localized behavior of electrons when going away from Slater towards Heisenberg regime of magnetic fluctuations. As a consequence, for stronger interactions the formation of the AFM pseudogap can be captured by simpler ladderlike theories. We also note that at moderate interactions the discrepancy between the D-TRILEX and the LDF approaches slightly increases upon lowering the temperature. However, the self-consistent update of the hybridization function Δ_ν again improves the agreement between both methods. As explicitly stated in Sec. II, in dual theories the hybridization

function Δ_ν is added to the reference system \mathcal{S}_{imp} and subtracted from the remaining part of the action \mathcal{S}_{rem} so that the initial problem (1) remains unchanged. Therefore, if the dual problem (6) is solved exactly, Δ_ν can be taken arbitrarily. At the same time, any approximate solution depends on the choice for the hybridization function. In the latter case, the imposed self-consistency condition aims at tuning Δ_ν in such a way that it accounts for the effect of missing diagrams. In this context the fact that at $U = 2$ both sc and non-sc D-TRILEX methods produce identical results demonstrates that the impurity problem of DMFT serves as good reference system in the weakly interacting regime. On the contrary, already for moderate interaction $U = 4$ the self-consistency clearly improves the result of the D-TRILEX approach, which shows that in this case the DMFT impurity problem does not provide the best possible starting point for partial diagrammatic resummations.

D. Doped regime of the t - t' Hubbard model

The two-dimensional Hubbard model on a square lattice with nearest-neighbor t and next-nearest-neighbor t' hopping amplitudes is widely known as a prototype model for high-temperature superconducting cuprate compounds. The opening of a pseudogap and the dichotomy between the N and AN points in this model has been studied recently in Ref. [93] in the framework of the exact DiagMC method. There, the authors considered the following set of model parameters $t' = -0.3$, $U = 5.6$, $\beta = 5$, and 4% hole doping that leads to a largest onset temperature for the pseudogap. In our work we address this physically interesting regime for a comparable hole doping of 3.4% within the scD-TRILEX and DiagMC@DF approaches. The obtained self-energies are compared with the exact result of DiagMC method that was provided by the authors of the Ref. [93]. For the sake of consistency, the DiagMC@DF expansion was performed based on the impurity problem of the scD-TRILEX approach.

In Fig. 7 we compare the imaginary part of the non-local self-energy $\Sigma_{\mathbf{k},\nu_0}^{\text{nonloc}}$ calculated for the first Matsubara frequency along the high-symmetry path in momentum space for all three approaches. To obtain this quantity we subtract the local part $\Sigma_{\mathbf{k},\nu_0}^{\text{loc}}$ from the lattice self-energy $\Sigma_{\mathbf{k},\nu_0}^{\text{latt}}$, where $\Sigma_{\mathbf{k},\nu_0}^{\text{loc}} = \sum_{\mathbf{k}} \Sigma_{\mathbf{k},\nu_0}^{\text{latt}}$. Due to the lack of reference DiagMC data, the sum over the Brillouin zone in this expression is approximated by the sum over the high-symmetry path in momentum space. We find that the nonlocal part of the DiagMC@DF self-energy is in a very good agreement with the reference DiagMC result. The scD-TRILEX approach also performs remarkably good in this physically nontrivial regime, especially given that the considered value of the local Coulomb interaction $U = 5.6$ exceeds the half of the bandwidth. This good agreement in $\text{Im} \Sigma_{\mathbf{k},\nu_0}^{\text{nonloc}}$ indicates that the simple ladderlike scD-TRILEX method accurately captures the N/AN dichotomy in the formation of a pseudogap in this regime [93]. This fact additionally confirms our finding that going away from the Slater regime allows to use less sophisticated methods to capture the effect of collective fluctuations.

At the same time we find that the DiagMC@DF and the scD-TRILEX methods do not provide a good value for the local part of the lattice self-energy. Indeed, $\text{Im} \Sigma_{\mathbf{k},\nu_0}^{\text{loc}}$ of the

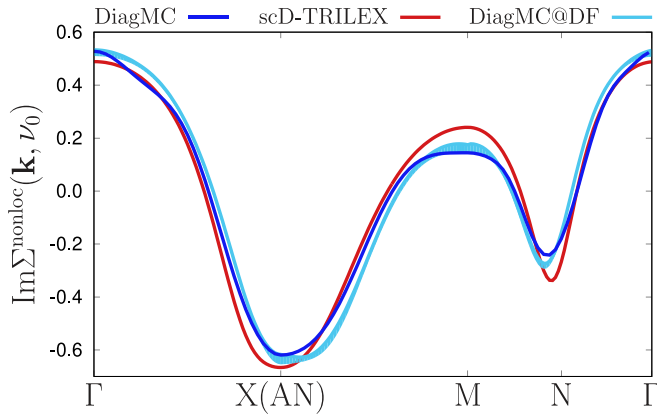


FIG. 7. Imaginary part of the nonlocal self-energy obtained for the zeroth Matsubara frequency $\nu_0 = \pi/\beta$ along the high-symmetry path in momentum space \mathbf{k} . Calculations are performed for $U = 5.6$, $t' = -0.3$, and $\beta = 5$ using scD-TRILEX (red line) and DiagMC@DF (light blue line) methods for 3.4% hole doping. The DiagMC result (dark blue line) for 4% doping is provided by the authors of Ref. [93].

DiagMC@DF calculated for the zeroth Matsubara frequency is equal to -0.77 . The corresponding value for the scD-TRILEX approach is -0.80 , while the exact DiagMC result reads as -1.04 . This discrepancy can again be explained by the fact that DMFT impurity problem does not provide a good starting point for a diagrammatic expansion already for moderate interactions. To address this issue, we exploited the dual self-consistency condition to update the fermionic hybridization as an attempt for the improvement of the reference system (see Sec. III C). However, the result obtained in this section clearly demonstrates the need for an even better starting point, which should be able to provide more accurate local quantities to reproduce the exact result.

IV. CONCLUSION

To conclude, in this work we investigated the effect of different collective fluctuations on the single-particle properties of correlated electronic systems. In order to disentangle local and nonlocal effects, we introduced an effective reference system: a local impurity problem. This effective local problem has been solved numerically exactly providing building blocks for a diagrammatic expansion aiming at describing nonlocal correlation effects. Following the dual fermion and boson idea, we performed this diagrammatic expansion in the dual space truncating the interaction at the two-particle level and thus preserving only the local renormalized four-point vertex function. Using the partially bosonized representation for this four-point vertex, we investigated the effect of different bosonic modes contributing to the vertex on the electronic self-energy. Performing a comprehensive analysis based on DiagMC, DiagMC@DF, LDF, and D-TRILEX approaches, we have found that irreducible contributions that are not accounted for by the partially bosonized vertex function can be excluded from the theory in a broad range of physical parameters. Indeed, they can be completely eliminated in the ladder approximation by a special choice of the bare local interac-

tion in different channels. In a weakly interacting regime, the remaining nonladder contributions have only a minor effect on the electronic self-energy, and at large interactions these contributions are nearly canceled by transverse singlet fluctuations. In turn, these transverse singlet modes partially cancel transverse particle-hole fluctuations in weakly and moderately interacting regimes. Finally, longitudinal singlet bosonic modes have been found to be negligibly small in all considered cases. All these results confirm that in a broad regime of physical parameters the leading contribution to the self-energy is given by the longitudinal particle-hole bosonic modes. This important statement allows for a drastic simplification of the diagrammatic expansion, which implies a huge reduction of computational efforts. Consequently, the D-TRILEX theory, which appears as the result of this simplification, looks as a very promising and powerful tool for solving a broad class of interacting electronic problems.

At the same time, the theory should not be oversimplified. Thus, we have shown that considering only second-order dual self-energy does not provide a good result even at weak and moderate interactions when the system enters the correlated regime lowering the temperature. Instead, the D-TRILEX method performs remarkably good even below the DMFT Néel temperature in the regime where the AFM pseudogap starts to develop. A good performance of the D-TRILEX theory has been confirmed in the moderately correlated half-filled regime of the Hubbard model, and in the case of a t - t' model for hole-doped cuprate compounds. Importantly, in the latter case we have found that the D-TRILEX approach provides a reasonably accurate result for the nonlocal part of the self-energy, while the local part is not reproduced correctly. This fact indicates that DMFT does not always provide an optimal way of constructing the local reference (impurity) problem. We have also found that the simple ladderlike D-TRILEX theory fails to correctly reproduce the pseudogap formation in the weakly interacting Slater regime of magnetic fluctuations. This can be explained by a strong anharmonicity of collective fluctuations of itinerant electrons close to the AFM instability. On the contrary, increasing the local Coulomb interaction drives the system away from the Slater regime. Thus, the electrons become more localized and their collective behavior turns more harmonic, which can be captured by less demanding ladderlike methods.

ACKNOWLEDGMENTS

The authors thank A. Georges, E. Kozik, M. Ferrero, F. Šimkovic, R. Rossi, and W. Wu for discussions and for providing the DiagMC data. The authors also thank J. Gukelberger for the help with the original DiagMC@DF code. The work of E.A.S. was supported by the European Union's Horizon 2020 Research and Innovation programme under the Marie Skłodowska Curie Grant Agreement No. 839551-2DMAGICS. The work of A.I.L. is supported by European Research Council via Synergy Grant No. 854843-FASTCORR. V.H., M.V., S.B., and A.I.L. acknowledge the support by the Cluster of Excellence "CUI: Advanced Imaging of Matter" of the Deutsche Forschungsgemeinschaft (DFG) - EXC 2056 - project ID 390715994. The authors also

acknowledge the support by North-German Supercomputing Alliance (HLRN) under the Project No. hhp00042.

APPENDIX A: DUAL BOSON THEORY

The explicit derivation of the DB method can be found in many previous papers on the topic [30–34,60]. However, for the purpose of this work we have to additionally intro-

duce bosonic variables for the singlet channel. For this reason here we present a brief derivation of the dual boson theory one more time. We start with the remaining part of the lattice action (1)

$$\mathcal{S}_{\text{rem}} = - \sum_{k,\sigma} c_{k\sigma}^* [\Delta_\nu - \varepsilon_{\mathbf{k}}] c_{k\sigma} + \sum_{q,\vartheta} \xi^\vartheta \{ \rho_q^{*\vartheta} V_{\mathbf{q}}^\vartheta \rho_q^\vartheta \}. \quad (\text{A1})$$

Let us perform two Hubbard-Stratonovich transformations:

$$\exp \left\{ \sum_{k,\sigma} c_{k\sigma}^* [\Delta_\nu - \varepsilon_{\mathbf{k}}] c_{k\sigma} \right\} = \mathcal{D}_f \int D[f^*, f] \exp \left\{ - \sum_{k,\sigma} (f_{k\sigma}^* g_{v\sigma}^{-1} [\Delta_\nu - \varepsilon_{\mathbf{k}}]^{-1} g_{v\sigma}^{-1} f_{k\sigma} + f_{k\sigma}^* g_{v\sigma}^{-1} c_{k\sigma} + c_{k\sigma}^* g_{v\sigma}^{-1} f_{k\sigma}) \right\}, \quad (\text{A2})$$

$$\exp \left\{ - \sum_{q,\vartheta} \xi^\vartheta (\rho_q^{*\vartheta} V_{\mathbf{q}}^\vartheta \rho_q^\vartheta) \right\} = \mathcal{D}_\varphi \int D[\varphi^\vartheta] \exp \left\{ \sum_{q,\vartheta} \xi^\vartheta (\varphi_q^{*\vartheta} \alpha_\omega^{\vartheta-1} V_{\mathbf{q}}^{\vartheta-1} \alpha_\omega^{\vartheta-1} \varphi_q^\vartheta - \varphi_q^{*\vartheta} \alpha_\omega^{\vartheta-1} \rho_q^\vartheta - \rho_q^{*\vartheta} \alpha_\omega^{\vartheta-1} \varphi_q^\vartheta) \right\}. \quad (\text{A3})$$

Here, quantities g_ν and w_ω^ϑ are the full Green's function and the renormalized interaction of the local impurity problem, respectively, and $\alpha_\omega^\vartheta = w_\omega^\vartheta / U^\vartheta$. Terms $\mathcal{D}_f = \det[g_\nu(\Delta_\nu - \varepsilon_{\mathbf{k}})g_\nu]$ and $\mathcal{D}_\varphi^{-1} = -\sqrt{\det[\alpha_\omega^\vartheta V_{\mathbf{q}}^\vartheta \alpha_\omega^\vartheta]}$ can be neglected when calculating expectation values. After these transformations the action takes the form

$$\begin{aligned} \mathcal{S}'_{\text{rem}} = & \sum_i \mathcal{S}_{\text{imp}}^{(i)} + \sum_{k,\sigma} (f_{k\sigma}^* g_{v\sigma}^{-1} c_{k\sigma} + c_{k\sigma}^* g_{v\sigma}^{-1} f_{k\sigma}) + \sum_{q,\vartheta} \xi^\vartheta (\varphi_q^{*\vartheta} \alpha_\omega^{\vartheta-1} \rho_q^\vartheta + \rho_q^{*\vartheta} \alpha_\omega^{\vartheta-1} \varphi_q^\vartheta) \\ & - \sum_{k,\sigma} f_{k\sigma}^* g_{v\sigma}^{-1} [\varepsilon_{\mathbf{k}} - \Delta_\nu]^{-1} g_{v\sigma}^{-1} f_{k\sigma} - \sum_{q,\vartheta} \xi^\vartheta (\varphi_q^{*\vartheta} [\alpha_\omega^\vartheta V_{\mathbf{q}}^\vartheta \alpha_\omega^\vartheta]^{-1} \varphi_q^\vartheta). \end{aligned} \quad (\text{A4})$$

Then, the impurity problem can be integrated out as

$$\begin{aligned} & \int D[c^*, c] \exp \left\{ - \sum_i \mathcal{S}_{\text{imp}}^{(i)} - \sum_{k,\sigma} (f_{k\sigma}^* g_{v\sigma}^{-1} c_{k\sigma} + c_{k\sigma}^* g_{v\sigma}^{-1} f_{k\sigma}) - \sum_{q,\vartheta} \xi^\vartheta (\varphi_q^{*\vartheta} \alpha_\omega^{\vartheta-1} \rho_q^\vartheta + \rho_q^{*\vartheta} \alpha_\omega^{\vartheta-1} \varphi_q^\vartheta) \right\} \\ & = \mathcal{Z}_{\text{imp}} \times \exp \left\{ - \sum_{k,\sigma} f_{k\sigma}^* g_{v\sigma}^{-1} f_{k\sigma} - \sum_{q,\vartheta} \xi^\vartheta (\varphi_q^{*\vartheta} \alpha_\omega^{\vartheta-1} \chi_\omega^\vartheta \alpha_\omega^{\vartheta-1} \varphi_q^\vartheta) - \tilde{\mathcal{F}}[f, \varphi] \right\}, \end{aligned} \quad (\text{A5})$$

where \mathcal{Z}_{imp} and $\chi_\omega^\vartheta = -\langle \rho_\omega^\vartheta \rho_\omega^{*\vartheta} \rangle$ are the partition function and the susceptibility of the impurity problem, respectively. This results in the dual boson action

$$\tilde{\mathcal{S}} = - \sum_{k,\sigma} f_{k\sigma}^* \tilde{\mathcal{G}}_{k\sigma}^{-1} f_{k\sigma} - \sum_{q,\vartheta} \xi^\vartheta \{ \varphi_q^{*\vartheta} \tilde{\mathcal{W}}_q^{\vartheta-1} \varphi_q^\vartheta \} + \tilde{\mathcal{F}}[f, \varphi]. \quad (\text{A6})$$

The explicit form of the bare fermionic and bosonic propagators of the dual problem is

$$\tilde{\mathcal{G}}_{k\sigma} = g_{v\sigma} [\varepsilon_{\mathbf{k}} - \Delta_\nu]^{-1} - g_{v\sigma} = \check{\mathcal{G}}_{k\sigma} - g_{v\sigma}, \quad (\text{A7})$$

$$\tilde{\mathcal{W}}_q^\vartheta = \alpha_\omega^\vartheta [V_{\mathbf{q}}^{\vartheta-1} - \chi_\omega^\vartheta]^{-1} \alpha_\omega^\vartheta = \check{\mathcal{W}}_q^\vartheta - w_\omega^\vartheta, \quad (\text{A8})$$

where $\check{\mathcal{G}}_{k\sigma}$ and $\check{\mathcal{W}}_q^\vartheta$ are the Green's function and renormalized interaction of EDMFT.

The interaction part of the action $\tilde{\mathcal{F}}[f, \varphi]$ being truncated to the two-particle level explicitly reads as

$$\begin{aligned} \tilde{\mathcal{F}}[f, \varphi] \simeq & \sum_{q,k,\vartheta} \xi^\vartheta \{ \Lambda_{v\omega}^\vartheta \eta_{q,k}^{*\vartheta} \varphi_q^\vartheta + \Lambda_{v\omega}^{*\vartheta} \varphi_q^{*\vartheta} \eta_{q,k}^\vartheta \} \\ & + \frac{1}{4} \sum_{q,\{k\},\{\sigma\}} \Gamma_{ph, v\nu'\omega}^{\sigma\sigma'\sigma''\sigma'''} f_{k\sigma}^* f_{k+q,\sigma'} f_{k'+q,\sigma''}^* f_{k'\sigma'''}, \end{aligned} \quad (\text{A9})$$

where $\eta_{q,k}^\vartheta$ have been defined in Eqs. (14), (15), and (16). The four-point vertex functions in the particle-hole Γ_{ph} and particle-particle Γ_{pp} form are defined as

$$\begin{aligned} \Gamma_{ph, v\nu'\omega}^{\sigma_1\sigma_2\sigma_3\sigma_4} &= \frac{\langle c_{v\sigma_1} c_{v+\omega,\sigma_2}^* c_{v'\sigma_3}^* c_{v'+\omega,\sigma_4} \rangle_c}{g_{v\sigma_1} g_{v+\omega,\sigma_2} g_{v'\sigma_3} g_{v'+\omega,\sigma_4}}, \\ \Gamma_{pp, v\nu'\omega}^{\sigma_1\sigma_2\sigma_3\sigma_4} &= \frac{\langle c_{v\sigma_1} c_{\omega-\nu,\sigma_2}^* c_{v'\sigma_3}^* c_{\omega-\nu',\sigma_4} \rangle_c}{g_{v\sigma_1} g_{\omega-\nu,\sigma_2} g_{v'\sigma_3} g_{\omega-\nu',\sigma_4}}, \end{aligned} \quad (\text{A10})$$

where $\langle \dots \rangle_c$ denotes the connected part of the correlation function. The following relation between two representations holds:

$$\Gamma_{pp, v\nu'\omega}^{\sigma_1\sigma_2\sigma_3\sigma_4} = \Gamma_{ph, v,\omega-\nu',\nu'-\nu}^{\sigma_1\sigma_3\sigma_4\sigma_2} = -\Gamma_{ph, v,\nu',\omega-\nu-\nu'}^{\sigma_1\sigma_4\sigma_3\sigma_2}. \quad (\text{A11})$$

Density (d), magnetic (m), singlet (s), and triplet (t) components of the four-point vertex are defined as

$$\begin{aligned} \Gamma_{v\nu'\omega}^{\text{d/m}} &= \Gamma_{ph, v\nu'\omega}^{\uparrow\uparrow\uparrow\uparrow} \pm \Gamma_{ph, v\nu'\omega}^{\uparrow\uparrow\downarrow\downarrow}, \\ \Gamma_{v\nu'\omega}^{\text{s/t}} &= \frac{1}{2} \Gamma_{pp, v\nu'\omega}^{\uparrow\downarrow\uparrow\downarrow} \mp \frac{1}{2} \Gamma_{pp, v\nu'\omega}^{\uparrow\downarrow\downarrow\uparrow}. \end{aligned} \quad (\text{A12})$$

The three-point interactions in the channel representation are defined as

$$\Lambda_{\nu\omega}^{\zeta} = \frac{\langle c_{\nu\uparrow} c_{\nu+\omega\uparrow}^* \rho_{\omega}^{\zeta} \rangle}{g_{\nu\uparrow} g_{\nu+\omega\uparrow} \alpha_{\omega}^{\zeta}}; \quad \Lambda_{\nu\omega}^{*\zeta} = \frac{\langle c_{\nu+\omega\uparrow} c_{\nu\uparrow}^* \rho_{\omega}^{\zeta} \rangle}{g_{\nu+\omega\uparrow} g_{\nu\uparrow} \alpha_{\omega}^{\zeta}};$$

$$\Lambda_{\nu\omega}^s = \frac{\langle c_{\nu\uparrow} c_{\omega-\nu\downarrow} \rho_{\omega}^s \rangle}{g_{\nu\uparrow} g_{\omega-\nu\downarrow} \alpha_{\omega}^s}; \quad \Lambda_{\nu\omega}^{*s} = \frac{\langle c_{\omega-\nu\downarrow} c_{\nu\uparrow}^* \rho_{\omega}^s \rangle}{g_{\omega-\nu\downarrow} g_{\nu\uparrow} \alpha_{\omega}^s}. \quad (\text{A13})$$

In the particle-hole channel the three-point vertex obeys the useful relation $\Lambda_{\nu\omega}^{*\zeta} = \Lambda_{\nu+\omega,-\omega}^{\zeta}$. The three-point vertex in the triplet channel is not introduced because the composite variable ρ^t is identically zero in the single-band case.

It is important to note that in dual diagrams the bosonic line always connects two three-point vertex functions. Using Eqs. (A8) and (A13), one finds that

$$\Lambda_{\nu\omega}^{\vartheta} \tilde{W}_q^{\vartheta} \Lambda_{\nu\omega}^{*\vartheta} \sim \alpha_{\nu\omega}^{\vartheta-1} \tilde{W}_q^{\vartheta} \alpha_{\nu\omega}^{\vartheta-1} = [V_q^{\vartheta-1} - \chi_{\omega}^{\vartheta}]^{-1}. \quad (\text{A14})$$

This relation shows that $\alpha_{\omega}^{\vartheta}$, which is the only quantity that explicitly contains the bare local interaction U^{ϑ} , drops out from the dual diagrammatics. Therefore, physical observables that can be found via the exact relation between correlation function written in terms of dual f and original c fermion variables also do not depend on the choice of the bare in-

teraction U^{ϑ} for different bosonic channels. This fact is not surprising because the onsite Coulomb interaction U is fully accounted by the impurity problem and is already contained in the four-point vertex.

APPENDIX B: D-TRILEX THEORY

In this Appendix we explicitly show the transformation that reduces the dual boson problem (6) to the fermion-boson action (13) of the D-TRILEX theory. The key idea is to find such Hubbard-Stratonovich transformation that produces the interaction in the partially bosonized form of Eq. (9) that nearly cancels the exact four-point vertex function from the theory. To this aim let us first add and subtract the term

$$\sum_{q,\vartheta} \xi^{\vartheta} (\varphi_q^{*\vartheta} \bar{w}_{\omega}^{\vartheta-1} \varphi_q^{\vartheta}) \quad (\text{B1})$$

from the dual action (A6). At this step one can consider $\bar{w}_{\omega}^{\vartheta}$ as an arbitrary function that will be determined later. This procedure will allow us to integrate out dual bosonic fields φ with respect to the arbitrary Gaussian part of the action introduced in Eq. (B1). To illustrate this point, we make use of following Hubbard-Stratonovich transformations:

$$\exp \left\{ \sum_{q,\vartheta} \xi^{\vartheta} \varphi_q^{*\vartheta} [\tilde{W}_q^{\vartheta-1} + \bar{w}_{\omega}^{\vartheta-1}] \varphi_q^{\vartheta} \right\}$$

$$= \mathcal{D}_b \int D[b^{\vartheta}] \exp \left\{ - \sum_{q,\vartheta} \xi^{\vartheta} (b_q^{*\vartheta} \bar{w}_{\omega}^{\vartheta-1} [\tilde{W}_q^{\vartheta-1} + \bar{w}_{\omega}^{\vartheta-1}]^{-1} \bar{w}_{\omega}^{\vartheta-1} b_q^{\vartheta} - \varphi_q^{*\vartheta} \bar{w}_{\omega}^{\vartheta-1} b_q^{\vartheta} - b_q^{*\vartheta} \bar{w}_{\omega}^{\vartheta-1} \varphi_q^{\vartheta}) \right\}, \quad (\text{B2})$$

where $\mathcal{D}_b^{-1} = \sqrt{\det[\bar{w}_{\omega}^{\vartheta} (\tilde{W}_q^{\vartheta-1} + \bar{w}_{\omega}^{\vartheta-1}) \bar{w}_{\omega}^{\vartheta}]}$. The action transforms to

$$\tilde{\mathcal{S}} = - \sum_{k,\sigma} f_{k\sigma}^* \tilde{\mathcal{G}}_{k\sigma}^{-1} f_{k\sigma} + \sum_{q,\vartheta} \xi^{\vartheta} \{ b_q^{*\vartheta} \bar{w}_{\omega}^{\vartheta-1} [\tilde{W}_q^{\vartheta-1} + \bar{w}_{\omega}^{\vartheta-1}]^{-1} \bar{w}_{\omega}^{\vartheta-1} b_q^{\vartheta} \}$$

$$+ \sum_{q,\vartheta} \xi^{\vartheta} \{ \varphi_q^{*\vartheta} \bar{w}_{\omega}^{\vartheta-1} \varphi_q^{\vartheta} - \varphi_q^{*\vartheta} \bar{w}_{\omega}^{\vartheta-1} b_q^{\vartheta} - b_q^{*\vartheta} \bar{w}_{\omega}^{\vartheta-1} \varphi_q^{\vartheta} \} + \tilde{\mathcal{F}}[f, \varphi]. \quad (\text{B3})$$

Finally, dual bosonic fields φ can be integrated out with respect to the new Gaussian part of the dual action as

$$\int D[\varphi^{\zeta}] \exp \left\{ - \sum_{q,k,\vartheta} \xi^{\vartheta} (\varphi_q^{*\vartheta} \bar{w}_{\omega}^{\vartheta-1} \varphi_q^{\vartheta} - \varphi_q^{*\vartheta} [\bar{w}_{\omega}^{\vartheta-1} b_q^{\vartheta} - \Lambda_{\nu\omega}^{*\vartheta} \eta_{q,k}^{\vartheta}] - [b_q^{*\vartheta} \bar{w}_{\omega}^{\vartheta-1} - \eta_{q,k}^{*\vartheta} \Lambda_{\nu\omega}^{\vartheta}] \varphi_q^{\vartheta}) \right\}$$

$$= \mathcal{Z}_{\varphi} \times \exp \left\{ \sum_{q,k,\vartheta} \xi^{\vartheta} (b_q^{*\vartheta} \bar{w}_{\omega}^{\vartheta-1} b_q^{\vartheta} - \Lambda_{\nu\omega}^{\vartheta} \eta_{q,k}^{*\vartheta} b_q^{\vartheta} - \Lambda_{\nu\omega}^{*\vartheta} b_q^{*\vartheta} \eta_{q,k}^{\vartheta} + \eta_{q,k}^{*\vartheta} \Lambda_{\nu\omega}^{\vartheta} \bar{w}_{\omega}^{\vartheta} \Lambda_{\nu\omega}^{*\vartheta} \eta_{q,k}^{\vartheta}) \right\}, \quad (\text{B4})$$

where \mathcal{Z}_{φ} is a partition function of the Gaussian part of the bosonic action. Being written in the antisymmetrized form, the quartic term $\eta_{q,k}^{*\vartheta} \Lambda_{\nu\omega}^{\vartheta} \bar{w}_{\omega}^{\vartheta} \Lambda_{\nu\omega}^{*\vartheta} \eta_{q,k}^{\vartheta}$ in Eq. (B4) makes the partially bosonized representation for the four-point vertex specified in Eq. (9) [60]. Since this effective vertex function is generated with the opposite sign, it cancels the exact four-point vertex if $\bar{w}_{\omega}^{\vartheta}$ is defined as in Eqs. (11) and (12). After that, the dual problem reduces to the action of the D-TRILEX theory (13).

APPENDIX C: RELATION BETWEEN DB AND D-TRILEX DIAGRAMS

In this Appendix we establish the relation between ladder DB and D-TRILEX diagrams for the self-energy. As shown in Ref. [32], the LDB diagrams for the self-energy and polarization operator can be obtained from the dual functional, which yields

$$\tilde{\Sigma}_{k\sigma}^{\text{LDB}} = \tilde{\Sigma}_{k\sigma}^{\text{LDF}} + \tilde{\Sigma}_{k\sigma}^{\text{mix}}. \quad (\text{C1})$$

The ladder DF self-energy

$$\tilde{\Sigma}_{k\sigma}^{\text{LDF}} = \tilde{\Sigma}_{k\sigma}^{\text{ladd}} - \tilde{\Sigma}_{k\sigma}^{(2)} \quad (\text{C2})$$

is given by the two-particle ladder diagram

$$\tilde{\Sigma}_{k\sigma}^{\text{ladd}} = - \sum_{q,k',\{\sigma\}} \tilde{G}_{k+q,\sigma'} \mathbf{P}_{ph, v\nu'q}^{\sigma\sigma'\sigma''\sigma'''} \delta_{kk'} \delta_{\sigma\sigma''} \delta_{\sigma'\sigma'''} \quad (\text{C3})$$

As follows from the Schwinger-Dyson for the dual self-energy, the ladder diagram accounts for twice the contribution of the second-order self-energy [82]

$$\Sigma_{k\sigma}^{(2)} = -\frac{1}{2} \sum_{q,k',\{\sigma\}} \Gamma_{ph, v\nu'\omega}^{\sigma\sigma'\sigma''\sigma'''} \tilde{G}_{k',\sigma''} \tilde{G}_{k'+q,\sigma'''} \tilde{G}_{k+q,\sigma'} \Gamma_{ph, v'\nu\omega}^{\sigma''\sigma'''\sigma\sigma'} \quad (\text{C4})$$

which has to be excluded from the expression (C2) in order to avoid the double counting. The mixed diagram that additionally appears in the DB theory due to the presence of the bosonic propagator \tilde{W}_q^ζ is as follows:

$$\tilde{\Sigma}_{k\sigma}^{\text{mix}} = - \sum_{q,\zeta} L_{\nu q}^\zeta \tilde{G}_{q+k,\sigma} \tilde{W}_q^\zeta L_{\nu q}^{*\zeta} \quad (\text{C5})$$

Dressed dual fermionic and bosonic propagators can be found using corresponding Dyson equations

$$\tilde{G}_{k\sigma}^{-1} = \tilde{G}_{k\sigma}^{-1} - \tilde{\Sigma}_{k\sigma}, \quad (\text{C6})$$

$$\tilde{W}_q^{\zeta-1} = \tilde{W}_q^{\zeta-1} - \tilde{\Pi}_q^\zeta, \quad (\text{C7})$$

where the dual polarization operator in the ladder approximation reads as

$$\tilde{\Pi}_q^\zeta = \sum_{k,\sigma} \Lambda_{\nu\sigma}^{*\zeta} \tilde{G}_{k\sigma} \tilde{G}_{q+k,\sigma} L_{\nu q}^\zeta \quad (\text{C8})$$

The screened three- and four-point vertices in the horizontal particle-hole (charge and spin) and particle-particle (singlet) channels are

$$L_{\nu q}^\vartheta = \Lambda_{\nu\omega}^\vartheta + \sum_{k_1} \mathbf{P}_{\nu\nu_1q}^\vartheta \tilde{X}_{k_1,q}^{0\vartheta} \Lambda_{\nu_1\omega}^\vartheta, \quad (\text{C9})$$

$$\mathbf{P}_{\nu\nu'q}^\vartheta = \Gamma_{\nu\nu'\omega}^\vartheta + \sum_{k_1} \mathbf{P}_{\nu\nu_1q}^\vartheta \tilde{X}_{k_1,q}^{0\vartheta} \Gamma_{\nu_1\nu'\omega}^\vartheta. \quad (\text{C10})$$

Here, $\tilde{X}_{k,q}^{0\zeta} = \tilde{G}_{k\sigma} \tilde{G}_{k+q,\sigma}$ and $\tilde{X}_{k,q}^{0s} = -\tilde{G}_{k\uparrow} \tilde{G}_{q-k,\downarrow}$. The screened vertices in the vertical $\tilde{\mathbf{P}}^\zeta$ and horizontal \mathbf{P}^ζ particle-hole channels are connected via the relation $\tilde{\mathbf{P}}_{kk'\omega}^\zeta = -\mathbf{P}_{\nu,\nu+\omega,k'-k}^\zeta$. Note that the DB theory does not account for fluctuations in the particle-particle channel because they are negligibly small in the ladder approximation. Therefore, the LDB self-energy (C1) contains the three- and four-point vertices that are screened only in the particle-hole (ζ) channel. Diagrammatic expressions for the LDB self-energy and polarization operator, as well as for the screened three- and four-point vertices, are shown in Fig. 8.

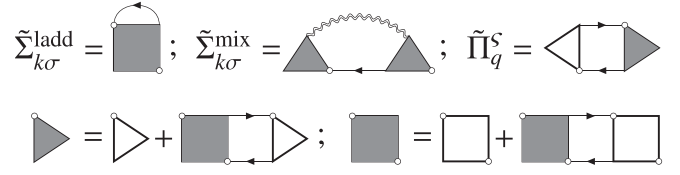


FIG. 8. Top row: ladder $\tilde{\Sigma}_{k\sigma}^{\text{ladd}}$ (C3) and mixed $\tilde{\Sigma}_{k\sigma}^{\text{mix}}$ (C5) contributions to the LDB self-energy, and the LDB polarization operator $\tilde{\Pi}_q^\zeta$ (C8). Bottom row: Screened three-point $L_{\nu q}^\vartheta$ (C9) and four-point $\mathbf{P}_{\nu\nu'q}^\vartheta$ (C10) vertex functions in the LDB approximation.

Let us derive D-TRILEX diagrams for the self-energy as an approximation of the ladder DB theory. To this aim, one can use the partially bosonized representation for the four-point vertex function (9) and keep only longitudinal bosonic fluctuations.

1. First-order self-energy

The first-order contribution to the ladder part of the self-energy (C3) written in the channel representation becomes

$$\begin{aligned} \tilde{\Sigma}_{\nu\sigma}^{(1)} &= - \sum_{q,\sigma'} \tilde{G}_{k+q,\sigma'} \Gamma_{\nu\nu\omega}^{\sigma\sigma'\sigma\sigma'} \\ &= -\frac{1}{2} \sum_{q,\zeta} \tilde{G}_{k+q,\sigma} \Gamma_{\nu\nu\omega}^\zeta \\ &\simeq - \sum_{q,\zeta} \tilde{G}_{k+q,\sigma} M_{\nu\nu\omega}^\zeta + \sum_q \tilde{G}_{q-k,\sigma} M_{\nu\nu\omega}^s \\ &= - \sum_{q,\zeta} \{ \Lambda_{\nu\omega}^\zeta \tilde{G}_{q+k,\sigma} \tilde{w}_\omega^\zeta \Lambda_{\nu\omega}^{*\zeta} - \Lambda_{\nu\omega}^s \tilde{G}_{q-k,\sigma} \tilde{w}_\omega^s \Lambda_{\nu\omega}^{*s} \}. \end{aligned} \quad (\text{C11})$$

Here, a trivial Hartree-type contribution to the dual self-energy $\tilde{\Sigma}_{\nu\sigma}^{\text{H}} = 2\Lambda_{\nu,0}^d \tilde{w}_0^d \sum_{k'} \Lambda_{\nu',0}^d \tilde{G}_{k'\sigma}$ that appears due to $M_{\nu,\nu+\omega,\nu'-\nu}$ terms in Eq. (9) have been omitted for simplicity.

2. Second-order self-energy

The second-order self-energy (C4) can be simplified in the same way. Equation (C4) can first be rewritten in the channel representation as

$$\tilde{\Sigma}_{k,\sigma_1}^{(2)} = -\frac{1}{4} \sum_{k',q,\zeta} \tilde{G}_{k+q} \Gamma_{\nu\nu'\omega}^\zeta \tilde{G}_{k'} \tilde{G}_{k'+q} \Gamma_{\nu'\nu\omega}^\zeta. \quad (\text{C12})$$

We omit spin labels for Green's functions in this expression because in the considered paramagnetic case the Green's function does not depend on the projection of spin. One can again use the partially bosonized representations for the four-point vertex function (9), which leads to

$$\begin{aligned} \tilde{\Sigma}_k^{(2)} &= -\frac{1}{4} \sum_{k',q} \left\{ 4 \sum_s (M_{\nu,\nu',\omega}^s M_{\nu',\nu,\omega}^s + M_{\nu,\nu+\omega,\nu'-\nu}^s M_{\nu',\nu'+\omega,\nu-\nu'}^s) + 4M_{\nu,\nu',\nu+\nu'+\omega}^s M_{\nu',\nu,\nu+\nu'+\omega}^s - 4M_{\nu,\nu',\omega}^d M_{\nu',\nu'+\omega,\nu-\nu'}^d \right. \\ &\quad \left. + 12M_{\nu,\nu',\omega}^m M_{\nu',\nu'+\omega,\nu-\nu'}^m - 24M_{\nu,\nu',\omega}^m M_{\nu',\nu'+\omega,\nu-\nu'}^d + 8M_{\nu,\nu',\omega}^d M_{\nu',\nu,\nu+\nu'+\omega}^s - 24M_{\nu,\nu',\omega}^m M_{\nu',\nu,\nu+\nu'+\omega}^s \right\} \tilde{G}_{k'} \tilde{G}_{k'+q} \tilde{G}_{k+q}. \end{aligned} \quad (\text{C13})$$

Shifting momentum and frequency indices as $k' \rightarrow k + q''$ and $q \rightarrow k'' - k$ one can show that the product of two transverse fluctuations results in the same contribution to the self-energy as the product of two longitudinal ones

$$\begin{aligned} \sum_{k',q} M_{v,v+\omega,v'-v}^{\zeta} M_{v',v'+\omega,v-v'}^{\zeta} \tilde{G}_{k'} \tilde{G}_{k'+q} \tilde{G}_{k+q} &\rightarrow \sum_{k'',q''} M_{v,v'',\omega''}^{\zeta} M_{v+\omega'',v''+\omega'',-\omega''}^{\zeta} \tilde{G}_{k+q''} \tilde{G}_{k''+q''} \tilde{G}_{k''} \\ &= \sum_{k'',q''} M_{v,v'',\omega''}^{\zeta} M_{v'',v,\omega''}^{\zeta} \tilde{G}_{k''} \tilde{G}_{k''+q''} \tilde{G}_{k+q''}. \end{aligned} \quad (\text{C14})$$

The last relation can be obtained imposing the symmetry of the four- and three-point vertex functions (A10) and (A13). The product of two singlet fluctuations can also be simplified shifting $q \rightarrow q'' - k - k'$ as

$$\begin{aligned} \sum_{k',q} M_{v,v',v+v'+\omega}^{\zeta} M_{v',v,v+v'+\omega}^{\zeta} \tilde{G}_{k'} \tilde{G}_{k'+q} \tilde{G}_{k+q} \\ \rightarrow \sum_{k',q''} M_{v,v',\omega''}^{\zeta} M_{v',v,\omega''}^{\zeta} \tilde{G}_{k'} \tilde{G}_{q-k} \tilde{G}_{q-k'}. \end{aligned} \quad (\text{C15})$$

Then, keeping only longitudinal contributions in $\tilde{\Sigma}_{k,\sigma_1}^{(2)}$, one gets the second-order self-energy of the D-TRILEX approach

$$\begin{aligned} \tilde{\Sigma}_{k,\sigma}^{(2)} &\simeq - \sum_{q,\zeta} \tilde{G}_{q+k,\sigma} \Lambda_{v\omega}^{\zeta} \tilde{w}_{\omega}^{\zeta} \left(\sum_{k',\sigma'} \Lambda_{v'\omega}^{*\zeta} \tilde{G}_{k'\sigma'} \tilde{G}_{k'+q,\sigma'} \Lambda_{v'\omega}^{\zeta} \right) \\ &\quad \times \tilde{w}_{\omega}^{\zeta} \Lambda_{v\omega}^{*\zeta} \\ &\quad + \sum_q \tilde{G}_{q-k,\bar{\sigma}} \Lambda_{v\omega}^s \tilde{w}_{\omega}^s \left(- \sum_{k'} \Lambda_{v'\omega}^{*s} \tilde{G}_{k'\uparrow} \tilde{G}_{q-k'\downarrow} \Lambda_{v'\omega}^s \right) \\ &\quad \times \tilde{w}_{\omega}^s \Lambda_{v\omega}^{*s} \\ &= - \sum_{q,\zeta} \Lambda_{v\omega}^{\zeta} \tilde{G}_{q+k,\sigma} \tilde{w}_{\omega}^{\zeta} \tilde{\Pi}_q^{\zeta} \tilde{w}_{\omega}^{\zeta} \Lambda_{v\omega}^{*\zeta} \\ &\quad + \sum_q \Lambda_{v\omega}^s \tilde{G}_{q-k,\bar{\sigma}} \tilde{w}_{\omega}^s \tilde{\Pi}_q^s \tilde{w}_{\omega}^s \Lambda_{v\omega}^{*s}. \end{aligned} \quad (\text{C16})$$

Neglecting nonlongitudinal contributions in Eq. (C13) explains the mismatch in the real part of the D-TRILEX self-energy in the trivial regime of high temperatures ($\beta = 2$) and weak interactions ($U = 2$).

3. Remaining part of the LDB self-energy

The D-TRILEX form of the remaining part of the LDB self-energy can be obtained preserving only longitudinal fluctuations in the partially bosonized representation for the four-point vertex (9) $\Gamma_{vv'\omega}^{\zeta} \simeq 2M_{vv'\omega}^{\zeta}$. Then, the renormalized three-point (C9) and four-point vertices (C10) become

$$L_{vq}^{\zeta} \simeq \Lambda_{v\omega}^{\zeta} (1 + \bar{W}_q^{\zeta} \tilde{\Pi}_q^{\zeta}), \quad (\text{C17})$$

$$P_{vv'q}^{\zeta} \simeq 2\Lambda_{v\omega}^{\zeta} \bar{W}_q^{\zeta} \Lambda_{v\omega}^{*\zeta}, \quad (\text{C18})$$

where

$$\bar{W}_q^{\zeta -1} = \tilde{w}_{\omega}^{\zeta -1} - \tilde{\Pi}_q^{\zeta}. \quad (\text{C19})$$

Substituting these expressions to the remaining part of the ladder contribution to the self-energy (C3), one gets

$$\begin{aligned} \tilde{\Sigma}_{k\sigma}^{(3+)} &\simeq - \sum_{q,\zeta} \Lambda_{v\omega}^{\zeta} \tilde{G}_{q+k,\sigma} \bar{W}_q^{\zeta} \tilde{\Pi}_q^{\zeta} \tilde{w}_{\omega}^{\zeta} \tilde{\Pi}_q^{\zeta} \tilde{w}_{\omega}^{\zeta} \Lambda_{v\omega}^{*\zeta} \\ &\quad + \sum_q \Lambda_{v\omega}^s \tilde{G}_{q-k,\bar{\sigma}} \bar{W}_q^s \tilde{\Pi}_q^s \tilde{w}_{\omega}^s \tilde{\Pi}_q^s \tilde{w}_{\omega}^s \Lambda_{v\omega}^{*s}. \end{aligned} \quad (\text{C20})$$

In this expression we additionally introduced the screening of the four-point vertex in the particle-particle channel, which is usually not accounted for the LDF theory. Combining all ladder terms (C11), (C16), and (C20) together, the LDF self-energy simplifies to

$$\tilde{\Sigma}_{k\sigma}^{\text{LDF}} = - \sum_{q,\zeta} \{ \Lambda_{v\omega}^{\zeta} \tilde{G}_{q+k,\sigma} \bar{W}_q^{\zeta} \Lambda_{v\omega}^{*\zeta} - \Lambda_{v\omega}^s \tilde{G}_{q-k,\bar{\sigma}} \bar{W}_q^s \Lambda_{v\omega}^{*s} \}. \quad (\text{C21})$$

Under the same approximation, the mixed diagram (C5) becomes

$$\begin{aligned} \tilde{\Sigma}_{k\sigma}^{\text{mix}} &= - \sum_{q,\zeta} \Lambda_{v\omega}^{\zeta} \tilde{G}_{q+k,\sigma} (1 + \bar{W}_q^{\zeta} \tilde{\Pi}_q^{\zeta}) \bar{W}_q^{\zeta} (1 + \tilde{\Pi}_q^{\zeta} \bar{W}_q^{\zeta}) \Lambda_{v\omega}^{*\zeta} \\ &\quad + \sum_q \Lambda_{v\omega}^s \tilde{G}_{q-k,\bar{\sigma}} (1 + \bar{W}_q^s \tilde{\Pi}_q^s) \bar{W}_q^s (1 + \tilde{\Pi}_q^s \bar{W}_q^s) \Lambda_{v\omega}^{*s}, \end{aligned} \quad (\text{C22})$$

where we also added the contribution from the particle-particle channel. Using the Dyson equation (C7) for the dual bosonic propagator \bar{W}_q^{ϑ} with the approximate dual polarization operator (C8)

$$\bar{\Pi}_q^{\vartheta} = \tilde{\Pi}_q^{\vartheta} (1 + \bar{W}_q^{\vartheta} \tilde{\Pi}_q^{\vartheta}), \quad (\text{C23})$$

the total self-energy reduces to the D-TRILEX result (19)

$$\begin{aligned} \tilde{\Sigma}_{k\sigma}^{\text{D-TRILEX}} &= \tilde{\Sigma}_{k\sigma}^{\text{LDF}} + \tilde{\Sigma}_{k\sigma}^{\text{mix}} \\ &\simeq - \sum_{q,\zeta} \{ \Lambda_{v\omega}^{\zeta} \tilde{G}_{q+k,\sigma} \bar{W}_q^{\zeta} \Lambda_{v\omega}^{*\zeta} \\ &\quad - \Lambda_{v\omega}^s \tilde{G}_{q-k,\bar{\sigma}} \bar{W}_q^s \Lambda_{v\omega}^{*s} \}. \end{aligned} \quad (\text{C24})$$

The renormalized interaction of the theory can be found as follows:

$$\mathcal{W}_q^{\vartheta -1} = \mathcal{W}_q^{\vartheta -1} - \bar{\Pi}_q^{\vartheta}, \quad (\text{C25})$$

where the partially dressed bosonic propagator [see Eqs. (17) and (18)] is

$$\tilde{\mathcal{W}}_q^{\vartheta} = \tilde{\mathcal{W}}_q^{\vartheta} + \tilde{w}_{\omega}^{\vartheta}. \quad (\text{C26})$$

- [1] A. Georges, G. Kotliar, W. Krauth, and M. J. Rozenberg, Dynamical mean-field theory of strongly correlated fermion systems and the limit of infinite dimensions, *Rev. Mod. Phys.* **68**, 13 (1996).
- [2] W. Metzner and D. Vollhardt, Correlated Lattice Fermions in $d = \infty$ Dimensions, *Phys. Rev. Lett.* **62**, 324 (1989).
- [3] J. Gukelberger, L. Huang, and P. Werner, On the dangers of partial diagrammatic summations: Benchmarks for the two-dimensional hubbard model in the weak-coupling regime, *Phys. Rev. B* **91**, 235114 (2015).
- [4] T. Schäfer, N. Wentzell, F. Šimkovic, Y.-Y. He, C. Hille, M. Klett, C. J. Eckhardt, B. Arzhang, V. Harkov, François-Marie Le Régent, A. Kirsch, Y. Wang, A. J. Kim, E. Kozik, E. A. Stepanov, A. Kauch, S. Andergassen, P. Hansmann, D. Rohe, Y. M. Vilk *et al.*, Tracking the Footprints of Spin Fluctuations: A MultiMethod, MultiMessenger Study of the Two-Dimensional Hubbard Model, *Phys. Rev. X* **11**, 011058 (2021).
- [5] A. N. Rubtsov, E. A. Stepanov, and A. I. Lichtenstein, Collective magnetic fluctuations in Hubbard plaquettes captured by fluctuating local field method, *Phys. Rev. B* **102**, 224423 (2020).
- [6] M. H. Hettler, A. N. Tahvildar-Zadeh, M. Jarrell, T. Pruschke, and H. R. Krishnamurthy, Nonlocal dynamical correlations of strongly interacting electron systems, *Phys. Rev. B* **58**, R7475(R) (1998).
- [7] A. I. Lichtenstein and M. I. Katsnelson, Antiferromagnetism and d-wave superconductivity in cuprates: A cluster dynamical mean-field theory, *Phys. Rev. B* **62**, R9283 (2000).
- [8] T. A. Maier, M. Jarrell, T. Pruschke, and M. Hettler, Quantum cluster theories, *Rev. Mod. Phys.* **77**, 1027 (2005).
- [9] G. Kotliar, S. Y. Savrasov, G. Pálsson, and G. Biroli, Cellular Dynamical Mean Field Approach to Strongly Correlated Systems, *Phys. Rev. Lett.* **87**, 186401 (2001).
- [10] A.-M. S. Tremblay, B. Kyung, and D. Sénéchal, Pseudogap and high-temperature superconductivity from weak to strong coupling. Towards a quantitative theory (Review Article), *Low Temp. Phys.* **32**, 424 (2006).
- [11] G. Kotliar, S. Y. Savrasov, K. Haule, V. S. Oudovenko, O. Parcollet, and C. A. Marianetti, Electronic structure calculations with dynamical mean-field theory, *Rev. Mod. Phys.* **78**, 865 (2006).
- [12] M. Harland, M. I. Katsnelson, and A. I. Lichtenstein, Plaquette valence bond theory of high-temperature superconductivity, *Phys. Rev. B* **94**, 125133 (2016).
- [13] G. Rohringer, H. Hafermann, A. Toschi, A. A. Katanin, A. E. Antipov, M. I. Katsnelson, A. I. Lichtenstein, A. N. Rubtsov, and K. Held, Diagrammatic routes to nonlocal correlations beyond dynamical mean field theory, *Rev. Mod. Phys.* **90**, 025003 (2018).
- [14] P. Sun and G. Kotliar, Many-Body Approximation Scheme beyond GW, *Phys. Rev. Lett.* **92**, 196402 (2004).
- [15] S. Biermann, F. Aryasetiawan, and A. Georges, First-Principles Approach to the Electronic Structure of Strongly Correlated Systems: Combining the GW Approximation and Dynamical Mean-Field Theory, *Phys. Rev. Lett.* **90**, 086402 (2003).
- [16] T. Ayrál, P. Werner, and S. Biermann, Spectral Properties of Correlated Materials: Local Vertex and Nonlocal Two-Particle Correlations from Combined GW and Dynamical Mean Field Theory, *Phys. Rev. Lett.* **109**, 226401 (2012).
- [17] T. Ayrál, S. Biermann, and P. Werner, Screening and non-local correlations in the extended Hubbard model from self-consistent combined GW and dynamical mean field theory, *Phys. Rev. B* **87**, 125149 (2013).
- [18] L. Huang, T. Ayrál, S. Biermann, and P. Werner, Extended dynamical mean-field study of the Hubbard model with long-range interactions, *Phys. Rev. B* **90**, 195114 (2014).
- [19] L. Boehnke, F. Nilsson, F. Aryasetiawan, and P. Werner, When strong correlations become weak: Consistent merging of GW and DMFT, *Phys. Rev. B* **94**, 201106(R) (2016).
- [20] T. Ayrál, S. Biermann, P. Werner, and L. Boehnke, Influence of Fock exchange in combined many-body perturbation and dynamical mean field theory, *Phys. Rev. B* **95**, 245130 (2017).
- [21] T. Ayrál and O. Parcollet, Mott physics and spin fluctuations: A unified framework, *Phys. Rev. B* **92**, 115109 (2015).
- [22] T. Ayrál and O. Parcollet, Mott physics and spin fluctuations: A functional viewpoint, *Phys. Rev. B* **93**, 235124 (2016).
- [23] T. Ayrál, J. Vučičević, and O. Parcollet, Fierz Convergence Criterion: A Controlled Approach to Strongly Interacting Systems With Small Embedded Clusters, *Phys. Rev. Lett.* **119**, 166401 (2017).
- [24] A. Toschi, A. A. Katanin, and K. Held, Dynamical vertex approximation: A step beyond dynamical mean-field theory, *Phys. Rev. B* **75**, 045118 (2007).
- [25] A. A. Katanin, A. Toschi, and K. Held, Comparing pertinent effects of antiferromagnetic fluctuations in the two- and three-dimensional Hubbard model, *Phys. Rev. B* **80**, 075104 (2009).
- [26] A. N. Rubtsov, M. I. Katsnelson, and A. I. Lichtenstein, Dual fermion approach to nonlocal correlations in the Hubbard model, *Phys. Rev. B* **77**, 033101 (2008).
- [27] A. N. Rubtsov, M. I. Katsnelson, A. I. Lichtenstein, and A. Georges, Dual fermion approach to the two-dimensional hubbard model: Antiferromagnetic fluctuations and fermi arcs, *Phys. Rev. B* **79**, 045133 (2009).
- [28] H. Hafermann, G. Li, A. N. Rubtsov, M. I. Katsnelson, A. I. Lichtenstein, and H. Monien, Efficient Perturbation Theory for Quantum Lattice Models, *Phys. Rev. Lett.* **102**, 206401 (2009).
- [29] S. Brener, E. A. Stepanov, A. N. Rubtsov, M. I. Katsnelson, and A. I. Lichtenstein, Dual fermion method as a prototype of generic reference-system approach for correlated fermions, *Ann. Phys.* **422**, 168310 (2020).
- [30] A. N. Rubtsov, M. I. Katsnelson, and A. I. Lichtenstein, Dual boson approach to collective excitations in correlated fermionic systems, *Ann. Phys.* **327**, 1320 (2012).
- [31] E. G. C. P. van Loon, A. I. Lichtenstein, M. I. Katsnelson, O. Parcollet, and H. Hafermann, Beyond extended dynamical mean-field theory: Dual boson approach to the two-dimensional extended Hubbard model, *Phys. Rev. B* **90**, 235135 (2014).
- [32] E. A. Stepanov, E. G. C. P. van Loon, A. A. Katanin, A. I. Lichtenstein, M. I. Katsnelson, and A. N. Rubtsov, Self-consistent dual boson approach to single-particle and collective excitations in correlated systems, *Phys. Rev. B* **93**, 045107 (2016).
- [33] E. A. Stepanov, A. Huber, E. G. C. P. van Loon, A. I. Lichtenstein, and M. I. Katsnelson, From local to nonlocal correlations: The Dual Boson perspective, *Phys. Rev. B* **94**, 205110 (2016).
- [34] L. Peters, E. G. C. P. van Loon, A. N. Rubtsov, A. I. Lichtenstein, M. I. Katsnelson, and E. A. Stepanov, Dual boson approach with instantaneous interaction, *Phys. Rev. B* **100**, 165128 (2019).

- [35] N. V. Prokof'ev and B. V. Svistunov, Polaron Problem by Diagrammatic Quantum Monte Carlo, *Phys. Rev. Lett.* **81**, 2514 (1998).
- [36] E. Kozik, K. Van Houcke, E. Gull, L. Pollet, N. Prokof'ev, B. Svistunov, and M. Troyer, Diagrammatic Monte Carlo for correlated fermions, *Europhys. Lett.* **90**, 10004 (2010).
- [37] S. Isakov, A. E. Antipov, and E. Gull, Diagrammatic Monte Carlo for dual fermions, *Phys. Rev. B* **94**, 035102 (2016).
- [38] J. Gukelberger, E. Kozik, and H. Hafermann, Diagrammatic Monte Carlo approach for diagrammatic extensions of dynamical mean-field theory: Convergence analysis of the dual fermion technique, *Phys. Rev. B* **96**, 035152 (2017).
- [39] M. Vandelli, V. Harkov, E. A. Stepanov, J. Gukelberger, E. Kozik, A. Rubio, and A. I. Lichtenstein, Dual boson diagrammatic Monte Carlo approach applied to the extended Hubbard model, *Phys. Rev. B* **102**, 195109 (2020).
- [40] A. van Roekeghem, T. Ayrat, J. M. Tomczak, M. Casula, N. Xu, H. Ding, M. Ferrero, O. Parcollet, H. Jiang, and S. Biermann, Dynamical Correlations and Screened Exchange on the Experimental Bench: Spectral Properties of the Cobalt Pnictide BaCo_2As_2 , *Phys. Rev. Lett.* **113**, 266403 (2014).
- [41] J. M. Tomczak, M. Casula, T. Miyake, F. Aryasetiawan, and S. Biermann, Combined GW and dynamical mean-field theory: Dynamical screening effects in transition metal oxides, *Europhys. Lett.* **100**, 67001 (2012).
- [42] C. Taranto, M. Kaltak, N. Parragh, G. Sangiovanni, G. Kresse, A. Toschi, and K. Held, Comparing quasiparticle GW+DMFT and LDA+DMFT for the test bed material SrVO_3 , *Phys. Rev. B* **88**, 165119 (2013).
- [43] R. Sakuma, Ph. Werner, and F. Aryasetiawan, Electronic structure of SrVO_3 within GW+DMFT, *Phys. Rev. B* **88**, 235110 (2013).
- [44] J. M. Tomczak, M. Casula, T. Miyake, and S. Biermann, Asymmetry in band widening and quasiparticle lifetimes in SrVO_3 : Competition between screened exchange and local correlations from combined GW and dynamical mean-field theory GW + DMFT, *Phys. Rev. B* **90**, 165138 (2014).
- [45] F. Aryasetiawan and S. Biermann, Generalized Hedin's Equations for Quantum Many-Body Systems with Spin-Dependent Interactions, *Phys. Rev. Lett.* **100**, 116402 (2008).
- [46] L. Sponza, P. Pisanti, A. Vishina, D. Pashov, C. Weber, M. van Schilfgaarde, S. Acharya, J. Vidal, and G. Kotliar, Self-energies in itinerant magnets: A focus on Fe and Ni, *Phys. Rev. B* **95**, 041112(R) (2017).
- [47] H. Kontani, Optical Conductivity and Hall Coefficient in High-Tc Superconductors: Significant Role of Current Vertex Corrections, *J. Phys. Soc. Jpn.* **75**, 013703 (2006).
- [48] N. Lin, E. Gull, and A. J. Millis, Optical conductivity from cluster dynamical mean-field theory: Formalism and application to high-temperature superconductors, *Phys. Rev. B* **80**, 161105(R) (2009).
- [49] M. I. Katsnelson and A. I. Lichtenstein, Theory of optically forbidden dd transitions in strongly correlated crystals, *J. Phys.: Condens. Matter* **22**, 382201 (2010).
- [50] D. Bergeron, V. Hankevych, B. Kyung, and A.M. S. Tremblay, Optical and dc conductivity of the two-dimensional Hubbard model in the pseudogap regime and across the antiferromagnetic quantum critical point including vertex corrections, *Phys. Rev. B* **84**, 085128 (2011).
- [51] I. A. Ado, I. A. Dmitriev, P. M. Ostrovsky, and M. Titov, Anomalous Hall effect with massive Dirac fermions, *Europhys. Lett.* **111**, 37004 (2015).
- [52] I. A. Ado, I. A. Dmitriev, P. M. Ostrovsky, and M. Titov, Anomalous Hall Effect in a 2D Rashba Ferromagnet, *Phys. Rev. Lett.* **117**, 046601 (2016).
- [53] J. Vučković, J. Kokalj, R. Žitko, N. Wentzell, D. Tanasković, and J. Mravlje, Conductivity in the Square Lattice Hubbard Model at High Temperatures: Importance of Vertex Corrections, *Phys. Rev. Lett.* **123**, 036601 (2019).
- [54] A. Kauch, P. Pudleiner, K. Astleithner, P. Thunström, T. Ribic, and K. Held, Generic Optical Excitations of Correlated Systems: π -tons, *Phys. Rev. Lett.* **124**, 047401 (2020).
- [55] O. Simard, S. Takayoshi, and P. Werner, Diagrammatic study of optical excitations in correlated systems, *Phys. Rev. B* **103**, 104415 (2021).
- [56] S. Isakov, H. Terletska, and E. Gull, Momentum-space cluster dual fermion method, *Phys. Rev. B* **97**, 125114 (2018).
- [57] A. Galler, P. Thunström, P. Gunacker, J. M. Tomczak, and K. Held, Ab initio dynamical vertex approximation, *Phys. Rev. B* **95**, 115107 (2017).
- [58] A. Galler, J. Kaufmann, P. Gunacker, M. Pickem, P. Thunström, J. M. Tomczak, and K. Held, Towards ab initio Calculations with the Dynamical Vertex Approximation, *J. Phys. Soc. Jpn.* **87**, 041004 (2018).
- [59] J. Kaufmann, C. Eckhardt, M. Pickem, M. Kitatani, A. Kauch, and K. Held, Self-consistent ladder dynamical vertex approximation, *Phys. Rev. B* **103**, 035120 (2021).
- [60] E. A. Stepanov, V. Harkov, and A. I. Lichtenstein, Consistent partial bosonization of the extended Hubbard model, *Phys. Rev. B* **100**, 205115 (2019).
- [61] E. A. Stepanov, S. Brener, F. Krien, M. Harland, A. I. Lichtenstein, and M. I. Katsnelson, Effective Heisenberg Model and Exchange Interaction for Strongly Correlated Systems, *Phys. Rev. Lett.* **121**, 037204 (2018).
- [62] E. A. Stepanov, A. Huber, A. I. Lichtenstein, and M. I. Katsnelson, Effective Ising model for correlated systems with charge ordering, *Phys. Rev. B* **99**, 115124 (2019).
- [63] C. Husemann and M. Salmhofer, Efficient parametrization of the vertex function, Ω scheme, and the t, t' Hubbard model at van Hove filling, *Phys. Rev. B* **79**, 195125 (2009).
- [64] S. Friederich, H. C. Krahl, and C. Wetterich, Four-point vertex in the Hubbard model and partial bosonization, *Phys. Rev. B* **81**, 235108 (2010).
- [65] O. Gunnarsson, T. Schäfer, J. P. F. LeBlanc, E. Gull, J. Merino, G. Sangiovanni, G. Rohringer, and A. Toschi, Fluctuation Diagnostics of the Electron Self-Energy: Origin of the Pseudogap Physics, *Phys. Rev. Lett.* **114**, 236402 (2015).
- [66] F. Krien, A. Valli, and M. Capone, Single-boson exchange decomposition of the vertex function, *Phys. Rev. B* **100**, 155149 (2019).
- [67] E. A. Stepanov, Y. Nomura, A. I. Lichtenstein, and S. Biermann, Orbital isotropy of magnetic fluctuations in correlated electron materials induced by Hund's exchange coupling, [arXiv:2010.03433](https://arxiv.org/abs/2010.03433).
- [68] J. Jaekel and C. Wetterich, Flow equations without mean field ambiguity, *Phys. Rev. D* **68**, 025020 (2003).
- [69] T. Baier, E. Bick, and C. Wetterich, Temperature dependence of antiferromagnetic order in the Hubbard model, *Phys. Rev. B* **70**, 125111 (2004).

- [70] J. Jaeckel, Understanding the Fierz Ambiguity of Partially Bosonized Theories, [arXiv:hep-ph/0205154](https://arxiv.org/abs/hep-ph/0205154).
- [71] C.-H. Pao and N. E. Bickers, Renormalization-group acceleration of self-consistent field solutions: Two-dimensional Hubbard model, *Phys. Rev. B* **49**, 1586 (1994).
- [72] A. M. Sengupta and A. Georges, Non-Fermi-liquid behavior near a $T=0$ spin-glass transition, *Phys. Rev. B* **52**, 10295 (1995).
- [73] Q. Si and J. L. Smith, Kosterlitz-Thouless Transition and Short Range Spatial Correlations in an Extended Hubbard Model, *Phys. Rev. Lett.* **77**, 3391 (1996).
- [74] J. L. Smith and Q. Si, Spatial correlations in dynamical mean-field theory, *Phys. Rev. B* **61**, 5184 (2000).
- [75] R. Chitra and G. Kotliar, Effect of Long Range Coulomb Interactions on the Mott Transition, *Phys. Rev. Lett.* **84**, 3678 (2000).
- [76] R. Chitra and G. Kotliar, Effective-action approach to strongly correlated fermion systems, *Phys. Rev. B* **63**, 115110 (2001).
- [77] A. N. Rubtsov, V. V. Savkin, and A. I. Lichtenstein, Continuous-time quantum Monte Carlo method for fermions, *Phys. Rev. B* **72**, 035122 (2005).
- [78] P. Werner, A. Comanac, L. de' Medici, M. Troyer, and A. J. Millis, Continuous-Time Solver for Quantum Impurity Models, *Phys. Rev. Lett.* **97**, 076405 (2006).
- [79] P. Werner and A. J. Millis, Dynamical Screening in Correlated Electron Materials, *Phys. Rev. Lett.* **104**, 146401 (2010).
- [80] E. Gull, A. J. Millis, A. I. Lichtenstein, A. N. Rubtsov, M. Troyer, and P. Werner, Continuous-time Monte Carlo methods for quantum impurity models, *Rev. Mod. Phys.* **83**, 349 (2011).
- [81] C.-O. Almladh, U. von Barth, and R. van Leeuwen, Variational total energies from Φ - and Ψ - Derivable Theories, *Int. J. Mod. Phys. B* **13**, 535 (1999).
- [82] H. Hafermann, Numerical approaches to spatial correlations in strongly interacting fermion systems, Ph.D. thesis, Universität Hamburg, 2010.
- [83] H. Hafermann, K. R. Patton, and P. Werner, Improved estimators for the self-energy and vertex function in hybridization-expansion continuous-time quantum Monte Carlo simulations, *Phys. Rev. B* **85**, 205106 (2012).
- [84] P. Gunacker, M. Wallerberger, T. Ribic, A. Hausoel, G. Sangiovanni, and K. Held, Worm-improved estimators in continuous-time quantum Monte Carlo, *Phys. Rev. B* **94**, 125153 (2016).
- [85] J. Kaufmann, P. Gunacker, A. Kowalski, G. Sangiovanni, and K. Held, Symmetric improved estimators for continuous-time quantum Monte Carlo, *Phys. Rev. B* **100**, 075119 (2019).
- [86] I. S. Krivenko, A. N. Rubtsov, M. I. Katsnelson, and A. I. Lichtenstein, Analytical approximation for single-impurity Anderson model, *JETP Lett.* **91**, 319 (2010).
- [87] H. Hafermann, P. Werner, and E. Gull, Efficient implementation of the continuous-time hybridization expansion quantum impurity solver, *Comput. Phys. Commun.* **184**, 1280 (2013).
- [88] H. Hafermann, Self-energy and vertex functions from hybridization-expansion continuous-time quantum monte carlo for impurity models with retarded interaction, *Phys. Rev. B* **89**, 235128 (2014).
- [89] B. Bauer, L. D. Carr, H. G. Evertz, A. Feiguin, J. Freire, S. Fuchs, L. Gamper, J. Gukelberger, E. Gull, S. Guertler, A. Hehn, R. Igarashi, S. V. Isakov, D. Koop, P. N. Ma, P. Mates, H. Matsuo, O. Parcollet, G. Pawłowski, J. D. Picon *et al.*, The ALPS project release 2.0: open source software for strongly correlated systems, *J. Stat. Mech.: Theory Exp.* (2011) P05001.
- [90] R. Rossi, Determinant Diagrammatic Monte Carlo Algorithm in the Thermodynamic Limit, *Phys. Rev. Lett.* **119**, 045701 (2017).
- [91] A. Moutenet, W. Wu, and M. Ferrero, Determinant Monte Carlo algorithms for dynamical quantities in fermionic systems, *Phys. Rev. B* **97**, 085117 (2018).
- [92] F. Šimkovic and E. Kozik, Determinant Monte Carlo for irreducible Feynman diagrams in the strongly correlated regime, *Phys. Rev. B* **100**, 121102(R) (2019).
- [93] W. Wu, M. Ferrero, A. Georges, and E. Kozik, Controlling Feynman diagrammatic expansions: Physical nature of the pseudogap in the two-dimensional Hubbard model, *Phys. Rev. B* **96**, 041105(R) (2017).
- [94] N. D. Mermin and H. Wagner, Absence of Ferromagnetism or Antiferromagnetism in One- or Two-Dimensional Isotropic Heisenberg Models, *Phys. Rev. Lett.* **17**, 1133 (1966).
- [95] J. Otsuki, H. Hafermann, and A. I. Lichtenstein, Superconductivity, antiferromagnetism, and phase separation in the two-dimensional hubbard model: A dual fermion approach, *Phys. Rev. B* **90**, 235132 (2014).
- [96] J. C. Slater, Magnetic Effects and the Hartree-Fock Equation, *Phys. Rev.* **82**, 538 (1951).
- [97] V. Harkov, A. I. Lichtenstein, and F. Krien, Parameterizations of local vertex corrections from weak to strong coupling: importance of the hedin three-leg vertex, [arXiv:2104.11534](https://arxiv.org/abs/2104.11534).

5.3 Coexisting charge density wave and ferromagnetic instabilities in monolayer InSe

In this work [130], we apply the D-TRILEX approach to study many-body effects in a recently discovered monolayer indium selenide (InSe) system – a material with unique characteristics of the electronic spectrum. Due to large on-site Coulomb repulsion, InSe monolayer can not be treated using perturbative methods like *GW* or RPA to investigate the many-body correlation effects. A weakly-screened and long-ranged character of the Coulomb interaction also does not allow one to use DMFT for describing this system. Therefore, in order to take into account the non-local correlations we perform calculations using the D-TRILEX method, which allows one to consider collective electronic fluctuations in the charge and spin channels simultaneously without any restriction on the range. We demonstrate that the 2D phase of InSe is a rare example of a system, where collective electronic fluctuations lead to the formation of exotic states of matter, such as coexisting charge density wave and ferromagnetic ordering. This behavior is highly unusual for a *sp*-electron system.

The electronic spectral function of the monolayer InSe has prominent van Hove singularities that are usually responsible for a very rich and exotic many-body physics in the system. This kind of band topology is now intensively studied in twisted bilayer graphene, which is, however, a very complicated system to work with, both experimentally and theoretically. InSe is more accessible from both, the experimental and the computational points of view. At the same time, InSe can be considered a prototype for flat band systems with largely unexplored properties. To study this material, we use a combination of first-principles calculations and advanced many-body techniques that allow us to consider dynamical correlation effects at arbitrary wavelengths. We find that upon moderate hole doping and realistic temperatures monolayer InSe tends to form an ordered phase with commensurate charge density wave ordering which is driven by non-local Coulomb interactions. Remarkably, there is a regime where this phase coexists with a ferromagnetic ordering, which is highly unexpected for a system without localized *d*-electrons. This makes the monolayer InSe a promising candidate for exploring collective electronic effects, which paves the way for further theoretical and experimental studies.

Under normal conditions InSe monolayer is an indirect semiconductor with a fully filled valence band, therefore we investigate the system at different temperatures for realistic dopings so that the van Hove singularity (vHS) appears close to the Fermi energy. The obtained results show a commensurate CDW ordering for a broad range of doping levels. We find that the formation of the CDW can be seen in the single-particle spectral function through the development of a pseudogap at the Fermi

energy, which is due to the feedback effect of the collective fluctuations on the single-particle quantities. Inside the CDW phase, we found a ferromagnetic phase that has a dome-like shape. The top of the dome is located at the doping where the vHS meets the Fermi energy. We find that taking the electron-photon coupling into account does not lead to qualitative changes in the obtained phase diagram. This result shows that the formation of the CDW phase in the monolayer InSe is driven by strong electronic correlations rather than by the electron-phonon mechanism.

ARTICLE OPEN



Coexisting charge density wave and ferromagnetic instabilities in monolayer InSe

Evgeny A. Stepanov¹✉, Viktor Harkov^{2,3}, Malte Rösner⁴, Alexander I. Lichtenstein^{2,3,5}, Mikhail I. Katsnelson⁴ and Alexander N. Rudenko⁴✉

Recently fabricated InSe monolayers exhibit remarkable characteristics that indicate the potential of this material to host a number of many-body phenomena. In this work, we systematically describe collective electronic effects in hole-doped InSe monolayers using advanced many-body techniques. To this end, we derive a realistic electronic-structure model from first principles that takes into account the most important characteristics of this material, including a flat band with prominent van Hove singularities in the electronic spectrum, strong electron–phonon coupling, and weakly screened long-ranged Coulomb interactions. We calculate the temperature-dependent phase diagram as a function of band filling and observe that this system is in a regime with coexisting charge density wave and ferromagnetic instabilities that are driven by strong electronic Coulomb correlations. This regime can be achieved at realistic doping levels and high enough temperatures, and can be verified experimentally. We find that the electron–phonon interaction does not play a crucial role in these effects, effectively suppressing the local Coulomb interaction without changing the qualitative physical picture.

npj Computational Materials (2022)8:118; <https://doi.org/10.1038/s41524-022-00798-4>

INTRODUCTION

Two-dimensional (2D) group III–VI metal chalcogenides have recently attracted great interest because of their appealing characteristics. Among them are high charge carrier mobility, controllable energy gaps, excellent thermoelectric and optical properties, as well as excellent stability at ambient conditions^{1–6}. The electronic structure of ultrathin InSe features flat regions in the valence band dispersion leading to prominent van Hove singularities (vHS) in the hole density of states (DOS)⁷. Importantly, this kind of electronic structure is only observed in the monolayer limit of these materials, as has been experimentally demonstrated by means of angular resolved photoemission spectroscopy^{8,9}. If the vHS appears at the Fermi energy, it may result in numerous competing channels of instabilities such as magnetic, charge, or superconducting order with a very non-trivial interplay between them^{10–12}. Scientific interest to flat-band materials has been triggered in recent years by the discovery of unconventional superconductivity and related exotic phenomena in twisted bilayer graphene^{13–15}. Therefore, thin films group III–VI materials turn out to be prospective candidates for studying many-body correlation effects, which are closely related to the above-mentioned features in the electronic spectrum¹⁶, circumventing the need for any twist engineering.

The theoretical description of many-body effects in monolayer InSe is challenging and is limited to a few works mainly focusing on the electron–phonon coupling. In particular, it has been shown that hole states in this material undergo significant renormalization due to the interaction with acoustic phonons, which gives rise to the appearance of unusual temperature-dependent optical excitations¹⁷. Also, a strong electron–phonon interaction may result in a charge density wave (CDW) instability predicted

recently¹⁸. At the same time, monolayer InSe is expected to possess strong many-body electronic effects that have not been accurately studied yet. For instance, the presence of the Mexican-hat-like band in this material might favor a magnetic instability that could lead to the formation of a magnetically ordered state at low temperatures. Up to now the existence of a magnetic solution for InSe monolayer has been demonstrated based on density functional theory (DFT)¹⁹ without systematic consideration of many-body effects. In addition, the weakly screened Coulomb interaction in 2D may result in a Coulomb-driven CDW instability. However, a systematic many-body consideration of these effects is still missing in the literature.

In this work, we address the problem of collective electronic effects in monolayer InSe. For this purpose, we derive a realistic model that considers both, long-range Coulomb interactions and the electron–phonon coupling. The introduced interacting electronic problem is further solved using an advanced many-body approach that explicitly takes into account non-local collective electronic fluctuations. In the regime of hole-doping, we find that charge ordering represents the main instability. It is formed in a broad range of doping levels and corresponds to a commensurate CDW, which indicates that this instability is rather driven by strong electronic Coulomb correlations than by an electron–phonon mechanism as discussed previously. Inside the CDW phase, we detect another collective effect that drives the system towards a ferromagnetic (FM) ordering. This instability is formed in close proximity to the vHS in the DOS. Finally, we observe that the electron–phonon coupling tends to suppress the FM ordering, enlarging the CDW phase. However, the presence of the electron–phonon coupling does not qualitatively affect the observed effects.

¹CPHT, CNRS, Ecole Polytechnique, Institut Polytechnique de Paris, F-91128 Palaiseau, France. ²I. Institute of Theoretical Physics, University of Hamburg, Notkestraße 9, 22607 Hamburg, Germany. ³European X-Ray Free-Electron Laser Facility, Holzkoppel 4, 22869 Schenefeld, Germany. ⁴Radboud University, Institute for Molecules and Materials, 6525AJ Nijmegen, The Netherlands. ⁵The Hamburg Centre for Ultrafast Imaging, Luruper Chaussee 149, 22761 Hamburg, Germany. ✉email: evgeny.stepanov@polytechnique.edu; a.rudenko@science.ru.nl

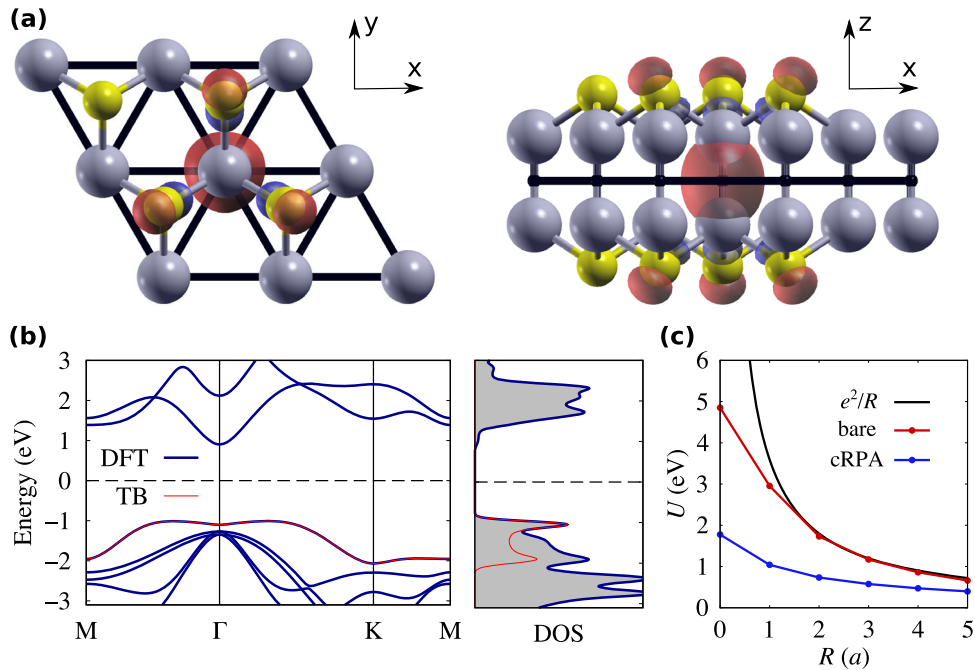


Fig. 1 First-principle calculation of model parameters. **a** Schematic crystal structure of monolayer InSe shown in two projections. Superimposed is an isosurface of the Wannier function describing the valence states in InSe. The black lines depict an effective electronic lattice; **(b)** Band structure and DOS calculated in DFT (blue), and from tight-binding model parametrization (red); **(c)** The Coulomb interaction between the Wannier orbitals shown as a function of the distance calculated within the cRPA scheme. The bare (unscreened) Coulomb interaction is shown for comparison.

RESULTS

Model

InSe is a layered van der Waals material, where each layer consists of two vertically displaced In-Se honeycombs, giving rise to four Se-In-In-Se atomic planes (Fig. 1a). Each layer has D_{3h} point group symmetry. In the monolayer limit DFT calculations predict InSe to be a semiconductor with an indirect energy gap of ~ 2 eV. The electronic dispersion shows a single well-separated valence band, which has the shape of a Mexican hat, as depicted in Fig. 1b. This shape is characterized by a ring of radius $k_0 \approx 0.3 \text{ \AA}^{-1}$ formed by the valence band edge, and by a well of $E_0 = 0.09$ eV deep at the Γ point. These parameters are in reasonable agreement with those obtained from photoemission spectroscopy in Ref. 8. This peculiar band structure is of great advantage for many-body considerations as it allows us to reduce the correlated subspace to a single band. To this end, we construct a tractable tight-binding model that accurately reproduces this highest valence band (Fig. 1b). The corresponding model is defined in terms of maximally localized Wannier functions on an effective triangular lattice, as shown in Fig. 1a. Each Wannier function is reminiscent of an In-In bonding orbital with tails on Se atoms. The resulting single-band model Hamiltonian on a triangular lattice reads

$$H = \sum_{ij,\sigma} t_{ij} c_{i\sigma}^\dagger c_{j\sigma} + U \sum_i n_{i\uparrow} n_{i\downarrow} + \frac{1}{2} \sum_{i,j,\sigma,\sigma'} V_{ij} n_{i\sigma} n_{j\sigma'} + \omega_{\text{ph}} \sum_i b_i^\dagger b_i + g \sum_{i,\sigma} n_{i\sigma} (b_i + b_i^\dagger) \quad (1)$$

where $c_{i\sigma}^{(\dagger)}$ operator annihilates (creates) an electron on the site i with the spin projection $\sigma = \{\uparrow, \downarrow\}$. The ab initio electronic dispersion is reproduced by five neighboring hopping amplitudes t_{ij} : $t_{01} = 127.9$ meV, $t_{02} = -41.8$ meV, $t_{03} = -45.0$ meV, $t_{04} = 13.0$ meV, and $t_{05} = -4.4$ meV. We neglect spin-orbit coupling because it is not important in truly 2D crystals with the mirror symmetry²⁰, which is also supported by earlier DFT calculations showing that the relevant valence states in monolayer InSe remain unaffected by the presence of spin-orbit coupling²¹.

Figure 1c shows the bare and screened Coulomb interaction between the Wannier orbitals calculated as a function of R within the constrained random phase approximation (cRPA) to avoid a double counting of the screening channels from the correlated subspace (see Methods for more details). $R(a)$ corresponds to the distance between the sites of an effective triangular lattice and is expressed in units of the lattice constant a . The on-site screened Coulomb repulsion $U = 1.78$ eV greatly exceeds the bandwidth ≈ 1 eV, which usually indicates strong magnetic fluctuations in the system²². As expected for a 2D material²³, the non-local Coulomb interaction V_{ij} in monolayer InSe is weakly screened and long-ranged (see blue line in Fig. 1c). Weak long-range screening in 2D is a direct consequence of the reduced dimensionality. In particular, the softer \mathbf{q} -dependence of the bare Coulomb interaction $V^{2D}(\mathbf{q}) = 2\pi e^2/q$ (in contrast to $\sim 1/q^2$ in 3D) ensures that the dielectric constant $\epsilon(\mathbf{q}, \omega) \rightarrow 1$ as $\mathbf{q} \rightarrow 0$ for any gapped 2D system (see, e.g., Ref. 24). At finite wave vectors this behavior is less obvious, yet the trend is similar^{23,25,26}. Thus, cRPA Coulomb matrix elements for layered materials indeed show as a general trend the described weakly screened and long-ranged behavior with graphene²⁷ and NbS_2 ²⁸ being representative metallic examples. Moreover, in monolayer InSe the interaction $V_{01} = 1.04$ eV between nearest-neighbor electronic densities $n_{i\sigma} = c_{i\sigma}^\dagger c_{i\sigma}$ is larger than the half of the on-site Coulomb repulsion U . This suggests that the considered system may have a tendency to form a CDW phase due to the competition between local and non-local Coulomb interactions^{29,30}. The full form of the long-range Coulomb interaction is presented in Methods.

To estimate the phonon properties without double counting screening channels from the correlated subspace we utilize the constrained Density Functional Perturbation Theory (cDFPT)³¹ at hole doping. We find that the effective electron-phonon coupling $\lambda = 2 \int d\omega \frac{\alpha^2 F(\omega)}{\omega}$ is dominated by a rather sharp resonance at low phonon frequency, which we can approximate with a local phonon model, i.e. $\alpha^2 F(\omega) = N_0 g^2 \delta(\omega - \omega_{\text{ph}})$. Here, N_0 is the DOS at

the Fermi level, $\omega_{\text{ph}} = 8.5$ meV the phonon energy, and $g = 34.7$ meV its coupling strength to the topmost valence band (see Methods). The strong local coupling of electrons to phonons renders the CDW formation even more favorable. Indeed, upon integrating out bosonic operators $b^{(\dagger)}$ that correspond to phonon degrees of freedom one gets an effective local frequency-dependent attractive interaction $U_{\omega}^{\text{ph}} = 2g^2 \frac{\omega_{\text{ph}}}{\omega^2 - \omega_{\text{ph}}^2}$ that reduces the repulsive on-site Coulomb potential as $U_{\omega}^{\text{ph}} \bar{U} - U_{\omega}^{\text{ph}32-34}$ and thus enhances the effect of the non-local Coulomb interaction V_{ij} .

An accurate theoretical investigation of many-body instabilities in InSe monolayer cannot be performed within conventional perturbative methods like the random phase approximation^{35–37} or the *GW* approach^{38–40}. Local correlation effects that are governed by such a large value of the local Coulomb interaction U require a systematic many-body consideration using, e.g., the dynamical mean-field theory (DMFT)⁴¹. At the same time, spatial collective electronic fluctuations and the long-range Coulomb interaction cannot be captured by DMFT and require diagrammatic extensions of this theory⁴². In this work, we solve the considered many-body problem using the dual triply irreducible

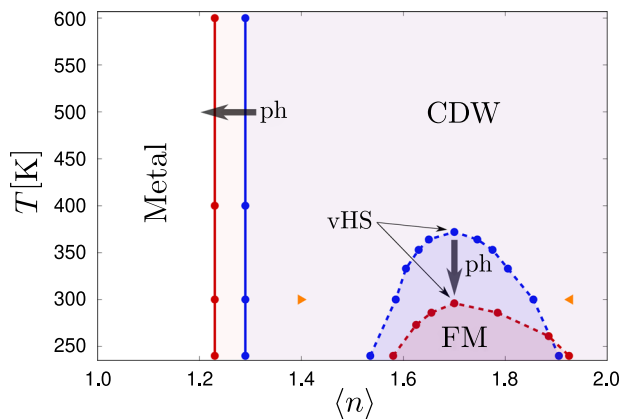


Fig. 2 Phase diagram for the monolayer InSe as a function of temperature and doping. Solid vertical lines correspond to the CDW phase boundaries, dashed lines depict the FM instabilities. Results are obtained in the presence (red line) and in the absence (blue line) of the electron–phonon coupling. The top of the FM dome corresponds to the filling $\langle n \rangle = 1.70$ at which the vHS appears at the Fermi energy. Black arrows with the label “ph” illustrate the effect of phonons that tend to suppress the FM instability and favor the CDW ordering. Orange triangles indicate the CDW transition points $\langle n \rangle = 1.40$ and $\langle n \rangle = 1.92$ obtained at $T = 300$ K taking into account the electron–phonon coupling in the absence of the non-local Coulomb interaction.

local expansion (D-TRILEX) method^{43–45} that allows one to account for leading collective electronic fluctuations on equal footing without any limitation on the range⁴⁶. More details on the theoretical approach are provided in Methods.

Collective electronic instabilities

One of the most remarkable features of the InSe monolayer is the presence of a Mexican-hat-like valence band in the electronic dispersion^{8,9}. The top of this band exhibits flat regions that lead to a sharp vHS in the DOS. However, under normal conditions this valence band is fully filled, making the material an indirect semiconductor. To enhance correlation effects in the system we consider realistic hole dopings with the Fermi level close to the vHS^{10–12}. Practically, high concentration of holes of the order of 10^{14} cm^{-2} can be achieved in 2D materials by means of electrostatic solid- or liquid-electrolyte gating⁴⁷ or by surface molecular doping⁴⁸. First, we solve the many-body problem without considering the electron–phonon coupling in order to investigate purely Coulomb correlation effects. For detecting main instabilities in the system we perform single-shot D-TRILEX calculations for the charge and spin susceptibilities $X_{\mathbf{q}\omega}^c$. In this case, divergences of charge and spin susceptibilities do not affect each other through the self-energy, which allows one to detect instabilities inside broken-symmetry phases (see Methods for more details). Fig. 2 shows the obtained phase diagram for the InSe monolayer, where $\langle n \rangle$ is the filling of the considered valence band ($\langle n \rangle = 2$ in the fully filled band that corresponds to the undoped case). Phase boundaries indicate points in the temperature (T) vs. doping space, where corresponding susceptibilities diverge. We find that the charge susceptibility diverges in a broad range of hole dopings $\langle n \rangle \geq 1.29$, and the corresponding phase boundary is independent of temperature. Fig. 3a displays the momentum resolved charge susceptibility $X_{\mathbf{q}\omega}^c$ obtained at the zero frequency $\omega = 0$ near the transition point ($T = 300$ K, $\langle n \rangle = 1.29$). It shows that the corresponding Bragg peaks in the charge susceptibility appear at the K points of the Brillouin zone (BZ), which indicates the formation of a commensurate CDW ordering. In turn, the spin susceptibility remains finite at the CDW transition point and diverges only inside the CDW phase. The corresponding instability has a dome shape as depicted in Fig. 2 by a blue dashed line. Remarkably, we find that the top of the dome corresponds to the filling $\langle n \rangle = 1.70$ at which the vHS appears exactly at the Fermi level. The momentum resolved spin susceptibility obtained close to the top of the dome ($T = 375$ K, $\langle n \rangle = 1.70$) is shown in Fig. 3b. It reveals a sharp Bragg peak at the Γ point of the BZ, which indicates the tendency towards FM ordering.

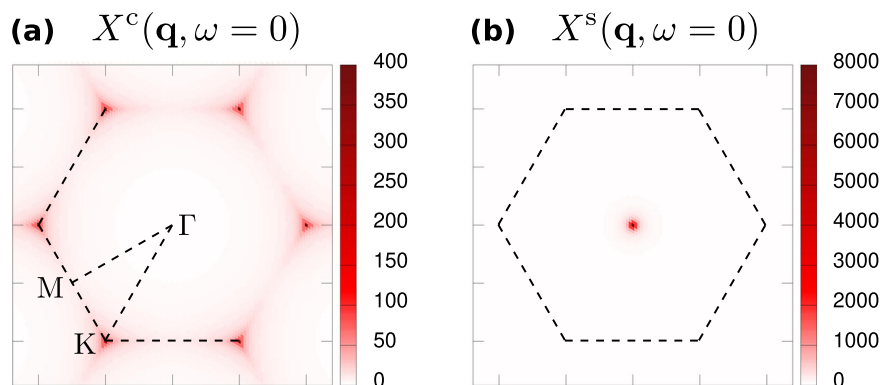


Fig. 3 Momentum resolved susceptibilities $X_{\mathbf{q}\omega}^c$ calculated at zero frequency $\omega = 0$ in the absence of the electron–phonon coupling. Results are obtained close to the CDW ($T = 300$ K, $\langle n \rangle = 1.29$) and the FM ($T = 375$ K, $\langle n \rangle = 1.70$) instabilities, respectively. Bragg peaks that appear in the charge susceptibility (a) at the K points of the hexagonal BZ correspond to a commensurate CDW ordering. A single peak at the Γ point in the spin susceptibility (b) confirms that the observed instability is FM.

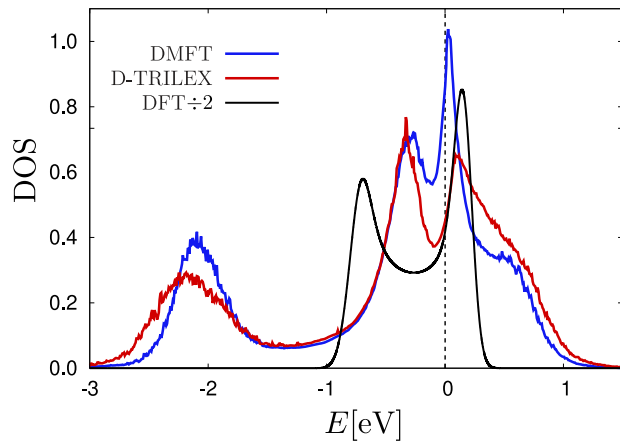


Fig. 4 DOS of the InSe monolayer. Results are obtained within DMFT (blue), D-TRILEX (red), and DFT (black) methods close to a CDW phase boundary at $T = 300$ K and $\langle n \rangle = 1.29$ without taking into account the electron–phonon coupling. Note that the DOS of DFT is divided by a factor of 2 for easier comparison.

Electronic density of states

The obtained phase diagram illustrates that the commensurate CDW represents the main instability in the InSe monolayer contrary to the DFT prediction¹⁹. The formation of this phase is associated with strong long-range collective charge fluctuations that are expected to renormalize the electronic dispersion. Therefore, the development of the CDW ordering should also be reflected in single-particle observables such as the electronic DOS. In order to account for the feedback effects of long-range collective electronic fluctuations to single-particle quantities^{49,50} we perform self-consistent D-TRILEX calculations^{43–45}. The obtained result is compared to the one of the DMFT that does not take into account spatial correlation effects. Fig. 4 shows the DOS calculated close to the CDW phase boundary ($T = 300$ K and $\langle n \rangle = 1.29$). We find that the DOS obtained within DMFT (blue) is similar to the one of DFT (black) and shows a sharp peak in the vicinity of the Fermi energy, which reflects the presence of the vHS in the electronic spectrum. However, if one includes the effect of spatial correlations via the D-TRILEX approach, one observes that at the transition point this peak turns into a pseudogap (red). In this particular case, the pseudogap appears due to strong collective charge fluctuations that lead to an almost diverged charge susceptibility $X_{\mathbf{q}\omega}^c$ at the $\mathbf{q} = \mathbf{K}$ point of the BZ close to a phase transition. As a consequence, the renormalized interaction $W_{\mathbf{q}\omega}^c$ that enters the self-energy also becomes nearly divergent, which causes the formation of a pseudogap according to the tendency towards electron–hole pairing. This mechanism is similar to the formation of the excitonic insulator state^{51–53} with the only difference that in our case electrons and holes belong to the same band and that excitons in the condensate have non-zero momentum corresponding to the CDW wave vector. If the tendency towards electron–hole pairing results in long-range order, one gets a true gap whereas strong short-range order without long-range order leads to a pseudogap in the electronic spectrum^{54,55}.

Effect of the electron–phonon coupling

In order to investigate the effect of phonons on the observed instabilities we repeat the same calculation in the presence of the electron–phonon coupling. As Fig. 2 shows, in this case the CDW phase boundary is shifted to smaller values of the filling $\langle n \rangle = 1.23$. At the same time, the FM instability is pushed down to lower temperatures, but the top of the FM dome remains at the vHS filling $\langle n \rangle = 1.70$ as in the absence of phonons. This result is

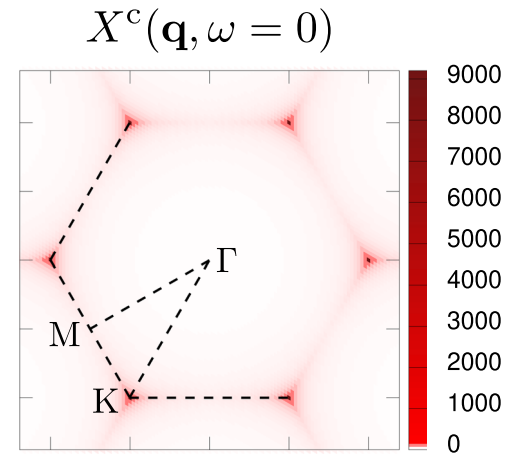


Fig. 5 Momentum resolved charge susceptibility $X^c(\mathbf{q}, \omega = 0)$. Result is obtained close to the CDW transition point $T = 300$ K and $\langle n \rangle = 1.23$ taking into account the electron–phonon coupling.

consistent with the fact that the electron–phonon coupling effectively reduces the on-site Coulomb potential, which consequently decreases the critical temperature for the magnetic instability. The observed shift of the CDW phase boundary can also be explained by the same argument. Indeed, the local Coulomb repulsion favors single occupation of lattice sites. On the contrary, the non-local Coulomb interaction promotes the CDW ordering, which upon reducing the local Coulomb interaction becomes energetically preferable.

Remarkably, Fig. 5 demonstrates that taking into account the electron–phonon coupling does not change the position of Bragg peaks in the charge susceptibility calculated close to the CDW phase transition point $T = 300$ K and $\langle n \rangle = 1.23$. As in the absence of phonons, the momentum-space structure of this susceptibility $X_{\mathbf{q}}^c(\omega = 0)$ consists of six delta-function-like Bragg peaks that appear at K points of the BZ. This fact illustrates that the developed charge ordering also corresponds to a commensurate CDW. Moreover, we do not observe any additional Bragg peaks in the charge susceptibility at twice the Fermi wave vector $\mathbf{q}^* = 2\mathbf{k}_F$, which would indicate a tendency to the charge ordering due to the electron–phonon mechanism.

The effect of phonons can be revealed only upon excluding the contribution of the non-local Coulomb interaction $V_{\mathbf{q}}$ from the charge susceptibility. In this case, an additional exclusion of phonons eliminates both sources of the CDW instability, and $X_{\mathbf{q}\omega}^c$ remains finite at any filling. If the electron–phonon coupling is taken into account, the maximum value of $X_{\mathbf{q}}^c(\omega = 0)$ corresponds to the wave vector \mathbf{q}^* that changes with doping. For instance, at $\langle n \rangle = 1.23$ this wave vector lies between Γ and K points of the BZ (Fig. 6a). However, the value of this susceptibility is negligibly small compared to the almost diverged one calculated in the presence of the non-local Coulomb interaction (see Fig. 5). Increasing the filling, the maximum of the charge susceptibility calculated for the case of $V_{\mathbf{q}} = 0$ also increases, and the corresponding wave vector \mathbf{q}^* shifts towards the K point of the BZ (Fig. 6b). At $\langle n \rangle \simeq 1.40$ ($T = 300$ K) the \mathbf{q}^* reaches the K point (Fig. 6c), and the charge susceptibility diverges. This means that the CDW instability mediated purely by phonons is shifted to much larger values of the filling compared to the one driven by strong Coulomb correlations (orange triangles in Fig. 2). Increasing the filling even more, the charge susceptibility becomes finite again at $\langle n \rangle = 1.92$ (Fig. 6d). Remarkably, Figs. 6c and d show that Bragg peaks that correspond to CDW ordering vectors \mathbf{q}^* are drastically different for two fillings $\langle n \rangle = 1.40$ and $\langle n \rangle = 1.92$. This means that the ordering vector of the phonon-driven CDW also changes inside the CDW phase. These results confirm that the

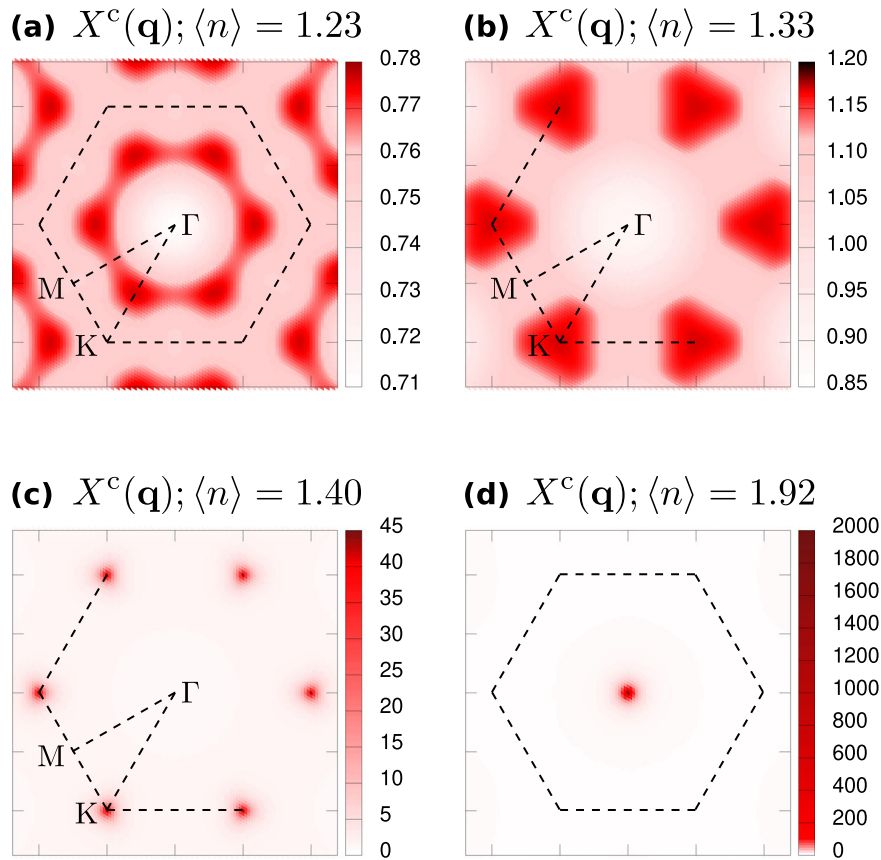


Fig. 6 Momentum resolved charge susceptibility $X^c(\mathbf{q})$ calculated at zero frequency $\omega = 0$. Results are obtained at $T = 300$ K for different values of the filling $\langle n \rangle = 1.23$ (a), $\langle n \rangle = 1.33$ (b), $\langle n \rangle = 1.40$ (c), and $\langle n \rangle = 1.92$ (d) taking into account the electron–phonon coupling and excluding the effect of the non-local Coulomb interaction ($V_q = 0$).

metal-to-CDW phase transition in the monolayer InSe is driven by strong Coulomb correlations rather than by the electron–phonon mechanism as suggested previously¹⁸.

The momentum-structure of the spin susceptibility also changes with doping. At the CDW transition point it stays finite and has a Néel antiferromagnetic (AFM) behavior that manifests itself in the largest value of the susceptibility at K point of the BZ (Fig. 7a). At a larger filling $\langle n \rangle = 1.42$ the Néel AFM form of the spin susceptibility changes to a more complex structure with the largest value at Γ point of the BZ, which indicates the FM instability, and less pronounced intensities at M points corresponding to row-wise AFM fluctuations (Fig. 7b). Increasing the filling to $\langle n \rangle = 1.70$ the van Hove singularity (vHS) in the electronic spectral function appears at the Fermi energy, which strongly enhances collective electronic fluctuations. Fig. 7c shows that close to the magnetic instability the spin susceptibility becomes purely FM, which is indicated by the single delta-function-like Bragg peak that at the Γ point of the BZ. At even larger filling of the band $\langle n \rangle = 1.92$ the spin susceptibility remains FM, but the value of the susceptibility at Γ point decreases compared to the case of the vHS filling (Fig. 7d), which confirms the dome-like structure of the FM instability.

For completeness, we also show the electronic DOS calculated close to the CDW phase transition point $T = 300$ K and $\langle n \rangle = 1.23$ in the presence of the electron–phonon coupling (Fig. 8). We find that in this case the effect of spatial correlations on the DOS is qualitatively the same as in the absence of phonons. Note that in this case DMFT considers the effect of the local electron–phonon coupling via the renormalized on-site Coulomb potential $U^* = U - U_{\omega}^{\text{ph}}$.

DISCUSSION

We have systematically studied many-body effects in the hole-doped InSe monolayer. We have found that this material displays coexisting instabilities that are mainly driven by non-local Coulomb correlations. The commensurate CDW ordering represents the main instability in the system and is revealed in a broad range of doping levels and temperatures. The presence of this ordering is confirmed by the appearance of a pseudogap in the DOS close to the transition point, which illustrates the importance of considering spatial electronic fluctuations. We also observed the tendency to a FM ordering that manifests itself only inside the CDW phase and is related to a vHS in the electronic spectrum. The inclusion of the electron–phonon coupling results in a shift of the CDW and FM ordering phases on the phase diagram, which can be explained by an effective reduction of the local Coulomb interaction. However, the qualitative physical picture does not change in the presence of phonons. Our results suggest that monolayer InSe can serve as an attractive playground for investigation of coexisting many-body correlation effects and, in particular, of 2D magnetism, although in a bulk phase this material is non-magnetic.

In general, the Coulomb-driven CDW instability in electronic systems appears as the result of a competition between local and non-local electron–electron interactions that favor different distribution of electrons on a lattice. In order to change the balance between these interactions, the free standing InSe monolayer considered here could be exposed to external dielectric screening as, e.g., resulting from a substrate or from encapsulation. This mechanism is especially effective in 2D as the environmental screening is non-local in layered materials, which reduces long-ranged interactions stronger than the on-site interaction^{25,26,56}. This kind of Coulomb engineering paves the

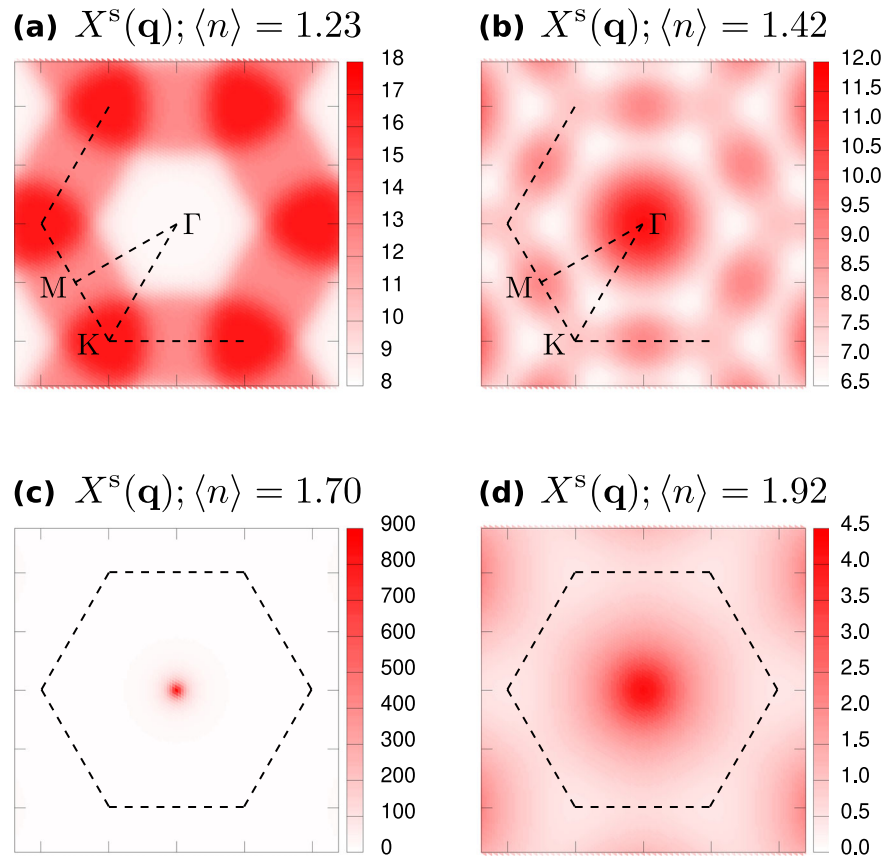


Fig. 7 Momentum resolved spin susceptibility $X^s(\mathbf{q})$ calculated at zero frequency $\omega = 0$ taking into account the electron–phonon coupling. Results are obtained at $T = 300$ K for different values of the filling $\langle n \rangle = 1.23$ (a), $\langle n \rangle = 1.42$ (b), $\langle n \rangle = 1.70$ (c), and $\langle n \rangle = 1.92$ (d).

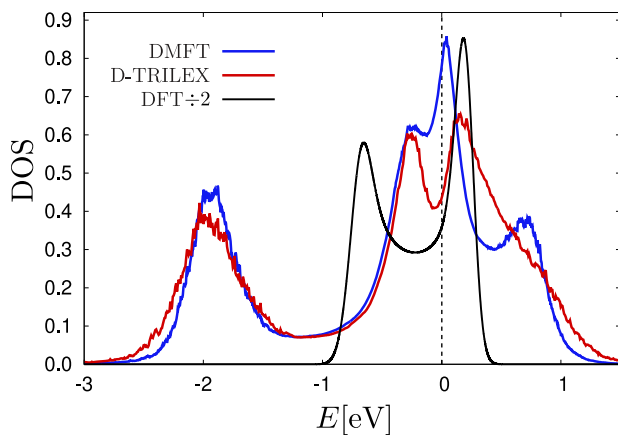


Fig. 8 DOS of the monolayer InSe. Results are obtained within DMFT (blue), D-TRILEX (red), and DFT (black) methods close to a CDW phase boundary at $T = 300$ K and $\langle n \rangle = 1.23$ taking into account the electron–phonon coupling. Note that the DOS of DFT is divided by a factor of 2 for easier comparison.

way for exploring additional degrees of freedom to tune the correlation effects in this 2D material.

METHODS

First-principle calculations

The band structure presented in Fig. 1b was calculated within density functional theory utilizing the projected augmented wave (PAW)

formalism^{57,58} as implemented in the Vienna *ab initio* simulation package (VASP)^{59,60} version 5.4. The exchange–correlation effects were considered using the generalized gradient approximation (GGA)⁶¹ and the standard In and Se pseudopotentials in version 5.4. A 500 eV energy cutoff for the plane-waves and a convergence threshold of 10^{-7} eV were used in the calculations together with tetrahedron method for all involved integrals. The Brillouin zone was sampled by a (36×36) \mathbf{k} -point mesh. We adopted fully relaxed atomic structure with a lattice constant of 3.94 Å, In–In vertical distance of 2.76 Å, and Se–Se vertical distance of 5.37 Å. A ~ 30 Å-thick vacuum layer was added in the direction perpendicular to the 2D plane in order to avoid spurious interactions between supercell images. The Wannier functions and the tight-binding Hamiltonian were calculated within the scheme of maximal localization^{62,63} using the WANNIER90 package⁶⁴ version 1.2.

The Coulomb interaction was evaluated using the maximally localized Wannier functions within the constrained random phase approximation (cRPA)^{65,66} as $U_{ij} = \langle w_i w_j | U | w_j w_i \rangle$, where U is the partially screened Coulomb interaction defined by $U = v + v\Pi U$ with v being the bare Coulomb interaction, Π the cRPA polarization, and w_i is the Wannier function at the lattice site i . The polarization operator Π describes screening from all electronic states except those given by the tight-binding Hamiltonian obtained in the Wannier basis. For these calculations, we used a recent cRPA implementation by Kaltak within VASP⁶⁶. To converge the cRPA polarization with respect to the number of empty states with used in total 64 bands. To derive a light-weighted Coulomb model for arbitrary q -grids, we fitted the cRPA Coulomb interaction in momentum space according to:

$$U(q) = v(q)/\epsilon(q) \quad (2)$$

with the bare Coulomb interaction of a monolayer

$$v(q) = \frac{h}{2\pi} \int_{-\pi/h}^{+\pi/h} \frac{4\pi e^2}{Vq^2} dq_z = \frac{4e^2 \arctan\left(\frac{\pi}{qh}\right)}{A q} \quad (3)$$

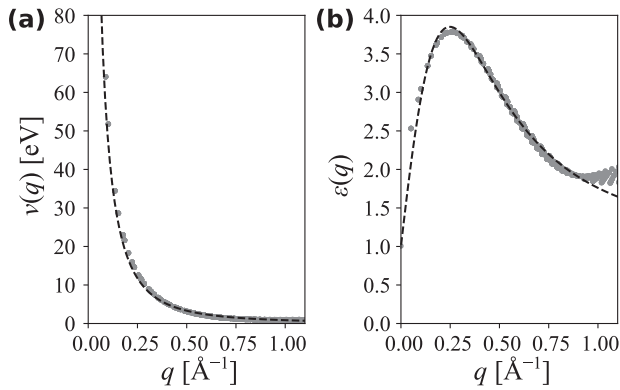


Fig. 9 Coulomb interaction from first-principle calculations. Bare Coulomb interaction (a) and cRPA dielectric function (b) within the Wannier basis. Markers represent ab initio data and dashed lines the corresponding fits.

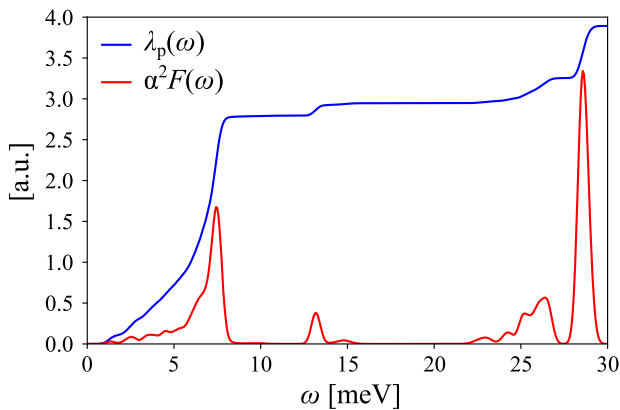


Fig. 10 Phonon properties from first-principle calculations. cDFPT Eliashberg function together with the partial effective electron-phonon coupling $\lambda_p(\omega) = 2 \int_0^\omega d\omega' \frac{\alpha^2 F(\omega')}{\omega'}$.

and the dielectric function

$$\epsilon(q) = \epsilon_0(q) \frac{\epsilon_0(q) + 1 - (\epsilon_0(q) - 1)e^{-qd}}{\epsilon_0(q) + 1 + (\epsilon_0(q) - 1)e^{-qd}} \quad (4)$$

with

$$\epsilon_0(q) = \frac{a + q^2}{\frac{a \sin(qc)}{bc} + q^2}. \quad (5)$$

Here, e , A , and h are the elementary electron charge, the InSe unit cell area and its effective height, respectively, and a , b , c , and d are fitting parameter. In Fig. 9 we show the corresponding ab initio values together with their fits using $h = 15.35 \text{ \AA}$, $a = 1.07 \text{ \AA}^{-2}$, $b = 5.79$, $c = 0.14 \text{ \AA}$, and $d = 8.09 \text{ \AA}$. In this expression $\epsilon_0(q)$ represents the (semi-conducting) cRPA screening in the middle of the film, i.e., $z=0$, which is assumed to be the same for the entire film thickness d and which we parameterized following Ref. 67. The surrounding of the film is supposed to be vacuum. This defines a classical electrostatics problem, which can be analytically solved (see e.g., Ref. 68). The full non-local cRPA background screening then takes the form of Eq. (4). More details on this can be found in Ref. 26. The real-space U_{ij} are calculated via a conventional Fourier transform of $U(q)$ from Eq. (2) and using these fits.

The phonon properties are calculated within QUANTUM ESPRESSO⁶⁹ version 6.5 using norm-conserving pseudopotentials generated using the “atomic” code by A. Dal Corso (v.5.0.99 svn rev. 10869, 2014), the local density approximation, an energy cutoff of 80 Ry, and a finite hole doping of 0.04 holes per unit cell. For the initial constrained Density Functional Perturbation Theory (cDFPT)³¹ calculation we use (16×16) \mathbf{k} and (8×8) \mathbf{q} -point meshes and exclude the highest (hole doped) valence band within the evaluation of the Sternheimer equation. Afterwards we use the EPW code⁷⁰ version 5.0.0 to extrapolate the cDFPT results to (32×32) \mathbf{k} - and

\mathbf{q} -point meshes using a Wannier interpolation based on a single Wannier projection for the highest valence band (in the very same way as we constructed them in VASP for the cRPA calculations). This allows us to accurately calculate the cDFPT Eliashberg function $\alpha^2 F(\omega)$ as shown in Fig. 10. From this we calculate the effective electron-phonon coupling $\lambda = 2 \int d\omega \frac{\alpha^2 F(\omega)}{\omega}$ which we finally use to fit our local phonon model via $\alpha^2 F(\omega) \approx N_0 g^2 \delta(\omega - \omega_{ph})$ with $N_0 = 3.88 \text{ eV}^{-1}$ per spin per unit cell.

Many-body calculations

The introduced many-body electronic model (1) is solved using the finite-temperature diagrammatic D-TRILEX approach^{43–45}. In this method, local correlation effects are treated via the self-energy $\Sigma_{\mathbf{q}\omega}^{\text{imp}}$ and the polarization operator $\Pi_{\mathbf{q}\omega}^{\text{imp}}$ of an effective local impurity problem of DMFT. These quantities are written in the fermionic (ν) and bosonic (ω) Matsubara frequency space, respectively. The corresponding impurity problem is solved numerically exactly using the open source CT-HYB solver^{71,72} based on ALPS libraries⁷³.

Within the self-consistent calculations, the spatial fluctuations are considered in a partially bosonized form of the renormalized charge ($\zeta=c$) and spin ($\zeta=s$) interactions $W_{\mathbf{q}\omega}^{\zeta}$ that enter the diagrammatic part of the self-energy $\bar{\Sigma}_{\mathbf{k}\nu}$ introduced beyond DMFT^{43–45}. The dressed Green’s function $G_{\mathbf{k}\nu}$ of the problem can be found using the standard Dyson equation $G_{\mathbf{k}\nu}^{-1} = i\nu + \mu - \epsilon_{\mathbf{k}} - \Sigma_{\mathbf{k}\nu}$ written in momentum \mathbf{k} space. In this expression μ is the chemical potential, $\epsilon_{\mathbf{k}}$ is the electronic dispersion that can be obtained as a Fourier transform of the hopping amplitudes t_{ij} , and $\Sigma_{\mathbf{k}\nu} = \Sigma_{\mathbf{k}\nu}^{\text{imp}} + \bar{\Sigma}_{\mathbf{k}\nu}$ is the total self-energy. The renormalized interaction $W_{\mathbf{q}\omega}^{\zeta}$ can be found via the following Dyson equation $W_{\mathbf{q}\omega}^{\zeta-1} = U_{\mathbf{q}\omega}^{\zeta-1} - \Pi_{\mathbf{q}\omega}^{\zeta}$, where $U_{\mathbf{q}\omega}^{\zeta} = U/2 - U_{\omega}^{\text{ph}} + V_{\mathbf{q}}$ and $U_{\mathbf{q}\omega}^s = -U/2$ are the bare interactions in the charge and spin channels, respectively^{43–45}. $\Pi_{\mathbf{q}\omega}^{\zeta} = \Pi_{\mathbf{q}\omega}^{\text{imp}\zeta} + \bar{\Pi}_{\mathbf{q}\omega}^{\zeta}$ is the total polarization operator of the problem, where $\bar{\Pi}_{\mathbf{q}\omega}^{\zeta}$ is the diagrammatic contribution introduced in the D-TRILEX approach^{43–45}. In this way, the dressed lattice Green’s function $G_{\mathbf{k}\nu}$ takes into account both, local and non-local correlation effects. To obtain the electronic DOS, we take the local part of the lattice Green’s function $G_{\nu}^{\text{loc}} = \frac{1}{N} \sum_{\mathbf{k}} G_{\mathbf{k}\nu}$ and perform an analytical continuation from Matsubara frequency space (ν) to real energies (E) using the stochastic optimization method⁷⁴.

In the single-shot D-TRILEX calculations for the susceptibility the diagrammatic part of the polarization operator $\bar{\Pi}_{\mathbf{q}\omega}^{\zeta}$ is obtained non-self-consistently. In this case, $\bar{\Pi}_{\mathbf{q}\omega}^{\zeta}$ accounts only for DMFT Green’s functions $G_{\mathbf{k}\nu}^{\text{D}}$ that are dressed by the local self-energies: $G_{\mathbf{k}\nu}^{\text{D}-1} = i\nu + \mu - \epsilon_{\mathbf{k}} - \Sigma_{\mathbf{k}\nu}^{\text{imp}}$. Charge and spin susceptibilities $\chi_{\mathbf{q}\omega}^{\zeta}$ can then be obtained straightforwardly as $\chi_{\mathbf{q}\omega}^{\zeta-1} = \Pi_{\mathbf{q}\omega}^{\zeta-1} - U_{\mathbf{q}\omega}^{\zeta}$. We note that this form of the D-TRILEX susceptibility resembles the DMFT susceptibility^{75–77} with a longitudinal dynamical vertex corrections⁴⁴.

DATA AVAILABILITY

The data that support the findings of this work are available from the corresponding author upon reasonable request.

CODE AVAILABILITY

First-principle calculations have been performed on the basis of VASP^{59,60} and QUANTUM ESPRESSO⁶⁹ codes that can be requested from the developers. Many-body calculations have been performed using the implementation of the D-TRILEX method^{43,44} that can be obtained from the corresponding authors upon reasonable request.

Received: 18 January 2022; Accepted: 21 April 2022;

Published online: 24 May 2022

REFERENCES

- Bandurin, D. A. et al. High electron mobility, quantum Hall effect and anomalous optical response in atomically thin InSe. *Nat. Nanotechnol.* **12**, 223–227 (2017).
- Sucharitakul, S. et al. Intrinsic electron mobility exceeding $10^3 \text{ cm}^2/(\text{V s})$ in multilayer InSe FETs. *Nano Lett.* **15**, 3815–3819 (2015).
- Tamalampudi, S. R. et al. High performance and bendable few-layered InSe photodetectors with broad spectral response. *Nano Lett.* **14**, 2800–2806 (2014).

4. Mudd, G. W. et al. The direct-to-indirect band gap crossover in two-dimensional van der Waals Indium Selenide crystals. *Sci. Rep.* **6**, 39619 (2016).
5. Hung, N. T., Nugraha, A. R. T. & Saito, R. Two-dimensional InSe as a potential thermoelectric material. *Appl. Phys. Lett.* **111**, 092107 (2017).
6. Shang, J. et al. Tunable electronic and optical properties of InSe/InTe van der Waals heterostructures toward optoelectronic applications. *J. Mater. Chem. C* **6**, 7201–7206 (2018).
7. Zólyomi, V., Drummond, N. D. & Fal'ko, V. I. Electrons and phonons in single layers of hexagonal indium chalcogenides from ab initio calculations. *Phys. Rev. B* **89**, 205416 (2014).
8. Kibirev, I. A., Matetskiy, A. V., Zotov, A. V. & Saranin, A. A. Thickness-dependent transition of the valence band shape from parabolic to Mexican-hat-like in the MBE grown InSe ultrathin films. *Appl. Phys. Lett.* **112**, 191602 (2018).
9. Henck, H. et al. Evidence of direct electronic band gap in two-dimensional van der Waals indium selenide crystals. *Phys. Rev. Mater.* **3**, 034004 (2019).
10. Irkhin, V. Y., Katanin, A. A. & Katsnelson, M. I. Effects of van Hove singularities on magnetism and superconductivity in the $t-t'$ Hubbard model: A parquet approach. *Phys. Rev. B* **64**, 165107 (2001).
11. Kampf, A. P. & Katanin, A. A. Competing phases in the extended $U-V-J$ Hubbard model near the Van Hove fillings. *Phys. Rev. B* **67**, 125104 (2003).
12. Metzner, W., Salmhofer, M., Honerkamp, C., Meden, V. & Schönhammer, K. Functional renormalization group approach to correlated fermion systems. *Rev. Mod. Phys.* **84**, 299–352 (2012).
13. Cao, Y. et al. Unconventional superconductivity in magic-angle graphene superlattices. *Nature* **556**, 43–50 (2018).
14. Cao, Y. et al. Correlated insulator behaviour at half-filling in magic-angle graphene superlattices. *Nature* **556**, 80–84 (2018).
15. Yankowitz, M. et al. Tuning superconductivity in twisted bilayer graphene. *Science* **363**, 1059–1064 (2019).
16. Yudin, D. et al. Fermi condensation near van Hove singularities within the Hubbard model on the triangular lattice. *Phys. Rev. Lett.* **112**, 070403 (2014).
17. Lugovskoi, A. V., Katsnelson, M. I. & Rudenko, A. N. Strong electron-phonon coupling and its influence on the transport and optical properties of hole-doped single-layer inSe. *Phys. Rev. Lett.* **123**, 176401 (2019).
18. Alidoosti, M., Esfahani, D. N. & Asgari, R. Charge density wave and superconducting phase in monolayer InSe. *Phys. Rev. B* **103**, 035411 (2021).
19. Iordanidou, K. et al. Hole-doped 2D InSe for spintronic applications. *ACS Appl. Nano Mater.* **1**, 6656–6665 (2018).
20. Ceferino, A. et al. Tunable spin-orbit coupling in two-dimensional inSe. *Phys. Rev. B* **104**, 125432 (2021).
21. Zólyomi, V., Drummond, N. D. & Fal'ko, V. I. Electrons and phonons in single layers of hexagonal indium chalcogenides from ab initio calculations. *Phys. Rev. B* **89**, 205416 (2014).
22. Li, G., Antipov, A. E., Rubtsov, A. N., Kirchner, S. & Hanke, W. Competing phases of the Hubbard model on a triangular lattice: Insights from the entropy. *Phys. Rev. B* **89**, 161118 (2014).
23. Das Sarma, S. & Hwang, E. H. Screening and transport in 2D semiconductor systems at low temperatures. *Sci. Rep.* **5**, 16655 (2015).
24. Katsnelson, M. I. *The Physics of Graphene 2nd edn* (Cambridge University Press, 2020).
25. Andersen, K., Latini, S. & Thygesen, K. S. Dielectric Genome of van der Waals Heterostructures. *Nano Lett.* **15**, 4616–4621 (2015).
26. Rösner, M., Şaşıoğlu, E., Friedrich, C., Blügel, S. & Wehling, T. O. Wannier function approach to realistic Coulomb interactions in layered materials and heterostructures. *Phys. Rev. B* **92**, 085102 (2015).
27. Wehling, T. O. et al. Strength of Effective Coulomb Interactions in Graphene and Graphite. *Phys. Rev. Lett.* **106**, 236805 (2011).
28. van Loon, E. G. C. P., Rösner, M., Schönhoff, G., Katsnelson, M. I. & Wehling, T. O. Competing Coulomb and electron-phonon interactions in NbS₂. *npj Quantum Mater.* **3**, 1–8 (2018).
29. Vonsovsky, S. V. & Katsnelson, M. I. Some types of instabilities in the electron energy spectrum of the polar model of the crystal. I. The maximum-polarity state. *J. Phys. C: Solid State Phys.* **12**, 2043–2053 (1979).
30. Zhang, Y. & Callaway, J. Extended Hubbard model in two dimensions. *Phys. Rev. B* **39**, 9397–9404 (1989).
31. Nomura, Y. & Arita, R. Ab initio downfolding for electron-phonon-coupled systems: Constrained density-functional perturbation theory. *Phys. Rev. B* **92**, 245108 (2015).
32. Berger, E., Valášek, P. & von der Linden, W. Two-dimensional Hubbard-Holstein model. *Phys. Rev. B* **52**, 4806–4814 (1995).
33. Sangiovanni, G., Capone, M., Castellani, C. & Grilli, M. Electron-phonon interaction close to a mott transition. *Phys. Rev. Lett.* **94**, 026401 (2005).
34. Werner, P. & Millis, A. J. Efficient dynamical mean field simulation of the Holstein-Hubbard model. *Phys. Rev. Lett.* **99**, 146404 (2007).
35. Pines, D. & Nozieres, P. *The theory of quantum liquids: normal fermi liquids. theory of quantum liquids* (W.A. Benjamin, Philadelphia, 1966).
36. Platzman, P. M. & Wolff, P. A. *Waves and interactions in solid state plasmas*, vol. 13 (Academic Press, New York, 1973).
37. Vonsovsky, S. V. & Katsnelson, M. I. *Quantum solid-state physics* (Springer Verlag, Berlin, 1989).
38. Hedin, L. New method for calculating the one-particle green's function with application to the electron-gas problem. *Phys. Rev.* **139**, A796–A823 (1965).
39. Aryasetiawan, F. & Gunnarsson, O. The GW method. *Rep. Prog. Phys.* **61**, 237 (1998).
40. Hedin, L. On correlation effects in electron spectroscopies and the GW approximation. *J. Phys. Condens. Matter* **11**, R489 (1999).
41. Georges, A., Kotliar, G., Krauth, W. & Rozenberg, M. J. Dynamical mean-field theory of strongly correlated fermion systems and the limit of infinite dimensions. *Rev. Mod. Phys.* **68**, 13–125 (1996).
42. Rohringer, G. et al. Diagrammatic routes to nonlocal correlations beyond dynamical mean field theory. *Rev. Mod. Phys.* **90**, 025003 (2018).
43. Stepanov, E. A., Harkov, V. & Lichtenstein, A. I. Consistent partial bosonization of the extended Hubbard model. *Phys. Rev. B* **100**, 205115 (2019).
44. Harkov, V., Vandelli, M., Brenner, S., Lichtenstein, A. I. & Stepanov, E. A. Impact of partially bosonized collective fluctuations on electronic degrees of freedom. *Phys. Rev. B* **103**, 245123 (2021).
45. Vandelli, M. et al. Multi-band D-TRILEX approach to materials with strong electronic correlations. <https://arxiv.org/abs/2204.06426> (2022).
46. Stepanov, E. A., Nomura, Y., Lichtenstein, A. I. & Biermann, S. Orbital isotropy of magnetic fluctuations in correlated electron materials induced by Hund's exchange coupling. *Phys. Rev. Lett.* **127**, 207205 (2021).
47. Efetov, D. K. & Kim, P. Controlling electron-phonon interactions in graphene at ultrahigh carrier densities. *Phys. Rev. Lett.* **105**, 256805 (2010).
48. Crowther, A. C., Ghassaei, A., Jung, N. & Brus, L. E. Strong charge-transfer doping of 1 to 10 layer graphene by NO₂. *ACS Nano* **6**, 1865–1875 (2012).
49. Vandelli, M. et al. Extended regime of coexisting metallic and insulating phases in a two-orbital electronic system. <https://arxiv.org/abs/2204.02116> (2022).
50. Stepanov, E. A. Eliminating orbital selectivity from the metal-insulator transition by strong magnetic fluctuations. <https://arxiv.org/abs/2204.02895> (2022).
51. Keldysh, L. V. & Kopayev, Y. V. Possible instability of semimetallic state toward Coulomb interaction. *Soviet Phys. Solid State* **6**, 2219 (1965).
52. Kozlov, A. N. & Maksimov, L. A. The metal-dielectric divalent crystal phase transition. *Sov. Phys. JETP* **21**, 790 (1965).
53. Halperin, B. I. & Rice, T. M. The excitonic state at the semiconductor-semimetal transition. In *Solid State Physics*, vol. 21, 115–192 (Academic Press, 1968). <https://www.sciencedirect.com/science/article/pii/S0081194708607407>.
54. Irkhin, V. Y. & Katsnelson, M. I. Current carriers in a quantum two-dimensional antiferromagnet. *J. Phys. Condens. Matter* **3**, 6439–6453 (1991).
55. Rudenko, A. N., Stepanov, E. A., Lichtenstein, A. I. & Katsnelson, M. I. Excitonic instability and pseudogap formation in nodal line semimetal ZrSiS. *Phys. Rev. Lett.* **120**, 216401 (2018).
56. Waldecker, L. et al. Rigid band shifts in two-dimensional semiconductors through external dielectric screening. *Phys. Rev. Lett.* **123**, 206403 (2019).
57. Blöchl, P. E. Projector augmented-wave method. *Phys. Rev. B* **50**, 17953–17979 (1994).
58. Kresse, G. & Joubert, D. From ultrasoft pseudopotentials to the projector augmented-wave method. *Phys. Rev. B* **59**, 1758–1775 (1999).
59. Kresse, G. & Furthmüller, J. Efficiency of ab-initio total energy calculations for metals and semiconductors using a plane-wave basis set. *Comput. Mater. Sci.* **6**, 15–50 (1996).
60. Kresse, G. & Furthmüller, J. Efficient iterative schemes for ab initio total-energy calculations using a plane-wave basis set. *Phys. Rev. B* **54**, 11169–11186 (1996).
61. Perdew, J. P., Burke, K. & Ernzerhof, M. Generalized gradient approximation made simple. *Phys. Rev. Lett.* **77**, 3865–3868 (1996).
62. Marzari, N. & Vanderbilt, D. Maximally localized generalized Wannier functions for composite energy bands. *Phys. Rev. B* **56**, 12847–12865 (1997).
63. Marzari, N., Mostofi, A. A., Yates, J. R., Souza, I. & Vanderbilt, D. Maximally localized Wannier functions: Theory and applications. *Rev. Mod. Phys.* **84**, 1419–1475 (2012).
64. Mostofi, A. A. et al. wannier90: a tool for obtaining maximally localised Wannier functions. *Comput. Phys. Commun.* **178**, 685 – 699 (2008).
65. Miyake, T. & Aryasetiawan, F. Screened coulomb interaction in the maximally localized wannier basis. *Phys. Rev. B* **77**, 085122 (2008).
66. Kaltak, M. Merging GW with DMFT (2015). <http://othes.univie.ac.at/38099/>. PhD Thesis, University of Vienna, 2015, 231 pp.
67. Resta, R. Thomas-Fermi dielectric screening in semiconductors. *Phys. Rev. B* **16**, 2717–2722 (1977).
68. Keldysh, L. V. Coulomb interaction in thin semiconductor and semimetal films. *JETP Lett.* **29**, 658 (1979). [*Pis'ma Zh. Eksp. Teor. Fiz.* **29**, 716 (1979)].

69. Giannozzi, P. et al. Advanced capabilities for materials modelling with Quantum ESPRESSO. *J. Phys. Condens. Matter* **29**, 465901 (2017).
70. Poncè, S., Margine, E. R., Verdi, C. & Giustino, F. EPW: electron-phonon coupling, transport and superconducting properties using maximally localized Wannier functions. *Comput. Phys. Commun.* **209**, 116–133 (2016).
71. Hafermann, H., Werner, P. & Gull, E. Efficient implementation of the continuous-time hybridization expansion quantum impurity solver. *Comput. Phys. Commun.* **184**, 1280–1286 (2013).
72. Hafermann, H. Self-energy and vertex functions from hybridization-expansion continuous-time quantum monte carlo for impurity models with retarded interaction. *Phys. Rev. B* **89**, 235128 (2014).
73. Bauer, B. et al. The ALPS project release 2.0: open source software for strongly correlated systems. *J. Stat. Mech.: Theory Exp.* **2011**, P05001 (2011).
74. Krivenko, I. & Harland, M. TRIQS/SOM: implementation of the stochastic optimization method for analytic continuation. *Comput. Phys. Commun.* **239**, 166–183 (2019).
75. Boehnke, L. & Lechermann, F. Competing orders in Na_xCoO_2 from strong correlations on a two-particle level. *Phys. Rev. B* **85**, 115128 (2012).
76. Boehnke, L., Werner, P. & Lechermann, F. Multi-orbital nature of the spin fluctuations in Sr_2RuO_4 . *Europhys. Lett.* **122**, 57001 (2018).
77. Strand, H. U. R., Zingl, M., Wentzell, N., Parcollet, O. & Georges, A. Magnetic response of Sr_2RuO_4 : Quasi-local spin fluctuations due to Hund's coupling. *Phys. Rev. B* **100**, 125120 (2019).

ACKNOWLEDGEMENTS

We thank Andy J. Millis for fruitful discussions, Jan Berges for sharing his cDFPT-related changes to QUANTUM ESPRESSO with us, and Igor Krivenko for technical support of SOM. The work of E.A.S. was supported by the European Union's Horizon 2020 Research and Innovation programme under the Marie Skłodowska Curie grant agreement No. 839551 - 2DMAGICS. The work of M.I.K., A.N.R., and A.I.L. was supported by European Research Council via Synergy Grant 854843 - FASTCORR. V.H. and A.I.L. acknowledge the support by the Cluster of Excellence "Advanced Imaging of Matter" of the Deutsche Forschungsgemeinschaft (DFG) - EXC 2056 - Project No. ID390715994. E.A.S., V.H., and A.I.L. also acknowledge the support by North-German Supercomputing Alliance (HLRN) under the Project No. hhp00042.

AUTHOR CONTRIBUTIONS

All authors discussed the results and contributed to the preparation of the manuscript.

COMPETING INTERESTS

The authors declare no competing interests.

ADDITIONAL INFORMATION

Correspondence and requests for materials should be addressed to Evgeny A. Stepanov or Alexander N. Rudenko.

Reprints and permission information is available at <http://www.nature.com/reprints>

Publisher's note Springer Nature remains neutral with regard to jurisdictional claims in published maps and institutional affiliations.



Open Access This article is licensed under a Creative Commons Attribution 4.0 International License, which permits use, sharing, adaptation, distribution and reproduction in any medium or format, as long as you give appropriate credit to the original author(s) and the source, provide a link to the Creative Commons license, and indicate if changes were made. The images or other third party material in this article are included in the article's Creative Commons license, unless indicated otherwise in a credit line to the material. If material is not included in the article's Creative Commons license and your intended use is not permitted by statutory regulation or exceeds the permitted use, you will need to obtain permission directly from the copyright holder. To view a copy of this license, visit <http://creativecommons.org/licenses/by/4.0/>.

© The Author(s) 2022

Chapter 6

SBE

This chapter is based on the following publication:

V. Harkov, A. I. Lichtenstein, F. Krien, “Parameterizations of local vertex corrections from weak to strong coupling: Importance of the Hedin three-leg vertex”. *Phys. Rev. B* **104**, 125141 (2021)

6.1 Parametrizations of local vertex corrections from weak to strong coupling: Importance of the Hedin three-leg vertex

Previously we have shown that the local four-point vertex of the impurity model can be parameterized in terms of the three-point Hedin vertex and screened interaction. Moreover, we have shown that the irreducible part of the vertex can be excluded in a broad range of parameters. A similar parametrization of the four-point vertex, called SBE decomposition (3.90), was recently introduced in [70]. In the approximation, the four-point vertex is decomposed in terms of effective exchange bosons and their coupling to fermions mediated by the three-point Hedin vertex similar to [128, 131, 136, 185, 190–192].

In the following study [75] we apply the SBE approximation on the two-dimensional single-band Hubbard model to calculate the DMFT susceptibility on the two-dimensional single-band Hubbard model and show that the results are recovered to a good approximation in the limits of weak and strong couplings. At the same time, neglecting the irreducible part of the four-point vertex φ^{Uirr} (as it is done in the SBE approximation) reduces the computational costs drastically. In our extensive study, we show the importance of the frequency-dependent Hedin vertex by comparing the results of the SBE decomposition with the *w approximation* where the vertex in SBE is set to its non-interactive limit and with parametrization based on its asymptotic limits [193]

which we call *asymptotic approximation*. Thereby, we find that the Hedin vertex captures the Kanamori screening at weak coupling and suppresses the Néel temperature compared to the static mean-field approximation, while at strong couplings the vertex is important for a correct description of the spin fluctuations and therefore the results where the vertex is partially (or totally) neglected become qualitatively wrong. Furthermore, comparing the SBE approximation with the asymptotic approximation at $U/t = 8$ for different temperatures in a nontrivial crossover regime (from a local moment phase¹ to the Fermi liquid) we show that the SBE decomposition should be preferred over the asymptotic approximation since the former retains the correspondence to all resonant features of the full four-point vertex at all energy scales.

In an additional study, we apply the SBE approximation to compute the momentum-dependent self-energy within the ladder DF approximation at weak coupling $U/t = 2$ to investigate the formation of the pseudo gap as it was done in Ref. [85] and in Ref. [128]. We find that the SBE approximation underestimates the magnetic fluctuations and shows the opening of the pseudo gap at lower temperatures, compared to numerical exact results. However, the SBE approximation results are in good quantitative agreement with the results of the ladder DF approximation.

Since the SBE approximation reduces the computational costs drastically, generalizing it to multi-orbital settings may provide solutions for systems where the computation of the four-point is numerically challenging or not even possible [65, 66, 197]. It can be also used in advanced schemes like state-of-the-art fRG [198] and parquet schemes [136, 137] to reduce computational costs.

¹For the recent progress regarding the formation of the local moment see, i.a., Ref. [194–196].

Parametrizations of local vertex corrections from weak to strong coupling: importance of the Hedin three-leg vertex

Viktor Harkov,^{1,2} Alexander I. Lichtenstein,^{1,2} and Friedrich Krien^{3,4}

¹*Institute of Theoretical Physics, University of Hamburg, 20355 Hamburg, Germany*

²*European X-Ray Free-Electron Laser Facility, Holzkoppel 4, 22869 Schenefeld, Germany*

³*Institute for Solid State Physics, TU Wien, 1040 Vienna, Austria*

⁴*Jožef Stefan Institute, Jamova 39, SI-1000, Ljubljana, Slovenia*

In the study of correlated systems, approximations based on the dynamical mean-field theory (DMFT) provide a practical way to take local vertex corrections into account, which capture, respectively, particle-particle screening at weak coupling and the formation of the local moment at strong coupling. We show that in both limits the local vertex corrections can be efficiently parametrized in terms of single-boson exchange, such that the two-particle physics described by DMFT and its diagrammatic extensions is recovered to good approximation and at a reduced computational cost. Our investigation highlights the importance of the frequency-dependent fermion-boson coupling (Hedin vertex) for local vertex corrections. Namely, at weak coupling the fermion-spin-boson coupling suppresses the Néel temperature of the DMFT approximation compared to the static mean-field, whereas for large interaction it facilitates a huge enhancement of local spin-fluctuation exchange, giving rise to the effective-exchange energy scale $4t^2/U$. We find that parametrizations of the vertex which neglect the nontrivial part of the fermion-boson coupling fail qualitatively at strong coupling.

Two-particle electronic correlations provide an essential and complementary viewpoint on correlated systems [1]. For example, the calculation of susceptibilities greatly simplifies the study of second order phase transitions, compared to calculations on the one-particle level which require the introduction of complicated unit cells and conjugate fields [2–5]. Further, in a great variety of perturbative many-body techniques the electronic self-energy is given as a set of vertex diagrams, so that in effect two-particle quantities need to be evaluated before one obtains information about the one-particle correlations [6]. In fact, even the celebrated Fermi liquid theory is at its core defined through two-particle scattering amplitudes, the Landau parameters [7–10].

However, two problems are often encountered in the study of two-particle correlations. First, even in case of simple systems, it is exceedingly difficult to compute or even only memorize [11] on present-day computing devices the complete two-particle information, as represented by the four-point vertex function. Second, a clear organizing principle for two-particle correlations is often missing, which would allow to decode the physics encapsulated in the vertex function.

Here we like to put forth the notion, and demonstrate in practice on a particular example, that the two mentioned problems are in fact related: When the two-particle correlations are organized in a way that mirrors the key physics at play, the computational effort can be reduced. Or one can more easily define suitable approximations which achieve this goal.

We derive this guiding theme from both established and recently introduced (partial) bosonizations of the vertex function [12–14]. Namely, in the context of the functional renormalization group (fRG, [15, 16]) the vertex is often decomposed into various channels [17–24], or parametrized in terms of bosonic fluctuations and their (Yukawa) coupling to fermions [25–28]. In particular the

latter procedure provides, simultaneously, and in accord with the guiding theme of this work, (i) an organizing principle for two-particle correlations and (ii) a reduction of the computational effort. This is because, on the one hand, the bosonic propagators and Yukawa couplings have a transparent physical interpretation, and, on the other hand, they can be computed and stored more easily than a genuine four-point vertex.

In this context, it can be shown under very general assumptions [29] that vertex diagrams have special properties when they are reducible with respect to the interaction. Namely, interaction-reducible diagrams give rise to the high-frequency asymptotics of the vertex function [22], and in the case of a lattice model, they carry crucial information about its dependence on the momenta [30–32]. In the single-boson exchange (SBE) decomposition [33] the vertex diagrams are grouped into three interaction-reducible classes and one irreducible class. Each reducible class corresponds to the exchange of a single boson and the irreducible class represents multiple boson exchange [30, 31]. In this formalism the bosons and Yukawa couplings can be identified, respectively, as the screened interaction and the Hedin three-leg vertex of the $GW\gamma$ theory [34]. In this way, the SBE decomposition provides a conceptual link between Hedin’s equations [31], vertex asymptotics [22], partial bosonizations [14, 35–37], and the parquet approach [38–40].

Here we apply this general framework to a specific problem, namely, the calculation of two-particle correlation functions within dynamical mean-field theory [41] and its diagrammatic extensions [6]. These methods rely on the solution of an auxiliary Anderson impurity model (AIM) which provides the local correlations non-perturbatively. Here, the computationally most expensive step is in general the evaluation of the local vertex function $f(\nu, \nu', \omega)$ of the impurity model, for example, using continuous-time quantum Monte Carlo (CTQMC)

algorithms [42], due to its dependence on one bosonic (ω) and two fermionic (ν, ν') Matsubara frequencies. This step is especially expensive in multi-orbital settings, where the calculation of a single vertex function may require hundreds of thousands of core hours [43], raising questions regarding the feasibility of frequent calculations and parameter scans.

We address this problem in the spirit of the discussed strategy to first find a useful organizing principle for the two-particle correlations, and second to define a cheap approximation for the impurity vertex based on this insight. To this end, we employ the approximation for the impurity vertex sketched on the top of Fig. 1, where the vertex is parametrized in terms of the screened interaction (wiggly lines) and the Hedin vertex (triangles), which are computationally cheap to obtain. On the other hand, the approximation neglects a residual (interaction-irreducible) four-point vertex ‘ φ^{Uirr} ’, whose calculation is computationally expensive.

In the following, we show that this ‘SBE approximation’ is *sufficient* in the sense that it recovers the two-particle physics described by DMFT and its extensions at both weak and strong coupling. But we also show that it is *necessary* to keep this much information about the impurity vertex function. In particular, the nontrivial (interacting) part of the Hedin vertex should not be neglected, because it leads to qualitatively wrong results at strong coupling. In this limit parametrizations based only on the screened interaction or on vertex asymptotics fail. In the latter case, we show that this can be related to qualitative differences in the frequency structure of the residual vertices (also called rest functions [22]) of, respectively, the SBE decomposition and the vertex asymptotics.

For concreteness, we consider the paramagnetic Hubbard model on the square lattice at half-filling,

$$H = - \sum_{\langle ij \rangle \sigma} t_{ij} c_{i\sigma}^\dagger c_{j\sigma} + U \sum_i n_{i\uparrow} n_{i\downarrow}, \quad (1)$$

where t_{ij} denotes the hopping between nearest neighbors i and j , its absolute value $t = 1$ sets the unit of energy. c, c^\dagger are the annihilation and creation operators with the spin index $\sigma = \uparrow, \downarrow$. The Coulomb repulsion between the densities $n_\sigma = c_\sigma^\dagger c_\sigma$ is denoted by U .

LOCAL VERTEX CORRECTIONS

In DMFT [41] the Hubbard model (1) is mapped to the auxiliary AIM with the action,

$$S_{\text{AIM}} = - \sum_{\nu\sigma} c_{\nu\sigma}^* (\nu + \mu - \Delta_\nu) c_{\nu\sigma} + U \sum_\omega n_{\uparrow\omega} n_{\downarrow\omega}, \quad (2)$$

where c and c^* are Grassmann numbers and ν and ω are fermionic and bosonic Matsubara frequencies, respectively. Half-filling is implied by setting the chemical potential to $\mu = \frac{U}{2}$ to enforce particle-hole symmetry.

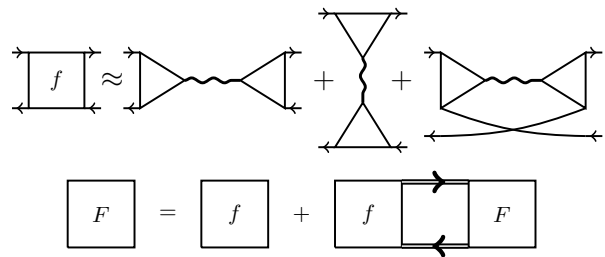


FIG. 1. Top: Symbolic representation of the *SBE approximation*. Wiggly lines and triangles represent, respectively, the screened interaction w and the Hedin vertices λ . The w -approximation corresponds to setting $|\lambda| = 1$. Arrows denote the impurity Green’s function g ; prefactors, flavor labels, and a double counting correction are omitted. Bottom: The nonlocal Bethe-Salpeter equation constructs the lattice vertex function F from impurity vertex f and nonlocal propagator \tilde{G} (double arrows).

Summations over Matsubara frequencies ν, ω contain implicitly the factor T , the temperature. The DMFT hybridization function Δ_ν is fixed by the self-consistency condition, $G_{ii}(\nu) = g(\nu)$, for the local Green’s function G_{ii} of the Hubbard model (1) and the Green’s function of the impurity model (2), $g_\sigma(\nu) = -\langle c_{\nu\sigma} c_{\nu\sigma}^* \rangle$. The label σ is suppressed where unambiguous.

In the DMFT approximation the *nonlocal* two-particle correlations arise from a Bethe-Salpeter equation with *local* vertex corrections [41, 44]. In the equivalent dual fermion formulation [45–47] one avoids the (particle-hole) irreducible vertex and instead builds the vertex corrections from the full vertex function f of the AIM (2), cf. Fig. 1 bottom,

$$F_{\nu\nu'}^\alpha(q) = f_{\nu\nu'\omega}^\alpha + \sum_{\nu''} f_{\nu\nu''\omega}^\alpha \tilde{X}_{\nu''}^0(q) F_{\nu''\nu'}^\alpha(q). \quad (3)$$

Here, $\tilde{X}_\nu^0(q) = \sum_{\mathbf{k}} \tilde{G}_k \tilde{G}_{k+q}$ is a bubble of nonlocal propagators \tilde{G} , where $k = (\mathbf{k}, \nu)$, $q = (\mathbf{q}, \omega)$, and the summation over the momentum \mathbf{k} implies division by the number of lattice sites N . For the precise definition of the impurity vertex function f see Appendix A. At DMFT level $\tilde{G} = \mathcal{G}$, where $\mathcal{G}_k \equiv G_k - g_\nu$ is the nonlocal DMFT Green’s function, whereas in the dual fermion approach \tilde{G} is further dressed with a self-energy [45], $\tilde{G}_k^{-1} = \mathcal{G}_k^{-1} - \tilde{\Sigma}_k$. In the following, Eq. (3) serves us as a generic starting point to evaluate the two-particle correlations within DMFT ($\tilde{\Sigma} = 0$) and in the ladder dual fermion approach (LDFA, [48]; with $\tilde{\Sigma}$ given as described further below).

In our applications we evaluate Eq. (3) with a physical cutoff $\nu^{\text{max}} = 45t$ for the fermionic Matsubara frequencies ν_n , that is, a variable grid with $-\lfloor \nu^{\text{max}}/(2\pi T) \rfloor - 1 \leq n \leq \lfloor \nu^{\text{max}}/(2\pi T) \rfloor$, and similarly $0 \leq m \leq \lfloor \nu^{\text{max}}/(\pi T) \rfloor$ for bosonic frequencies ω_m . The lattice size is 64×64 .

VERTEX PARAMETRIZATIONS

The Bethe-Salpeter Eq. (3) above requires the local vertex function f of the AIM (2) as an input. In this work we focus on the two-particle level of DMFT and on the LDFA, however, this requirement is quite general. Indeed, all diagrammatic extensions of DMFT [6] which take local four-point vertex corrections into account require, by construction, knowledge of f . However, this is connected with the calculation of the four-point correlation function of the AIM,

$$f^\alpha(\nu, \nu', \omega) \propto \sum_{\sigma_i} s_{\sigma'_1 \sigma_1}^\alpha s_{\sigma'_2 \sigma_2}^\alpha \langle c_{\nu \sigma_1} c_{\nu+\omega, \sigma'_1}^* c_{\nu'+\omega, \sigma_2} c_{\nu' \sigma'_2}^* \rangle,$$

where s^α are the Pauli matrices ($\alpha = \text{ch}$ or $\alpha = x, y, z \equiv \text{sp}$) and $\langle \dots \rangle$ denotes an impurity average, see also Appendix A.

Previously, this correlation function has been calculated using a variety of different methods, for example, full exact diagonalization (ED, [44]), Lanczos ED [49], CTQMC, and, very recently, the numerical renormalization group (NRG, [50, 51]). All these methods have in common that the evaluation of f is computationally expensive, in fact, at the present stage only CTQMC solvers are applicable in multi-orbital settings [52, 53]. To alleviate this problem we investigate in the following approximations for the impurity vertex function f , which do not require the calculation of the four-point correlation function of the AIM. A suitable approximation should recover the two-particle physics described by DMFT and its extensions, if not quantitatively, at least qualitatively.

To this end, we make use of the fact that the vertex f can be decomposed into single-boson exchange (SBE) diagrams and a residual four-fermion vertex [33],

$$f_{\nu\nu'\omega}^\alpha = \varphi_{\nu\nu'\omega}^{\text{Uirr},\alpha} + \nabla_{\nu\nu'\omega}^{\text{SBE},\alpha}. \quad (4)$$

Only the residual vertex φ^{Uirr} is intrinsically a four-point quantity, whereas the single-boson exchange can be constructed from the screened interaction $w^\alpha(\omega)$ and the Hedin vertex $\lambda^\alpha(\nu, \omega)$ of the AIM, where $\alpha = \text{ch, sp, s}$ denotes the charge, spin, or singlet flavor.

The measurement of these quantities requires much less computational resources than the measurement of the four-point vertex because they can be expressed, respectively, in terms of two- and three-point correlation functions of the AIM (cf. Appendix A, [54]),

$$\begin{aligned} w_\omega^\alpha &\propto \langle \rho_{-\omega}^\alpha \rho_\omega^\alpha \rangle, & \lambda_{\nu,\omega}^\alpha &\propto \sum_{\sigma\sigma'} s_{\sigma'\sigma}^\alpha \langle c_{\nu\sigma} c_{\nu+\omega\sigma'}^* \rho_\omega^\alpha \rangle, \\ w_\omega^s &\propto \langle \rho_{-\omega}^+ \rho_\omega^- \rangle, & \lambda_{\nu,\omega}^s &\propto \langle c_{\nu\uparrow} c_{\omega-\nu,\downarrow} \rho_\omega^+ \rangle, \end{aligned}$$

where in the first line $\alpha = \text{ch, sp}$ and $\rho^{\text{ch}} = n_\uparrow + n_\downarrow$ and $\rho^{\text{sp}} = n_\uparrow - n_\downarrow$ are the charge and spin densities; in the second line $\rho^+ = c_\uparrow^* c_\downarrow^*$ and $\rho^- = c_\downarrow c_\uparrow$ describe creation and annihilation of electron pairs, respectively.

In terms of w and λ the SBE diagrams ∇^{SBE} in Eq. (4) are given as the sum of three SBE contributions and a

double counting correction $2U$, for $\alpha = \text{ch, sp}$ it reads,

$$\nabla_{\nu\nu'\omega}^{\text{SBE},\alpha} = \nabla_{\nu\nu'\omega}^{\text{ph},\alpha} + \nabla_{\nu\nu'\omega}^{\overline{\text{ph}},\alpha} + \nabla_{\nu\nu',\omega+\nu+\nu'}^{\text{pp},\alpha} - 2U^\alpha, \quad (5)$$

where $U^{\text{ch}} = +U, U^{\text{sp}} = -U$ is the bare interaction in the respective channel and the ∇ 's are defined as,

$$\nabla_{\nu\nu'\omega}^{\text{ph},\alpha} = \lambda_{\nu\omega}^\alpha w_\omega^\alpha \lambda_{\nu'\omega}^\alpha, \quad (6a)$$

$$\nabla_{\nu\nu'\omega}^{\overline{\text{ph}},\alpha} = -\frac{1}{2} \nabla_{\nu,\nu+\omega,\nu'-\nu}^{\text{ph, ch}} - \frac{3-4\delta_{\alpha,\text{sp}}}{2} \nabla_{\nu,\nu+\omega,\nu'-\nu}^{\text{ph, sp}}, \quad (6b)$$

$$\nabla_{\nu\nu'\omega}^{\text{pp},\alpha} = \frac{1-2\delta_{\alpha,\text{sp}}}{2} \lambda_{\nu\omega}^s w_\omega^s \lambda_{\nu'\omega}^s. \quad (6c)$$

In the following we investigate parametrizations of the impurity vertex function based on SBE diagrams, where we test the following three approximations:

- In the ‘*SBE approximation*’ [33] we keep the diagrams shown symbolically on the top of Fig. 1,

$$f_{\nu\nu'\omega}^\alpha \approx \nabla_{\nu\nu'\omega}^{\text{SBE},\alpha}. \quad (7)$$

The organizing principle here is to parametrize the vertex in terms of bosonic fluctuations $w(\omega)$ and their coupling $\lambda(\nu, \omega)$ to the fermions.

- The ‘*w approximation*’ is similar to the SBE approximation but we simplify also the fermion-boson couplings, setting $\lambda^{\text{ch/sp}} = 1$ and $\lambda^s = -1$. As a result, this approximation requires only knowledge of the screened interaction $w(\omega)$. Here the organizing principle is to parametrize the vertex in terms of bosonic fluctuations only. Similar approximations were introduced in Refs. [55–57].
- In the ‘*asymptotic approximation*’ the vertex f is parametrized based on its asymptotic value when one or multiple frequencies [58] are large [22]. To be unbiased with respect to the limit that is taken, the asymptotic expressions are combined so that the correct vertex asymptote is recovered in each limit [57]. The asymptotic approximation can be obtained from the SBE approximation by replacing

$$\begin{aligned} \nabla_{\nu\nu'\omega}^\alpha &= \lambda_{\nu\omega}^\alpha w_\omega^\alpha \lambda_{\nu'\omega}^\alpha \\ &\approx \lambda_{\nu\omega}^\alpha w_\omega^\alpha (\pm 1) + (\pm 1) w_\omega^\alpha \lambda_{\nu'\omega}^\alpha - w_\omega^\alpha, \end{aligned} \quad (8)$$

where $+$ corresponds to $\alpha = \text{ch, sp}$ and $-$ to $\alpha = \text{s}$, and inserting into Eq. (7) using Eqs. (5) and (6). The organizing principle here is, of course, to recover the vertex asymptotically. Since the asymptotic approximation can be derived from the SBE approximation they become equivalent at high frequencies. This parametrization is used frequently in fRG schemes, combined with a more elaborate treatment of the corresponding rest function [22].

The three approximations defined above all have in common that they do not require the four-point vertex f of the AIM. The w approximation requires even only the

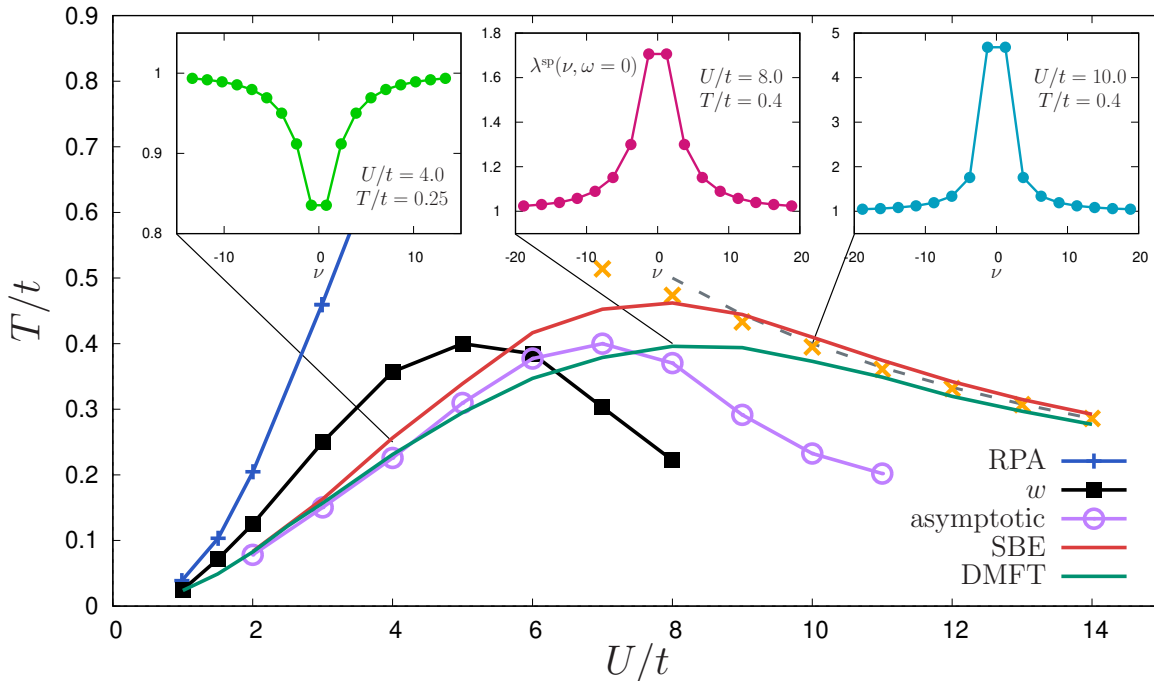


FIG. 2. Main panel: Néel temperature of the half-filled Hubbard model (1) in various approximations (see text). A dashed line indicates $4t^2/U = T$; orange crosses show points where $J = T$, with the effective exchange J calculated from Eq. (11). Insets: Local fermion-spin-boson coupling of the self-consistent AIM corresponding to indicated (U, T) in main panel.

screened interaction as an input and is therefore computationally very cheap. It is motivated by the fact that the asymptotic value of the Hedin vertex is unity,

$$\lim_{|\nu| \rightarrow \infty} \lambda_{\nu\omega}^{\text{ch/sp}} = 1, \quad \lim_{|\nu| \rightarrow \infty} \lambda_{\nu\omega}^{\text{s}} = -1. \quad (9)$$

Therefore, the asymptotic approximation lies in between the SBE approximation and the w approximation, because of the two fermion-boson couplings λ one is kept and the other is set to its asymptotic value, cf. Eq. (8).

DMFT – PHASE DIAGRAM

To benchmark the three approximations defined in the previous section, we first calculate the antiferromagnetic phase boundary of the Hubbard model (1).

In fact, in two dimensions this phase transition is forbidden by the Mermin-Wagner theorem. Nevertheless, the phase boundary predicted by DMFT is a useful indicator for the region of the phase diagram with strong spin fluctuations [6]. Furthermore, it has been shown in various studies that even below the critical temperature of DMFT both the paramagnetic and the ordered DMFT solution capture remarkably well many aspects of the phases that can be realized in accord with the Mermin-Wagner theorem or in the experiment. This includes local observables [59], the effective exchange J at strong coupling [60–62], commensurate and incommensurate spin-density waves out of half-filling [63], Fermi

surface reconstruction [64], and even stripe order [65]. It is therefore of a vital interest to gain insight into the mechanism of the Néel order predicted by DMFT and to identify its key ingredients [66].

Fig. 2 shows the various phase boundaries obtained from the random phase approximation (RPA, blue line) and DMFT, where the green line is obtained from the leading eigenvalue of the Bethe-Salpeter kernel [cf. Eq. (3)],

$$\sum_{\nu''} f_{\nu\nu''\omega=0}^{\text{sp}} \tilde{X}_{\nu''}^0(\mathbf{q} = (\pi, \pi), \omega = 0), \quad (10)$$

where \tilde{X}^0 is the nonlocal bubble defined below Eq. (3) (with $\tilde{\Sigma} = 0$). At the phase transition the leading eigenvalue approaches unity. Note that here f still corresponds to the numerically exact four-point vertex of the self-consistent AIM (2).

The comparison of DMFT and RPA at weak coupling highlights the fact that, in two dimensions, the exponential Néel temperature $\propto \exp(-2\pi\sqrt{t/U})$ of the RPA is *nowhere* quantitatively predictive of the onset of strong spin fluctuations. This is instead the case for DMFT which includes an important vertex correction due to particle-particle (Kanamori) screening, leading to renormalization of the exponent [67–70]. It has been emphasized that this vertex correction is included in the fermion-spin-boson coupling [30, 31, 71]. For large $U \gtrsim 12$ the Néel temperature of DMFT inflects towards its strong-coupling asymptote $4t^2/U$ (dashed line) [41].

Next, we apply the parametrizations of the local vertex corrections defined in the previous section and estimate the leading eigenvalue of the Bethe-Salpeter kernel (10) using the corresponding approximation for the impurity vertex f . First, using the w approximation we obtain the black curve in Fig. 2. Apparently, this approximation deviates from the original DMFT curve already at weak coupling and fails qualitatively at strong coupling, in fact, its Néel temperature drops sharply already at intermediate U . Second, we consider the asymptotic approximation represented by the purple curve in Fig. 2. This approximation agrees well with the original DMFT phase boundary for weak coupling. However, at intermediate coupling the Néel temperature drops similar to the w approximation and shows an inflection point near $U/t \approx 9$ that connects to a strong-coupling asymptote $\propto 1/U$ with a coefficient different from $4t^2$. Finally, the red curve shows the SBE approximation, which is quantitatively accurate both in the weak and strong coupling limits and agrees qualitatively with the original DMFT curve throughout the phase diagram. In terms of quantitative accuracy the asymptotic approximation lies closer to DMFT for weak to intermediate couplings, which seems to be a result of its overall smaller Néel temperature compared to the SBE approximation.

As shown in Ref. [33], the SBE approximation can be justified in the weak coupling limit [72] because it recovers all diagrams for f up to order $\mathcal{O}(U^3)$. However, the agreement with the full DMFT solution at strong coupling requires a further explanation. Indeed, it has been shown for the ordered [61] and for the paramagnetic [62] DMFT solution that at strong coupling it is sufficient to approximate $f^{\text{SP}} \approx \nabla^{\text{ph,SP}}$, where $\nabla^{\text{ph,SP}}$ is defined in Eq. (6a). On the top of Fig. 1 this corresponds to keeping only the first diagram on the right-hand-side. Using this approximation the effective exchange is given as [62]

$$J = \frac{2t^2}{(\pi_{\omega=0}^{\text{SP}})^2} \sum_{\nu} \lambda_{\nu,\omega=0}^{\text{SP}} (g_{\nu})^4 \lambda_{\nu,\omega=0}^{\text{SP}}, \quad (11)$$

where π^{SP} is the spin polarization of the impurity. As shown in Ref. [62], for large U this expression approaches $4t^2/U$ (see orange crosses in Fig. 2). Since ∇^{ph} corresponds to a subset of the SBE diagrams, the SBE approximation also recovers the effective exchange in this limit. Importantly, the Hedin vertex λ^{SP} makes a large contribution to Eq. (11) and hence approximations may fail to recover the energy scale J when λ^{SP} is set to 1 in some place, as is confirmed by the results shown in Fig. 2.

Notice that, while the SBE approximation recovers the strong-coupling limit exactly, this does not imply that the residual vertex $\varphi^{\text{Uirr,SP}}$ is small. Instead, at strong coupling the DMFT Green's function turns insulating, suppressing contributions of the residual vertex [9, 62].

We will now analyze and explain in detail the behavior of the different approximations, where we rely on the useful insights of Ref. [66] into the role of different fluctuations for DMFT's Néel temperature. We begin by comparing the SBE approximation (red curve) to the w

approximation (black curve), whose difference is particularly transparent on a formal level: The SBE approximation on the top of Fig. 1 retains the Hedin vertices, but they are set to ± 1 in the w approximation. Hence, remarkably, the Hedin vertices make all the difference between the red and the black curves in Fig. 2. This is even more surprising considering the fact that the SBE approximation is composed of the *same* basic fluctuations as the w approximation ($w^{\text{ch}}, w^{\text{sp}}, w^{\text{s}}$), and therefore the Hedin vertices can only emphasize or suppress contributions of fluctuations that are already included in the w approximation, nevertheless leading to the substantial differences between the two approximations.

As seems natural, we find that the key difference between the Néel temperatures of the w and SBE approximations originates in their different emphasis of the spin fluctuations represented by w^{sp} . It is shown in Ref. [66] that the contribution of spin fluctuations to the impurity vertex f works to *enhance* the Néel temperature of DMFT. Therefore, in order to get from the black curve in Fig. 2 to the red curve, the fermion-spin-boson coupling $\lambda^{\text{SP}}(\nu, \omega = 0)$ needs to slightly suppress the contribution of spin fluctuations at weak coupling [73] and hugely enhance it in the strong coupling limit. This quantity is shown in the insets of Fig. 2 for three pairs (U, T) . Indeed, at weak coupling $\lambda^{\text{SP}}(\nu, \omega = 0)$ is suppressed due to the Kanamori screening [30], while at strong coupling it is enhanced by multiple times of its noninteracting value 1; in both cases these features are localized at small frequencies. In fact, in the deeply insulating regime λ^{SP} grows without limit, for example, for $U/t = 11, T/t \approx 0.2$ values as large as 25 were observed [74].

Finally, this comparison also explains the behavior of the asymptotic approximation for strong coupling, which lies in the middle between the two other approximations (compare black, purple, and red curves in Fig. 2). This is the case because compared to the w approximation only one of the Hedin vertices $\lambda^{\text{SP}}(\nu, \omega = 0)$ is set to 1 [cf. Eq. (8)] and thus the effect of this truncation is alleviated. However, as Fig. 2 and Eq. (11) underline, the effective exchange J is mediated by *both* Hedin vertices [62] and thus also the asymptotic approximation eventually fails at strong coupling.

DMFT – SUSCEPTIBILITIES

As a further benchmark we calculate the DMFT susceptibility using the vertex F [75] obtained from the Bethe-Salpeter Eq. (3),

$$X^{\alpha}(q) = \sum_{\nu} X_{\nu}^0(q) + \sum_{\nu\nu'} X_{\nu}^0(q) F_{\nu\nu'}^{\alpha}(q) X_{\nu'}^0(q). \quad (12)$$

Here, $X_{\nu}^0(q) = \sum_{\mathbf{k}} G_{\mathbf{k}} G_{\mathbf{k}+q}$ denotes a bubble of DMFT Green's functions.

We evaluate the static homogeneous charge susceptibility $X^{\text{ch}}(\mathbf{q} = \mathbf{0}, \omega = 0) = -\frac{dn}{d\mu}$ and spin susceptibility

$X^{\text{sp}}(\mathbf{q} = \mathbf{0}, \omega = 0) = -\frac{dm}{dh}$ and compare the SBE approximation to the full DMFT solution (for simplicity we do not consider here the w and asymptotic approximations). The result is shown in Fig. 3, showing excellent agreement over a wide range of temperatures and interactions, regardless of whether the DMFT solution describes a good/bad metal or a Mott insulating phase. The largest absolute deviations occur in the spin channel for intermediate $U/t \approx 8$. Actually, the relative deviations in the charge channel are similar, but the charge susceptibility is vanishingly small in this case.

Using the SBE approximation, we also confirm qualitative agreement of the momentum dependence with the DMFT solution in the most delicate coupling regime $U/t = 8$. Fig. 4 shows $-X^{\text{ch/sp}}(\mathbf{q}, \omega = 0)$ for \mathbf{q} on the high-symmetry path. $-X^{\text{ch}}$ is shown at a low temperature, where the DMFT solution corresponds to a strongly correlated Fermi liquid (cf. also left panel of Fig. 3). The spin susceptibility was computed slightly above the Néel temperature of the SBE approximation, showing a sizable quantitative difference compared to DMFT but qualitatively correct momentum dependence. Of course, since the SBE approximation has a different Néel temperature compared to DMFT, the quantitative difference can be arbitrarily large near this point.

LDFA – PSEUDOGAP AT WEAK COUPLING

As our last benchmark, we use the SBE approximation to evaluate the momentum-dependent self-energy within the ladder dual fermion approach (LDFA). We calculate the dual self-energy $\tilde{\Sigma}$ via the Schwinger-Dyson equation

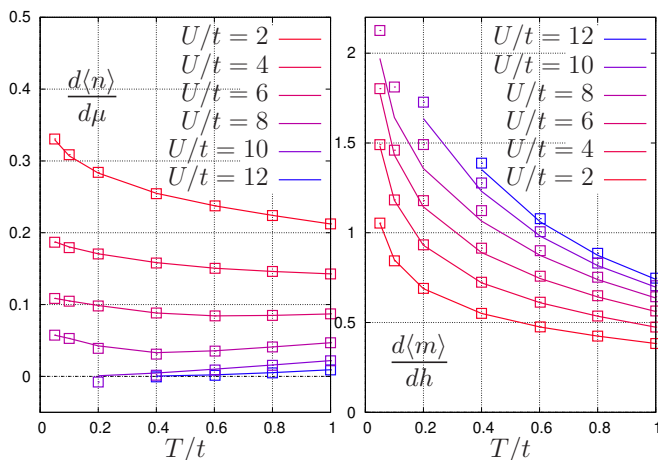


FIG. 3. Static homogeneous charge (left) and spin (right) susceptibility. Lines show the DMFT result, symbols denote the SBE approximation.

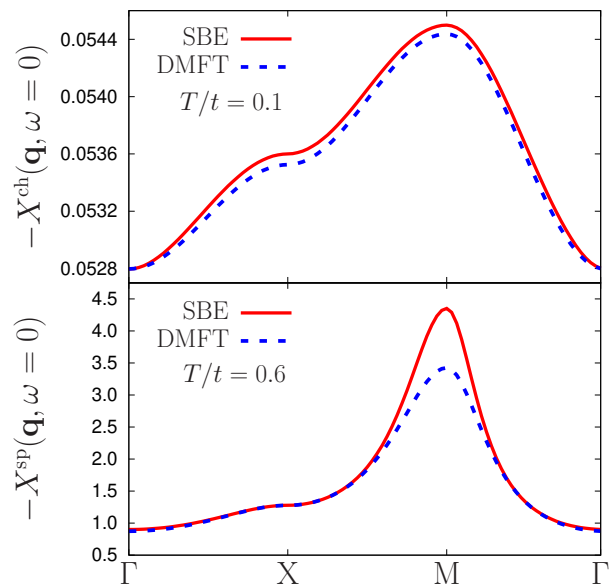


FIG. 4. Static charge (top) and spin (bottom) susceptibility for $U/t = 8$ as a function of momentum \mathbf{q} .

in the following form [76],

$$\tilde{\Sigma}(k) = - \sum_{k'} f_{\nu\nu'}^{\text{ch}, \omega=0} \tilde{G}(k') \quad (13)$$

$$+ \frac{1}{4} \sum_q \tilde{G}(k+q) [V_{\nu\nu'}^{\text{ch}}(q) + 3V_{\nu\nu'}^{\text{sp}}(q)],$$

where V^α is defined as

$$V_{\nu\nu'}^\alpha(q) = \sum_{\nu''} f_{\nu\nu''}^\alpha \tilde{X}_{\nu''}^0(q) [2F_{\nu''\nu'}^\alpha(q) - f_{\nu''\nu'}^\alpha]. \quad (14)$$

Note that here $\tilde{G}(k)$ denotes the dual Green's functions dressed with the dual self-energy $\tilde{\Sigma}$. At the end of the calculation the lattice self-energy is obtained using the relation $\Sigma_k^{\text{latt}} = \Sigma_\nu + \tilde{\Sigma}_k(1 + g_\nu \tilde{\Sigma}_k)^{-1}$, where Σ_ν is the local self-energy of the AIM [77]. As we are interested in the low-energy behavior of the self-energy we use a physical cutoff $\nu^{\text{max}} = 15t$ for improved performance.

We apply the LDFA to the Hubbard model (1) at weak coupling $U/t = 2$, this regime was recently investigated in Ref. [59] using diagrammatic Monte Carlo (DiagMC, [78]). Top panel of Fig. 5 shows the LDFA result for $\Sigma^{\text{latt}}(\mathbf{k}_N/\mathbf{k}_{AN}, \nu)$ (open symbols), where $\mathbf{k}_N = (\frac{\pi}{2}, \frac{\pi}{2})$ and $\mathbf{k}_{AN} = (\pi, 0)$ correspond to the nodal and antinodal point, respectively. The LDFA captures the opening of the pseudogap at a temperature $T_{PG} \approx 0.059t$, which lies below the numerically exact value of $0.065t$ (see Ref. [59] and black dashed lines in Fig. 5). To achieve a better quantitative agreement with DiagMC parquet diagrams need to be taken into account [32]. The top panel also shows the LDFA result when the SBE approximation is used for the impurity vertex f (closed symbols), in quantitative agreement with the original LDFA. Hence, the

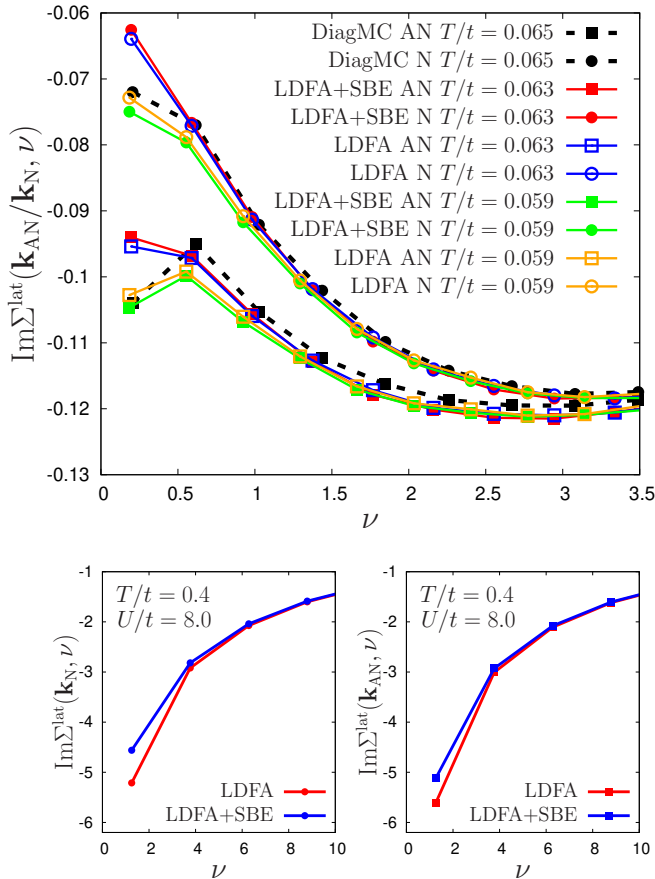


FIG. 5. Top: Imaginary part of the LDFA self-energy obtained for $U/t = 2$ with the temperature above and below T_{PG} (see text). Circles (squares) show the nodal (antinodal) point. Open symbols correspond to LDFA, and solid symbols show LDFA using the SBE approximation for the impurity vertex. Black dashed lines show the DiagMC result of Ref. [59] for $T/t = 0.065$. Bottom: LDFA and LDFA+SBE self-energy at intermediate coupling.

SBE approximation recovers signature physics also of diagrammatic extensions of DMFT [6].

LDFA – INTERMEDIATE COUPLING

We benchmark the combination of LDFA and SBE approximation also for $U/t = 8$ and $T/t = 0.4$. The bottom panels of Fig. 5 show a reasonable agreement of the self-energy at node and antinode, which are both insulating in this regime. Interestingly, we observe that the leading eigenvalue of the matrix (10) is larger for LDFA+SBE ($\lambda^{\max} \approx 0.81$) compared to LDFA ($\lambda^{\max} \approx 0.75$), while the absolute value of the self-energy is smaller. This implies a nontrivial relationship between the frequency structure of the impurity vertex and the feedback on the self-energy. This is not obvious from comparison of LDFA self-energies at different temperatures, where it may ap-

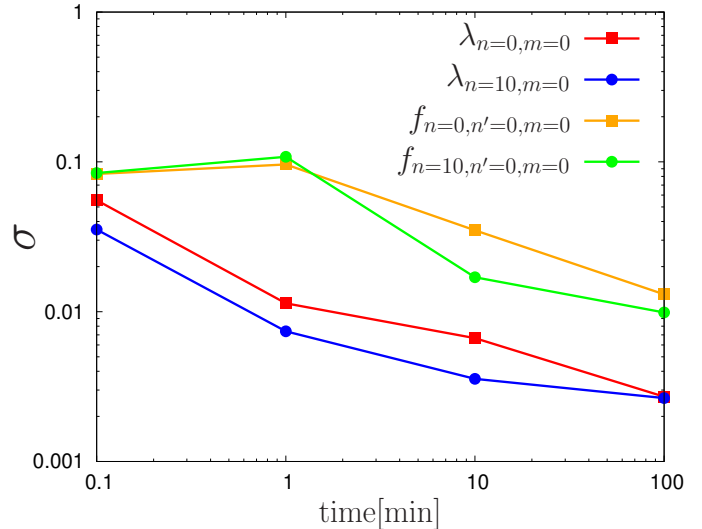


FIG. 6. Relative standard deviation of indicated matrix elements of three- and four-leg vertices λ and f , respectively, as functions of the measurement time using 192 CPUs.

pear that the feedback is mainly controlled by the leading eigenvalue.

However, let us note that the essential physics of the Hubbard model in this interaction regime corresponds to localized spins interacting via the effective exchange. Hence, it is plausible that the mere self-consistent feedback of spin fluctuations on the electronic self-energy captured by the ladder approximation is *not* the salient physical effect, but that instead self-renormalization of (i.e., interaction between) spin fluctuations should be taken into account, see, e.g., Ref. [79]. This requires more sophisticated diagrammatic resummation schemes, such as the parquet diagrams [32, 80, 81].

COMPUTATIONAL COST

The SBE approximation depicted in Fig. 1 avoids the measurement of the four-point vertex function $f(\nu, \nu', \omega)$, which is the computationally most demanding task in calculations of the DMFT susceptibility and in ladder extensions of DMFT [43]. The measurement of the three-leg vertices $\lambda(\nu, \omega)$ is cheaper, however, the reduction of computational cost depends on details of the implementation, on the autocorrelation time that is specific both to the observable and to the physical regime, and on the method of measurement (e.g. segment or worm sampling). Fig. 6 provides an illustrative example of a DMFT calculation at $U/t = 8, T/t = 0.1$ where $f^{\text{ch/sp}}$ and $\lambda^{\text{ch/sp}}$ were measured on 142 fermionic and 142 bosonic frequencies using the segment solver with improved estimators presented in Refs. [52, 82]. We used 192 CPUs for the measurements. Fig. 6 shows the relative standard deviations of $f(\nu_0, \nu_0, \omega_0)$, $f(\nu_{10}, \nu_0, \omega_0)$, $\lambda(\nu_0, \omega_0)$, and $\lambda(\nu_{10}, \omega_0)$ against the total measurement time in

	λ	f
1 orb. + SU(2)	2.13 MB	92.7 MB
3 orb. + SU(2)	44.73 MB	1946.7 MB
3 orb. w/o SU(2)	134.19 MB	5840.1 MB

TABLE I. Size of three- and four-leg vertices λ and f for 142 fermionic/bosonic frequencies. First line shows the single-band case with SU(2) symmetry, second and third line correspond to a three orbital Hubbard-Kanamori model

minutes. Apparently, in this setup, obtaining f and λ to similar accuracy requires roughly a one hundred times longer measurement time for f .

Further, the SBE approximation also preserves memory and disk space. The first line of Table I shows the size of λ and f calculated above, corresponding to the single-band Hubbard model (1). The second and third line indicate corresponding sizes for a three-orbital Hubbard-Kanamori Hamiltonian either with or without SU(2) symmetry [43, 53]. Notice that the center column corresponds to the *particle-hole* quantities $\lambda^{\text{ch/sp}}$ [cf. Appendix Eq. (A4)]. The singlet vertex λ^{s} [cf. Eq. (A5)] is of similar size and, furthermore, the multi-orbital case requires in general also the measurement of a triplet component (it vanishes in the single-band case due to the Pauli principle), which needs to be taken into account in the derivation of the SBE decomposition [33].

PROPERTIES OF THE RESIDUAL VERTEX

The benchmarks in the previous sections confirm that the SBE approximation recovers the two-particle physics of DMFT and its diagrammatic extensions from weak to strong coupling quantitatively. While at strong coupling an analytical argument favors the SBE approximation over the w and asymptotic approximations, one may still doubt whether it is preferable in general.

In this section we provide numerical evidence that, for the purpose of a parametrization of the vertex, the organizing principle of the SBE approximation should be favored over that of the asymptotic approximation: At all energy scales, the local vertex corrections should be parametrized through bosonic fluctuations and their coupling to the fermions, rather than through a combination of asymptotic expressions [83]. To show this, we compute the residual vertices (rest functions) of, respectively, the SBE decomposition and of the vertex asymptotics and compare them at small frequencies.

The residual vertex φ^{Uirr} of the SBE decomposition is defined as the set of vertex diagrams which do not contain insertions of the bare interaction U [33]. On the other hand, we refer to the residual vertex of the vertex asymptotics as φ^{as} . To get at a clearer picture what φ^{as} is, we pinpoint its difference to φ^{Uirr} as follows. First, we recall that the asymptotic approximation can be obtained from the SBE approximation by combining dif-

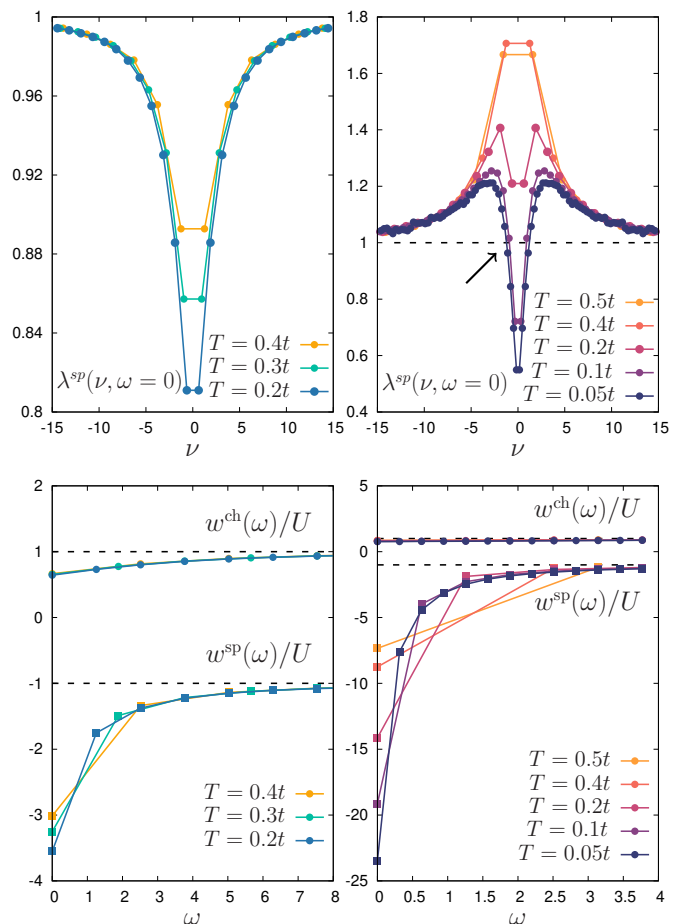


FIG. 7. Top: Local fermion-spin-boson coupling ($\omega = 0$) corresponding to DMFT calculations at $U/t = 4$ (left) and $U/t = 8$ (right) for various temperatures. Bottom: Screened interaction for the same parameters.

ferent high-frequency limits of the SBE diagrams as in Eq. (8). Let us determine explicitly what is neglected in the asymptotic approximation, for example, looking at ∇^{ph} defined in Eq. (6a) [$\alpha = \text{ch, sp}$],

$$\begin{aligned} \nabla_{\nu\nu'}^{\text{ph},\alpha} &= \lambda_{\nu\omega}^{\alpha} w_{\omega}^{\alpha} \lambda_{\nu'\omega}^{\alpha} \\ &= \lambda_{\nu\omega}^{\alpha} w_{\omega}^{\alpha} + w_{\omega}^{\alpha} \lambda_{\nu'\omega}^{\alpha} - w_{\omega}^{\alpha} \\ &\quad + (\lambda_{\nu\omega}^{\alpha} - 1) w_{\omega}^{\alpha} (\lambda_{\nu'\omega}^{\alpha} - 1). \end{aligned}$$

In the asymptotic approximation the term in the last line is neglected (that is, absorbed into φ^{as}). Similar terms arise from taking the asymptotic limits of ∇^{ph} and of ∇^{pp} . As a result, the difference between the residual vertices φ^{Uirr} and φ^{as} is that the latter contains remainders of the form $R = (\lambda \mp 1)w(\lambda \mp 1)$. They correspond to the boson w coupled to fermions only via the nontrivial (interacting) part of the fermion-boson coupling λ . In the following we evaluate φ^{Uirr} and φ^{as} in a nontrivial parameter regime and pay special attention to the behavior of the remainders R .

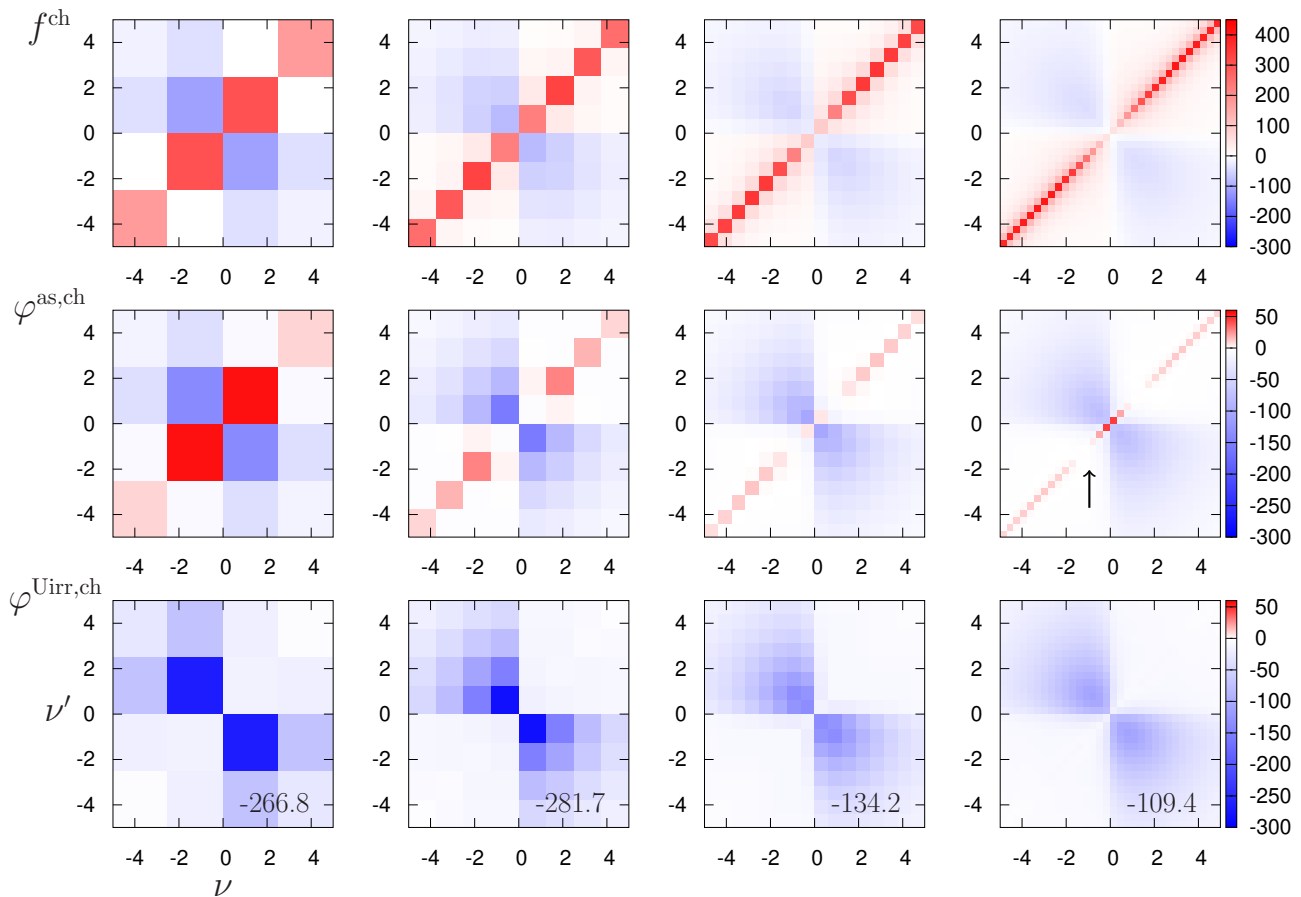


FIG. 8. Top: Full charge vertex $f^{\text{ch}}(\nu, \nu', \omega = 0)$ for $U/t = 8$ focused on small ν, ν' . From left to right panels correspond to $T/t = 0.4, 0.2, 0.1$, and 0.05 . Center and bottom: Residual vertices of the vertex asymptotics (center) and of the SBE decomposition (bottom). The arrow indicates an ‘accidental’ cancellation of the diagonal by the vertex asymptotics, which occurs when λ^{sp} crosses its asymptotic value 1 (see text and arrow in Fig. 7). Color schemes are consistent in each row. Numbers in the bottom panels indicate the global minimum of $\varphi^{\text{Uirr, ch}}$.

As the test ground we choose $U/t = 8$ and perform DMFT calculations at temperatures $T/t = 0.5, 0.4, 0.2, 0.1$, and 0.05 . This sequence is interesting in DMFT because at high temperature the self-consistent AIM exhibits a local moment, but crosses over into a Fermi liquid at low temperature. This change manifests itself in the impurity correlation functions, as can be observed in the right panels of Fig. 7 which show the Hedin vertex $\lambda^{\text{sp}}(\nu, \omega = 0)$ and the screened interaction $w(\omega)$.

The former shows a strong enhancement in the local moment regime at high temperature, and a similar strong suppression in the Fermi liquid at low temperature. Actually, this is comparable to the sequence of Hedin vertices shown in the insets of Fig. 2, where the interaction was changed to switch between the two regimes. In the present case, however, it is the peculiar temperature dependence of the DMFT approximation that drives the crossover. The latter can also be observed in the static screened interaction $w^{\text{sp}}(\omega = 0)$, which roughly doubles going from $T/t = 0.4$ to $T/t = 0.2$, consistent with a local moment $\propto \beta$, whereas at low temperature the in-

crease of $w^{\text{sp}}(\omega = 0)$ is markedly slower. On the other hand, w^{ch} is tiny in comparison, and hence we can ignore this quantity (and λ^{ch}) in the following [84].

To fully characterize the setting, let us also compare to a case of weaker coupling $U/t = 4$ shown in the left panels of Fig. 7. In this case $\lambda^{\text{sp}}(\nu, \omega = 0)$ does not show an enhancement at high temperature. Interestingly, the comparison to the right panels suggests that the screening of fermions from spin fluctuations, mediated by a suppression of $\lambda^{\text{sp}}(\nu, \omega = 0)$, is not *per se* a feature of the weak coupling regime, but rather of the Fermi liquid phase (although in the strongly correlated Fermi liquid the mechanism may be more multifaceted than the simple Kanamori screening at weak coupling [30]).

At the same time, however, we note the qualitative difference between the Fermi liquid regimes at $U/t = 4$ and $U/t = 8$: In the latter case $\lambda^{\text{sp}}(\nu, \omega = 0)$ is strongly suppressed at very small frequencies (see e.g. $T/t = 0.05$), but it shows an enhancement for intermediate frequencies which is not there for $U/t = 4$. This indicates that for $U/t = 8$ only low-energetic fermions are screened from

spin fluctuations and reminds of the ‘onion shape’ of the generalized charge susceptibility recently observed in Ref. [85].

In summary, we have identified a crossover from a local moment to a Fermi liquid phase that manifests itself as a qualitative change in the quantities λ and w , which are used to formulate the SBE approximation and the asymptotic approximation. Next, we observe the behavior of the residual vertices φ^{Uirr} and φ^{as} at the crossover.

The bottom panels of Fig. 8 show the residual charge vertex $\varphi^{\text{Uirr, ch}}(\nu, \nu', \omega = 0)$ of the SBE decomposition for different temperatures, where the energy window for ν and ν' is consistent. In the local moment regime (Fermi liquid) $\varphi^{\text{Uirr, ch}}$ increases (decreases) in absolute magnitude as T is lowered (see numbers in the bottom panels), but otherwise exhibits a remarkable uniformity, showing the same features, as it were, in different resolutions. Indeed, in Fig. 9 we find the same behavior in $\varphi^{\text{Uirr, sp}}(\nu, \nu', \omega = 0)$, albeit with the opposite sign.

As observed previously [33], $\varphi^{\text{Uirr}}(\omega = 0)$ has no significant features in the two sectors where $\text{sgn}(\nu) = \text{sgn}(\nu')$, indicating an almost perfect cancellation of the SBE diagrams ∇^{SBE} with the full vertex f in these sectors. On the other hand, there are features located in the two sectors where $\text{sgn}(\nu) = -\text{sgn}(\nu')$, respectively, provided ν and ν' are both small. Consistently, and also at smaller interaction [33], these features correspond to attraction in the charge channel, $\varphi^{\text{Uirr, ch}}(\omega = 0) < 0$, and repulsion in the spin channel, $\varphi^{\text{Uirr, sp}}(\omega = 0) > 0$.

The origin and physical nature of these features are unknown. One may speculate that they are related to particle-particle scatterings, because the secondary diagonal $\nu + \nu' \approx 0$ that crosses through the sectors with $\text{sgn}(\nu) = -\text{sgn}(\nu')$ is associated with the singlet pairing channel [1]. However, φ^{Uirr} does not exhibit any resonances for a particular frequency combination. The simple structure of φ^{Uirr} , which does not change qualitatively at the crossover from local moment regime to Fermi liquid, suggests that it could represent two-particle correlations which play a similar role in both regimes. A candidate explanation is, hence, that φ^{Uirr} captures, in the strongly correlated Fermi liquid, the *pre-formed* local moment.

The described phenomenology is in strong contrast with the full vertex f^{ch} drawn in the top panels of Fig. 8, which exhibits both repulsive and attractive features, with some cancellations between them for small ν and/or ν' that vary with the temperature. In fact, $\varphi^{\text{Uirr, ch}}$ represents in essence the attractive features of f^{ch} , whereas repulsive single-boson exchange contributes a resonant structure on the diagonal $\nu - \nu' \approx 0$. On the other hand, in the spin channel the repulsive contribution of $\varphi^{\text{Uirr, sp}}$ to f^{sp} is cancelled out completely by attractive single-boson exchange [86], see Fig. 9. Also here, the residual vertex $\varphi^{\text{Uirr, sp}}$ does not exhibit resonant features.

Next, we examine the residual vertex φ^{as} of the vertex asymptotics drawn in the second row of the panels in Fig. 8 and 9, respectively. Since this quantity corre-

sponds to a superset of the diagrams contained in φ^{Uirr} , it is not surprising that the features of φ^{Uirr} can also be observed in φ^{as} . However, they overlap with remainder structures $R = (\lambda \mp 1)w(\lambda \mp 1)$, as explained in the beginning of this section. The remainders necessarily decay at high frequencies, where the SBE and asymptotic approximations become equivalent, however, Figs. 8 and 9 focus on small frequencies.

A prominent remainder structure is visible on the diagonal of the residual charge vertex $\varphi^{\text{as, ch}}$ in Fig. 8, both at high and at low temperatures. We obtain an expression for this feature as follows. The remainder stemming from the *horizontal* particle-hole channel is given as,

$$R_{\nu\nu'\omega}^{\text{ph}, \alpha} = (\lambda_{\nu\omega}^{\alpha} - 1)w_{\omega}^{\alpha}(\lambda_{\nu'\omega}^{\alpha} - 1), \quad (15)$$

where $\alpha = \text{ch, sp}$. Since $w^{\text{ch}}/U \approx 1$ is comparatively tiny in the considered regime (cf. Fig. 7, bottom right), $R^{\text{ph, ch}}$ is negligible and hence not easily visible in $\varphi^{\text{as, ch}}$. However, a remainder R^{ph} contributes to φ^{as} also in the *vertical* particle-hole channel. This remainder arises from the crossing relation (6b) and is *not* small, because the crossing relation mixes the charge and spin flavors. Neglecting a contribution from $R^{\text{ph, ch}}$ we obtain,

$$\overline{R}_{\nu, \nu', \omega=0}^{\text{ph, ch}} \propto (\lambda_{\nu, \nu' - \nu}^{\text{sp}} - 1)w_{\nu' - \nu}^{\text{sp}}(\lambda_{\nu, \nu' - \nu}^{\text{sp}} - 1). \quad (16)$$

As expected, this quantity decays for large ν or ν' where the Hedin vertex approaches 1, however, for small $\nu \approx \nu'$ it contributes to $\varphi^{\text{as, ch}}$, that is, the red features in the second row of panels in Fig. 8.

Comparison with Fig. 7 elucidates the peculiar structure of this feature: Firstly, the screened interaction $w^{\text{sp}}(\omega)$ decays quickly for finite ω , hence $R^{\text{ph, ch}}$ displays a strong resonance only on the diagonal of $\varphi^{\text{as, ch}}$. Secondly, at low temperature (e.g. $T = 0.05$) the Hedin vertex $\lambda_{\nu, \omega=0}^{\text{sp}}$ changes for $\nu \approx \pm 1$ from suppression ($\lambda^{\text{sp}} < 1$) to enhancement ($\lambda^{\text{sp}} > 1$). Therefore, $R^{\text{ph, ch}}$ vanishes at this point. Indeed, the red feature in $\varphi^{\text{as, ch}}$ disappears near $\nu \approx \pm 1$ (see arrows in Figs. 7 and 8), but reemerges again at larger frequencies.

The described effect serves as strong evidence that in the asymptotic approximation cancellations with the full vertex f occur at small frequencies only *accidentally*. In contrast, we have confirmed in a nontrivial setting, featuring a crossover from local moment to Fermi liquid phase, that the SBE diagrams capture the resonant features of f even at the smallest frequencies. Therefore, we conclude that the formal construction of the SBE decomposition retains a *physical* correspondence to the full vertex function at all energy scales.

CONCLUSIONS

We benchmarked an efficient approximation scheme for the local vertex function of the Anderson impurity model in terms of single-boson exchange (SBE, [33]). The

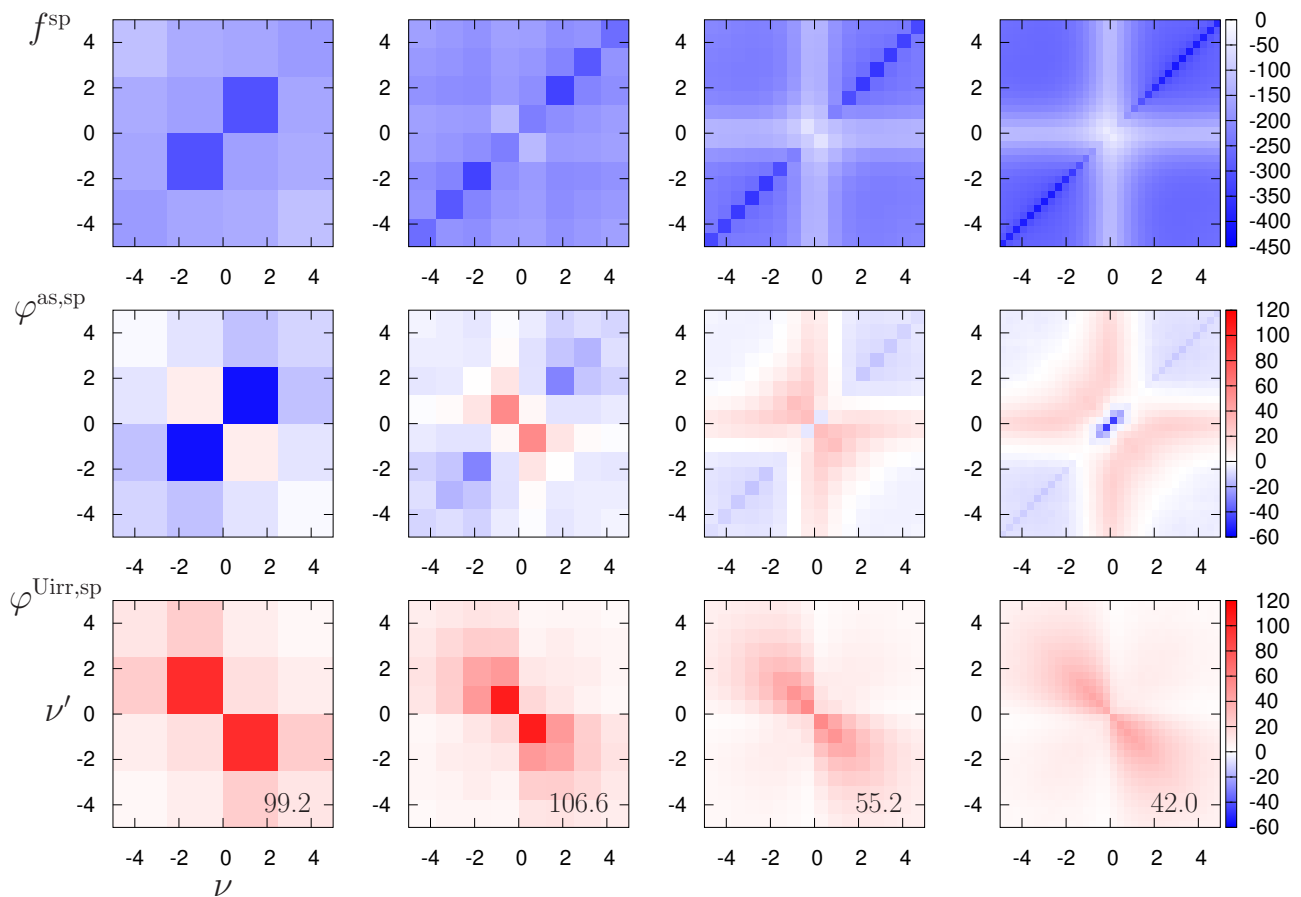


FIG. 9. Full (top) and residual (center, bottom) vertices of the spin channel for the same parameters as in Fig. 9. Numbers in the bottom panels indicate the global maximum of $\varphi^{\text{Uirr,sp}}$.

SBE approximation is based on the proven and successful organizing principle to parametrize two-particle correlations in terms of bosonic fluctuations and their coupling to fermions [14, 25–27, 30, 37, 87]. We presented analytical arguments for the validity of the SBE approximation at weak and strong coupling and emphasized the importance of the fermion-boson coupling (Hedin vertex) in both limits. This quantity captures the Kanamori screening at weak coupling and strongly enhances the contribution of spin fluctuations to the vertex function at strong coupling. Hence, in the latter case, setting this quantity to its noninteracting value leads to qualitatively wrong results. This may be of relevance for the extension of recent diagrammatic studies of the optical conductivity [88, 89] to the strong coupling regime.

In our numerical applications to the single-band Hubbard model the SBE approximation recovered the two-particle physics of DMFT and of the ladder dual fermion approach to good quantitative accuracy. As a result, the computational cost of evaluating correlation functions of the auxiliary Anderson impurity model was reduced to a level comparable with the TRILEX [90] and dual TRILEX approaches [36, 37], however, the Bethe-Salpeter equation still needs to be solved. In the estima-

tion of the Néel temperature of DMFT the SBE approximation does not reach the excellent accuracy and efficiency of the strong-coupling limit (SCL) formula for the static spin susceptibility of DMFT [91], but it has a wider range of applicability, for example, to charge excitations and two-particle correlations in general. These results call for the generalization of the SBE approximation to multi-orbital settings, where it may be applied in cases where the computational bottleneck is the evaluation of the vertex function of the impurity model [43, 92, 93]. The SBE approximation may also be combined with the efficient formula for the DMFT polarization [62] and other schemes [94] that help to reduce the computational cost of solving the Bethe-Salpeter equation.

Our results are also of relevance to the development of unbiased methods such as the fRG [15, 16] and parquet schemes [40]. We compared the SBE approximation to a widely used parametrization of the vertex based on its asymptotic limits [22], which are a crucial ingredient of recent progress in the theory of vertex corrections and two-particle excitations, see, for example, Refs. [28, 30, 31, 33, 62, 95, 96]. We showed in a non-trivial crossover regime from a local moment phase to the Fermi liquid that the SBE decomposition generalizes

the vertex asymptotics in a physically meaningful way to small frequencies. In particular, it retains the correspondence to all resonant features of the full vertex function down to the smallest energy scales. As is natural for a high-frequency limit, the approximation based on vertex asymptotics does not show this correspondence. Therefore, resonant features remain in the rest function of the vertex asymptotics, which in the case of long-ranged spin-density wave correlations may carry a strong momentum dependence. The rest function of the SBE decomposition is short-ranged even in this case [31, 32] and, as a result, its momentum dependence can be captured with only a small number of form factors [30, 97]. It seems therefore promising to include the SBE decomposition into state-of-the-art fRG [98] and parquet schemes [30, 31].

Finally, we noted that, in the considered cases, the residual vertex of the SBE decomposition has a remarkably simple frequency structure, which does not change qualitatively at the crossover from the local moment regime to the Fermi liquid, or by changing the interaction. Based on this, we speculate that this vertex represents a connecting element of the two regimes, namely, the pre-formed local moment, either screened or unscreened, respectively. Indeed, the full two-particle information can be reconstructed from the residual vertex [99], including the corresponding fingerprints of the local moment [85]. However, further investigation is required, for example, an intriguing option is to study the residual vertex of the SBE decomposition on the real axis [50, 51].

ACKNOWLEDGMENTS

We thank F. Šimkovic for providing the DiagMC data and S. Andergassen, P. Bonetti, K. Held, C. Hille, F. Kugler, J. Mravlje, L. Del Re, G. Rohringer, A. Toschi, D. Vilaridi, M. Wallerberger for fruitful discussions and comments. We acknowledge support from the European Research Council through the Synergy Grant No. 854843 - FASTCORR (A.I.L., V.H.), from the Austrian Science Fund (FWF) through Projects No. P32044 and No. P30997 (F.K.) and from the North-German Supercomputing Alliance (HLRN) under the Project No. hhp00042 (A.I.L., V.H.).

Appendix A: Impurity correlation functions

In this work we employ two different methods (DMFT and LDFA) which both use the vertex function of the AIM, and the aim of this work is to test efficient parametrizations of this quantity. However, for compar-

ison we also obtain the *exact* vertex function from the four-point correlation function, which is defined as,

$$g_{\nu\nu'\omega}^{(4),\alpha} = -\frac{1}{2} \sum_{\sigma_i} s_{\sigma'_1\sigma_1}^\alpha s_{\sigma'_2\sigma_2}^\alpha \langle c_{\nu\sigma_1} c_{\nu+\omega,\sigma'_1}^* c_{\nu'+\omega,\sigma_2} c_{\nu'\sigma'_2}^* \rangle, \quad (\text{A1})$$

where s^α are the Pauli matrices and the label $\alpha = \text{ch, sp}$ denotes the charge and spin channel, respectively. The vertex function is obtained by subtracting the disconnected parts and removing four Green's function legs from the four-point correlation function $g^{(4)}$,

$$f_{\nu\nu'\omega}^\alpha = \frac{g_{\nu\nu'\omega}^{(4),\alpha} - \beta g_\nu g_{\nu+\omega} \delta_{\nu\nu'} + 2\beta g_\nu g_{\nu'} \delta_\omega \delta_{\alpha,\text{ch}}}{g_\nu g_{\nu+\omega} g_{\nu'} g_{\nu'+\omega}}. \quad (\text{A2})$$

The three-point correlation function is defined as,

$$g_{\nu\omega}^{(3),\alpha} = -\frac{1}{2} \sum_{\sigma\sigma'} s_{\sigma'\sigma}^\alpha \langle c_{\nu\sigma} c_{\nu+\omega,\sigma'}^* \rho_\omega^\alpha \rangle, \quad (\text{A3})$$

where $\rho^{\text{ch}} = n_\uparrow + n_\downarrow$ and $\rho^{\text{sp}} = n_\uparrow - n_\downarrow$ are the charge and spin densities. The Hedin vertex is obtained from $g^{(3)}$ as,

$$\lambda_{\nu\omega}^\alpha = \frac{g_{\nu\omega}^{(3),\alpha} + \beta g_\nu \langle n \rangle \delta_\omega \delta_{\alpha,\text{ch}}}{g_\nu g_{\nu+\omega} w_\omega^\alpha / U^\alpha}, \quad (\text{A4})$$

where w_ω^α and U^α are defined below and

$$\lambda_{\nu\omega}^{\text{s}} = \frac{\langle c_{\nu\uparrow} c_{\omega-\nu,\downarrow} \rho_\omega^+ \rangle}{g_\nu g_{\omega-\nu} w_\omega^{\text{s}} / U^{\text{s}}}. \quad (\text{A5})$$

The charge, spin, and singlet impurity susceptibilities are defined as,

$$\chi_\omega^\alpha = -\langle \rho_{-\omega}^\alpha \rho_\omega^\alpha \rangle + \beta \langle n \rangle \langle n \rangle \delta_\omega \delta_{\alpha,\text{ch}}, \quad (\text{A6})$$

$$\chi_\omega^{\text{s}} = -\langle \rho_{-\omega}^+ \rho_\omega^- \rangle, \quad (\text{A7})$$

and $\rho^+ = c_\uparrow^* c_\downarrow^*$ and $\rho^- = c_\downarrow c_\uparrow$ describe creation/annihilation of electron pairs, respectively. The label 's' in Eq. (A7) refers to the singlet pairing channel. The screened interaction is obtained from the susceptibility as,

$$w^\alpha(\omega) = U^\alpha + \frac{1}{2} U^\alpha \chi^\alpha(\omega) U^\alpha, \quad (\text{A8})$$

for each corresponding channel $\alpha = \text{ch, sp, s}$. Finally, the bare interaction is defined as,

$$U^{\text{ch}} = +U, \quad U^{\text{sp}} = -U, \quad U^{\text{s}} = +2U. \quad (\text{A9})$$

[1] G. Rohringer, A. Valli, and A. Toschi, *Phys. Rev. B* **86**, 125114 (2012).

[2] L. Boehnke and F. Lechermann, *Phys. Rev. B* **85**, 115128

- (2012).
- [3] D. Geffroy, J. Kaufmann, A. Hariki, P. Gunacker, A. Hausoel, and J. Kuneš, *Phys. Rev. Lett.* **122**, 127601 (2019).
- [4] H. U. R. Strand, M. Zingl, N. Wentzell, O. Parcollet, and A. Georges, *Phys. Rev. B* **100**, 125120 (2019).
- [5] J. Mußhoff, A. Kiani, and E. Pavarini, *Phys. Rev. B* **103**, 075136 (2021).
- [6] G. Rohringer, H. Hafermann, A. Toschi, A. A. Katanin, A. E. Antipov, M. I. Katsnelson, A. I. Lichtenstein, A. N. Rubtsov, and K. Held, *Rev. Mod. Phys.* **90**, 025003 (2018).
- [7] L. Landau, *Zh. Eksp. Teor. Fiz.* **30**, 1058 (1956), [*Sov. Phys. JETP* **3**, 920 (1957)].
- [8] P. Nozières, *Theory Of Interacting Fermi Systems*, Advanced Books Classics (Avalon Publishing, 1997).
- [9] F. Krien, E. G. C. P. van Loon, M. I. Katsnelson, A. I. Lichtenstein, and M. Capone, *Phys. Rev. B* **99**, 245128 (2019).
- [10] C. Melnick and G. Kotliar, *Phys. Rev. B* **101**, 165105 (2020).
- [11] G. Li, A. Kauch, P. Pudleiner, and K. Held, *Computer Physics Communications* **241**, 146 (2019).
- [12] H. Krahl and C. Wetterich, *Physics Letters A* **367**, 263 (2007).
- [13] S. Friederich, H. C. Krahl, and C. Wetterich, *Phys. Rev. B* **81**, 235108 (2010).
- [14] T. Denz, M. Mitter, J. M. Pawłowski, C. Wetterich, and M. Yamada, *Phys. Rev. B* **101**, 155115 (2020).
- [15] W. Metzner, M. Salmhofer, C. Honerkamp, V. Meden, and K. Schönhammer, *Rev. Mod. Phys.* **84**, 299 (2012).
- [16] N. Dupuis, L. Canet, A. Eichhorn, W. Metzner, J. Pawłowski, M. Tissier, and N. Wschebor, *Physics Reports* **910**, 1 (2021).
- [17] C. Karrasch, R. Hedden, R. Peters, T. Pruschke, K. Schönhammer, and V. Meden, *Journal of Physics: Condensed Matter* **20**, 345205 (2008).
- [18] W.-S. Wang, Y.-Y. Xiang, Q.-H. Wang, F. Wang, F. Yang, and D.-H. Lee, *Phys. Rev. B* **85**, 035414 (2012).
- [19] D. Vildardi, C. Taranto, and W. Metzner, *Phys. Rev. B* **96**, 235110 (2017).
- [20] D. Vildardi, C. Taranto, and W. Metzner, *Phys. Rev. B* **99**, 104501 (2019).
- [21] A. Tagliavini, C. Hille, F. B. Kugler, S. Andergassen, A. Toschi, and C. Honerkamp, *SciPost Phys.* **6**, 9 (2019).
- [22] N. Wentzell, G. Li, A. Tagliavini, C. Taranto, G. Rohringer, K. Held, A. Toschi, and S. Andergassen, *Phys. Rev. B* **102**, 085106 (2020).
- [23] F. B. Kugler and J. von Delft, *Phys. Rev. Lett.* **120**, 057403 (2018).
- [24] F. B. Kugler and J. von Delft, *Phys. Rev. B* **97**, 035162 (2018).
- [25] C. Husemann and M. Salmhofer, *Phys. Rev. B* **79**, 195125 (2009).
- [26] C. Husemann, K.-U. Giering, and M. Salmhofer, *Phys. Rev. B* **85**, 075121 (2012).
- [27] A. Eberlein, “Functional renormalization group study of fluctuation effects in fermionic superfluids,” (2014), [arXiv:1407.7661](https://arxiv.org/abs/1407.7661).
- [28] P. M. Bonetti, *Phys. Rev. B* **102**, 235160 (2020).
- [29] For a description of these general assumptions see Appendix E of Ref. [62].
- [30] F. Krien, A. Valli, P. Chalupa, M. Capone, A. I. Lichtenstein, and A. Toschi, *Phys. Rev. B* **102**, 195131 (2020).
- [31] F. Krien, A. Kauch, and K. Held, *Phys. Rev. Research* **3**, 013149 (2021).
- [32] F. Krien, A. I. Lichtenstein, and G. Rohringer, *Phys. Rev. B* **102**, 235133 (2020).
- [33] F. Krien, A. Valli, and M. Capone, *Phys. Rev. B* **100**, 155149 (2019).
- [34] L. Hedin, *Phys. Rev.* **139**, A796 (1965).
- [35] O. Gunnarsson, T. Schäfer, J. P. F. LeBlanc, E. Gull, J. Merino, G. Sangiovanni, G. Rohringer, and A. Toschi, *Phys. Rev. Lett.* **114**, 236402 (2015).
- [36] E. A. Stepanov, V. Harkov, and A. I. Lichtenstein, *Phys. Rev. B* **100**, 205115 (2019).
- [37] V. Harkov, M. Vandelli, S. Brener, A. I. Lichtenstein, and E. A. Stepanov, *Phys. Rev. B* **103**, 245123 (2021).
- [38] I. T. Dyatlov, V. V. Sudakov, and K. A. Ter-Martirosyan, *Zh. Eksp. Teor. Fiz.* **32**, 4 (1957)[*Sov. Phys. JETP* **5**, 631 (1957)].
- [39] C. De Dominicis and P. C. Martin, *Journal of Mathematical Physics* **5**, 31 (1964), <https://doi.org/10.1063/1.1704064>.
- [40] N. E. Bickers, “Self-consistent many-body theory for condensed matter systems,” in *Theoretical Methods for Strongly Correlated Electrons*, edited by D. Sénéchal, A.-M. Tremblay, and C. Bourbonnais (Springer New York, New York, NY, 2004) pp. 237–296.
- [41] A. Georges, G. Kotliar, W. Krauth, and M. J. Rozenberg, *Rev. Mod. Phys.* **68**, 13 (1996).
- [42] E. Gull, A. J. Millis, A. I. Lichtenstein, A. N. Rubtsov, M. Troyer, and P. Werner, *Rev. Mod. Phys.* **83**, 349 (2011).
- [43] A. Galler, P. Thunström, J. Kaufmann, M. Pickem, J. M. Tomczak, and K. Held, *Computer Physics Communications* **245**, 106847 (2019).
- [44] A. Toschi, A. A. Katanin, and K. Held, *Phys. Rev. B* **75**, 045118 (2007).
- [45] A. N. Rubtsov, M. I. Katsnelson, and A. I. Lichtenstein, *Phys. Rev. B* **77**, 033101 (2008).
- [46] H. Hafermann, E. G. C. P. van Loon, M. I. Katsnelson, A. I. Lichtenstein, and O. Parcollet, *Phys. Rev. B* **90**, 235105 (2014).
- [47] E. G. C. P. van Loon, F. Krien, and A. A. Katanin, *Phys. Rev. Lett.* **125**, 136402 (2020).
- [48] H. Hafermann, G. Li, A. N. Rubtsov, M. I. Katsnelson, A. I. Lichtenstein, and H. Monien, *Phys. Rev. Lett.* **102**, 206401 (2009).
- [49] A. Tanaka, *Phys. Rev. B* **99**, 205133 (2019).
- [50] S.-S. B. Lee, F. B. Kugler, and J. von Delft, “Computing local multipoint correlators using the numerical renormalization group,” (2021), [arXiv:2101.00708](https://arxiv.org/abs/2101.00708).
- [51] F. B. Kugler, S.-S. B. Lee, and J. von Delft, “Multipoint correlation functions: spectral representation and numerical evaluation,” (2021), [arXiv:2101.00707](https://arxiv.org/abs/2101.00707).
- [52] B. Bauer, L. D. Carr, H. G. Evertz, A. Feiguin, J. Freire, S. Fuchs, L. Gamper, J. Gukelberger, E. Gull, S. Guertler, A. Hehn, R. Igarashi, S. V. Isakov, D. Koop, P. N. Ma, P. Mates, H. Matsuo, O. Parcollet, G. Pawłowski, J. D. Picon, L. Pollet, E. Santos, V. W. Scarola, U. Schollwöck, C. Silva, B. Surer, S. Todo, S. Trebst, M. Troyer, M. L. Wall, P. Werner, and S. Wesel, *Journal of Statistical Mechanics: Theory and Experiment* **2011**, P05001 (2011).
- [53] M. Wallerberger, A. Hausoel, P. Gunacker, A. Kowalski, N. Parragh, F. Goth, K. Held, and G. Sangiovanni,

- Computer Physics Communications **235**, 388 (2019).
- [54] E. G. C. P. van Loon, F. Krien, H. Hafermann, A. I. Lichtenstein, and M. I. Katsnelson, *Phys. Rev. B* **98**, 205148 (2018).
- [55] H. Kusunose, *Journal of the Physical Society of Japan* **79**, 094707 (2010), <https://doi.org/10.1143/JPSJ.79.094707>.
- [56] J. Kuneš, *Phys. Rev. B* **83**, 085102 (2011).
- [57] A. Tagliavini, S. Hummel, N. Wentzell, S. Andergassen, A. Toschi, and G. Rohringer, *Phys. Rev. B* **97**, 235140 (2018).
- [58] One needs to consider separately the limits where only $|\nu| \rightarrow \infty$ or $|\nu'| \rightarrow \infty$; or $|\nu|$ and $|\nu'| \rightarrow \infty$ but either $\nu' - \nu = \text{const}$ or $\nu' + \nu + \omega = \text{const}$, see also Ref. [22].
- [59] T. Schäfer, N. Wentzell, F. Šimkovic, Y.-Y. He, C. Hille, M. Klett, C. J. Eckhardt, B. Arzhang, V. Harkov, F. m. c.-M. Le Régent, A. Kirsch, Y. Wang, A. J. Kim, E. Kozik, E. A. Stepanov, A. Kauch, S. Andergassen, P. Hansmann, D. Rohe, Y. M. Vilck, J. P. F. LeBlanc, S. Zhang, A.-M. S. Tremblay, M. Ferrero, O. Parcollet, and A. Georges, *Phys. Rev. X* **11**, 011058 (2021).
- [60] A. Kiani and E. Pavarini, *Phys. Rev. B* **94**, 075112 (2016).
- [61] E. A. Stepanov, S. Brener, F. Krien, M. Harland, A. I. Lichtenstein, and M. I. Katsnelson, *Phys. Rev. Lett.* **121**, 037204 (2018).
- [62] F. Krien, *Phys. Rev. B* **99**, 235106 (2019).
- [63] D. Vilardi, C. Taranto, and W. Metzner, *Phys. Rev. B* **97**, 235110 (2018).
- [64] P. M. Bonetti, J. Mitscherling, D. Vilardi, and W. Metzner, *Phys. Rev. B* **101**, 165142 (2020).
- [65] R. Peters and N. Kawakami, *Phys. Rev. B* **89**, 155134 (2014).
- [66] L. Del Re and G. Rohringer, “Fluctuations diagnostic of the spin susceptibility: Neel ordering revisited in dmft,” (2021), [arXiv:2104.11737](https://arxiv.org/abs/2104.11737).
- [67] A. Georges and J. S. Yedidia, *Phys. Rev. B* **43**, 3475 (1991).
- [68] P. Kopietz, *Phys. Rev. B* **48**, 13789 (1993).
- [69] H. Heiselberg, C. J. Pethick, H. Smith, and L. Viverit, *Phys. Rev. Lett.* **85**, 2418 (2000).
- [70] A. Toschi, P. Barone, M. Capone, and C. Castellani, *New Journal of Physics* **7**, 7 (2005).
- [71] A. A. Katanin, A. Toschi, and K. Held, *Phys. Rev. B* **80**, 075104 (2009).
- [72] Other than for the square lattice Hubbard model (1) itself, a weak-coupling expansion can be applied to the AIM (2) corresponding to the DMFT solution of this model at small U [1].
- [73] The case of weak coupling is complicated by the interplay of different fluctuations with the incoherence introduced by the DMFT self-energy [66]. One should note that the authors of Ref. [66] consider a different Bethe-Salpeter equation using the particle-hole-irreducible vertex of the AIM, whereas Eq. (3) is formulated in terms of the full vertex f . This may slightly change the effect of different truncations at the two-particle level.
- [74] It therefore appears that in a local moment regime $\lambda^{\text{sp}}(\nu, \omega = 0)$ may diverge for small ν as $T \rightarrow 0$. However, the spin polarization $\pi^{\text{sp}}(\omega = 0) = \sum_{\nu} g_{\nu} g_{\nu} \lambda^{\text{sp}}(\nu, \omega = 0) \rightarrow -\frac{1}{T}$ and the effective exchange J in Eq. (11) remain finite. This requires that the divergence of λ^{sp} is cancelled by a zero of g_{ν} , which is plausible because the ground state of the AIM is insulating in the local moment regime. This corrects a previous statement made in the conclusions of Ref. [62].
- [75] In practice we use the formula presented in Ref. [62] to evaluate the susceptibility X , which converges faster with the Matsubara cutoff than Eq. (12). Using Eq. (12) in the text allows us to discuss DMFT and the LDFA self-energy (14) on equal footing.
- [76] J. Otsuki, H. Hafermann, and A. I. Lichtenstein, *Phys. Rev. B* **90**, 235132 (2014).
- [77] The AIM corresponds to the DMFT solution, that is, we keep the hybridization function Δ in Eq. (2) fixed to its DMFT value.
- [78] N. V. Prokof'ev and B. V. Svistunov, *Phys. Rev. Lett.* **81**, 2514 (1998).
- [79] A. A. Katanin, *Phys. Rev. B* **103**, 054415 (2021).
- [80] N. E. Bickers and D. J. Scalapino, *Phys. Rev. B* **46**, 8050 (1992).
- [81] F. Krien, P. Worm, P. Chalupa, A. Toschi, and K. Held, “Spin scattering turns complex at strong coupling: the key to pseudogap and fermi arcs in the hubbard model,” (2021), [arXiv:2107.06529](https://arxiv.org/abs/2107.06529).
- [82] H. Hafermann, K. R. Patton, and P. Werner, *Phys. Rev. B* **85**, 205106 (2012).
- [83] It may seem that the guiding principle of the asymptotic approximation is also to parametrize the vertex in terms of bosons and their coupling λ to fermions. However, this would not be an accurate description, because one vertex λ is always set to its asymptotic value ± 1 , cf. Eq. (8), which at small frequencies does not correspond to the fermion-boson coupling of the interacting system.
- [84] Due to particle-hole symmetry the singlet quantities w^{s} and λ^{s} can be obtained from the charge channel [33] and hence they are also small and can be ignored.
- [85] P. Chalupa, T. Schäfer, M. Reitner, D. Springer, S. Andergassen, and A. Toschi, *Phys. Rev. Lett.* **126**, 056403 (2021).
- [86] It is plausible that the Néel temperature of the SBE approximation is higher than that of DMFT because the neglected $\varphi^{\text{Uirr,sp}}$ is repulsive, cf. Fig. 2.
- [87] M. Vandelli, V. Harkov, E. A. Stepanov, J. Gukelberger, E. Kozik, A. Rubio, and A. I. Lichtenstein, “Dual boson diagrammatic monte carlo approach applied to the extended hubbard model,” (2020), [arXiv:2007.04669](https://arxiv.org/abs/2007.04669) [cond-mat.str-el].
- [88] P. Worm, C. Watzenböck, M. Pickem, A. Kauch, and K. Held, “Broadening and sharpening of the drude peak through antiferromagnetic fluctuations,” (2020), [arXiv:2010.15797](https://arxiv.org/abs/2010.15797).
- [89] O. Simard, S. Takayoshi, and P. Werner, *Phys. Rev. B* **103**, 104415 (2021).
- [90] T. Ayrál and O. Parcollet, *Phys. Rev. B* **92**, 115109 (2015).
- [91] J. Otsuki, K. Yoshimi, H. Shinaoka, and Y. Nomura, *Phys. Rev. B* **99**, 165134 (2019).
- [92] J. Kaufmann, C. Eckhardt, M. Pickem, M. Kitatani, A. Kauch, and K. Held, *Phys. Rev. B* **103**, 035120 (2021).
- [93] E. G. C. P. van Loon, *Journal of Physics: Condensed Matter* **33**, 135601 (2021).
- [94] M. Wallerberger, H. Shinaoka, and A. Kauch, *Phys. Rev. Research* **3**, 033168 (2021).
- [95] G. Li, N. Wentzell, P. Pudleiner, P. Thunström, and K. Held, *Phys. Rev. B* **93**, 165103 (2016).
- [96] C. Hille, F. B. Kugler, C. J. Eckhardt, Y.-Y. He, A. Kauch, C. Honerkamp, A. Toschi, and S. Ander-

- gassen, *Phys. Rev. Research* **2**, 033372 (2020).
- [97] C. J. Eckhardt, C. Honerkamp, K. Held, and A. Kauch, *Phys. Rev. B* **101**, 155104 (2020).
- [98] P. M. Bonetti, A. Toschi, C. Hille, S. Andergassen, and D. Vilardi, “Single boson exchange representation of the functional renormalization group for strongly interacting many-electron systems,” (2021), [arXiv:2105.11749](https://arxiv.org/abs/2105.11749) [[cond-mat.str-el](https://arxiv.org/archive/cond)].
- [99] F. Krien and A. Valli, *Phys. Rev. B* **100**, 245147 (2019).

Summary and Outlook

As the main part of the thesis, the D-TRILEX method for single-band systems was introduced and benchmarked for the Hubbard model on a square lattice. In conclusion, we find that D-TRILEX is an efficient and balanced method that takes into account the main nonlocal correlations of the system. Thereby, the main advantages of the theory are that, on one hand, unlike other partially bosonized theories, D-TRILEX is not affected by the Fierz ambiguity problem due to the unique choice of the bare interaction and, on the other hand, it has a simple diagrammatic structure reminiscent of the one of the *GW* theory. The low computational complexity of the method makes it a promising candidate for realistic calculations of magnetic materials.

In our study [72], where the D-TRILEX theory was introduced, we present a partially bosonized approximation for the full local four-point vertex of the impurity model (3.90). This approximation allows one to express the four-point vertex in terms of the three-point vertices and screened interaction, which drastically reduces the computational costs of numerical calculations. With this approximation, we further derived an action for an effective fermion-boson model (3.79). This action not only allows one to construct single- and two-particle quantities in the framework of the D-TRILEX approach, as it was done in [72], but can also be used in more elaborate methods like functional renormalization group (fRG) [199–204], parquet [53, 205–207], or diagrammatic Monte Carlo [168, 169] methods.

In [72] we showed that for a single-shot calculation the self-energy of D-TRILEX is in good agreement with the ladder DF results for an intermediate interaction strength. For small and large interaction strengths the results show a larger mismatch due to the missing transversal contributions to the vertex in D-TRILEX. Furthermore, we showed that the D-TRILEX approach provides a qualitatively good estimation for the metal-to-Mott-insulator phase transition.

In the next work [128] we performed a comprehensive analysis of the effect of different partially bosonized collective fluctuations on single-particle quantities. To investigate the importance of different classes of diagrams several approaches with different diagrammatic structures were compared. Thereby, two of the methods, DiagMC@DF and LDF, are based on the dual action (3.36) and the methods DiagMC@PBDT and D-TRILEX are based on the action of the effective fermion-boson

model (3.79). In the latter methods, the partially bosonized representation of the four-point vertex is used. As the reference system, the exactly solvable impurity model (3.59) was used, which provided the building blocks for the diagrammatic expansion of all considered methods. For all approaches interactions up to the two-particle level were considered.

Comparing the results of all considered methods, our first important observation is that the irreducible part of the four-point vertex can be safely excluded for a broad range of control parameters. Especially, in the regions where the nonlocal fluctuations remain small to moderate. Further, we found that the non-ladder diagrams appearing in both DiagMC methods have a small contribution, if the Coulomb interaction U is small, or they are almost completely canceled, by the diagrams describing transverse singlet correlations, at large U . The same transverse singlet diagrams are partially canceled by transverse particle-hole contributions at small and moderate interaction strength. To make the discussion complete, for all interaction strengths the longitudinal singlet contributions remain small and can be neglected. All of these findings provide the assessment that for a broad range of parameters the longitudinal particle-hole channel provides the main diagrammatic contribution and, therefore, D-TRILEX with its simple diagrammatic structure provides a reasonable and promising approximation for a broad class of interacting electron systems, especially in the case of realistic multi-orbital systems. In particular, D-TRILEX appears to provide an accurate result in the regimes where LDF turns out to be a good approximation compared to the exact result. Moreover, we found that D-TRILEX provides good results, compared to LDF, at moderately-correlated regimes around and even just below the Néel temperature where the pseudo gap starts to open. However, in the weakly-interacting Slater regime of the magnetic fluctuations [208], as was already discussed in Section 4.1, methods based on ladder approximations tend to underestimate the magnetic fluctuations in general. Especially, a simple method like D-TRILEX which merely accounts for longitudinal contributions to the vertex function fails to predict the formation of the pseudogap at the correct temperature due to a strong anharmonic behavior of collective correlations of itinerant electrons [189], which arises near the AFM instability. In this regime, transversal diagrams become important and have to be considered for a correct description of magnetic fluctuations and pseudogap formation. However, by increasing the Coulomb interaction the electrons become more localized resulting in a more harmonic behavior of the collective modes. In this case, the ladder-like approximations perform more accurately.

As our final result in [128] we performed calculations using the $t - t'$ model, which is considered to be the prototype model for high-temperature superconducting cuprate compounds, at 4% hole-doping. Comparing our results with exact DiagMC results provided by [175] we found that sc-D-TRILEX provides a very accurate agreement for the nonlocal part of the self-energy in such a non-trivial regime and

even precisely captures the N/AN dichotomy in the formation of a pseudogap in this regime. In addition, however, we found that the local parts of the self-energy differ which leads to the assumption that for this regime DMFT does not provide a good starting point.

In [130] D-TRILEX was put to a test by applying it for the first time to a realistic electron-structure model from first principles. Thereby, we performed a comprehensive investigation of collective electronic correlations in the hole-doped InSe monolayers. To this end, we derived a model which includes most characteristics of the material. Performing single-shot D-TRILEX we found several coexisting instabilities. The commensurate CDW ordering is found for a broad range of considered parameters indicating the main instability in the system. Close to the CDW phase boundary, we found that the strong spatial charge correlations have a large impact on the DOS resulting in a formation of a pseudogap. This emphasizes the importance of considering spatial electronic fluctuations. Furthermore, we found a FM phase inside the CDW, which is related to a vHS in the electronic spectrum. As a final result, we found that the effect of the electron-phonon coupling has no major impact on the qualitative physical picture. In fact, including the coupling only results in a shift of the phase boundaries due to an effective reduction of the local Coulomb interaction.

Bibliography

- [1] L. Landau. “Theory of Fermi-liquids”. In: *Zh. Eksp. Teor. Fiz.* 30 (1956), p. 1058.
- [2] P. Hohenberg and W. Kohn. “Inhomogeneous Electron Gas”. In: *Phys. Rev.* 136 (3B Nov. 1964), B864–B871. URL: <https://link.aps.org/doi/10.1103/PhysRev.136.B864>.
- [3] W. Kohn and L. J. Sham. “Self-Consistent Equations Including Exchange and Correlation Effects”. In: *Phys. Rev.* 140 (4A Nov. 1965), A1133–A1138. URL: <https://link.aps.org/doi/10.1103/PhysRev.140.A1133>.
- [4] R. O. Jones and O. Gunnarsson. “The density functional formalism, its applications and prospects”. In: *Rev. Mod. Phys.* 61 (3 July 1989), pp. 689–746. URL: <https://link.aps.org/doi/10.1103/RevModPhys.61.689>.
- [5] F. H. L. Essler, H. Frahm, F. Göhmann, A. Klümper, and V. E. Korepin. *The One-Dimensional Hubbard Model*. Cambridge University Press, 2005. URL: <https://doi.org/10.1017/CB09780511534843>.
- [6] A. Georges, G. Kotliar, W. Krauth, and M. J. Rozenberg. “Dynamical mean-field theory of strongly correlated fermion systems and the limit of infinite dimensions”. In: *Rev. Mod. Phys.* 68 (1 Jan. 1996), pp. 13–125. URL: <https://link.aps.org/doi/10.1103/RevModPhys.68.13>.
- [7] A. Georges and W. Krauth. “Numerical solution of the $d=\infty$ Hubbard model: Evidence for a Mott transition”. In: *Phys. Rev. Lett.* 69 (8 Aug. 1992), pp. 1240–1243. URL: <https://link.aps.org/doi/10.1103/PhysRevLett.69.1240>.
- [8] G. Kotliar, S. Y. Savrasov, K. Haule, V. S. Oudovenko, O. Parcollet, and C. A. Marianetti. “Electronic structure calculations with dynamical mean-field theory”. In: *Rev. Mod. Phys.* 78 (3 Aug. 2006), pp. 865–951. URL: <https://link.aps.org/doi/10.1103/RevModPhys.78.865>.
- [9] A. I. Lichtenstein, M. I. Katsnelson, and G. Kotliar. “Finite-Temperature Magnetism of Transition Metals: An ab initio Dynamical Mean-Field Theory”. In: *Phys. Rev. Lett.* 87 (6 July 2001), p. 067205. URL: <https://link.aps.org/doi/10.1103/PhysRevLett.87.067205>.

- [10] S. Das Sarma and E. Hwang. “Screening and transport in 2D semiconductor systems at low temperatures”. In: *Scientific Reports* 5.1 (2015), pp. 1–20. URL: <https://doi.org/10.1038/srep16655>.
- [11] K. Andersen, S. Latini, and K. S. Thygesen. “Dielectric genome of van der Waals heterostructures”. In: *Nano letters* 15.7 (2015), pp. 4616–4621. URL: <https://doi.org/10.1021/acs.nanolett.5b01251>.
- [12] M. Rösner, E. Şaşıo ğlu, C. Friedrich, S. Blügel, and T. O. Wehling. “Wannier function approach to realistic Coulomb interactions in layered materials and heterostructures”. In: *Phys. Rev. B* 92 (8 Aug. 2015), p. 085102. URL: <https://link.aps.org/doi/10.1103/PhysRevB.92.085102>.
- [13] T. O. Wehling, E. Şa ş i o ğlu, C. Friedrich, A. I. Lichtenstein, M. I. Katsnelson, and S. Blügel. “Strength of Effective Coulomb Interactions in Graphene and Graphite”. In: *Phys. Rev. Lett.* 106 (23 June 2011), p. 236805. URL: <https://link.aps.org/doi/10.1103/PhysRevLett.106.236805>.
- [14] E. G. van Loon, M. Rösner, G. Schönhoff, M. I. Katsnelson, and T. O. Wehling. “Competing Coulomb and electron–phonon interactions in NbS₂”. In: *npj Quantum Materials* 3.1 (2018), pp. 1–8. URL: <https://doi.org/10.1038/s41535-018-0105-4>.
- [15] A. I. Lichtenstein and M. I. Katsnelson. “Antiferromagnetism and d-wave superconductivity in cuprates: A cluster dynamical mean-field theory”. In: *Phys. Rev. B* 62 (14 Oct. 2000), R9283–R9286. URL: <https://link.aps.org/doi/10.1103/PhysRevB.62.R9283>.
- [16] G. Kotliar, S. Y. Savrasov, G. Pálsson, and G. Biroli. “Cellular Dynamical Mean Field Approach to Strongly Correlated Systems”. In: *Phys. Rev. Lett.* 87 (18 Oct. 2001), p. 186401. URL: <https://link.aps.org/doi/10.1103/PhysRevLett.87.186401>.
- [17] T. Maier, M. Jarrell, T. Pruschke, and M. H. Hettler. “Quantum cluster theories”. In: *Rev. Mod. Phys.* 77 (3 Oct. 2005), pp. 1027–1080. URL: <https://link.aps.org/doi/10.1103/RevModPhys.77.1027>.
- [18] M. H. Hettler, A. N. Tahvildar-Zadeh, M. Jarrell, T. Pruschke, and H. R. Krishnamurthy. “Nonlocal dynamical correlations of strongly interacting electron systems”. In: *Phys. Rev. B* 58 (12 Sept. 1998), R7475–R7479. URL: <https://link.aps.org/doi/10.1103/PhysRevB.58.R7475>.
- [19] M. H. Hettler, M. Mukherjee, M. Jarrell, and H. R. Krishnamurthy. “Dynamical cluster approximation: Nonlocal dynamics of correlated electron systems”. In: *Phys. Rev. B* 61 (19 May 2000), pp. 12739–12756. URL: <https://link.aps.org/doi/10.1103/PhysRevB.61.12739>.

- [20] F. Ducastelle. “Analytic properties of the coherent potential approximation and of its molecular generalizations”. In: *Journal of Physics C: Solid State Physics* 7.10 (May 1974), pp. 1795–1816. URL: <https://doi.org/10.1088/0022-3719/7/10/007>.
- [21] P. Sun and G. Kotliar. “Many-Body Approximation Scheme beyond GW”. In: *Phys. Rev. Lett.* 92 (19 May 2004), p. 196402. URL: <https://link.aps.org/doi/10.1103/PhysRevLett.92.196402>.
- [22] S. Biermann, F. Aryasetiawan, and A. Georges. “First-Principles Approach to the Electronic Structure of Strongly Correlated Systems: Combining the GW Approximation and Dynamical Mean-Field Theory”. In: *Phys. Rev. Lett.* 90 (8 Feb. 2003), p. 086402. URL: <https://link.aps.org/doi/10.1103/PhysRevLett.90.086402>.
- [23] T. Ayrál, P. Werner, and S. Biermann. “Spectral Properties of Correlated Materials: Local Vertex and Nonlocal Two-Particle Correlations from Combined GW and Dynamical Mean Field Theory”. In: *Phys. Rev. Lett.* 109 (22 Nov. 2012), p. 226401. URL: <http://link.aps.org/doi/10.1103/PhysRevLett.109.226401>.
- [24] T. Ayrál, S. Biermann, and P. Werner. “Screening and nonlocal correlations in the extended Hubbard model from self-consistent combined GW and dynamical mean field theory”. In: *Phys. Rev. B* 87 (12 Mar. 2013), p. 125149. URL: <https://link.aps.org/doi/10.1103/PhysRevB.87.125149>.
- [25] L. Huang, T. Ayrál, S. Biermann, and P. Werner. “Extended dynamical mean-field study of the Hubbard model with long-range interactions”. In: *Phys. Rev. B* 90 (19 Nov. 2014), p. 195114. URL: <http://link.aps.org/doi/10.1103/PhysRevB.90.195114>.
- [26] L. Boehnke, F. Nilsson, F. Aryasetiawan, and P. Werner. “When strong correlations become weak: Consistent merging of GW and DMFT”. In: *Phys. Rev. B* 94 (20 Nov. 2016), 201106(R). URL: <https://link.aps.org/doi/10.1103/PhysRevB.94.201106>.
- [27] T. Ayrál, S. Biermann, P. Werner, and L. Boehnke. “Influence of Fock exchange in combined many-body perturbation and dynamical mean field theory”. In: *Phys. Rev. B* 95 (24 June 2017), p. 245130. URL: <https://link.aps.org/doi/10.1103/PhysRevB.95.245130>.
- [28] T. Ayrál and O. Parcollet. “Mott physics and spin fluctuations: A unified framework”. In: *Phys. Rev. B* 92 (11 Sept. 2015), p. 115109. URL: <https://link.aps.org/doi/10.1103/PhysRevB.92.115109>.

- [29] T. Ayrál and O. Parcollet. “Mott physics and spin fluctuations: A functional viewpoint”. In: *Phys. Rev. B* 93 (23 June 2016), p. 235124. URL: <https://link.aps.org/doi/10.1103/PhysRevB.93.235124>.
- [30] T. Ayrál, J. Vučićević, and O. Parcollet. “Fierz Convergence Criterion: A Controlled Approach to Strongly Interacting Systems with Small Embedded Clusters”. In: *Phys. Rev. Lett.* 119 (16 Oct. 2017), p. 166401. URL: <https://link.aps.org/doi/10.1103/PhysRevLett.119.166401>.
- [31] J. M. Tomczak, M. Casula, T. Miyake, F. Aryasetiawan, and S. Biermann. “Combined GW and dynamical mean-field theory: Dynamical screening effects in transition metal oxides”. In: *EPL (Europhysics Letters)* 100.6 (Dec. 2012), p. 67001. URL: <https://doi.org/10.1209%2F0295-5075%2F100%2F67001>.
- [32] J. M. Tomczak, M. van Schilfhaarde, and G. Kotliar. “Many-Body Effects in Iron Pnictides and Chalcogenides: Nonlocal Versus Dynamic Origin of Effective Masses”. In: *Phys. Rev. Lett.* 109 (23 Dec. 2012), p. 237010. URL: <https://link.aps.org/doi/10.1103/PhysRevLett.109.237010>.
- [33] C. Taranto, M. Kaltak, N. Parragh, G. Sangiovanni, G. Kresse, A. Toschi, and K. Held. “Comparing quasiparticle $GW+DMFT$ and $LDA+DMFT$ for the test bed material $SrVO_3$ ”. In: *Phys. Rev. B* 88 (16 Oct. 2013), p. 165119. URL: <https://link.aps.org/doi/10.1103/PhysRevB.88.165119>.
- [34] R. Sakuma, P. Werner, and F. Aryasetiawan. “Electronic structure of $SrVO_3$ within $GW+DMFT$ ”. In: *Phys. Rev. B* 88 (23 Dec. 2013), p. 235110. URL: <https://link.aps.org/doi/10.1103/PhysRevB.88.235110>.
- [35] J. M. Tomczak, M. Casula, T. Miyake, and S. Biermann. “Asymmetry in band widening and quasiparticle lifetimes in $SrVO_3$: Competition between screened exchange and local correlations from combined GW and dynamical mean-field theory $GW + DMFT$ ”. In: *Phys. Rev. B* 90 (16 Oct. 2014), p. 165138. URL: <https://link.aps.org/doi/10.1103/PhysRevB.90.165138>.
- [36] A. van Roekeghem, T. Ayrál, J. M. Tomczak, M. Casula, N. Xu, H. Ding, M. Ferrero, O. Parcollet, H. Jiang, and S. Biermann. “Dynamical Correlations and Screened Exchange on the Experimental Bench: Spectral Properties of the Cobalt Pnictide $BaCo_2As_2$ ”. In: *Phys. Rev. Lett.* 113 (26 Dec. 2014), p. 266403. URL: <http://link.aps.org/doi/10.1103/PhysRevLett.113.266403>.
- [37] L. Sponza, P. Pisanti, A. Vishina, D. Pashov, C. Weber, M. van Schilfhaarde, S. Acharya, J. Vidal, and G. Kotliar. “Self-energies in itinerant magnets: A focus on Fe and Ni”. In: *Phys. Rev. B* 95 (4 Jan. 2017), p. 041112. URL: <https://link.aps.org/doi/10.1103/PhysRevB.95.041112>.

- [38] E. A. Stepanov, Y. Nomura, A. I. Lichtenstein, and S. Biermann. “Orbital Isotropy of Magnetic Fluctuations in Correlated Electron Materials Induced by Hund’s Exchange Coupling”. In: *Phys. Rev. Lett.* 127 (20 Nov. 2021), p. 207205. URL: <https://link.aps.org/doi/10.1103/PhysRevLett.127.207205>.
- [39] O. Simard, S. Takayoshi, and P. Werner. “Diagrammatic study of optical excitations in correlated systems”. In: *Phys. Rev. B* 103 (10 Mar. 2021), p. 104415. URL: <https://link.aps.org/doi/10.1103/PhysRevB.103.104415>.
- [40] H. Kontani. “Optical Conductivity and Hall Coefficient in High-Tc Superconductors: Significant Role of Current Vertex Corrections”. In: *Journal of the Physical Society of Japan* 75.1 (2006), p. 013703. URL: <https://doi.org/10.1143/JPSJ.75.013703>.
- [41] F. Aryasetiawan and S. Biermann. “Generalized Hedin’s Equations for Quantum Many-Body Systems with Spin-Dependent Interactions”. In: *Phys. Rev. Lett.* 100 (11 Mar. 2008), p. 116402. URL: <https://link.aps.org/doi/10.1103/PhysRevLett.100.116402>.
- [42] N. Lin, E. Gull, and A. J. Millis. “Optical conductivity from cluster dynamical mean-field theory: Formalism and application to high-temperature superconductors”. In: *Phys. Rev. B* 80 (16 Oct. 2009), 161105(R). URL: <https://link.aps.org/doi/10.1103/PhysRevB.80.161105>.
- [43] M. I. Katsnelson and A. I. Lichtenstein. “Theory of optically forbidden d–d transitions in strongly correlated crystals”. In: *Journal of Physics: Condensed Matter* 22.38 (Sept. 2010), p. 382201. URL: <http://dx.doi.org/10.1088/0953-8984/22/38/382201>.
- [44] D. Bergeron, V. Hankevych, B. Kyung, and A.-M. S. Tremblay. “Optical and dc conductivity of the two-dimensional Hubbard model in the pseudogap regime and across the antiferromagnetic quantum critical point including vertex corrections”. In: *Phys. Rev. B* 84 (8 Aug. 2011), p. 085128. URL: <https://link.aps.org/doi/10.1103/PhysRevB.84.085128>.
- [45] J. Vučićević, J. Kokalj, R. Žitko, N. Wentzell, D. Tanasković, and J. Mravlje. “Conductivity in the Square Lattice Hubbard Model at High Temperatures: Importance of Vertex Corrections”. In: *Phys. Rev. Lett.* 123 (3 July 2019), p. 036601. URL: <https://link.aps.org/doi/10.1103/PhysRevLett.123.036601>.

- [46] A. Kauch, P. Puddleiner, K. Astleithner, P. Thunström, T. Ribic, and K. Held. “Generic Optical Excitations of Correlated Systems: π -tons”. In: *Phys. Rev. Lett.* 124 (4 Jan. 2020), p. 047401. URL: <https://link.aps.org/doi/10.1103/PhysRevLett.124.047401>.
- [47] L. Hedin. “New Method for Calculating the One-Particle Green’s Function with Application to the Electron-Gas Problem”. In: *Phys. Rev.* 139 (3A Aug. 1965), A796–A823. URL: <http://link.aps.org/doi/10.1103/PhysRev.139.A796>.
- [48] J. Jaeckel and C. Wetterich. “Flow equations without mean field ambiguity”. In: *Phys. Rev. D* 68 (2 July 2003), p. 025020. URL: <https://link.aps.org/doi/10.1103/PhysRevD.68.025020>.
- [49] J. Jaeckel. *Understanding the Fierz Ambiguity of Partially Bosonized Theories*. 2002. URL: <https://arxiv.org/abs/hep-ph/0205154>.
- [50] A. Toschi, A. A. Katanin, and K. Held. “Dynamical vertex approximation: A step beyond dynamical mean-field theory”. In: *Phys. Rev. B* 75 (4 Jan. 2007), p. 045118. URL: <https://link.aps.org/doi/10.1103/PhysRevB.75.045118>.
- [51] A. A. Katanin, A. Toschi, and K. Held. “Comparing pertinent effects of anti-ferromagnetic fluctuations in the two- and three-dimensional Hubbard model”. In: *Phys. Rev. B* 80 (7 Aug. 2009), p. 075104. URL: <https://link.aps.org/doi/10.1103/PhysRevB.80.075104>.
- [52] T. Schäfer, F. Geles, D. Rost, G. Rohringer, E. Arrigoni, K. Held, N. Blümer, M. Aichhorn, and A. Toschi. “Fate of the false Mott-Hubbard transition in two dimensions”. In: *Phys. Rev. B* 91 (12 Mar. 2015), p. 125109. URL: <https://link.aps.org/doi/10.1103/PhysRevB.91.125109>.
- [53] A. Valli, T. Schäfer, P. Thunström, G. Rohringer, S. Andergassen, G. Sangiovanni, K. Held, and A. Toschi. “Dynamical vertex approximation in its parquet implementation: Application to Hubbard nanorings”. In: *Phys. Rev. B* 91 (11 Mar. 2015), p. 115115. URL: <https://link.aps.org/doi/10.1103/PhysRevB.91.115115>.
- [54] A. N. Rubtsov, M. I. Katsnelson, and A. I. Lichtenstein. “Dual fermion approach to nonlocal correlations in the Hubbard model”. In: *Phys. Rev. B* 77 (3 Jan. 2008), p. 033101. URL: <http://link.aps.org/doi/10.1103/PhysRevB.77.033101>.

- [55] A. N. Rubtsov, M. I. Katsnelson, A. I. Lichtenstein, and A. Georges. “Dual fermion approach to the two-dimensional Hubbard model: Antiferromagnetic fluctuations and Fermi arcs”. In: *Phys. Rev. B* 79 (4 Jan. 2009), p. 045133. URL: <http://link.aps.org/doi/10.1103/PhysRevB.79.045133>.
- [56] H. Hafermann, G. Li, A. N. Rubtsov, M. I. Katsnelson, A. I. Lichtenstein, and H. Monien. “Efficient Perturbation Theory for Quantum Lattice Models”. In: *Phys. Rev. Lett.* 102 (20 May 2009), p. 206401. URL: <https://link.aps.org/doi/10.1103/PhysRevLett.102.206401>.
- [57] S. Brener, E. A. Stepanov, A. N. Rubtsov, M. I. Katsnelson, and A. I. Lichtenstein. “Dual fermion method as a prototype of generic reference-system approach for correlated fermions”. In: *Annals of Physics* 422 (2020), p. 168310. URL: <http://www.sciencedirect.com/science/article/pii/S000349162030244X>.
- [58] A. N. Rubtsov, M. I. Katsnelson, and A. I. Lichtenstein. “Dual boson approach to collective excitations in correlated fermionic systems”. In: *Annals of Physics* 327.5 (2012), pp. 1320–1335. URL: <http://www.sciencedirect.com/science/article/pii/S0003491612000164>.
- [59] E. G. C. P. van Loon, A. I. Lichtenstein, M. I. Katsnelson, O. Parcollet, and H. Hafermann. “Beyond extended dynamical mean-field theory: Dual boson approach to the two-dimensional extended Hubbard model”. In: *Phys. Rev. B* 90 (23 Dec. 2014), p. 235135. URL: <https://link.aps.org/doi/10.1103/PhysRevB.90.235135>.
- [60] E. A. Stepanov, E. G. C. P. van Loon, A. A. Katanin, A. I. Lichtenstein, M. I. Katsnelson, and A. N. Rubtsov. “Self-consistent dual boson approach to single-particle and collective excitations in correlated systems”. In: *Phys. Rev. B* 93 (4 Jan. 2016), p. 045107. URL: <http://link.aps.org/doi/10.1103/PhysRevB.93.045107>.
- [61] E. A. Stepanov, A. Huber, E. G. C. P. van Loon, A. I. Lichtenstein, and M. I. Katsnelson. “From local to nonlocal correlations: The Dual Boson perspective”. In: *Phys. Rev. B* 94 (20 Nov. 2016), p. 205110. URL: <https://link.aps.org/doi/10.1103/PhysRevB.94.205110>.
- [62] “Dual boson approach with instantaneous interaction, author = Peters, L. and van Loon, E. G. C. P. and Rubtsov, A. N. and Lichtenstein, A. I. and Katsnelson, M. I. and Stepanov, E. A.” In: *Phys. Rev. B* 100 (16 Oct. 2019), p. 165128. URL: <https://link.aps.org/doi/10.1103/PhysRevB.100.165128>.

- [63] A. Galler, P. Thunström, P. Gunacker, J. M. Tomczak, and K. Held. “Ab initio dynamical vertex approximation”. In: *Phys. Rev. B* 95 (11 Mar. 2017), p. 115107. URL: <https://link.aps.org/doi/10.1103/PhysRevB.95.115107>.
- [64] A. Galler, J. Kaufmann, P. Gunacker, M. Pickem, P. Thunström, J. M. Tomczak, and K. Held. “Towards ab initio Calculations with the Dynamical Vertex Approximation”. In: *Journal of the Physical Society of Japan* 87.4 (2018), p. 041004. URL: <https://doi.org/10.7566/JPSJ.87.041004>.
- [65] J. Kaufmann, C. Eckhardt, M. Pickem, M. Kitatani, A. Kauch, and K. Held. “Self-consistent ladder dynamical vertex approximation”. In: *Phys. Rev. B* 103 (3 Jan. 2021), p. 035120. URL: <https://link.aps.org/doi/10.1103/PhysRevB.103.035120>.
- [66] E. G. C. P. van Loon. “Second-order dual fermion for multi-orbital systems”. In: *Journal of Physics: Condensed Matter* 33.13 (Jan. 2021), p. 135601. URL: <https://doi.org/10.1088/1361-648x/abd9ed>.
- [67] C. Husemann and M. Salmhofer. “Efficient parametrization of the vertex function, Ω scheme, and the t, t' Hubbard model at van Hove filling”. In: *Phys. Rev. B* 79 (19 May 2009), p. 195125. URL: <https://link.aps.org/doi/10.1103/PhysRevB.79.195125>.
- [68] S. Friederich, H. C. Krahl, and C. Wetterich. “Four-point vertex in the Hubbard model and partial bosonization”. In: *Phys. Rev. B* 81 (23 June 2010), p. 235108. URL: <https://link.aps.org/doi/10.1103/PhysRevB.81.235108>.
- [69] F. Krien. “Efficient evaluation of the polarization function in dynamical mean-field theory”. In: *Phys. Rev. B* 99 (23 June 2019), p. 235106. URL: <https://link.aps.org/doi/10.1103/PhysRevB.99.235106>.
- [70] F. Krien, A. Valli, and M. Capone. “Single-boson exchange decomposition of the vertex function”. In: *Phys. Rev. B* 100 (15 Oct. 2019), p. 155149. URL: <https://link.aps.org/doi/10.1103/PhysRevB.100.155149>.
- [71] O. Gunnarsson, T. Schäfer, J. P. F. LeBlanc, E. Gull, J. Merino, G. Sangiovanni, G. Rohringer, and A. Toschi. “Fluctuation Diagnostics of the Electron Self-Energy: Origin of the Pseudogap Physics”. In: *Phys. Rev. Lett.* 114 (23 June 2015), p. 236402. URL: <https://link.aps.org/doi/10.1103/PhysRevLett.114.236402>.

- [72] E. A. Stepanov, V. Harkov, and A. I. Lichtenstein. “Consistent partial bosonization of the extended Hubbard model”. In: *Phys. Rev. B* 100 (20 Nov. 2019), p. 205115. URL: <https://link.aps.org/doi/10.1103/PhysRevB.100.205115>.
- [73] M. Vandelli, J. Kaufmann, M. El-Nabulsi, V. Harkov, A. I. Lichtenstein, and E. A. Stepanov. “Multi-band D-TRILEX approach to materials with strong electronic correlations”. In: *SciPost Phys.* 13 (2022), p. 036. URL: <https://scipost.org/10.21468/SciPostPhys.13.2.036>.
- [74] M. Vandelli, J. Kaufmann, V. Harkov, A. I. Lichtenstein, K. Held, and E. A. Stepanov. *Extended regime of coexisting metallic and insulating phases in a two-orbital electronic system*. 2022. URL: <https://arxiv.org/abs/2204.02116>.
- [75] V. Harkov, A. I. Lichtenstein, and F. Krien. “Parametrizations of local vertex corrections from weak to strong coupling: Importance of the Hedin three-leg vertex”. In: *Phys. Rev. B* 104 (12 Sept. 2021), p. 125141. URL: <https://link.aps.org/doi/10.1103/PhysRevB.104.125141>.
- [76] J. W. Negele and H. Orland. *Quantum many-particle systems*. Westview Press, 2018.
- [77] A. Altland and B. D. Simons. *Condensed matter field theory*. Cambridge university press, 2010.
- [78] A. L. Fetter and J. D. Walecka. *Quantum theory of many-particle systems*. Courier Corporation, 2012.
- [79] G. D. Mahan. *Many-Particle Physics*. Springer US, 2000. URL: <https://doi.org/10.1007/978-1-4757-5714-9>.
- [80] J. Hubbard. “Electron correlations in narrow energy bands”. In: *Proceedings of the Royal Society of London. Series A. Mathematical and Physical Sciences* 276.1365 (1963), pp. 238–257.
- [81] J. Hubbard. “Electron correlations in narrow energy bands. II. The degenerate band case”. In: *Proceedings of the Royal Society of London. Series A. Mathematical and Physical Sciences* 277.1369 (1964), pp. 237–259.
- [82] J. Hubbard. “Electron correlations in narrow energy bands III. An improved solution”. In: *Proceedings of the Royal Society of London. Series A. Mathematical and Physical Sciences* 281.1386 (1964), pp. 401–419.
- [83] J. Hubbard. “Electron correlations in narrow energy bands-IV. The atomic representation”. In: *Proceedings of the Royal Society of London. Series A. Mathematical and Physical Sciences* 285.1403 (1965), pp. 542–560.

- [84] J. Hubbard. “Electron correlations in narrow energy bands V. A perturbation expansion about the atomic limit”. In: *Proceedings of the Royal Society of London. Series A. Mathematical and Physical Sciences* 296.1444 (1967), pp. 82–99.
- [85] T. Schäfer, N. Wentzell, F. Šimkovic, Y.-Y. He, C. Hille, M. Klett, C. J. Eckhardt, B. Arzhang, V. Harkov, F.-M. Le Régent, A. Kirsch, Y. Wang, A. J. Kim, E. Kozik, E. A. Stepanov, A. Kauch, S. Andergassen, P. Hansmann, D. Rohe, Y. M. Vilks, J. P. F. LeBlanc, S. Zhang, A.-M. S. Tremblay, M. Ferrero, O. Parcollet, and A. Georges. “Tracking the Footprints of Spin Fluctuations: A MultiMethod, MultiMessenger Study of the Two-Dimensional Hubbard Model”. In: *Phys. Rev. X* 11 (1 Mar. 2021), p. 011058. URL: <https://link.aps.org/doi/10.1103/PhysRevX.11.011058>.
- [86] A. Mielke and H. Tasaki. “Ferromagnetism in the Hubbard model”. In: *Communications in mathematical physics* 158.2 (1993), pp. 341–371. URL: <https://doi.org/10.1007/BF02108079>.
- [87] M. Jarrell. “Hubbard model in infinite dimensions: A quantum Monte Carlo study”. In: *Phys. Rev. Lett.* 69 (1 July 1992), pp. 168–171. URL: <https://link.aps.org/doi/10.1103/PhysRevLett.69.168>.
- [88] M. Imada, A. Fujimori, and Y. Tokura. “Metal-insulator transitions”. In: *Rev. Mod. Phys.* 70 (4 Oct. 1998), pp. 1039–1263. URL: <https://link.aps.org/doi/10.1103/RevModPhys.70.1039>.
- [89] N. F. MOTT. “Metal-Insulator Transition”. In: *Rev. Mod. Phys.* 40 (4 Oct. 1968), pp. 677–683. URL: <https://link.aps.org/doi/10.1103/RevModPhys.40.677>.
- [90] E. Dagotto. “Correlated electrons in high-temperature superconductors”. In: *Rev. Mod. Phys.* 66 (3 July 1994), pp. 763–840. URL: <https://link.aps.org/doi/10.1103/RevModPhys.66.763>.
- [91] F. C. Zhang and T. M. Rice. “Effective Hamiltonian for the superconducting Cu oxides”. In: *Phys. Rev. B* 37 (7 Mar. 1988), pp. 3759–3761. URL: <https://link.aps.org/doi/10.1103/PhysRevB.37.3759>.
- [92] L. F. Feiner, J. H. Jefferson, and R. Raimondi. “Effective single-band models for the high- T_c cuprates. I. Coulomb interactions”. In: *Phys. Rev. B* 53 (13 Apr. 1996), pp. 8751–8773. URL: <https://link.aps.org/doi/10.1103/PhysRevB.53.8751>.
- [93] D. Jaksch and P. Zoller. “The cold atom Hubbard toolbox”. In: *Annals of Physics* 315.1 (2005). Special Issue, pp. 52–79. URL: <https://www.sciencedirect.com/science/article/pii/S0003491604001782>.

- [94] M. Lewenstein, A. Sanpera, V. Ahufinger, B. Damski, A. Sen(De), and U. Sen. “Ultracold atomic gases in optical lattices: mimicking condensed matter physics and beyond”. In: *Advances in Physics* 56.2 (2007), pp. 243–379. URL: <https://doi.org/10.1080/00018730701223200>.
- [95] I. Bloch. “Ultracold quantum gases in optical lattices”. In: *Nature physics* 1.1 (2005), pp. 23–30.
- [96] P. Hansmann, T. Ayrál, L. Vaugier, P. Werner, and S. Biermann. “Long-Range Coulomb Interactions in Surface Systems: A First-Principles Description within Self-Consistently Combined *GW* and Dynamical Mean-Field Theory”. In: *Phys. Rev. Lett.* 110 (16 Apr. 2013), p. 166401. URL: <https://link.aps.org/doi/10.1103/PhysRevLett.110.166401>.
- [97] M. Alidoosti, D. N. Esfahani, and R. Asgari. “Charge density wave and superconducting phase in monolayer InSe”. In: *Phys. Rev. B* 103 (3 Jan. 2021), p. 035411. URL: <https://link.aps.org/doi/10.1103/PhysRevB.103.035411>.
- [98] P. W. Anderson. “Localized Magnetic States in Metals”. In: *Phys. Rev.* 124 (1 Oct. 1961), pp. 41–53. URL: <https://link.aps.org/doi/10.1103/PhysRev.124.41>.
- [99] E. Gull, P. Werner, O. Parcollet, and M. Troyer. “Continuous-time auxiliary-field Monte Carlo for quantum impurity models”. In: *EPL (Europhysics Letters)* 82.5 (May 2008), p. 57003. URL: <https://doi.org/10.1209/0295-5075/82/57003>.
- [100] E. Gull, P. Staar, S. Fuchs, P. Nukala, M. S. Summers, T. Pruschke, T. C. Schulthess, and T. Maier. “Submatrix updates for the continuous-time auxiliary-field algorithm”. In: *Phys. Rev. B* 83 (7 Feb. 2011), p. 075122. URL: <https://link.aps.org/doi/10.1103/PhysRevB.83.075122>.
- [101] A. N. Rubtsov, V. V. Savkin, and A. I. Lichtenstein. “Continuous-time quantum Monte Carlo method for fermions”. In: *Phys. Rev. B* 72 (3 July 2005), p. 035122. URL: <https://link.aps.org/doi/10.1103/PhysRevB.72.035122>.
- [102] P. Werner, A. Comanac, L. de’Medici, M. Troyer, and A. J. Millis. “Continuous-Time Solver for Quantum Impurity Models”. In: *Phys. Rev. Lett.* 97 (7 Aug. 2006), p. 076405. URL: <https://link.aps.org/doi/10.1103/PhysRevLett.97.076405>.

- [103] P. Werner and A. J. Millis. “Hybridization expansion impurity solver: General formulation and application to Kondo lattice and two-orbital models”. In: *Phys. Rev. B* 74 (15 Oct. 2006), p. 155107. URL: <https://link.aps.org/doi/10.1103/PhysRevB.74.155107>.
- [104] H. Hafermann, K. R. Patton, and P. Werner. “Improved estimators for the self-energy and vertex function in hybridization-expansion continuous-time quantum Monte Carlo simulations”. In: *Phys. Rev. B* 85 (20 May 2012), p. 205106. URL: <http://link.aps.org/doi/10.1103/PhysRevB.85.205106>.
- [105] P. Gunacker, M. Wallerberger, T. Ribic, A. Hausoel, G. Sangiovanni, and K. Held. “Worm-improved estimators in continuous-time quantum Monte Carlo”. In: *Phys. Rev. B* 94 (12 Sept. 2016), p. 125153. URL: <https://link.aps.org/doi/10.1103/PhysRevB.94.125153>.
- [106] J. Kaufmann, P. Gunacker, A. Kowalski, G. Sangiovanni, and K. Held. “Symmetric improved estimators for continuous-time quantum Monte Carlo”. In: *Phys. Rev. B* 100 (7 Aug. 2019), p. 075119. URL: <https://link.aps.org/doi/10.1103/PhysRevB.100.075119>.
- [107] G. Rohringer, A. Valli, and A. Toschi. “Local electronic correlation at the two-particle level”. In: *Phys. Rev. B* 86 (12 Sept. 2012), p. 125114. URL: <https://link.aps.org/doi/10.1103/PhysRevB.86.125114>.
- [108] G. Rohringer, H. Hafermann, A. Toschi, A. A. Katanin, A. E. Antipov, M. I. Katsnelson, A. I. Lichtenstein, A. N. Rubtsov, and K. Held. “Diagrammatic routes to nonlocal correlations beyond dynamical mean field theory”. In: *Rev. Mod. Phys.* 90 (2 May 2018), p. 025003. URL: <https://link.aps.org/doi/10.1103/RevModPhys.90.025003>.
- [109] G. Rohringer. “New routes towards a theoretical treatment of nonlocal electronic correlations”. PhD thesis. 2013.
- [110] J. A. Sobota, Y. He, and Z.-X. Shen. “Angle-resolved photoemission studies of quantum materials”. In: *Rev. Mod. Phys.* 93 (2 May 2021), p. 025006. URL: <https://link.aps.org/doi/10.1103/RevModPhys.93.025006>.
- [111] D. Lu, I. M. Vishik, M. Yi, Y. Chen, R. G. Moore, and Z.-X. Shen. “Angle-Resolved Photoemission Studies of Quantum Materials”. In: *Annual Review of Condensed Matter Physics* 3.1 (Jan. 2012). URL: <https://www.osti.gov/biblio/1642351>.
- [112] J.-E. Rubensson. “RIXS dynamics for beginners”. In: *Journal of Electron Spectroscopy and Related Phenomena* 110-111 (2000). Soft X Ray Emission Spectroscopy, pp. 135–151. URL: <https://www.sciencedirect.com/science/article/pii/S0368204800001614>.

- [113] C. Jia, K. Wohlfeld, Y. Wang, B. Moritz, and T. P. Devereaux. “Using RIXS to Uncover Elementary Charge and Spin Excitations”. In: *Phys. Rev. X* 6 (2 May 2016), p. 021020. URL: <https://link.aps.org/doi/10.1103/PhysRevX.6.021020>.
- [114] D. R. Nascimento and N. Govind. “Computational approaches for XANES, VtC-XES, and RIXS using linear-response time-dependent density functional theory based methods”. In: *Phys. Chem. Chem. Phys.* 24 (24 2022), pp. 14680–14691. URL: <http://dx.doi.org/10.1039/D2CP01132H>.
- [115] R. F. Egerton. *Electron energy-loss spectroscopy in the electron microscope*. Springer Science & Business Media, 2011.
- [116] P. T. Callaghan. *Principles of nuclear magnetic resonance microscopy*. Oxford University Press on Demand, 1993.
- [117] R. S. Macomber. “A complete introduction to modern NMR spectroscopy”. In: *Nova York* (1998).
- [118] J. Kaufmann and K. Held. “ana_cont: Python package for analytic continuation”. In: *Computer Physics Communications* 282 (2023), p. 108519. URL: <https://www.sciencedirect.com/science/article/pii/S0010465522002387>.
- [119] I. Krivenko and M. Harland. “TRIQS/SOM: Implementation of the stochastic optimization method for analytic continuation”. In: *Comput. Phys. Commun.* 239 (2019), pp. 166–183. URL: <https://www.sciencedirect.com/science/article/pii/S0010465519300402>.
- [120] F. Krien. “Conserving dynamical mean-field approaches to strongly correlated systems”. PhD thesis. Staats-und Universitätsbibliothek Hamburg Carl von Ossietzky, 2018.
- [121] A. A. Abrikosov, I. Dzyaloshinskii, L. P. Gorkov, and R. A. Silverman. *Methods of quantum field theory in statistical physics*. New York, NY: Dover, 1975. URL: <https://cds.cern.ch/record/107441>.
- [122] E. Pavarini, E. Koch, D. Vollhardt, and A. Lichtenstein. *Dmft at 25: Infinite dimensions: Lecture notes of the autumn school on correlated electrons 2014*. Vol. 4. Forschungszentrum Jülich, 2014.
- [123] N. E. Bickers. “Self-Consistent Many-Body Theory for Condensed Matter Systems”. In: *Theoretical Methods for Strongly Correlated Electrons*. Ed. by D. Sénéchal, A.-M. Tremblay, and C. Bourbonnais. New York, NY: Springer New York, 2004, pp. 237–296. URL: https://doi.org/10.1007/0-387-21717-7_6.
- [124] H. Hafermann. “Numerical approaches to spatial correlations in strongly interacting fermion systems”. PhD thesis. Universität Hamburg, 2010.

- [125] H. Hafermann, E. G. C. P. van Loon, M. I. Katsnelson, A. I. Lichtenstein, and O. Parcollet. “Collective charge excitations of strongly correlated electrons, vertex corrections, and gauge invariance”. In: *Phys. Rev. B* 90 (23 Dec. 2014), p. 235105. URL: <https://link.aps.org/doi/10.1103/PhysRevB.90.235105>.
- [126] E. G. C. P. van Loon, F. Krien, and A. A. Katanin. “Bethe-Salpeter Equation at the Critical End Point of the Mott Transition”. In: *Phys. Rev. Lett.* 125 (13 Sept. 2020), p. 136402. URL: <https://link.aps.org/doi/10.1103/PhysRevLett.125.136402>.
- [127] F. Krien and A. Kauch. “The plain and simple parquet approximation: single- and multi-boson exchange in the two-dimensional Hubbard model”. In: *The European Physical Journal B* 95.4 (2022), pp. 1–10.
- [128] V. Harkov, M. Vandelli, S. Brener, A. I. Lichtenstein, and E. A. Stepanov. “Impact of partially bosonized collective fluctuations on electronic degrees of freedom”. In: *Phys. Rev. B* 103 (24 June 2021), p. 245123. URL: <https://link.aps.org/doi/10.1103/PhysRevB.103.245123>.
- [129] T. Denz, M. Mitter, J. M. Pawłowski, C. Wetterich, and M. Yamada. “Partial bosonization for the two-dimensional Hubbard model”. In: *Phys. Rev. B* 101 (15 Apr. 2020), p. 155115. URL: <https://link.aps.org/doi/10.1103/PhysRevB.101.155115>.
- [130] E. A. Stepanov, V. Harkov, M. Rösner, A. I. Lichtenstein, M. I. Katsnelson, and A. N. Rudenko. “Coexisting charge density wave and ferromagnetic instabilities in monolayer InSe”. In: *npj Computational Materials* 8.1 (2022), pp. 1–9. URL: <https://doi.org/10.1038/s41524-022-00798-4>.
- [131] M. Vandelli, V. Harkov, E. A. Stepanov, J. Gukelberger, E. Kozik, A. Rubio, and A. I. Lichtenstein. “Dual boson diagrammatic Monte Carlo approach applied to the extended Hubbard model”. In: *Phys. Rev. B* 102 (19 Nov. 2020), p. 195109. URL: <https://link.aps.org/doi/10.1103/PhysRevB.102.195109>.
- [132] E. A. Stepanov. “Eliminating Orbital Selectivity from the Metal-Insulator Transition by Strong Magnetic Fluctuations”. In: *Phys. Rev. Lett.* 129 (9 Aug. 2022), p. 096404. URL: <https://link.aps.org/doi/10.1103/PhysRevLett.129.096404>.
- [133] E. A. Stepanov, S. Brener, F. Krien, M. Harland, A. I. Lichtenstein, and M. I. Katsnelson. “Effective Heisenberg Model and Exchange Interaction for Strongly Correlated Systems”. In: *Phys. Rev. Lett.* 121 (3 July 2018), p. 037204. URL: <https://link.aps.org/doi/10.1103/PhysRevLett.121.037204>.

- [134] E. A. Stepanov, A. Huber, A. I. Lichtenstein, and M. I. Katsnelson. “Effective Ising model for correlated systems with charge ordering”. In: *Phys. Rev. B* 99 (11 Mar. 2019), p. 115124. URL: <https://link.aps.org/doi/10.1103/PhysRevB.99.115124>.
- [135] F. Krien and A. Valli. “Parquetlike equations for the Hedin three-leg vertex”. In: *Phys. Rev. B* 100 (24 Dec. 2019), p. 245147. URL: <https://link.aps.org/doi/10.1103/PhysRevB.100.245147>.
- [136] F. Krien, A. Valli, P. Chalupa, M. Capone, A. I. Lichtenstein, and A. Toschi. “Boson-exchange parquet solver for dual fermions”. In: *Phys. Rev. B* 102 (19 Nov. 2020), p. 195131. URL: <https://link.aps.org/doi/10.1103/PhysRevB.102.195131>.
- [137] F. Krien, A. Kauch, and K. Held. “Tiling with triangles: parquet and $GW\gamma$ methods unified”. In: *Phys. Rev. Research* 3 (1 Feb. 2021), p. 013149. URL: <https://link.aps.org/doi/10.1103/PhysRevResearch.3.013149>.
- [138] W. Metzner and D. Vollhardt. “Correlated Lattice Fermions in $d = \infty$ Dimensions”. In: *Phys. Rev. Lett.* 62 (3 Jan. 1989), pp. 324–327. URL: <https://link.aps.org/doi/10.1103/PhysRevLett.62.324>.
- [139] A. Georges and G. Kotliar. “Hubbard model in infinite dimensions”. In: *Phys. Rev. B* 45 (12 Mar. 1992), pp. 6479–6483. URL: <https://link.aps.org/doi/10.1103/PhysRevB.45.6479>.
- [140] M. Wallerberger, A. Hausoel, P. Gunacker, A. Kowalski, N. Parragh, F. Goth, K. Held, and G. Sangiovanni. “w2dynamics: Local one- and two-particle quantities from dynamical mean field theory”. In: *Computer Physics Communications* 235 (2019), pp. 388–399. URL: <https://www.sciencedirect.com/science/article/pii/S0010465518303217>.
- [141] E. Gull, A. J. Millis, A. I. Lichtenstein, A. N. Rubtsov, M. Troyer, and P. Werner. “Continuous-time Monte Carlo methods for quantum impurity models”. In: *Rev. Mod. Phys.* 83 (2 May 2011), pp. 349–404. URL: <https://link.aps.org/doi/10.1103/RevModPhys.83.349>.
- [142] F. Krien, E. G. C. P. van Loon, H. Hafermann, J. Otsuki, M. I. Katsnelson, and A. I. Lichtenstein. “Conservation in two-particle self-consistent extensions of dynamical mean-field theory”. In: *Phys. Rev. B* 96 (7 Aug. 2017), p. 075155. URL: <https://link.aps.org/doi/10.1103/PhysRevB.96.075155>.

- [143] F. Krien, E. G. C. P. van Loon, M. I. Katsnelson, A. I. Lichtenstein, and M. Capone. “Two-particle Fermi liquid parameters at the Mott transition: Vertex divergences, Landau parameters, and incoherent response in dynamical mean-field theory”. In: *Phys. Rev. B* 99 (24 June 2019), p. 245128. URL: <https://link.aps.org/doi/10.1103/PhysRevB.99.245128>.
- [144] E. G. C. P. van Loon, F. Krien, H. Hafermann, A. I. Lichtenstein, and M. I. Katsnelson. “Fermion-boson vertex within dynamical mean-field theory”. In: *Phys. Rev. B* 98 (20 Nov. 2018), p. 205148. URL: <https://link.aps.org/doi/10.1103/PhysRevB.98.205148>.
- [145] R. L. Stratonovich. “On a method of calculating quantum distribution functions”. In: *Soviet Physics Doklady*. Vol. 2. 1957, p. 416.
- [146] J. Hubbard. “Calculation of Partition Functions”. In: *Phys. Rev. Lett.* 3 (2 July 1959), pp. 77–78. URL: <https://link.aps.org/doi/10.1103/PhysRevLett.3.77>.
- [147] S. Biermann, A. Poteryaev, A. I. Lichtenstein, and A. Georges. “Dynamical Singlets and Correlation-Assisted Peierls Transition in VO_2 ”. In: *Phys. Rev. Lett.* 94 (2 Jan. 2005), p. 026404. URL: <https://link.aps.org/doi/10.1103/PhysRevLett.94.026404>.
- [148] D. Hirschmeier, H. Hafermann, and A. I. Lichtenstein. “Multiband dual fermion approach to quantum criticality in the Hubbard honeycomb lattice”. In: *Phys. Rev. B* 97 (11 Mar. 2018), p. 115150. URL: <https://link.aps.org/doi/10.1103/PhysRevB.97.115150>.
- [149] M. Harland, M. I. Katsnelson, and A. I. Lichtenstein. “Plaquette valence bond theory of high-temperature superconductivity”. In: *Phys. Rev. B* 94 (12 Sept. 2016), p. 125133. URL: <https://link.aps.org/doi/10.1103/PhysRevB.94.125133>.
- [150] A. M. Sengupta and A. Georges. “Non-Fermi-liquid behavior near a $T=0$ spin-glass transition”. In: *Phys. Rev. B* 52 (14 Oct. 1995), pp. 10295–10302. URL: <https://link.aps.org/doi/10.1103/PhysRevB.52.10295>.
- [151] Q. Si and J. L. Smith. “Kosterlitz-Thouless Transition and Short Range Spatial Correlations in an Extended Hubbard Model”. In: *Phys. Rev. Lett.* 77 (16 Oct. 1996), pp. 3391–3394. URL: <http://link.aps.org/doi/10.1103/PhysRevLett.77.3391>.
- [152] J. L. Smith and Q. Si. “Spatial correlations in dynamical mean-field theory”. In: *Phys. Rev. B* 61 (8 Feb. 2000), pp. 5184–5193. URL: <http://link.aps.org/doi/10.1103/PhysRevB.61.5184>.

- [153] R. Chitra and G. Kotliar. “Effect of Long Range Coulomb Interactions on the Mott Transition”. In: *Phys. Rev. Lett.* 84 (16 Apr. 2000), pp. 3678–3681. URL: <http://link.aps.org/doi/10.1103/PhysRevLett.84.3678>.
- [154] R. Chitra and G. Kotliar. “Effective-action approach to strongly correlated fermion systems”. In: *Phys. Rev. B* 63 (11 Mar. 2001), p. 115110. URL: <http://link.aps.org/doi/10.1103/PhysRevB.63.115110>.
- [155] I. S. Krivenko, A. N. Rubtsov, M. I. Katsnelson, and A. I. Lichtenstein. “Analytical approximation for single-impurity Anderson model”. In: *Jetp Lett.* 91 (2010), pp. 319–325. URL: <https://doi.org/10.1134/S0021364010060123>.
- [156] E. van Loon. “collective phenomena in strongly correlated systems”. PhD thesis. [Sl: sn], 2018.
- [157] T. Baier, E. Bick, and C. Wetterich. “Temperature dependence of antiferromagnetic order in the Hubbard model”. In: *Phys. Rev. B* 70 (12 Sept. 2004), p. 125111. URL: <https://link.aps.org/doi/10.1103/PhysRevB.70.125111>.
- [158] A. I. Lichtenstein and M. I. Katsnelson. “Ab initio calculations of quasiparticle band structure in correlated systems: LDA++ approach”. In: *Phys. Rev. B* 57 (12 Mar. 1998), pp. 6884–6895. URL: <https://link.aps.org/doi/10.1103/PhysRevB.57.6884>.
- [159] O. Gunnarsson, T. Schäfer, J. P. F. LeBlanc, E. Gull, J. Merino, G. Sangiovanni, G. Rohringer, and A. Toschi. “Fluctuation Diagnostics of the Electron Self-Energy: Origin of the Pseudogap Physics”. In: *Phys. Rev. Lett.* 114 (23 June 2015), p. 236402. URL: <https://link.aps.org/doi/10.1103/PhysRevLett.114.236402>.
- [160] C.-O. Almbladh, U. v. Barth, and R. v. Leeuwen. “Variational total energies from Φ - and Ψ - Derivable Theories”. In: *International Journal of Modern Physics B* 13.05n06 (1999), pp. 535–541. URL: <https://doi.org/10.1142/S0217979299000436>.
- [161] K. Held, C. Taranto, G. Rohringer, and A. Toschi. *Hedin Equations, GW, GW+DMFT, and All That*. 2011. URL: <https://arxiv.org/abs/1109.3972>.
- [162] G. Giuliani and G. Vignale. *Quantum theory of the electron liquid / Gabriele Giuliani, Giovanni Vignale*. Cambridge University Press, 2005. URL: <http://search.ebscohost.com/login.aspx?direct=true&db=cat00961a&AN=sissa.16255&site=eds-live>.

- [163] G. Rohringer and A. Toschi. “Impact of nonlocal correlations over different energy scales: A dynamical vertex approximation study”. In: *Phys. Rev. B* 94 (12 Sept. 2016), p. 125144. URL: <http://link.aps.org/doi/10.1103/PhysRevB.94.125144>.
- [164] T. Timusk and B. Statt. “The pseudogap in high-temperature superconductors: an experimental survey”. In: *Reports on Progress in Physics* 62.1 (Jan. 1999), pp. 61–122. URL: <https://doi.org/10.1088/0034-4885/62/1/002>.
- [165] M. R. Norman, D. Pines, and C. Kallin. “The pseudogap: friend or foe of high T_c ?” In: *Advances in Physics* 54.8 (2005), pp. 715–733. URL: <https://doi.org/10.1080/00018730500459906>.
- [166] P. A. Lee, N. Nagaosa, and X.-G. Wen. “Doping a Mott insulator: Physics of high-temperature superconductivity”. In: *Rev. Mod. Phys.* 78 (1 Jan. 2006), pp. 17–85. URL: <https://link.aps.org/doi/10.1103/RevModPhys.78.17>.
- [167] B. Keimer, S. A. Kivelson, M. R. Norman, S. Uchida, and J. Zaanen. “From quantum matter to high-temperature superconductivity in copper oxides”. In: *Nature* 518.7538 (2015), pp. 179–186.
- [168] S. Isakov, A. E. Antipov, and E. Gull. “Diagrammatic Monte Carlo for dual fermions”. In: *Phys. Rev. B* 94 (3 July 2016), p. 035102. URL: <https://link.aps.org/doi/10.1103/PhysRevB.94.035102>.
- [169] J. Gukelberger, E. Kozik, and H. Hafermann. “Diagrammatic Monte Carlo approach for diagrammatic extensions of dynamical mean-field theory: Convergence analysis of the dual fermion technique”. In: *Phys. Rev. B* 96 (3 July 2017), p. 035152. URL: <https://link.aps.org/doi/10.1103/PhysRevB.96.035152>.
- [170] J. C. Slater. “Magnetic Effects and the Hartree-Fock Equation”. In: *Phys. Rev.* 82 (4 May 1951), pp. 538–541. URL: <https://link.aps.org/doi/10.1103/PhysRev.82.538>.
- [171] N. D. Mermin and H. Wagner. “Absence of Ferromagnetism or Antiferromagnetism in One- or Two-Dimensional Isotropic Heisenberg Models”. In: *Phys. Rev. Lett.* 17 (26 Dec. 1966), pp. 1307–1307. URL: <https://link.aps.org/doi/10.1103/PhysRevLett.17.1307>.
- [172] P. C. Hohenberg. “Existence of Long-Range Order in One and Two Dimensions”. In: *Phys. Rev.* 158 (2 June 1967), pp. 383–386. URL: <https://link.aps.org/doi/10.1103/PhysRev.158.383>.

- [173] P. Werner, E. Gull, O. Parcollet, and A. J. Millis. “Momentum-selective metal-insulator transition in the two-dimensional Hubbard model: An 8-site dynamical cluster approximation study”. In: *Phys. Rev. B* 80 (4 July 2009), p. 045120. URL: <https://link.aps.org/doi/10.1103/PhysRevB.80.045120>.
- [174] E. Gull, M. Ferrero, O. Parcollet, A. Georges, and A. J. Millis. “Momentum-space anisotropy and pseudogaps: A comparative cluster dynamical mean-field analysis of the doping-driven metal-insulator transition in the two-dimensional Hubbard model”. In: *Phys. Rev. B* 82 (15 Oct. 2010), p. 155101. URL: <https://link.aps.org/doi/10.1103/PhysRevB.82.155101>.
- [175] W. Wu, M. Ferrero, A. Georges, and E. Kozik. “Controlling Feynman diagrammatic expansions: Physical nature of the pseudogap in the two-dimensional Hubbard model”. In: *Phys. Rev. B* 96 (4 July 2017), p. 041105. URL: <https://link.aps.org/doi/10.1103/PhysRevB.96.041105>.
- [176] F. Šimkovic, J. P. F. LeBlanc, A. J. Kim, Y. Deng, N. V. Prokof’ev, B. V. Svistunov, and E. Kozik. “Extended Crossover from a Fermi Liquid to a Quasiantiferromagnet in the Half-Filled 2D Hubbard Model”. In: *Phys. Rev. Lett.* 124 (1 Jan. 2020), p. 017003. URL: <https://link.aps.org/doi/10.1103/PhysRevLett.124.017003>.
- [177] T. Schäfer, A. Toschi, and K. Held. “Dynamical vertex approximation for the two-dimensional Hubbard model”. In: *Journal of Magnetism and Magnetic Materials* 400 (2016). Proceedings of the 20th International Conference on Magnetism (Barcelona) 5-10 July 2015, pp. 107–111. URL: <https://www.sciencedirect.com/science/article/pii/S030488531530411X>.
- [178] P. Sun and G. Kotliar. “Extended dynamical mean-field theory and GW method”. In: *Phys. Rev. B* 66 (8 Aug. 2002), p. 085120. URL: <https://link.aps.org/doi/10.1103/PhysRevB.66.085120>.
- [179] E. G. C. P. van Loon, H. Hafermann, A. I. Lichtenstein, A. N. Rubtsov, and M. I. Katsnelson. “Plasmons in Strongly Correlated Systems: Spectral Weight Transfer and Renormalized Dispersion”. In: *Phys. Rev. Lett.* 113 (24 Dec. 2014), p. 246407. URL: <https://link.aps.org/doi/10.1103/PhysRevLett.113.246407>.
- [180] E. A. Stepanov, L. Peters, I. S. Krivenko, A. I. Lichtenstein, M. I. Katsnelson, and A. N. Rubtsov. “Quantum spin fluctuations and evolution of electronic structure in cuprates”. In: *npj Quantum Materials* 3 (1 Oct. 2018), p. 54. URL: <https://doi.org/10.1038/s41535-018-0128-x>.

- [181] H. Hafermann, P. Werner, and E. Gull. “Efficient implementation of the continuous-time hybridization expansion quantum impurity solver”. In: *Computer Physics Communications* 184.4 (2013), pp. 1280–1286. URL: <http://www.sciencedirect.com/science/article/pii/S0010465512004092>.
- [182] H. Hafermann. “Self-energy and vertex functions from hybridization-expansion continuous-time quantum Monte Carlo for impurity models with retarded interaction”. In: *Phys. Rev. B* 89 (23 June 2014), p. 235128. URL: <https://link.aps.org/doi/10.1103/PhysRevB.89.235128>.
- [183] B. Bauer, L. D. Carr, H. G. Evertz, A. Feiguin, J. Freire, S. Fuchs, L. Gamper, J. Gukelberger, E. Gull, S. Guertler, A. Hehn, R. Igarashi, S. V. Isakov, D. Koop, P. N. Ma, P. Mates, H. Matsuo, O. Parcollet, G. Pawłowski, J. D. Picon, L. Pollet, E. Santos, V. W. Scarola, U. Schollwöck, C. Silva, B. Surer, S. Todo, S. Trebst, M. Troyer, M. L. Wall, P. Werner, and S. Wessel. “The ALPS project release 2.0: open source software for strongly correlated systems”. In: *Journal of Statistical Mechanics: Theory and Experiment* 2011.05 (May 2011), P05001. URL: <https://doi.org/10.1088/1742-5468/2011/05/p05001>.
- [184] E. G. C. P. van Loon, F. Krien, H. Hafermann, E. A. Stepanov, A. I. Lichtenstein, and M. I. Katsnelson. “Double occupancy in dynamical mean-field theory and the dual boson approach”. In: *Phys. Rev. B* 93 (15 Apr. 2016), p. 155162. URL: <https://link.aps.org/doi/10.1103/PhysRevB.93.155162>.
- [185] C. Husemann and M. Salmhofer. “Efficient parametrization of the vertex function, Ω scheme, and the t, t' Hubbard model at van Hove filling”. In: *Phys. Rev. B* 79 (19 May 2009), p. 195125. URL: <https://link.aps.org/doi/10.1103/PhysRevB.79.195125>.
- [186] S. Friederich, H. C. Krahl, and C. Wetterich. “Four-point vertex in the Hubbard model and partial bosonization”. In: *Phys. Rev. B* 81 (23 June 2010), p. 235108. URL: <https://link.aps.org/doi/10.1103/PhysRevB.81.235108>.
- [187] H. Park, K. Haule, and G. Kotliar. “Cluster Dynamical Mean Field Theory of the Mott Transition”. In: *Phys. Rev. Lett.* 101 (18 Oct. 2008), p. 186403. URL: <https://link.aps.org/doi/10.1103/PhysRevLett.101.186403>.
- [188] E. G. C. P. van Loon, M. I. Katsnelson, and H. Hafermann. “Second-order dual fermion approach to the Mott transition in the two-dimensional Hubbard model”. In: *Phys. Rev. B* 98 (15 Oct. 2018), p. 155117. URL: <https://link.aps.org/doi/10.1103/PhysRevB.98.155117>.

- [189] A. N. Rubtsov, E. A. Stepanov, and A. I. Lichtenstein. “Collective magnetic fluctuations in Hubbard plaquettes captured by fluctuating local field method”. In: *Phys. Rev. B* 102 (22 Dec. 2020), p. 224423. URL: <https://link.aps.org/doi/10.1103/PhysRevB.102.224423>.
- [190] P. M. Bonetti. “Accessing the ordered phase of correlated Fermi systems: Vertex bosonization and mean-field theory within the functional renormalization group”. In: *Phys. Rev. B* 102 (23 Dec. 2020), p. 235160. URL: <https://link.aps.org/doi/10.1103/PhysRevB.102.235160>.
- [191] C. Husemann, K.-U. Giering, and M. Salmhofer. “Frequency-dependent vertex functions of the (t, t') Hubbard model at weak coupling”. In: *Phys. Rev. B* 85 (7 Feb. 2012), p. 075121. URL: <https://link.aps.org/doi/10.1103/PhysRevB.85.075121>.
- [192] A. Eberlein. *Functional renormalization group study of fluctuation effects in fermionic superfluids*. 2014. URL: <https://arxiv.org/abs/1407.7661>.
- [193] N. Wentzell, G. Li, A. Tagliavini, C. Taranto, G. Rohringer, K. Held, A. Toschi, and S. Andergassen. “High-frequency asymptotics of the vertex function: Diagrammatic parametrization and algorithmic implementation”. In: *Phys. Rev. B* 102 (8 Aug. 2020), p. 085106. URL: <https://link.aps.org/doi/10.1103/PhysRevB.102.085106>.
- [194] E. A. Stepanov, S. Brener, V. Harkov, M. I. Katsnelson, and A. I. Lichtenstein. “Spin dynamics of itinerant electrons: Local magnetic moment formation and Berry phase”. In: *Phys. Rev. B* 105 (15 Apr. 2022), p. 155151. URL: <https://link.aps.org/doi/10.1103/PhysRevB.105.155151>.
- [195] P. Chalupa, T. Schäfer, M. Reitner, D. Springer, S. Andergassen, and A. Toschi. “Fingerprints of the Local Moment Formation and its Kondo Screening in the Generalized Susceptibilities of Many-Electron Problems”. In: *Phys. Rev. Lett.* 126 (5 Feb. 2021), p. 056403. URL: <https://link.aps.org/doi/10.1103/PhysRevLett.126.056403>.
- [196] A. Szilva, Y. Kvashnin, E. A. Stepanov, L. Nordström, O. Eriksson, A. I. Lichtenstein, and M. I. Katsnelson. *Quantitative theory of magnetic interactions in solids*. 2022. URL: <https://arxiv.org/abs/2206.02415>.
- [197] A. Galler, P. Thunström, J. Kaufmann, M. Pickem, J. M. Tomczak, and K. Held. “The *Ab initio* DfA Project v1.0: Non-local correlations beyond and susceptibilities within dynamical mean-field theory”. In: *Computer Physics Communications* 245 (2019), p. 106847. URL: <http://www.sciencedirect.com/science/article/pii/S0010465519302243>.

- [198] P. M. Bonetti, A. Toschi, C. Hille, S. Andergassen, and D. Vilaridi. “Single-boson exchange representation of the functional renormalization group for strongly interacting many-electron systems”. In: *Phys. Rev. Research* 4 (1 Jan. 2022), p. 013034. URL: <https://link.aps.org/doi/10.1103/PhysRevResearch.4.013034>.
- [199] W. Metzner, M. Salmhofer, C. Honerkamp, V. Meden, and K. Schönhammer. “Functional renormalization group approach to correlated fermion systems”. In: *Rev. Mod. Phys.* 84 (1 Mar. 2012), pp. 299–352. URL: <https://link.aps.org/doi/10.1103/RevModPhys.84.299>.
- [200] C. Platt, W. Hanke, and R. Thomale. “Functional renormalization group for multi-orbital Fermi surface instabilities”. In: *Advances in Physics* 62.4-6 (2013), pp. 453–562. URL: <https://doi.org/10.1080/00018732.2013.862020>.
- [201] C. Taranto, S. Andergassen, J. Bauer, K. Held, A. Katanin, W. Metzner, G. Rohringer, and A. Toschi. “From Infinite to Two Dimensions through the Functional Renormalization Group”. In: *Phys. Rev. Lett.* 112 (19 May 2014), p. 196402. URL: <http://link.aps.org/doi/10.1103/PhysRevLett.112.196402>.
- [202] N. Wentzell, C. Taranto, A. Katanin, A. Toschi, and S. Andergassen. “Correlated starting points for the functional renormalization group”. In: *Phys. Rev. B* 91 (4 Jan. 2015), p. 045120. URL: <https://link.aps.org/doi/10.1103/PhysRevB.91.045120>.
- [203] A. A. Katanin. “Extended dynamical mean field theory combined with the two-particle irreducible functional renormalization-group approach as a tool to study strongly correlated systems”. In: *Phys. Rev. B* 99 (11 Mar. 2019), p. 115112. URL: <https://link.aps.org/doi/10.1103/PhysRevB.99.115112>.
- [204] A. Tagliavini, C. Hille, F. B. Kugler, S. Andergassen, A. Toschi, and C. Honerkamp. “Multiloop functional renormalization group for the two-dimensional Hubbard model: Loop convergence of the response functions”. In: *SciPost Phys.* 6 (1 2019), p. 9. URL: <https://scipost.org/10.21468/SciPostPhys.6.1.009>.
- [205] V. Y. Irkhin, A. A. Katanin, and M. I. Katsnelson. “Effects of van Hove singularities on magnetism and superconductivity in the $t - t'$ Hubbard model: A parquet approach”. In: *Phys. Rev. B* 64 (16 Oct. 2001), p. 165107. URL: <https://link.aps.org/doi/10.1103/PhysRevB.64.165107>.

- [206] G. Li, N. Wentzell, P. Pudleiner, P. Thunström, and K. Held. “Efficient implementation of the parquet equations: Role of the reducible vertex function and its kernel approximation”. In: *Phys. Rev. B* 93 (16 Apr. 2016), p. 165103. URL: <https://link.aps.org/doi/10.1103/PhysRevB.93.165103>.
- [207] O. Gunnarsson, T. Schäfer, J. P. F. LeBlanc, J. Merino, G. Sangiovanni, G. Rohringer, and A. Toschi. “Parquet decomposition calculations of the electronic self-energy”. In: *Phys. Rev. B* 93 (24 June 2016), p. 245102. URL: <https://link.aps.org/doi/10.1103/PhysRevB.93.245102>.
- [208] J. C. Slater. “Magnetic Effects and the Hartree-Fock Equation”. In: *Phys. Rev.* 82 (4 May 1951), pp. 538–541. URL: <https://link.aps.org/doi/10.1103/PhysRev.82.538>.

List of Publications

1. E. A. Stepanov, V. Harkov, A. I. Lichtenstein, “Consistent partial bosonization of the extended Hubbard model”. *Phys. Rev. B* **100**, 205115 (2019)

The author of this thesis implemented the D-TRILEX part of the code and performed the numerical calculations. He participated in the discussion and evaluation of the results.

2. M. Vandelli, V. Harkov, E. A. Stepanov, J. Gukelberger, E. Kozik, A. Rubio, A. I. Lichtenstein, “Dual boson diagrammatic Monte Carlo approach applied to the extended Hubbard model”. *Phys. Rev. B* **102**, 195109 (2020)

The author of this thesis performed the DB calculations and participated in the discussion and evaluation of the results.

3. T. Schäfer, N. Wentzell, F. Šimkovic, Y.-Y. He, C. Hille, M. Klett, C. J. Eckhardt, B. Arzhang, V. Harkov, F. M. C.-M. Le Régent, A. Kirsch, Y. Wang, A. J. Kim, E. Kozik, E. A. Stepanov, A. Kauch, S. Andergassen, P. Hansmann, D. Rohe, Y. M. Vilk, J. P. F. LeBlanc, S. Zhang, A.-M. S. Tremblay, M. Ferrero, O. Parcollet, A. Georges, “Tracking the Footprints of Spin Fluctuations: A MultiMethod, MultiMessenger Study of the Two-Dimensional Hubbard Model”. *Phys. Rev. X* **11**, 011058 (2021)

The author of this thesis implemented the additional W sc scheme to the code and performed the different DB calculations. He participated in the discussion, evaluation and writing of the results corresponding to the DB method.

4. V. Harkov, A. I. Lichtenstein, F. Krien, “Parameterizations of local vertex corrections from weak to strong coupling: Importance of the Hedin three-leg vertex”. *Phys. Rev. B* **104**, 125141 (2021)

The author of this thesis performed the numerical calculations of the results and contributed significantly to the writing of the manuscript. He also implemented the w and asymptotic approximations participated in the discussion and evaluation of the results.

5. V. Harkov, M. Vandelli, S. Brener, A. I. Lichtenstein, E. A. Stepanov, “Impact of partially bosonized collective fluctuations on electronic degrees of freedom”. *Phys. Rev. B* **103**, 245123 (2021)

The author of this thesis implemented the D-TRILEX part of the code and performed the numerical calculations of the LDA and D-TRILEX results. He contributed significantly to the writing of the manuscript and participated in the discussion and evaluation of the results.

6. E. A. Stepanov, S. Brener, V. Harkov, M. I. Katsnelson, A. I. Lichtenstein, “Spin dynamics of itinerant electrons: local magnetic moment formation and Berry phase”. *Phys. Rev. B* **105**, 155151 (2021)

The author of this thesis performed the implementation and numerical calculations of the results. He also participated in the discussion and evaluation of the results.

7. E. A. Stepanov, V. Harkov, M. Rösner, A. I. Lichtenstein, M. I. Katsnelson, A. N. Rudenko, “Coexisting charge density wave and ferromagnetic instabilities in monolayer InSe”. *npj Computational Materials* **8**, 118 (2022)

The author of this thesis implemented the D-TRILEX part of the code and helped to perform the numerical D-TRILEX calculations and visualize the results. He also performed the analytical continuations.

8. M. Vandelli, J. Kaufmann, M. El-Nabulsi, V. Harkov, A. I. Lichtenstein, E. A. Stepanov, “Multi-band D-TRILEX approach to materials with strong electronic correlations”. *SciPost Physics* **13**, 036 (2022)

The author of this thesis participated in the discussion and evaluation of the results and contributed to the writing. He also helped testing the multi-band D-TRILEX code.

Preprint:

9. M. Vandelli, J. Kaufmann, V. Harkov, A. I. Lichtenstein, K. Held, E. A. Stepanov, “Extended regime of coexisting metallic and insulating phases in a two-orbital electronic system”. *arXiv:2204.06426* (2022)

The author of this thesis performed the DMFT calculations and participated in the discussion and evaluation of the results.

Eidesstattliche Versicherung / Declaration on oath

Hiermit versichere ich an Eides statt, die vorliegende Dissertationsschrift selbst verfasst und keine anderen als die angegebenen Hilfsmittel und Quellen benutzt zu haben.

Hamburg, den 05.12.2022

Unterschrift der Doktorandin / des Doktoranden

Acknowledgments

First of all I want to thank my supervisor Alexander Lichtenstein who supported me over the years as a Bachelor, Master and PhD student and my supervisor Serguei Molodtsov for giving me the opportunity to work in a great team in the European XFEL and for his great and kind support. Special thanks go to my third supervisor Evgeny Stepanov for teaching me a lot about physics and beyond. Thanks to his commitment and his support I managed to achieve all my goals and even more. Especially, I will not forget the great time we have spent in Japan. I also want to thank my great friends Andrej Lehmann, Solomiya Terletska, Hristiana Atanasova, Matteo Vandelli and Mohammed El-Nabulsi, which I made during the time at the university. The time we spent together I will remember for the rest of my life. I am very thankful for your enormous support. Another special thank goes to Friedrich Krien for supervising me during my time as a Bachelor and Master student and even supporting me during the time as a PhD student. I learn a lot from you and always appreciate your support and great advises. Furthermore, I want to thank all our group members for the great time and fruitful discussions and my family and friends for the enormous support.

Viktor Harkov

Hamburg, 2022

Ich versichere, dass dieses gebundene Exemplar der Dissertation und das in elektronischer Form eingereichte Dissertationsexemplar und das bei der Fakultät zur Archivierung eingereichte gedruckte gebundene Exemplar der Dissertationsschrift identisch sind.

Hamburg, den 05.12.2022

Unterschrift der Doktorandin / des Doktoranden